A UNITED STATES DEPARTMENT OF COMMERCE PUBLICATION

SECTION A

JOURNAL OF RESEARCH

of the NATIONAL BUREAU OF STANDARDS

JNBAAR 77A (5) 569–690, Sept.–Oct. 1973

Physics and Chemistry

U.S. DEPARTMENT OF COMMERCE
National Bureau of Standards

Journal of Research

of the

National Bureau of Standards

A. Physics and Chemistry

Sept.–Oct. • 1973

VOLUME • 77A

NUMBER • 5

Editor: C. W. Beckett

Associate Editor: D. D. Wagman

Publication dates:
Feb. 1, Apr. 1, June 1, Aug. 1, Oct. 1, Dec. 1, 1973

J. Res. Nat. Bur. Stand. (U.S.), A

JOURNAL OF RESEARCH

The National Bureau of Standards Journal of Research reports research and development in the fields of activity shown at right. Also included from time to time are survey articles on topics closely related to the Bureau's scientific and technical program.

The Journal is published in two separate sections as follows:

A. Physics and Chemistry

Contains papers of interest primarily to scientists working in these fields. Issued six times a year. Annual subscription: domestic, $17.00; foreign $21.25. Single copy, varies.

B. Mathematical Sciences

Presents studies and compilations designed mainly for the mathematician and the theoretical physicist. Issued quarterly. Annual subscription: domestic, $9.00; foreign, $11.25. Single copy, $2.25.

The National Bureau of Standards[1] was established by an act of Congress March 3, 1901. The Bureau's overall goal is to strengthen and advance the Nation's science and technology and facilitate their effective application for public benefit. To this end, the Bureau conducts research and provides: (1) a basis for the Nation's physical measurement system, (2) scientific and technological services for industry and government, (3) a technical basis for equity in trade, and (4) technical services to promote public safety. The Bureau consists of the Institute for Basic Standards, the Institute for Materials Research, the Institute for Applied Technology, the Institute for Computer Sciences and Technology, and the Office for Information Programs.

THE INSTITUTE FOR BASIC STANDARDS provides the central basis within the United States of a complete and consistent system of physical measurement; coordinates that system with measurement systems of other nations; and furnishes essential services leading to accurate and uniform physical measurements throughout the Nation's scientific community, industry, and commerce. The Institute consists of a Center for Radiation Research, an Office of Measurement Services and the following divisions:

Applied Mathematics — Electricity — Mechanics — Heat — Optical Physics — Nuclear Sciences[3] — Applied Radiation[3] — Quantum Electronics[3] — Electromagnetics[3] — Time and Frequency[3] — Laboratory Astrophysics[3] — Cryogenics[3].

THE INSTITUTE FOR MATERIALS RESEARCH conducts materials research leading to improved methods of measurement, standards, and data on the properties of well-characterized materials needed by industry, commerce, educational institutions, and Government; provides advisory and research services to other Government agencies; and develops, produces, and distributes standard reference materials. The Institute consists of the Office of Standard Reference Materials and the following divisions:

Analytical Chemistry — Polymers — Metallurgy — Inorganic Materials — Reactor Radiation — Physical Chemistry.

THE INSTITUTE FOR APPLIED TECHNOLOGY provides technical services to promote the use of available technology and to facilitate technological innovation in industry and Government; cooperates with public and private organizations leading to the development of technological standards (including mandatory safety standards), codes and methods of test; and provides technical advice and services to Government agencies upon request. The Institute consists of a Center for Building Technology and the following divisions and offices:

Engineering and Product Standards — Weights and Measures — Invention and Innovation — Product Evaluation Technology — Electronic Technology — Technical Analysis — Measurement Engineering — Structures, Materials, and Life Safety[4] — Building Environment[4] — Technical Evaluation and Application[4] — Fire Technology.

THE INSTITUTE FOR COMPUTER SCIENCES AND TECHNOLOGY conducts research and provides technical services designed to aid Government agencies in improving cost effectiveness in the conduct of their programs through the selection, acquisition, and effective utilization of automatic data processing equipment; and serves as the principal focus within the executive branch for the development of Federal standards for automatic data processing equipment, techniques, and computer languages. The Center consists of the following offices and divisions:

Information Processing Standards — Computer Information — Computer Services — Systems Development — Information Processing Technology.

THE OFFICE FOR INFORMATION PROGRAMS promotes optimum dissemination and accessibility of scientific information generated within NBS and other agencies of the Federal Government; promotes the development of the National Standard Reference Data System and a system of information analysis centers dealing with the broader aspects of the National Measurement System; provides appropriate services to ensure that the NBS staff has optimum accessibility to the scientific information of the world. The Office consists of the following organizational units:

Office of Standard Reference Data — Office of Technical Information and Publications — Library — Office of International Relations.

---

[1] Headquarters and Laboratories at Gaithersburg, Maryland, unless otherwise noted; mailing address Washington, D.C. 20234.
[3] Part of the Center for Radiation Research.
[4] Located at Boulder, Colorado 80302.
[4] Part of the Center for Building Technology.

U.S. DEPARTMENT OF COMMERCE
Frederick B. Dent, Secretary
NATIONAL BUREAU OF STANDARDS
Richard W. Roberts, Director

Order all publications from the Superintendent of Documents
U.S. Government Printing Office, Washington, D.C. 20402

The Secretary of Commerce has determined that the publication of this periodical is necessary in the transaction of the public business required by law of this Department. Use of funds for printing this periodical has been approved by the Director of the Office of Management and Budget through June 30, 1976.

JOURNAL OF RESEARCH of the National Bureau of Standards—A. Physics and Chemistry
Vol. 77A, No. 5, September–October 1973

Enthalpies of Precipitation of Silver Halides; Entropy of the Aqueous Silver Ion

Donald D. Wagman and Marthada V. Kilday

Institute for Materials Research, National Bureau of Standards, Washington, D.C. 20234

(May 25, 1973)

The enthalpies of precipitation of silver halides and the enthalpies of solution of $AgNO_3$, KCl, and KBr in H_2O were measured in an adiabatic solution calorimeter.

From the enthalpy measurements of KCl(c) and KBr(c) in $AgNO_3$(aq), and of $AgNO_3$(c) in KCl(aq), in KBr(aq), and in KI(aq), we calculated (in $kJ \cdot mol^{-1}$) −65.724, −84.826, and −111.124 for $\Delta H°$ pptn(298.15 K) for the averages of the chloride, bromide, and iodide reactions, respectively.

A reevaluation of the data for the enthalpy of solution of $AgNO_3$(c) has resulted in our selected best value,

$$\Delta H°(\infty)\,(298.15\ \text{K}) = 22.730 + 0.084\ \text{kJ} \cdot \text{mol}^{-1}$$

$$= 5.433 \pm 0.020\ \text{kcal} \cdot \text{mol}^{-1}$$

A table of enthalpies of dilution of $AgNO_3$(aq) is also given.

The average standard entropy for the aqueous silver ion at 298.15 K is found to be

$$S°[Ag^+(aq)] = 73.42 \pm 0.20\ \text{J} \cdot \text{mol}^{-1} \cdot \text{K}^{-1}$$

$$= 17.55 \pm 0.05\ \text{cal} \cdot \text{mol}^{-1} \cdot \text{K}^{-1}.$$

Key words: AgBr; AgCl; AgI; $AgNO_3$; enthalpy of dilution; enthalpy of precipitation; enthalpy of solution; entropy; heat of reaction; KBr; KCl; solution calorimetry; thermochemistry.

1. Introduction

The thermodynamic properties of the silver halides, AgCl, AgBr, and AgI, are extremely important quantities in determining the properties of many other substances. In conjunction with metallic silver they form electrochemical half-cells of high reproducibility. These half-cells have been combined with many other electrodes to yield thermodynamic data of high precision for a number of chemical reactions. In particular, these electrodes have been combined with the corresponding half-cells containing the aqueous halogen acids and salts to determine the activities of the acids and salts at various temperatures [1];[1] these acids are in turn the keystones for the establishment of a self-consistent set of tables of enthalpies and Gibbs energies of formation [2]. However, the final verification of electrochemical data must come from other sources. To quote from Harned and Owen [3]:

"... Cell reactions, no matter how simple and obvious, must be treated as hypothetical until it can be shown that thermodynamic quantities calculated from the electromotive force, ΔF, ΔH, equilibrium constants, etc., have been checked by other evidence."

In the course of our reevaluation of the thermodynamic data on silver and silver compounds, we compared the electrochemical data on the silver-silver halide systems for the reaction $Ag^+(aq) + X^-(aq) \rightarrow AgX(c)$ [$X \equiv Cl^-$, Br^-, I^-] with the available calorimetric measurements for the reactions. For this comparison we reextrapolated the EMF measurements of Owen and Brinkley [4] using more recent values [45] for the various fundamental constants and converting to absolute electrical units. These results were then combined with the cell data for the silver-silver halide electrodes [1] to calculate the enthalpies of the precipitation reactions. The summary comparison is shown in table 1. Because of the scatter in the various calorimetric measurements we decided to redetermine the enthalpies of precipitation of the three silver halides and establish more precisely the thermodynamic validity of the EMF data for these systems. The reaction scheme used is as follows:

$$AgNO_3(c) + KX(\infty) \longrightarrow AgX(c) + KNO_3(\infty);\ \Delta H_1$$
$$AgNO_3(c) \longrightarrow AgNO_3(\infty);\ \Delta H_2$$

$$AgNO_3(\infty) + KX(\infty) \longrightarrow AgX(c) + KNO_3(\infty);\ \Delta H_1 - \Delta H_2$$

[1] Figures in brackets indicate literature references at the end of this paper.

508-076 O - 73 - 2

TABLE 1. *Comparison of data for the enthalpy of precipitation of the silver halides obtained from various methods*

Authors and year	Method	$-\Delta H°(298.15\ K)$ [a]	Reference
		$kJ \cdot mol^{-1}$	
$Ag^+ + Cl^- \rightarrow AgCl(c)$:			
Lange and Fuoss (1927)	Calorimetric	65.710	[5]
Thomsen (1883)	do	64.98	[6]
Owen and Brinkley (1938) [b]	EMF	65.643	[4]
Gledhill and Malan (1954)	Solubility	66.78	[13]
$Ag^+ + Br^- \rightarrow AgBr(c)$:			
Berthelot (1881)	Calorimetric	84.1	[7]
Gellner and Skinner (1949)	do	84.9	[8]
Roth (1944)	do	90.58	[9]
Thomsen (1883)	do	82.84	[6]
Owen and Brinkley (1938) [b]	EMF	84.655	[4]
Gledhill and Malan (1954)	Solubility	85.56	[13]
$Ag^+ + I^- \rightarrow AgI(c)$:			
Gellner and Skinner (1949)	Calorimetric	109.9	[8]
Berthelot (1875)	do	110.96	[10]
Berthelot (1881)	do	110.08	[7]
Lange and Shibata (1930)	do	111.50	[11]
Yatsimirskii and Skutov (1954)	do	105.18	[12]
Thomsen (1883)	do	109.37	[6]
Owen and Brinkley (1938) [b]	EMF	111.01	[4]

[a] All calorimetric experimental data have been converted to conditions of infinite dilution at 298.15 K using necessary data from Parker [14]; 1 calorie = 4.1840 joules.

[b] Recalculated; see text.

In addition, for both chloride and bromide, we used the reciprocal scheme:

$$KX(c) + AgNO_3(\infty) \longrightarrow AgX(c) + KNO_3(\infty);\ \Delta H_1'$$
$$KX(c) \longrightarrow KX(\infty);\ \Delta H_2'$$

$$KX(\infty) + AgNO_3(\infty) \longrightarrow AgX(c) + KNO_3(\infty);\ \Delta H_1' - \Delta H_2'$$

2. Apparatus and Procedures

The vacuum-jacketed adiabatic solution calorimeter used in this work has been described in detail [15]. All parts of the calorimeter in contact with the calorimetric solutions are of platinum-iridium alloys or polytetrafluoroethylene (PTFE). The platinum sample holder shown in figure 1 has three interchangeable cylinders; the largest cylinder (volume, 2.7 cm^3) was used for the crystalline potassium halide samples and a smaller cylinder (volume, 1.9 cm^3), for the crystalline silver nitrate samples. The calorimetric solutions were approximately 300 cm^3 in volume.

The calorimeter temperatures were measured with a 25-Ω platinum resistance thermometer on which one kelvin is 0.10104 Ω at 298.15 K, or with a quartz-oscillator thermometer calibrated by comparison with the platinum resistance thermometer (see [15] for calibration data on these thermometers). The last certified calibrations on the standard resistors and the standard cell were made in June and July 1969, respectively. Dial corrections are based on our calibrations of the six-dial potentiometer in January 1969, and of the G–3 Mueller-type resistance bridge, in November 1970. The previous history of this equipment indicates that no significant drift occurred subsequent to these calibrations.

For the experiments reported in sections 3, 4, and 5, the analytical reagent grade (ACS certified) salts, KCl, KBr, KI, and $AgNO_3$ were used for the crystalline samples and for the aqueous solutions. The reagents were not dried nor further purified. The weight loss on drying the $AgNO_3$ indicated less than 0.01 percent moisture content.

The 1969 atomic weights [16] were used to calculate the following molar masses: $AgNO_3$, 169.8729; KCl, 74.555; KBr, 119.006; KI, 166.0065; and H_2O, 18.0154. For energy conversions, 1 thermochemical calorie = 4.1840 joules.

To obtain the buoyancy factors for calculating the mass of the crystalline samples, the following densities (in $g \cdot cm^{-3}$) were used: KCl, 1.988; KBr, 2.75; and $AgNO_3$, 4.352 [17a]. For the average conditions in this laboratory, the density of air was 0.00118 $g \cdot cm^{-3}$. The densities (in $g \cdot cm^{-3}$) at 296 K of the aqueous solutions of the salts were taken [17b] as follows: KCl (0.75 wt. %), 1.0013; KBr (1.19 wt. %), 1.0061; KI (1.67 wt. %), 1.0100; $AgNO_3$ Stock Soln. No. 1 (2.55 wt. %), 1.0194; and $AgNO_3$ Stock Soln. No. 2 (2.48 wt. %) and $AgNO_3$ Stock Soln. No. 3 (2.49 wt. %), 1.0188. Each stock solution was initially 2 dm^3 in volume and was stored in polyethylene bottles in a dark cabinet when not in use.

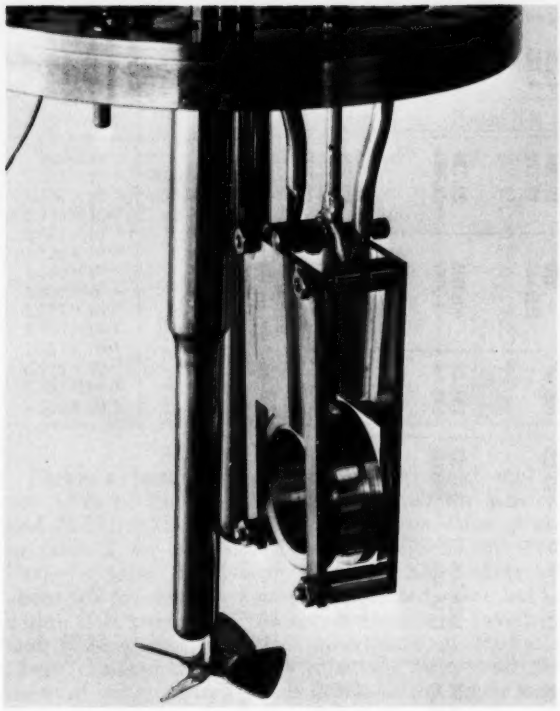

FIGURE 1. *Platinum parts inside the vessel of the adiabatic solution calorimeter.*

From left, the thermometer well, the stirrer, the heater well (rear), and the sample holder. The sample is contained in the cylinder which initially is at the top and sealed between the two flat plates by the PTFE o-rings. The plates are held together by the "trigger" bar (at top) until the initiation of reaction when the trigger bar releases the front plate, allowing the cylinder to drop to the position shown here.

In each experiment, the chemical reaction was preceded by an electrical calibration of the initial system and followed by an electrical calibration of the final system. Details of procedures and calculations for electrical calibrations and temperature measurements have been described [15].

3. Enthalpies of Solution of the Reagent Salts in H_2O

The enthalpies of solution in H_2O were measured for each of the salts used as crystalline samples in the experiments reported in sections 4 and 5. The data are given in table 2.

In the table, the Expt. No. is the serial number of experiments measured in this calorimeter, ΔRc is the corrected temperature rise during the chemical reaction period, $\overline{EEE}$ is the mean of the electrical energy equivalents for the initial and final systems (the average difference between the values for the initial and final systems was 0.1% and the maximum difference, 0.35%), Qr is the product of ΔRc and $\overline{EEE}$, and $\overline{T}$ reaction is the mean temperature of reaction. The corrected temperature rise, ΔRc, is calculated as the difference between the final and initial temperatures, obtained by solving the linear least-squares-fitted equations of the final and initial rating periods for the temperatures at the time of initiating the reaction. The stirring energy represents the difference between the total and the corrected temperature rise (see [15] for details about the stirring energy). The uncertainty in the stirring energy is about 5 percent or less of the stirring energy.

The heat of the chemical reaction, Qs, is obtained by subtracting the precisely-measured "Electrical energy added" during the endothermic chemical reaction from Qr. The isothermal enthalpy of reaction, $\Delta Hr(T)$, at the temperature of reaction (defined as the mean temperature of reaction) is $-Qs/$(mass of solute). The temperature of reaction for all of these measurements was near 298.15 K. The concentrations of the final solutions were varied by using differing amounts of solute. Corrections, given in column 12, were made to the enthalpy of reaction using the heat capacity and dilution data from the review by Parker [14] to obtain the enthalpy of solution at 298.15 K and infinite dilution, $\Delta H°(\infty)$, except for $AgNO_3$, where the dilution data obtained in this work (see table 3 and sec. 4) were used. The differences in concentration of the solute had little if any effect on the values obtained for $\Delta H°(\infty)$.

In Expt. No. 570, the rate of electrical heating during the chemical reaction was not sufficient to compensate for the heat absorbed by the chemical reaction when the sample holder was opened. Consequently, an abnormal temperature difference between the calorimeter vessel and the adiabatic shield occurred. A correction of -0.06 J (see [15] for the method of calculating the correction) was applied to the net heat evolved during the chemical reaction period, Qr.

In Expt. No. 582 the calorimeter was sealed by replacing the usual polytetrafluoroethylene o-ring bearing for the stirrer with a heavily lubricated nitrile o-ring and sealing the vent tube with the weighted platinum rod as described in [18]. This was to test the effect on the enthalpy of solution of the unvented calorimeter as compared to the usual vented calorimeter. It was found in our work with Standard Reference Material No. 724a, tris(hydroxymethyl)aminomethane, in 0.1 *N* HCl solution [18] that the enthalpy values obtained with the unvented (closed) calorimeter were about 3 percent more exothermic than those obtained with the calorimeter which was vented or open to the atmosphere. On the other hand no venting effect was found in the reactions of $H_2SO_4 \cdot 8\ H_2O$ with 0.02 and 0.08 *N* NaOH solutions [15], nor in the endothermic reaction of TRIS in NaOH(aq) [18]. In the present work, the enthalpy of solution in Expt. No. 582 using the unvented calorimeter is in satisfactory agreement with those in Expt. Nos. 570 and 571 in which the calorimeter was vented to the atmosphere. This is further evidence that the venting effect is characteristic of the reaction of SRM 724a in HCl(aq), and not a peculiarity of this calorimeter.

TABLE 2. *Data for the calorimetric measurements of* ΔHsoln *in* H_2O *for the solute reagents used in the precipitation reactions*

Expt. No.	Mass of solute	Mole ratio solute H_2O:	$\overline{EEE}$	Stirring [a] energy	ΔRc	$\bar{T}$ reaction	Qr	Electrical energy added	Qs	$\Delta Hr(T)$	Correction	$\Delta H°(\infty)$ (298.15 K)	
	g		$J \cdot \Omega^{-1}$	Ω	Ω	*K*	*J*	*J*	*J*	$J \cdot g^{-1}$	$kJ \cdot mol^{-1}$	$kJ \cdot mol^{-1}$	$kcal \cdot mol^{-1}$
	Solute: KCl(c)												
570	2.23251	560.7	17,166.3	0.001494	0.021240	298.121	[b] 364.55	889.304	−524.75	235.05	−0.339	17.185	4.107
571	1.32476	945.0	17,173.3	.001066	.052533	297.950	902.16	1213.292	−311.13	234.86	−.300	17.210	4.113
582	2.21843	564.3	17,163.0	.001696	.041378	297.899	710.17	1233.850	−523.68	236.06	−.339	17.260	4.125
											(Mean)	17.218	4.115
	Solute: KBr(c)												
572	2.38555	837.7	17,172.6	0.001442	0.047350	298.256	813.12	1214.322	−401.20	168.18	−0.255	19.759	4.722
573	4.69414	425.7	17,161.3	.001462	.024852	298.084	426.49	1218.319	−791.83	168.68	−.290	19.784	4.728
											(Mean)	19.772	4.725
	Solute: $AgNO_3$(c)												
574	2.55356	1117.0	17,182.3	0.001023	0.050921	298.238	874.94	1216.506	−341.57	133.76	−0.003	22.719	5.430
575	5.00255	570.1	17,187.7	.001417	.031904	297.932	548.36	1216.424	−668.06	133.54	+.047	22.732	5.433
			$J \cdot K^{-1}$	*K*	*K*								
[c] 730	1.08990	2616.7	1,732.60	0.01108	0.13472	298.115	233.41	379.622	−146.21	134.15	−0.085	22.703	5.426
[c] 737	0.56601	5038.1	1,731.54	.01472	.17311	298.373	299.75	375.687	−75.94	134.17	−.071	22.721	5.430
[c] 739	0.28578	9979.1	1,733.53	.00623	.06395	298.174	110.85	149.280	−38.43	134.46	−.104	22.737	5.434
											(Graphical limit, see text)	22.727	5.432

[a] The stirring rate in all experiments was 550 rpm except Expt. Nos. 730 and 737 (450 rpm) and No. 739 (250 rpm).

[b] A correction of −0.06 J was applied because of the large departure of the shield temperature from the vessel temperature. (See text, sec. 3).

[c] The calorimeter temperature was measured with a quartz-oscillator thermometer.

TABLE 3. *Apparent relative molal heat content of* $AgNO_3 \cdot n\ H_2O$(aq) *at 298.15 K*

m	n	ϕ_L or $-\Delta H$diln		
		This work		Parker [14]
molality		$J \cdot mol^{-1}$	$cal \cdot mol^{-1}$	$cal \cdot mol^{-1}$
5.551×10^{-4}	100,000	46	11	9
1.110×10^{-3}	50,000	64	15	12
2.775×10^{-3}	20,000	89	21	17
5.551×10^{-3}	10,000	105	25	19
1.110×10^{-2}	5,000	102	24	21
1.388×10^{-2}	4,000	97	23	21
1.850×10^{-2}	3,000	86	21	20
2.775×10^{-2}	2,000	64	15	16
3.700×10^{-2}	1,500	42	10	12
5.551×10^{-2}	1,000	−3	−1	2
6.938×10^{-2}	800	−35	−8	−6
9.251×10^{-2}	600	−76	−18	−20
1.110×10^{-1}	500	−112	−27	−32

Parker's "best" values [14] for $\Delta H°(\infty)$ (in $kJ \cdot mol^{-1}$) are 17.22 ± 0.04 for KCl(c), 19.87 ± 0.08 for KBr(c), and 22.59 ± 0.21 for $AgNO_3$(c). Our mean value given in table 2 for KCl is in excellent agreement with Parker's value. Our mean value for KBr differs by about 0.5 percent from Parker's selected value but is within 0.02 percent of the recent results of Tsvetkov and Rabinovich [19]. The uncertainty in Parker's "best" value for $AgNO_3$ is relatively large, and the mean of our measured values falls near the upper limit of the uncertainty.

4. Enthalpies of Solution and Dilution of $AgNO_3$

The measurements on the enthalpy of solution of $AgNO_3$(c) given in table 2 were extrapolated to infinite dilution using the relation [20]

$$\Delta H - \phi_L = \Delta H°(\infty) = \Delta H - 2879 m^{1/2} \times \rho + f(m)$$

where

$$\rho = (1 + m^{1/2})^{-1} - (1/m^{3/2}) [1 + m^{1/2} - (1/(1 + m^{1/2})) - 2 \ln (1 + m^{1/2})].$$

A plot of $\Delta H - 2879 m^{1/2} \rho$ $(= \Delta H')$ against the molality, m, yielded a curve linear below $m = 0.05$ with the intercept, $\Delta H°(\infty) = 22.727 \pm 0.029$ $kJ \cdot mol^{-1}$ $(5.432 \pm 0.007$ $kcal \cdot mol^{-1})$. From this value of $\Delta H°(\infty)$, values of ϕ_L were calculated for each measured concentration and a smooth curve plotted versus $m^{1/2}$. Values of ϕ_L were interpolated from the curve and are given in table 3 for various values of m. We estimate the uncertainty in ϕ_L to be about ± 10 $J \cdot mol^{-1}$ $(\pm 2$ $cal \cdot mol^{-1})$. Corresponding values estimated by Parker [14] are also shown in the table. Parker's values were obtained from very limited data and the present work indicates that her estimates were only slightly in error.

A summary of earlier calorimetric measurements of the enthalpy of solution of $AgNO_3$(c) (corrected to infinite dilution) is given in table 4. We have combined our dilute solution measurements with those of Graham and Hepler [23] and extrapolated the combined set of data as described above to obtain a selected best value of $\Delta H°(\infty) = 22.730 \pm 0.042$ $kJ \cdot mol^{-1}$ or 5.433 ± 0.010 $kcal \cdot mol^{-1}$ (see fig. 2).

TABLE 4. *Enthalpy of solution of* $AgNO_3$ *in* H_2O *at 298.15 K*

Investigator	$\Delta H°(\infty)$		Reference
	$kJ \cdot mol^{-1}$	$kcal \cdot mol^{-1}$	
Thomsen (1883)	22.51 ± 0.21	5.38 ± 0.05	[6]
Roth (1944)	22.573 ± 0.21	5.395 ± 0.050	[9]
Lange and Martin (1937)	22.907	5.475	[21]
Smith, Brown, and Pitzer (1937)	22.468 ± 0.21	5.370 ± 0.050	[22]
Graham and Hepler (1958)	22.740 ± 0.17	5.435 ± 0.040	[23]
Shidlovskii and Voskresenskii (1963)	22.38	5.35	[24]
This work	22.727 ± 0.084	5.432 ± 0.020	
Selected Value	22.730 ± 0.084	5.433 ± 0.020	

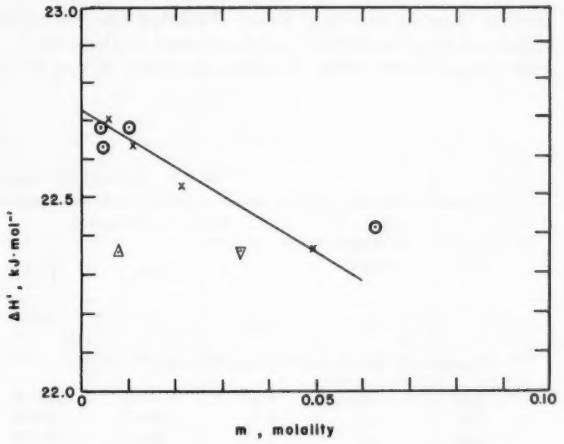

FIGURE 2. *Extrapolation of heat of solution measurements on* $AgNO_3$ *in the dilute range below 0.05 molal) to infinite dilution at 298.15 K.*

⊙ Graham and Hepler [23]; △ Smith, Brown, and Pitzer [22]; ▽ Roth [9]; X This work. (See sec. 4.)

5. Silver Halide Precipitation Experiments

The enthalpies of reaction were measured for five reactions in which the silver halide precipitates were formed: KCl(c) in 0.15 *N* $AgNO_3$(aq), reaction I; $AgNO_3$(c) in 0.1 *N* KCl(aq), reaction II; KBr(c) in 0.15 *N* $AgNO_3$(aq), reaction III; $AgNO_3$(c) in 0.1 *N* KBr(aq), reaction IV; and $AgNO_3$(c) in 0.1 *N* KI(aq), reaction V. The reaction which would complete the set, KI(c), in $AgNO_3$(aq), was not measured because of time limita-

tions. The results of the five reactions measured here were sufficient to produce the desired information. The fluoride reactions were not included because of large uncertainties in the related data.

The data for the 21 silver halide precipitation experiments are given in tables 5 and 6. Explanations of Expt. No., ΔRc, $\overline{EEE}$, Qr, $\bar{T}$ reaction, and Stirring energy are given in section 3 and [15]. In these tables and the discussions, solute refers to the crystalline samples of KCl, KBr, and $AgNO_3$, and solvent salt refers to the KCl, KBr, or $AgNO_3$ dissolved in the initial aqueous calorimetric solutions. In each group of reactions, there is one experiment in which the mass of solute was approximately half that used in the other experiments. The variations in the concentration of the solute had a negligible effect on the enthalpy of reaction in this range.

In preliminary experiments (not given in the tables) we encountered some of the difficulties to be expected in this type of reaction. Upon initiating the reaction, there was the expected rapid increase in the calorimeter temperature; after 15 min, the slope of the time-temperature curve was about ten times that preceding the reaction; after three hours, the slope was about three times that of the initial rating period for the reaction, indicating that heat was still being evolved but at a slowly decreasing rate. Upon opening the calorimeter vessel, we found (in addition to the expected flocculent precipitates, white AgCl and yellow AgBr) at the bottom of the vessel a solid mass of material (which assumed the shape of the vessel) covered by a thin sheet of material which had a paper-like consistency when dried. Apparently the samples, of higher density than the solutions, had fallen to the bottom of the vessel. The precipitates formed a protective layer over the unreacted sample and inhibited access of the solution to the crystalline sample. In Expt. No. 568 (reaction I, tables 5 and 6) the stirring rate was increased from 350 rpm to 550 rpm and after 50 min the slope of the time-temperature curve was approximately equal to that of the rating period preceding the reaction. All of the product was the flocculent, white AgCl with no evidence of the incomplete reaction. The stirring rate of 550 rpm was used in all experiments given in table 6.

TABLE 5. *Data for the silver halide precipitation experiments*

Expt. No.	Reaction period	Solvent composition			Solute	Mole ratios		
		Conc.	Salt	H_2O		H_2O : solute	Solvent salt : solute	H_2O : solvent salt
	min	*wt %*	*mol*	*mol*	*mol*			
Reaction I: KCl(c) in 0.15*N* $AgNO_3$(aq)								
568	50	2.55	0.04695	16.906	0.029933	565	1.57	360
581	50	2.55	.04697	16.906	.029840	567	1.57	360
605	25	2.49	.04576	16.916	.029109	581	1.57	370
606	170	2.49	.04575	16.916	.029208	579	1.57	370
607	> 30, < 95	2.49	.04576	16.917	.027368	618	1.67	370
608	25	2.49	.04575	16.916	.014717	1542	3.11	370
Reaction II: $AgNO_3$(c) in 0.1*N* KCl(aq)								
576	15	0.75	0.03031	16.666	0.015088	1104	2.01	550
577	20	0.75	.03031	16.667	.029455	566	1.03	550
610	20	0.75	.03031	16.668	.023224	718	1.30	550
Reaction III: KBr(c) in 0.15*N* $AgNO_3$(aq)								
569	15	2.55	0.04696	16.903	0.039752	425	1.18	360
601	15	2.48	.04569	16.918	.020192	838	2.26	370
604	165	2.49	.04574	16.916	.039782	425	1.15	370
609	> 45, < 75	2.48	.04569	16.917	.033619	503	1.36	370
Reaction IV: $AgNO_3$(c) in 0.1*N* KBr(aq)								
578	15	1.19	0.03025	16.591	0.014998	1106	2.02	548
579	20	1.19	.03024	16.590	.029396	564	1.03	549
580	70	1.19	.03025	16.591	.029491	563	1.03	548
Reaction V: $AgNO_3$(c) in 0.1*N* KI(aq)								
596	20	1.67	0.03040	16.513	0.023597	700	1.29	543
597	20	1.67	.03040	16.513	.015137	1091	2.01	543
598	20	1.67	.03040	16.513	.023668	698	1.28	543
599	20	1.67	.03040	16.512	.023666	698	1.28	543
600	20	1.67	.03040	16.512	.023471	704	1.30	543

TABLE 6. *Calorimetric data for the silver halide precipitation experiments*

Expt. No.	Stirring energy	ΔRc	$\bar{E}\bar{E}\bar{E}$	Qr	Mass of solute	$\bar{T}$ reaction	$-\Delta Hr(T)$		ΔCp	$-\Delta Hr$(298.15 K)	
	Ω	Ω	$J \cdot \Omega^{-1}$	J	g	K	$J \cdot g^{-1}$	$kJ \cdot mol^{-1}$	$J \cdot mol^{-1} \cdot K^{-1}$	$kJ \cdot mol^{-1}$	$kcal \cdot mol^{-1}$
Reaction I: KCl(c) in $AgNO_3$(aq)											
568	0.002368	0.084251	17,265.7	1454.65	2.23165	298.056	651.83	48.597	−19.5	48.599	11.615
581	.002628	.083919	17,336.4	1454.85	2.22464	308.518	653.97	48.757		48.555	11.605
605	.001748	.081933	17,337.7	1420.54	2.17024	308.552	654.55	48.800		48.597	11.615
606	.007200	.082146	17,267.8	1418.49	2.17762	298.147	651.40	48.565		48.565	11.607
607	.004361	.077058	17,339.4	1336.14	2.04045	308.489	654.83	48.821		48.619	11.620
608	.001622	.041431	17,264.3	715.28	1.09727	298.438	651.87	48.600		48.594	11.614
										Mean = 48.588	11.613
										sdm = ± 0.010	± 0.002
Reaction II: $AgNO_3$(c) in KCl(aq)											
576	0.001448	0.038460	17,068.8	656.48	2.56312	298.389	256.13	43.510	+21.8	43.515	10.400
577	.001739	.075132	17,085.2	1283.64	5.00369	297.448	256.54	43.579		43.564	10.412
610	.001756	.058692	17,140.8	1006.02	3.94511	308.424	255.00	43.318		43.542	10.407
										Mean = 43.540	10.406
										sdm = ± 0.014	± 0.003
Reaction III: KBr(c) in $AgNO_3$(aq)											
569	0.001553	0.149914	17,276.1	2589.92	4.73088	298.171	547.45	65.150	−13.0	65.150	15.571
601	.001593	.076239	17.268.5	1316.54	2.40302	298.218	547.87	65.200		65.199	15.583
604	.005978	.150107	17,267.6	2591.98	4.73452	297.849	547.46	65.151		65.155	15.572
609	.003698	.126733	17,324.2	2195.55	4.00098	308.785	548.75	65.304		65.166	15.575
										Mean = 65.168	15.575
										sdm = ± 0.011	± 0.003
Reaction IV: $AgNO_3$(c) in KBr(aq)											
578	0.001682	0.055171	17,011.4	938.54	2.54781	297.993	368.37	62.576	+63.	62.566	14.954
579	.003097	.108010	17,026.8	1839.07	4.99368	297.772	368.28	62.561		62.537	14.947
580	.005479	.106780	17,094.4	1825.34	5.00979	308.638	364.36	61.895		62.556	14.951
										Mean = 62.553	14.951
										sdm = ± 0.008	± 0.002
Reaction V: $AgNO_3$(c) in KI(aq)											
596	0.002112	0.122965	17,031.3	2094.26	4.00853	308.673	522.45	88.750	+9.6	88.851	21.236
597	.001929	.079234	16,957.6	1343.62	2.57140	298.640	522.52	88.762		88.767	21.216
598	.001894	.123197	17,028.9	2097.91	4.02068	308.772	521.78	88.636		88.738	21.209
599	.001895	.123855	16,965.1	2101.22	4.02032	297.877	522.65	88.784		88.781	21.219
600	001638	.122122	17,033.4	2080.16	3.98710	308.740	521.72	88.626		88.728	21.206
										Mean = 88.773	21.217
										sdm = ± 0.022	± 0.005

It may be seen in table 5 that there were occasional experiments (Nos. 580, 604, 606, and 609) where the reaction periods were longer than others in the group. We assume that this was caused by the way in which the sample holder (see fig. 1) opened. Initially the cylinder containing the sample is at the top, between the two flat plates. When the trigger is released to start the reaction, the cylinder falls to the lower crossbars. As the cylinder falls, if it tilts toward the stirrer, most of the sample will be quickly dispersed in the solution; however, if the cylinder tilts away from the stirrer, much of the sample falls to the bottom and is covered by the precipitate formed. This limits access of the solution to the sample. In all of the experiments listed in tables 5 and 6, the reactions were complete, as evidenced by the essentially equal slopes in the initial and final rating periods and by the absence of products of incomplete reaction such as were found in the first experiments described earlier in this section.

In table 6, the isothermal enthalpy of reaction at the temperature of reaction is $\Delta Hr(T) = -Qr/$(mass of solute). In each group of reactions, one or more enthalpy measurements were made at 309 K in order to obtain a value of ΔCp for the reaction. The enthalpy values at 298.15 K were calculated using the values of ΔCp given in the table for each reaction. The mean ΔHr(298.15 K) and the standard deviations of the mean are given for each group of experiments.

The average reactions for the five groups of experiments are represented by the following equations

(with uncertainties as the experimental imprecision at the 95 percent confidence level):

$$KCl(c) + 1.84(AgNO_3 \cdot 367\ H_2O) \rightarrow AgCl(c) + (KNO_3 \cdot 0.84\ AgNO_3 \cdot 675.28\ H_2O)_{soln}$$
$$\Delta Hr(298.15\ K) = -48.588 \pm 0.025\ kJ \cdot mol^{-1} = -11.613 \pm 0.006\ kcal \cdot mol^{-1} \quad (I)$$

$$AgNO_3(c) + 1.45(KCl \cdot 550\ H_2O) \rightarrow AgCl(c) + (KNO_3 \cdot 0.45\ KCl \cdot 797.5\ H_2O)_{soln}$$
$$\Delta Hr(298.15\ K) = -43.540 \pm 0.060\ kJ \cdot mol^{-1} = -10.406 \pm 0.014\ kcal \cdot mol^{-1} \quad (II)$$

$$KBr(c) + 1.49(AgNO_3 \cdot 368\ H_2O) \rightarrow AgBr(c) + (KNO_3 \cdot 0.49\ AgNO_3 \cdot 548.32\ H_2O)_{soln}$$
$$\Delta Hr(298.15\ K) = -65.168 \pm 0.035\ kJ \cdot mol^{-1} = -15.575 \pm 0.008\ kcal \cdot mol^{-1} \quad (III)$$

$$AgNO_3(c) + 1.36(KBr \cdot 548\ H_2O) \rightarrow AgBr(c) + (KNO_3 \cdot 0.36\ KBr \cdot 745.28\ H_2O)_{soln}$$
$$\Delta Hr(298.15\ K) = -62.553 \pm 0.034\ kJ \cdot mol^{-1} = -14.951 \pm 0.008\ kcal \cdot mol^{-1} \quad (IV)$$

$$AgNO_3(c) + 1.43(KI \cdot 543\ H_2O) \rightarrow AgI(c) + (KNO_3 \cdot 0.43\ KI \cdot 776.49\ H_2O)$$
$$\Delta Hr(298.15\ K) = -88.773 \pm 0.061\ kJ \cdot mol^{-1} = -21.217 \pm 0.014\ kcal \cdot mol^{-1} \quad (V)$$

Correction for enthalpy of mixing.

The quantity, $\Delta Hr(298.15\ K)$, given in table 6 represents the enthalpy change for the generalized reaction:

$$KX(c) + b[AgNO_3 + nH_2O] \rightarrow AgX(c) + [KNO_3 + (b-1)\ AgNO_3 + n \cdot bH_2O]$$

or

$$AgNO_3(c) + b[KX + nH_2O] \rightarrow AgX(c) + [KNO_3 + (b-1)\,KX + n \cdot bH_2O].$$

For the systems in which Ag^+ ion is in excess the enthalpy of mixing reaction,

$$[KNO_3 \cdot nH_2O(aq)] + (b-1)[AgNO_3 \cdot nH_2O](aq) \rightarrow [KNO_3 + (b-1)\ AgNO_3 + n \cdot bH_2O](aq)$$

was calculated from the measurement of Karapet'yants, Vlasenko, and Solov'eva [25]. Their data were fitted to a function of the form

$$\Delta Hmix = X(1-X)m^2RTh_0$$

in which X is the mole fraction of $AgNO_3$ in the solute mixture, m is the molality of the solution, and $\Delta Hmix$ is the enthalpy of mixing per kilogram of solvent [26]. For $m = 0.15$ we obtained the equation

$$\Delta Hmix = -3.95X(1-X),\ J \cdot (kgH_2O)^{-1}.$$

The enthalpy of mixing per mole of solute was then computed from the equation

$$\Delta Hmix = -\frac{b-1}{b} \times \frac{n}{55.51} \times 3.95,\ J \cdot mol^{-1}.$$

For the $KCl(c) - AgNO_3(aq)$ reactions, the correction to $\Delta Hr(-\Delta Hmix)$ is 9 $J \cdot mol^{-1}$ except for Expt. No. 608 in which the correction is 18 $J \cdot mol^{-1}$; the average correction is 10 $J \cdot mol^{-1}$(2.4 $cal \cdot mol^{-1}$). For the $KBr(c) - AgNO_3(aq)$ the corrections range from 3 to 15 $J \cdot mol^{-1}$, the average correction being 8 $J \cdot mol^{-1}$ (1.9 $cal \cdot mol^{-1}$).

The enthalpy of mixing reaction

$$[KNO_3 \cdot nH_2O](aq) + (b-1)[KCl \cdot nH_2O](aq) \rightarrow [KNO_3 + (b-1)KCl + n \cdot bH_2O](aq)$$

was calculated from the data given in Wu, Smith, and Young [26] and Wood and Smith [27] for the $KCl - KNO_3$ system to be less than 1 $J \cdot mol^{-1}$ and was omitted. The correction was also assumed to be negligible for the $KBr - KNO_3$ and $KI - KNO_3$ systems.

6. Enthalpies of Precipitation of the Silver Halides

The measured enthalpies for the five silver halide precipitation reactions (from table 6) and the thermodynamic quantities derived from them are given in table 7. The values of ϕ_L are taken from Parker [14], and the quantity, q(demix), represents the correction for demixing the final solutions as described in section 5. The values for the enthalpies of solution of the solute salts are taken from table 2.

All of the values for ΔH° pptn given in table 7 are in good agreement with those obtained from EMF measurements (see table 1). Our mean value for the chloride reactions, -65.724 $kJ \cdot mol^{-1}$, is in good agreement with the value of Lange and Fuoss; for the bromide reactions our mean value, -84.826 $kJ \cdot mol^{-1}$, agrees with those of Gellner and Skinner, and Berthelot; and for the iodide reaction our value, -111.125 $kJ \cdot mol^{-1}$ agrees best with that of Berthelot's first work.

7. Gibbs Energies of Precipitation of the Silver Halides

The available solubility data on the silver halides are presented in table 8 as the common logarithm of the solubility product. We have also calculated the values of log K_s for each silver halide from the appropriate values of the standard electrode potentials for

TABLE 7. *Data used in the calculation of the entropy of the aqueous silver ion from the enthalpies of the five silver halide precipitation reactions*

All values are at 298.15 K

Reaction	I KCl(c) in $AgNO_3$(aq)	II $AgNO_3$(c) in KCl(aq)	III KBr(c) in $AgNO_3$(aq)	IV $AgNO_3$(c) in KBr(aq)	V $AgNO_3$(c) in KI(aq)
ΔHr, kJ · mol^{-1}	−48.588	−43.540	−65.168	−62.553	−88.773
q (demix), kJ · mol^{-1}	+0.010	—	+0.008	—	—
ϕ_L (solvent), kJ · mol^{-1}	−0.238	+0.335	−0.238	+0.280	+0.209
$-\phi_L(KNO_3)$, kJ · mol^{-1}	+0.356	+0.163	+0.356	+0.163	+0.167
$\Delta H°$, kJ · mol^{-1}	−48.460	−43.042	−65.042	−62.110	−88.397
$\Delta H°(\infty)$ (solute), kJ · mol^{-1}	17.218	22.727	19.772	22.727	22.727
$\Delta H°$ *pptn*, kJ · mol^{-1}	−65.678	−65.769	−84.814	−84.837	−111.124
$\Delta G°$, kJ · mol^{-1}	−55.652	−55.652	−70.206	−70.206	−91.827
$\Delta S°$ *pptn*, J · mol^{-1} · K^{-1}	−33.63	−33.93	−49.00	−49.07	−64.72
$S°$ [AgX(c)], J · mol^{-1} · K^{-1}	96.36	96.36	107.11	107.11	115.48
$S°$ [X^-(aq)], J · mol^{-1} · K^{-1}	56.73	56.73	82.84	82.84	106.70
$S°$ [Ag^+(aq)], J · mol^{-1} · K^{-1}	73.26	73.56	73.27	73.34	73.50

TABLE 8. *Selection of* $\Delta G°$ *of the precipitation reaction*

All values are at 298.15 K.

Author	log K_s	Reference
AgCl:		
Goodwin (1894)	−9.865	[28]
Jonte and Martin (1952)	−9.752	[29]
Gledhill and Malan (1954)	−9.748	[13]
Bardin and Bystritskii (1971)	−9.765	[30]
Anderson, Butler, and Woolley (1971)	−9.75	[31]
Electrochemical (Ag/AgCl, Cl^- and Ag/Ag^+)	−9.752	
Broadbank, et al. (1968)	−9.755	[32]
Selected	−9.750	
$\Delta G°$ = −55.651 ± 0.012 kJ · mol^{-1} = −13.301 ± 0.003 kcal · mol^{-1}		
AgBr:		
Thiel (1900)	−12.18	[33]
Gledhill and Malan (1954)	−12.204	[13]
Hill (1908)	−12.270	[34]
Goodwin (1894)	−12.43	[28]
Do.	−12.38	
Berne and Leden (1953)	−12.34	[35]
Electrochemical	−12.309	
Selected	−12.300	
$\Delta G°$ = −70.206 ± 0.100 kJ · mol^{-1} = −16.780 ± 0.025 kcal · mol^{-1}		
AgI:		
Thiel (1900)	−15.958	[33]
Goodwin (1894)	−16.11	[28]
Do.	−16.01	
Hill (1908)	−15.978	[34]
Electrochemical	−16.088	
Selected	−16.088	
$\Delta G°$ = −91.827 ± 0.100 kJ · mol^{-1} = −21.947 ± 0.025 kcal · mol^{-1}		

the Ag/Ag^+(aq) and the Ag/AgX(c), X^-(aq) electrodes [1, 4]. These values are listed as "Electrochemical." The activity coefficients were taken as unity in all cases. The standard Gibbs energy of precipitation at 298.15 K is then

$$\Delta G° = RT \ln K_s = 5.7079 \log K_s, \text{ kJ} \cdot \text{mol}^{-1}$$
$$= 1.36422 \log K_s, \text{ kcal} \cdot \text{mol}^{-1}.$$

8. Entropy of the Aqueous Silver Ion

The calculation of the entropy of precipitation of the silver halides is summarized in table 7. $\Delta S°$pptn = $(\Delta H°\text{pptn} - \Delta G°)/T$. The entropies of the silver halide salts were calculated by graphical reintegration of the corresponding heat capacity data [36, 37]; the

entropies of the aqueous halide ions are the recommended CODATA values [38].

We have also calculated a value for the entropy of the silver ion from the data on $AgNO_3$(aq), using the CODATA preliminary value for the nitrate ion [39]. The solubility, 15.01 molal at 298.15 K, was taken from the measurements of Skarulis and Ricci [40]; the activity coefficient at saturation was calculated to be 0.082 [41, 42]. Combining these data with our selected best value of the enthalpy of solution we obtain

$$AgNO_3(c) \rightarrow Ag^+(aq) + NO_3^-(aq)$$

$$\Delta G^\circ = -1.029 \pm 0.040 \text{ kJ} \cdot \text{mol}^{-1}$$

$$= -0.246 \pm 0.010 \text{ kcal} \cdot \text{mol}^{-1}$$

$$\Delta H^\circ(\infty) = 22.730 \pm 0.42 \text{ kJ} \cdot \text{mol}^{-1}$$

$$= 5.433 \pm 0.010 \text{ kcal} \cdot \text{mol}^{-1}$$

$$\Delta S^\circ = 79.69 \text{ J} \cdot \text{mol}^{-1} \cdot \text{K}^{-1}$$

$$= 19.05 \text{ cal} \cdot \text{mol}^{-1} \cdot \text{K}^{-1}.$$

The entropy of $AgNO_3$(c), 140.92 ± 0.63 J · mol^{-1} · K^{-1} (33.68 ± 0.15 cal · mol^{-1} · K^{-1}), was measured by Smith, Brown, and Pitzer [22], and the CODATA value for NO_3^-(aq) = 146.94 J · mol^{-1} · K^{-1} (35.12 cal · mol^{-1} · K^{-1}). Hence, we obtain for the Ag^+(aq) from $AgNO_3$

$$S^\circ(298.15\text{ K}) = 73.67 \text{ J} \cdot \text{mol}^{-1} \cdot \text{K}^{-1}$$

$$= 17.61 \text{ cal} \cdot \text{mol}^{-1} \cdot \text{K}^{-1}.$$

in excellent agreement with the values obtained from the halides.

We can also obtain a value for the entropy of Ag^+(aq) from our recalculation and reextrapolation of the data of Owen and Brinkley [4] for the silver electrode. We have fitted the values of E° in volts to a quadratic function of the temperature, obtaining the equation (T in K):

$$E^\circ = -0.79910 + 9.930 \times 10^{-4}(T - 298.15) + 4.05 \times 10^{-7}(T - 298.15)^2.$$

Thus, for the reaction

$$Ag(c) + H^+(aq) \rightarrow Ag^+(aq) + \tfrac{1}{2} H_2(g)$$

$$\Delta S^\circ(298.15\text{ K}) = 95.81 \pm 0.13 \text{ J} \cdot \text{mol}^{-1} \cdot \text{K}^{-1}$$

$$S^\circ[Ag^+(aq)]\ (298.15\text{ K}) = 73.08 \text{ J} \cdot \text{mol}^{-1} \cdot \text{K}^{-1}$$

$$= 17.47 \text{ cal} \cdot \text{mol}^{-1} \cdot \text{K}^{-1}$$

The entropies of Ag(c) and H_2(g) are taken from [43] and [38] respectively.

Table 9 summarizes the values obtained in this paper for the entropy of Ag^+(aq) with estimated overall uncertainties. We have assigned a smaller weight to the value obtained from the EMF measurements because of the uncertainty in the temperature coefficient, and to the value from AgI because of the relatively large uncertainty in the entropy of AgI(c) [37]. As a final mean value we have selected

$$S^\circ[Ag^+(aq)]\ (298.15\text{ K}) = 73.42 \pm 0.20 \text{ J} \cdot \text{mol}^{-1} \cdot \text{K}^{-1}$$

$$= 17.55 \pm 0.05 \text{ cal} \cdot \text{mol}^{-1} \cdot \text{K}^{-1}$$

This value is in almost exact agreement with the value, 17.54 ± 0.15 cal · mol^{-1} · K^{-1}, obtained by Pitzer and Smith [44], based on the solution data on Ag_2O(c) and on earlier measurements of the precipitation of AgCl. We believe the excellent concordance obtained in the various determinations listed in table 9 indicates that the silver halides encountered in the various calorimetric experiments are in the same thermodynamic states as those in the solubility measurements and in the electrochemical measurements. The effects of such factors as particle size or degree of crystallinity for these halides under ordinary conditions must be smaller than can be detected by our present calorimetric techniques.

TABLE 9. *Selection of entropy of* Ag^+(aq)

Source	S° (298.15 K)	
	J · mol^{-1} · K^{-1}	cal · mol^{-1} · K^{-1}
EMF	73.08 ± 0.40	17.47 ± 0.10
AgCl	73.41 ± 0.20	17.55 ± 0.05
AgBr	73.31 ± 0.35	17.52 ± 0.09
AgI	73.50 ± 0.80	17.57 ± 0.20
$AgNO_3$	73.67 ± 0.15	17.61 ± 0.04
Weighted mean	73.42 ± 0.20	17.55 ± 0.05

9. References

[1] Bates, R. G., and Bower, V. E., J. Res. Nat. Bur. Stand. (U.S.), **53**, 283 (1954); Hetzer, H. B., Robinson, R. A., and Bates, R. G., J. Phys. Chem. **66**, 1423 (1962); Hetzer, H. B., Robinson, R. A., and Bates, R. G., J. Phys. Chem. **68**, 1929 (1964).

[2] Wagman, D. D., Evans, W. H., Parker, V. B., Halow, I., Bailey, S., and Schumm, R. H., Selected Values of Chemical Thermodynamic Properties, Nat. Bur. Stand. (U.S.), Tech. Note 270–3, et seq; Termicheski Constanty Veshchestv (Thermal Constants of Substances), Glushko, V. P., Ed., Academy of Sciences, U.S.S.R., Moscow.

[3] Harned, H. S., and Owen, B. B., The Physical Chemistry of Electrolytic Solutions, 3rd Edition, ACS Monograph 137 (Reinhold Publ. Co., New York, 1958) p. 428.

[4] Owen, B. B., and Brinkley, S. R., Jr., J. Am. Chem. Soc. **60**, 2233 (1938).

[5] Lange, E., and Fuoss, R., Z. physik. Chem. **125**, 431 (1927).

[6] Thomsen, J., Thermochemical Investigations III, Barth, J., Leipsig (1883).

[7] Berthelot, M., Compt. rend. **93**, 870 (1881).

[8] Gellner, O. H., and Skinner, H. A., J. Chem. Soc. **1949**, 1145.

[9] Roth, W. A., Z. Elektrochem. **50**, 107 (1944).

[10] Berthelot, M., Ann. chim. phys. [5] **4**, 160 (1875).

[11] Lange, E., and Shibata, Z., Z. physik. Chem. **A149**, 465 (1930).

[12] Yatsimirskii, K. B., and Skutov, A. A., Zhur. Fiz. Khim. **28**, 30 (1954).

[13] Gledhill, J. A., and Malan, G. M., Trans. Faraday Soc. **50**, 126 (1954).

[14] Parker, V. B., Thermal Properties of Aqueous Uni-univalent Electrolytes, Nat. Stand. Ref. Data Ser. Nat. Bur. Stand. (U.S.), 2, 66 pages (April 1965).
[15] Prosen, E. J., and Kilday, M. V., J. Res. Nat. Bur. Stand. (U.S.), **77A**, 179 (1973).
[16] Commission on Atomic Weights, Pure and Applied Chem. **21**, 91 (1970).
[17] International Critical Tables (McGraw Hill Book Co., Inc. New York), (a) Vol. **I**, 124, 154 (1926); (b) Vol. **III**, 67, 87–88 (1928).
[18] Prosen, E. J., and Kilday, M. V., J. Res. Nat. Bur. Stand. (U.S.) **77A**, 581 (1973).
[19] Tsvetkov, V. G., and Rabinovich, I. B., Zhur. Fiz. Khim. **43**, 1213 (1969).
[20] Lewis, G. N., and Randall, M., Thermodynamics revised by Pitzer, K. S., and Brewer, L. (McGraw Hill Book Co., Inc. New York, 1961), page 642.
[21] Lange, E., and Martin, W., Z. physik. Chem. **A180**, 233 (1937).
[22] Smith, W. V., Brown, O. L. I., and Pitzer, K. S., J. Am. Chem. Soc. **59**, 1213 (1937).
[23] Graham, R. L., and Hepler, L. G., J. Am. Chem. Soc. **80**, 3538 (1958).
[24] Shidlovskii, A. A., and Voskresenskii, A. A., Zhur. Fiz. Khim. **37**, 2062 (1963).
[25] Karapet'yants, M. Kh., Vlasenko, K. K., and Solov'eva, S. G., Russ. J. Phys. Chem. **44**, 305 (1970).
[26] Wu, Y. C., Smith, M. B., and Young, T. F., J. Phys. Chem. **69**, 1868 (1965).
[27] Wood, R. H., and Smith, R. W., J. Phys. Chem. **69**, 2974 (1965).
[28] Goodwin, H. M., Z. physik. Chem. **13**, 577 (1894).
[29] Jonte, J. H., and Martin, D. S., J. Am. Chem. Soc. **74**, 2052 (1952).
[30] Bardin, V. V., and Bystritskii, A. L., Zhur. Priklad. Khim. **44**, 1159 (1971).
[31] Anderson, K. P., Butler, E. A., Woolley, E. M., J. Phys. Chem. **75**, 93 (1971).
[32] Broadbank, R. W. C., Dhabanandana, S., and Morcum, K. W., J. Chem. Soc. (A) **1968**, 213.
[33] Thiel, A., Z. anorg. Chem. **24**, 1 (1900).
[34] Hill, A. E., J. Am. Chem. Soc. **30**, 68 (1908).
[35] Berne, E., and Leden, I., Z. Naturforsch. **8a**, 719 (1953).
[36] Eastman, E. D., and Milner, R. T., J. Chem. Phys. **1**, 444 (1933).
[37] Pitzer, K. S., J. Am. Chem. Soc. **63**, 516 (1941).
[38] CODATA Bulletin Number 5, ICSU Committee on Data for Science and Technology (December 1971).
[39] CODATA Bulletin Number 7, ICSU Committee on Data for Science and Technology (August 1972).
[40] Skarulis, J. A., and Ricci, J. E., J. Am. Chem. Soc. **63**, 3429 (1941).
[41] Robinson, R. A., and Tait, D. A., Trans. Faraday. Soc. **37**, 569 (1941).
[42] Kangro, W., and Groeneveld, A., Z. physik. Chem. [NF] **32**, 110 (1962).
[43] Furukawa, G. T., Saba, W. G., and Reilly, M. L., Nat. Stand. Ref. Data Ser. Nat. Bur. Stand. (U.S.), 18, 49 pages (April 1968).
[44] Pitzer, K. S., and Smith, W. V., J. Am. Chem. Soc. **59**, 2633 (1937).
[45] Nat. Bur. Stand. (U.S.) Tech. News Bull. **47** No. 10, 175 (1963).

(Paper 77A5–784)

JOURNAL OF RESEARCH of the National Bureau of Standards—A. Physics and Chemistry
Vol. 77A, No. 5, September–October 1973

Enthalpies of Reaction of Tris(hydroxymethyl)aminomethane in HCl(aq) and in NaOH(aq)

Edward J. Prosen and Marthada V. Kilday

Institute for Materials Research, National Bureau of Standards, Washington, D.C. 20234

(May 25, 1973)

The enthalpy of reaction of tris(hydroxymethyl)aminomethane, NBS Standard Reference Material 724a, measured in an adiabatic solution calorimeter at 298.15 K in 0.1 *N* HCl solution is -245.76 ± 0.26 J · g^{-1}, and in 0.0500 *N* NaOH solution is 141.80 ± 0.19 J · g^{-1}. The conditions applicable and the factors included in the overall uncertainties are discussed in detail. For the reaction in 0.1 *N* HCl in the range, 293 to 303 K, $\Delta Cp = 1.435 \pm 0.023$ J · g^{-1} · K^{-1}, and in 0.0500 *N* NaOH in the range, 295 to 303 K, $\Delta Cp = 1.025 \pm 0.025$ J · g^{-1} · K^{-1}.

Possible sources of error in measurements of the reactions are discussed. A summary of other enthalpy measurements of the reaction in 0.1 *N* HCl is given.

Key words: Enthalpy of reaction; heat of solution; solution calorimetry; standard reference material; THAM; TRIS; tris(hydroxymethyl)aminomethane; thermochemistry.

1. Introduction

Tris(hydroxymethyl)aminomethane or 2-amino-2-(hydroxymethyl)-1,3-propanediol, $(HOCH_2)_3CNH_2$, is popularly known as TRIS or by the trade name, THAM.[1] For some years it has been used in medicine and as a buffer in analytical chemistry. Recently it was issued by the National Bureau of Standards as a standard reference material for solution calorimetry, SRM 724 and 724a.[2] The experimental work which is the basis for the certified enthalpy values for this standard reference material is discussed in sections 3.3 and 3.4.

The neutralization reaction with excess aqueous hydrochloric acid may be written

$$n[(HOCH_2)_3CNH_2]\,(c) + (n+x)H^+(aq) \rightarrow$$

$$n[(HOCH_2)_3CNH_3]^+(aq) + xH^+(aq).$$

Under some conditions (described in secs. 3.1a and 3.1b) side reactions may occur which produce high enthalpy values. For the dissolution reaction in water, slightly alkaline solutions are preferred for calorimetric measurements to eliminate possible reaction with CO_2 dissolved in the water.

The use of the reaction of tris(hydroxymethyl)-aminomethane with 0.1 *N* hydrochloric acid solution "as a test reaction for rapid moderately exothermic reactions" was proposed by Irving and Wadsö [1][3] in 1964. The same year, the U.S. Calorimetry Conference requested that the National Bureau of Standards (U.S.) issue a sample to be used as a standard reference material for solution calorimetry. At that time, a new vacuum-jacketed adiabatic solution calorimeter had been constructed (in the Thermochemistry Section at NBS) which was still untested, but was believed to be capable of high precision and accuracy, and well-qualified to do the enthalpy certification work. It was assumed that the certification would involve only a series of simple calorimetric experiments to confirm the work of Irving and Wadsö. However, the first results obtained late in 1967 with the new Standard Reference Material No. 724 were approximately 0.1 percent more exothermic than the values reported by Irving and Wadsö, and the experimental imprecision of the measurements was about twice that expected of the calorimeter.

An intensive effort began to locate the cause of the discrepancy in the results. No difference was found in the enthalpy value obtained with samples from different sources, nor in samples which were stored for years in darkness when compared to those stored in the presence of fluorescent lighting, nor in samples stored in the room atmosphere as compared to those stored in a hygrostat of 50 percent relative humidity. The calibrations of our bridge, potentiometer, standard resistors, standard cell, and electronic counter were checked; a dummy heater with its leads directly in the calorimeter solution (thus at calorimeter tem-

[1] Fisher Scientific Co. Trademark. Commercial materials are identified in this paper in order to adequately specify the experimental procedure. Such identification does not imply recommendation or endorsement by the National Bureau of Standards.

[2] Available at Office of Standard Reference Materials, National Bureau of Standards, Washington, D.C. 20234.

[3] Figures in brackets indicate literature references at the end of this paper.

perature before leaving the vessel) was compared with the permanent calibrating heater in the platinum well—the difference between the results obtained with the two heaters was less than 0.004 percent; temperature differences at various points between the adiabatic shield and the vessel were measured and the currents in the shield were readjusted to produce minimal departures from the vessel temperatures; and the platinum resistence thermometer was replaced by a quartz-oscillator thermometer—none of these produced any detectable change in the results.

Having eliminated the sample composition and treatment, and the measuring equipment as likely sources of error, we decided to measure for comparison the enthalpy of another reaction on which published results were available [3], the reaction of $H_2SO_4 \cdot 8H_2O$ in 0.02 *N* and in 0.08 *N* sodium hydroxide solutions. The results we obtained [2] agree with Gunn's values [3] within a few hundredths of a percent. The standard deviation of the mean for our experiments was 0.01 percent, which was a definite improvement over the imprecision in the experiments with TRIS.

Our efforts were then directed to investigating conditions of the TRIS reaction in aqueous HCl which might explain the existing discrepancy in the enthalpy values obtained by various laboratories. Much is still not understood about this reaction, but we report here the results of some of our measurements which have led to our confidence in the experiments on which are based the certified enthalpy values for Standard Reference Materials 724 and 724a under certain specified conditions. We have also summarized values obtained by other laboratories (published and unpublished) for the TRIS reaction in aqueous HCl.

2. Materials, Apparatus, and Procedures

2.1. Tris(hydroxymethyl)aminomethane

Our measurements reported in this paper were made using two samples of TRIS, SRM 724 and SRM 724a. The latter sample is to be issued upon depletion of the first sample, SRM 724.

SRM 724 was prepared from tris(hydroxymethyl)-aminomethane obtained from several commercial sources, and the purifications[4] and assay[5] were performed in the Analytical Chemistry Division. In the purification, each 1-kg lot was washed twice by stirring with methanol and filtering. The material recovered from the second washing was dissolved in hot water and filtered. The TRIS was crystallized by slowly dripping the filtrate into vigorously agitated methanol. The crystalline TRIS was filtered, washed with cold methanol, and then the entire crystallization procedure was repeated. The crystals from the second crystallization were air-dried for a day or more, and then dried at about 338 K in a rotating vacuum drier until the product was free-flowing and showed no tendency to stick to the walls. The assay of this material is 99.94 ± 0.01 percent $(HOCH_2)_3CNH_2$. An indirect coulometric procedure was used for the assay (see [4] for details of the procedure).

The material for SRM 724a was 10 kg of TRIS obtained from a commercial source and was not further purified. (This material was part of a total of 60 kg, and 50 kg was used for acidimetric standard, SRM 723). The assay is 99.9690 ± 0.0030 weight percent.[5] The results of the coulometric analyses, the titration procedures, and the method of selecting the random samples have been described [5].

The general procedures recommended by the Standards Committee, U.S. Calorimetry Conference, October 1966, were followed (except as noted in this work) in the storage and use of the TRIS samples, i.e., the material was stored in a hygrostat containing a saturated solution of magnesium nitrate (50 percent relative humidity), it was used without further heating or crushing and the calorimetric samples were weighed in air, sealed with air in the sample holder at atmospheric pressure, and not exposed to heat.

2.2. Solutions

The calorimetric solutions (approximately 300 cm^3 in volume) were taken from stock solutions, 2 dm^3 in volume, which were stored in polyethylene bottles. The solutions for the reaction with HCl were prepared by dilution of ACS reagent grade hydrochloric acid (37.0–38.0%) with distilled water. The solutions were analysed by titration with (1) 0.1 *N* standardized sodium hydroxide solutions using a recording pH meter, or (2) ACS analytical reagent grade sodium carbonate which had been dried for 1 h at 545 K, using bromphenol blue as an end point indicator. The 0.1 *N* HCl solutions were within 2 percent of the nominal value and the estimated uncertainty in the analyses is 0.5 percent or less.

The distilled water used in the preparation of the 0.1 *N* HCl was in equilibrium with air (which contains 0.03% CO_2). The decision not to use CO_2-free solutions was based on the following considerations. The Standards Committee of the Calorimetry Conference made no recommendations regarding the treatment of the aqueous calorimetric solutions except that there should be "approximately one atmosphere air pressure in the vapor space over the solution; the solution may then be assumed to be essentially saturated with air." Furthermore, many solution calorimeters are constant pressure systems which are not sealed from the atmosphere and may be affected to some extent by the atmosphere. An important factor influencing the choice of the reaction of TRIS in aqueous HCl as a standard was that a reproducible enthalpy value could be obtained without the need for special procedures and analyses. It is not necessary that the reaction be accurately defined as long as the enthalpy values are reproducible and the defined conditions can be obtained in various calorimeters. We concluded that the most reproducible condition for the preparation of the HCl solutions (without using elaborate analyses and precautions in preparation and handling) was to use solutions which were in equilibrium with air; this

[4] D. Enagonio, Separation and Purification Section.
[5] G. Marinenko, Microchemical Analysis Section.

is one of the conditions for the certified enthalpy value for the reaction with HCl.

In preparing the aqueous NaOH solutions for the endothermic reactions, the distilled water was boiled at least 15 min and as it cooled it was guarded by a CO_2-absorption tube. Stock solutions, stored in closed polyethylene bottles, were prepared by dilution of 10 *N* NaOH and analyzed by titration using potassium acid phthalate (SRM 84g) and a pH meter or phenolphthalein as an end-point indicator. During the titrations, CO_2-free air was passed through the solution in the flask to reduce reaction with CO_2 in the atmosphere. The uncertainty in the analyses is estimated to be as much as 1 percent in some cases because of the possibility of some reaction with atmospheric CO_2. In the use of the solutions, the only precautions taken to avoid reaction with CO_2 were to use solutions prepared and analysed not more than 2 weeks prior to the calorimetric experiments, to transfer the solutions as quickly as possible from one container to another, and to avoid breathing directly on the solutions. In this way, carbonate formation in the solutions was minimized.

2.3. Apparatus

The vacuum-jacketed adiabatic solution calorimeter used for all of these measurements has been described in detail [2]. The sample holder and all parts in contact with the calorimetric solutions were of platinum-iridium alloys. The volume of the sample holder used in this work was 2.7 cm^3, the mass of the TRIS samples was 1.5 g, and the volume of the calorimetric solutions was approximately 300 cm^3. The volume of the vapor space above the solution was normally about 15 cm^3, but in certain special experiments (such as those using different masses of solutions described in sec. 3.2) the vapor space volume was from near 0 to 40 cm^3. The stirring rate was 350 rpm in these experiments (except as noted) and 3 to 5 $\mu K \cdot min^{-1}$. The uncertainty in the stirring energy in an experiment is estimated to be 5 percent of the total stirring energy or less, based on results obtained over a period of 8 years.

The experiments reported here were performed between February 1970 and May 1971, except some preliminary work on the endothermic reaction in January to March 1969 and some very recent work on the effects of CO_2 and on the effect of the presence of gold which was done between July and October 1972.

In various groups of experiments three different systems (described previously [2]) were used as noted to measure the calorimeter temperature. In each system the temperature-sensing unit was placed in the platinum well which projected from the vessel cover and extended into the solution to about 1 cm above the stirrer propeller. The well was centered on the same radius as were the vent and sample holder shown in figure 1. Between January and August 1970, an experimental system was used which employed a modified quartz-oscillator thermometer with digital read-out. A 25-Ω platinum resistance thermometer with a G–3 Mueller resistance bridge and an electronic null detector were used to measure the calorimeter temperature prior to January 1970, and between September 1970 and June 1972. Since June 1972, the temperature has been measured with a quartz-oscillator combined with direct frequency counting and digital print-out. Both of the quartz-oscillator systems were calibrated by comparison with the platinum resistance thermometer system.

2.4 Apparatus Modifications for This Work

This calorimeter was designed primarily to measure enthalpies of reaction or heats of reaction at constant pressure [2]. During the search for the cause of the small disagreement in enthalpy values measured by various laboratories for the reaction of TRIS in 0.1 *N* HCl, temporary modifications of the calorimeter were made in order to magnify certain effects and are explained in this section.

Figure 1 is a diagram of the calorimeter vessel and some of its associated parts. Five platinum tubes (two are not shown) lead up from the cover of the vessel; at left, the vent tube (B); in the center, the tube which surrounds the stirrer shaft; and at right, the tube containing the push-rod which opens the sample holder. In the upper right of figure 1 is an enlarged view of the original vent seal at the vessel cover. It consisted of a weighted platinum rod (D) which seated in a polytetrafluoroethylene (PTFE) ring (diameter of hole = 1.6 mm) located between the two parts of the vessel cover. In some experiments the rod was in place and it formed a seal; in other experiments the rod was withdrawn and there was a direct vent between the vapor space above the solution and the atmosphere. In some experiments the rod was withdrawn and the upper end of the vent tube was connected by rubber tubing to an open-end manometer (A) containing either mineral oil or mercury. This limited the diffusion of vapor from the calorimeter, and made possible observations of changes in pressure in the vapor space above the solutions during the experiment when there was a seal at the stirrer. The capillary tube, C, shown in figure 1 was used only in a special group of experiments and will be discussed later in this section.

The o-rings at the top of the platinum tubes for the stirrer and push-rod (fig. 1) also limit the extent to which the calorimeter is sealed from the atmosphere. Normally, since this is essentially a constant pressure system, PTFE o-rings are used. They are intended to function more as bearings than as seals; they wear with use and flow when heated; they form poor and unreliable seals under these conditions; however, they provide a good bearing surface for reproducible stirring energy. We have found that these bearings may hold pressures up to 10 cm of mineral oil. In experiments where good seals around the stirrer shaft and push-rod are needed, the PTFE o-rings are replaced by heavily lubricated rubber o-rings which are compressed by brass fittings (not shown in fig. 1).

In the measurements reported in this paper, four venting arrangements were used:

(1) In the "unvented" or sealed system, the vessel was sealed by nitrile rubber o-rings around the stirrer

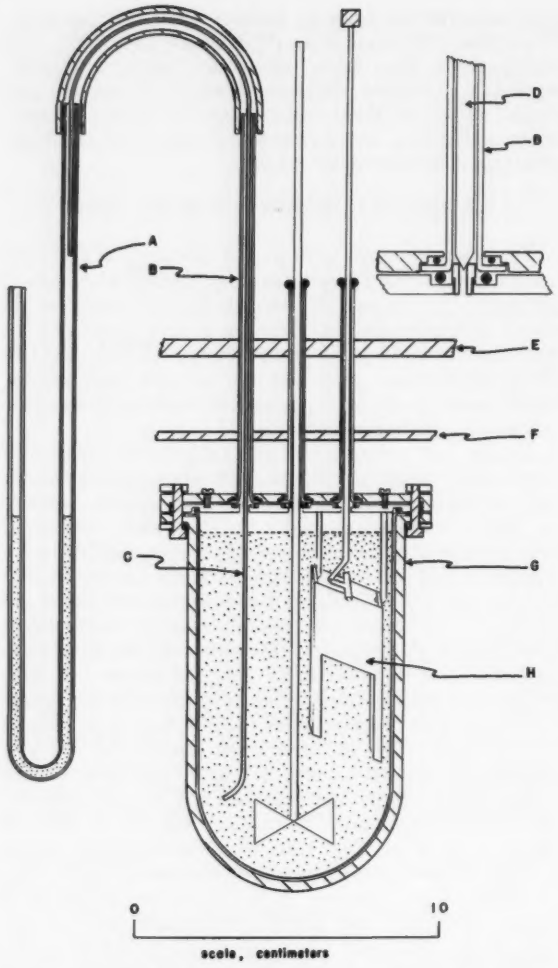

FIGURE 1. *Diagram of the calorimeter with modifications for some of this work.*

(A) Glass, open-end manometer filled with mineral oil or Hg; (B) Vent tube; (C) PTFE capillary tube; (D) Weighted platinum rod for sealing vent; (E) Cover of calorimeter jacket; (F) Cover of adiabatic shield; (G) The silver calorimeter vessel, platinum-lined; (H) Platinum sample holder.

shaft and the push-rod, and the vent was sealed at the vessel cover by the weighted platinum rod (see fig. 1, upper right).

(2) In the "vented" system which was partially closed to the atmosphere, the platinum rod was removed and the top of the vent tube was connected through rubber tubing to an open-end manometer. PTFE o-rings were used as bearings at the top of the stirrer and push-rod tubes.

(3) In the vented system open to the atmosphere, the arrangement was similar to (2) except that the rubber-tubing was disconnected from the manometer.

(4) In the system where the effects of various atmospheric gases on the TRIS reaction were studied, nitrile rubber o-rings formed seals at the top of the stirrer and push-rod tubes. The platinum rod and the PTFE ring were removed from the vent tube, and a PTFE capillary tube (C) was passed through the rubber tubing and vent tube as shown in figure 1. The lower end of the capillary tube was located a little above the stirrer and the upper end could be connected to a gas introduction line. The gas was passed through the capillary tube and bubbled through the solution; the exit gases passed through the space between the capillary and the vent tube and the rubber tubing to the atmosphere. When the gas flushing was completed, the capillary tube was disconnected from the gas introduction line and placed inside the top of the open-end manometer where the rubber tubing was connected as shown in figure 1. The calorimeter solution was thus essentially saturated with the gas under study and the space above the solution was filled with the gas at atmospheric pressure.

2.5. Calibrations and Physical Constants

The platinum resistance thermometer was calibrated in October 1961 and checked at the ice point in 1968 (see [2] for the calibration data), and 1 K equals 0.10104 Ω at 298.15 K. For converting the quartz-oscillator readings, Q, to the equivalent temperature, T (in °C) on the platinum resistance thermometer we use the linear equation, $T=A+B(Q)$. The constants, A and B, are 0.10030 and 1.01080, respectively, for the experimental quartz-oscillator system, and −8.41001 and 1.01273, respectively, based on a calibration in June 1972 for the system currently in use.

The last certified NBS calibrations of the three standard resistors (0.1 Ω, 10 Ω, and 10 kΩ used in the electrical energy measurement circuit) were made in June 1969, and of the standard cells in terms of the NBS absolute volt of 1968, in July 1969. The records of these calibrations at 1- or 2-year intervals provides additional confidence in the values used because of the consistent trends in the calibrated values. Dial calibrations of the G–3 Mueller resistance bridge were made in this laboratory in January 1969 and November 1970, and of the six-dial potentiometer, in January 1969.

The heat attributed to the chemical reaction is obtained from comparison of the calorimeter temperature rise with that resulting from the addition of precisely, measured electrical energy. The time of electrical heating is based on the standard frequency signals available at NBS.

The 1969 atomic weights [6] were used to obtain the molar mass for TRIS ($C_4H_{11}O_3N$), 121.1369. For energy conversions, 4.184 joules = 1 thermochemical calorie. The following densities were used in computing buoyancy factors: 1.35 $g \cdot cm^{-3}$ for TRIS [7], and 0.00118 $g \cdot cm^{-3}$ for air under the average conditions in this laboratory.

3. Experimental Results

The objective in this work was to provide certified enthalpy values for the reaction of Standard Reference

Material 724a (TRIS) with 0.100 *N* HCl, an exothermic reaction, and with 0.0500 *N* NaOH, an endothermic reaction, under the conditions recommended by the Standards Committee of the U.S. Calorimetry Conference in October 1966. We observed large variations in the enthalpy of the reaction in aqueous HCl under extreme conditions, and we conclude that under less extreme conditions small variations in the enthalpies of reaction occur when there are small departures from the standard conditions. The results of our measurements under the extreme conditions, some supplemental measurements, and the work which is the basis for the certified enthalpies of reaction are discussed in the following subsections.

3.1. Anomalous Effects in the Closed Calorimeter

The experiments described in sections 3.1a and 3.1b are not of high precision. It is unlikely that the conditions of these experiments would be used in precision calorimetry, however, the results under the extreme conditions may serve to explain small variations in the enthalpy of reaction when there are small departures from the conditions of the certified values. The possibility of the occurrence of these variations to an undetermined extent has prompted the assignment of a larger uncertainty to the certified value for the reaction in aqueous HCl than would otherwise have been necessary.

The calorimeter was designed primarily as a constant pressure calorimeter. The modifications made to seal the calorimeter did not result in a constant volume system in the usual sense because slow leakage sometimes occurred at the seal around the stirrer. However, the leakage rate was usually slow enough to allow observations of pressure changes above the solution during an experiment.

a. The Venting Effect

In an earlier investigation where the enthalpy of reaction of gaseous ketene in aqueous NaOH was measured [8], it was necessary to make the calorimeter sufficiently gas-tight so that the gaseous products could be collected and analysed. Following that investigation the reaction of TRIS in 0.1 *N* HCl was measured as a check on the performance of the calorimeter. The enthalpy values were about 3 percent higher than those previously measured under what were believed to be identical conditions; the only difference was that the PTFE o-ring bearing was replaced with a lubricated nitrile o-ring at the top of the tube surrounding the stirrer shaft. The calorimeter was an unvented system, arrangement (1) as described in section 2.4. When the nitrile o-ring seal around the stirrer was replaced by a PTFE o-ring bearing which was not a seal, the enthalpies measured for the TRIS reaction were again the lower values obtained before sealing the calorimeter.

In table 1 are the results of measurements of the reaction of SRM 724 or SRM 724a with 0.1 *N* HCl in the vented and in the unvented calorimeter, arrangements (2) and (1), respectively, as described in section 2.4. The pressure changes observed in the vented system appear to be insignificant and will be discussed in section 3.1b. The initial systems were always at

TABLE 1. *Results of measurements of the reaction of SRM 724 and 724a with* 0.1 N HCl *solutions in vented and unvented systems*

Expt. No.	Electrical energy equivalents		$-\Delta H$(298.15 K)			
			SRM 724		SRM 724a	
	Initial	Final	Vented	Unvented	Vented	Unvented
	$J \cdot K^{-1}$	$J \cdot K^{-1}$			$J \cdot g^{-1}$	
389	1729.06	1731.24	.....	.....	245.73	.....
390	1727.79	1730.15	245.87	.....	.....	.....
391	1728.19	1730.38	.....	.....	246.11	.....
392	1727.93	1730.15	245.61	.....	.....	.....
393	1727.72	1729.88	245.71	.....	.....	.....
394	1727.97	1730.82	.....	.....	246.18	.....
397	1728.07	1730.09	.....	251.75	.....	.....
398	1728.29	1730.20	.....	.....	245.83	.....
399	1727.80	1730.37	246.11	.....	.....	.....
400	1728.90	1730.66	.....	.....	.....	252.88
401	1728.06	1730.84	.....	255.35	.....	.....
402	1731.12	1730.88	.....	.....	.....	254.28
405	1728.58	1730.07	.....	.....	245.83	.....
406	1729.26	1729.45	245.61	.....	.....	.....
407	1727.83	1731.01	245.66	.....	.....	.....
408	1728.27	1730.14	.....	.....	245.78	.....
409	1729.96	1730.30	246.17	.....	.....	.....
410	1728.56	1731.52	.....	.....	245.91	.....
		Mean	245.82	253.55	245.91	253.58
		Sdm	±0.09		±0.06	

atmospheric pressure and the increase in the pressure above the solutions during an experiment amounted to only about 5 cm of mineral oil (approx. density = 0.9 $g \cdot cm^{-3}$).

The Expt. No. in table 1 is the serial number of experiments with this calorimeter. The temporary quartz-oscillator thermometer system (see sec. 2.3) was used in this group of experiments. The mean values of the enthalpies using SRM 724 and SRM 724a agree with each other within the experimental imprecision for both the vented and unvented systems. The mean enthalpies in the unvented system are more than 3 percent larger and less reproducible than those in the vented system. However, there is no significant difference in the electrical energy equivalents measured for the initial and final systems in these experiments. The energy equivalents may differ by as much as 0.1 percent between experiments because of small variations in the mass of the calorimetric solutions. The agreement between the electrical energy equivalents in the vented and unvented systems indicates that the calorimeter was performing properly in both systems. The disagreement between the enthalpy values for the reaction in the vented and unvented systems indicates the possibility of a side reaction causing a larger exothermic enthalpy value in the closed system. The observations of pressure above the solutions in the vented system indicated that the increase in pressure during the reaction was similar to that which occurred during the electrical calibrations; the temperature rise was essentially the same in the reaction and in the calibrations.

The vapor space volume above the solutions in these experiments was approximately 20 cm^3. Condensation within this vapor space would produce an exothermic heat which might be different in a vented system than in an unvented system. However, since there is no change in ionic strength for the hypothetical reaction, the condensation correction is assumed to be zero.

It was also possible that the venting effect was the result of a side reaction catalysed by the platinum which lines this calorimeter. However, this effect has been observed by Duer [9] in an isoperibol calorimeter with no platinum parts; the vessel was glass with a stainless steel lid. His enthalpy measurements with SRM 724 in 0.1 N HCl averaged -249.24 ± 0.96 $J \cdot g^{-1}$ in four experiments before providing a definite vent to the atmosphere; after venting the calorimeter, the average of five experiments was -246.19 ± 0.25 $J \cdot g^{-1}$. The uncertainties are 2 sdm, the difference between the two enthalpy values is 1.2 percent, and the experimental imprecision was definitely improved by venting the calorimeter.

P. J. Gardner [10] has given us permission to publish his results of measurements of the TRIS reaction with a new calorimeter constructed during his tenure of a Visiting Fellowship to the Chemistry Department at the University of Otago during 1971–72. The isoperibol calorimeter was glass with reentrant wells for the thermistor and heater. The stirrer was steel with PTFE bearings which presumably formed good seals initially, but after wearing did not seal the calorimeter. The following enthalpy values were first measured for the reaction of TRIS in 0.1 *N* HCl: −7520, −7150, −7300, −7150, −7130, and −7330 $cal \cdot mol^{-1}$; the average was 7263 ± 62(sdm) $cal \cdot mol^{-1}$ or 250.86 ± 2.14 $J \cdot g^{-1}$. These results were very erratic and high. He measured another test reaction which gave satisfactory agreement with published values. He then returned to the TRIS reaction. By this time he was using longer fore periods to insure thermal equilibrium before the reaction, and the PTFE stirrer bearings had worn and the calorimeter was probably vented to the atmosphere. This time the mean of seven experiments was 7118 ± 5(sdm) $cal \cdot mol^{-1}$ or 245.85 ± 0.17 $J \cdot g^{-1}$. These two sets of results are similar to ours in the vented and unvented systems.

Robie and Hemingway [11] found a venting effect, but in the opposite direction. Their isoperibol calorimeter is lined with gold. The average of their ten enthalpy measurements with SRM 724 in a sealed calorimeter was -245.16 ± 0.38 $J \cdot g^{-1}$ [12] and after venting the calorimeter, the average of five experiments was -245.64 ± 0.24 $J \cdot g^{-1}$ [11]; these two values are within the experimental imprecisions (2 sdm) given and may not be significantly different, however, there does appear to be an improvement in the precision of the measurements upon venting the calorimeter. In September 1972, we made four measurements of the TRIS reaction using 0.6 g of gold turnings with TRIS in the sample holder. The average enthalpy in these experiments was -245.78 ± 0.32 $J \cdot g^{-1}$ which agrees well with the certified value, -245.76 $J \cdot g^{-1}$ (discussed in sec. 3.3); the experimental imprecision, 2 sdm, is larger than normal because of stirring problems at that time. However, it appears that the presence of gold did not affect the enthalpy of reaction significantly.

We have looked for the venting effect in other reactions such as that of H_2SO_4 (aq) in NaOH(aq) [2] and in KCl(c) in H_2O [13]. These enthalpies of reaction were the same in the unvented calorimeter or in the calorimeter open to the atmosphere.

b. The CO_2 Effect

In June 1970, a preliminary investigation was made of the effects of dissolved gases (the major components of air: N_2, O_2, Ar, and CO_2) on the TRIS reaction in 0.1 *N* HCl. The results of this investigation were reported informally at the U.S. Calorimetry Conference in October 1970.

The gas under study was introduced into the calorimeter through a PTFE tube, (C), in figure 1. The compressed gas from a commercial cylinder was passed through a tube containing magnesium perchlorate and a CO_2 absorber (this was by-passed when CO_2 was used), and then through a bubbler containing 0.1 *N* HCl before entering the PTFE tube and the calorimeter as described in section 2.4. The gas was bubbled through the calorimetric solution at approximately 50 $cm^3 \cdot min^{-1}$ for about 90 min while stirring to saturate the solution and displace air above the solution with the gas under study. Small droplets of solution accumulated on the vessel cover as a result of gas bubbles bursting at the surface of the solutions. These

droplets probably caused errors due to evaporation to the main solution during the experiment, therefore, the results are not of high precision but are useful in showing gross effects.

The temporary quartz-oscillator thermometer system was used for measurement of the calorimeter temperature. The vent tube was connected to an open-end manometer and the pressures above the solutions were recorded during the experiment. Arrangement (4), section 2.4, was used for these measurements. In the nine preliminary experiments the enthalpies of reaction (in $J \cdot g^{-1}$) were: N_2 atmosphere, −246.8, −246.2, and −245.7; O_2 atmosphere, −247.3 and −246.0; Ar atmosphere, −248.5 and −246.0; and CO_2 atmosphere, −260.9 and −262.8. The last two values are obviously about 7 percent higher than the others which we regard as normal values within the experimental uncertainties of these rough experiments.

In all of these experiments, except the two using CO_2, the manometer contained mineral oil. With CO_2 the pressure changes were larger and it was necessary to use mercury in the manometer. One end of the manometer was open to the atmosphere and the readings indicated the difference between the pressure above the calorimetric solution and the atmospheric pressure. Figure 2 is a plot of the manometer readings, $P_{cal} - P_{atm}$, versus time for four of the experiments using different gaseous atmospheres. The pairs of vertical lines mark the electrical heating periods for the calibrations and the single vertical line marks the time when the TRIS reactions were started. At the left of figure 2, the set of points at the top are for the N_2 atmosphere; the second set, for the O_2 atmosphere; the third set, for the Ar atmosphere; and the fourth set at the bottom, for the CO_2 atmosphere. The larger circles marking the pressure readings for the CO_2 atmosphere indicate that the readings were actually made as cm of Hg and were converted to cm of mineral oil using a factor of 15; thus, the uncertainty in these readings is greater than for the other three gases and roughly proportional to the diameter of the circles. When the connection between the manometer and the vent tube was made initially, the readings were all zero (or at atmospheric pressure). With N_2 atmosphere, the pressure above the solution continuously increased during the experiment. The changes in pressure for the O_2 and Ar atmospheres were similar; there was initially a small reduction in pressure as the system continued to absorb the gas, a leveling off, and then increasing pressure above the solution during the remainder of the experiment. In the atmospheres of N_2, O_2, and Ar, the increase in pressure during the TRIS reaction was essentially equal to that during the electrical calibrations. This is to be expected since the temperature rise was the same for the reaction and for the calibrations.

The pressure changes in the CO_2 atmosphere were quite different. Initially there was a large and rapid reduction in pressure as the system continued to absorb CO_2. After reaching a minimum the pressure steadily increased and began to level off near atmospheric pressure. (It was learned that this was due to air leakage through the stirrer seal and will be discussed later in this section.) The pressure changes during the calibrations are negligible, but during the TRIS reaction there was a pressure increase of approximately 20 cm of mineral oil or more than 1 cm of Hg. This unmistakable increase in pressure above the solution was a result of the TRIS reaction in the presence of CO_2. This was accompanied by an additional exothermic heat effect when air was also present as shown by the high $-\Delta H_r$ values. When the calorimeter is not sealed, the additional exothermic effect in solutions saturated with CO_2 is not found.

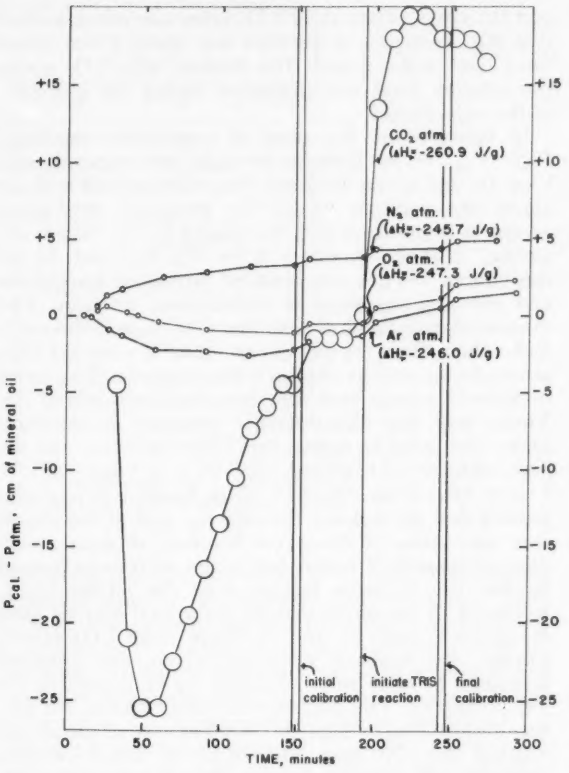

FIGURE 2. *Plots of observed pressures in the vapor space above the solutions during preliminary* TRIS *experiments in a sealed calorimeter where the* HCl *solutions were saturated with various gases: Curves at left (top to bottom)* N_2, O_2, Ar, *and* CO_2 *atmospheres.*

Negative pressure reading indicates reduced pressure above the solution.

To confirm our earlier results with the CO_2 atmospheres, we measured enthalpies of the TRIS reaction with and without CO_2 in July 1972, where the calorimeter temperatures were measured with the new quartz-oscillator system (see sec. 2.3). The precision of the calorimetry was improved in these experiments by preventing the accumulation of droplets of solution on the vessel cover during the preliminary gas flushing. This was accomplished by flushing the CO_2 through the solution before the cup of the vessel was attached to the cover, with a space of about 2 cm between the solution

and the cover. Then the PTFE tube was withdrawn so that the lower end of the tube was about 2 mm below the cover of the vessel. The flushing with CO_2 above the solution level was continued during the assembly of the calorimeter.

In figure 3 are the plots of manometer readings, $P_{cal} - P_{atm}$, versus time for the eight later experiments. Plots (a) and (e) are for Expt. Nos. 674 and 680 with air above the solution where the pressures are given as cm of mineral oil and the shapes of the curves are similar to those in figure 2 for N_2, O_2, and Ar atmospheres. No gas was bubbled through the solutions and the systems were in equilibrium with air. The measured enthalpies of reaction were close to the certified value. Plots (b) and (c) in figure 3 were for CO_2 atmospheres and are similar to the corresponding curve in figure 2 except that the pressures are in cm of Hg. There was the characteristic increase in pressure above the solution during the TRIS reaction and the high enthalpy of reaction, $-258.54\ J \cdot g^{-1}$ and $-251.91\ J \cdot g^{-1}$. After Expt. No. 678, (c) in figure 3, it was suspected that air leakage through the seal at the stirrer was the cause of the curve leveling off near atmospheric pressure. A better seal at the stirrer was formed by the use of more lubricant on the nitrile o-ring. Evidence of the improvement in the seal may be seen in figure 3, plots (d) and (f) where, with CO_2 atmospheres, the reduced pressures above the solutions remained at more than 20 cm of Hg until starting the TRIS reaction. The pressure increase in Expt. No. 681 was slower than in Expt. No. 679 because of the slower stirring rate, 200 rpm, instead of the usual 450 rpm used for other experiments in this group. It was unexpected that in these two experiments where the atmosphere was relatively pure CO_2, the enthalpies of the TRIS reactions were very close to those from the reactions in the presence of air alone. With the suspicion that both air and CO_2 are required to obtain the strongly exothermic side reaction, in two experiments, (g) and (h) in figure 3, some air was admitted to the CO_2- saturated system after the minimum pressure was reached. Again in the presence of CO_2 + air the enthalpies of reaction, $-280.07\ J \cdot g^{-1}$ (g) and $-269.71\ J \cdot g^{-1}$ (h), were significantly larger than in the presence of air or CO_2 alone.

It was also observed in the systems saturated with CO_2, that upon initiating the reaction the increase in pressure above the solution was relatively slow. It can be seen in figure 3 that the increase in pressure extended over a period of about 15 min. However, in atmospheres of air, N_2, O_2, and Ar, the increase in pressure was almost instantaneous. The gas which was in the sample holder obviously expanded rapidly because it was at the source of the heat of reaction.

Although these results cannot be regarded as quantitatively precise, they do indicate two effects in the TRIS reaction with 0.1 *N* HCl in a closed system: (1) an increase in the pressure above the solution during the reaction in the presence of CO_2, and (2) a side reaction in the presence of CO_2 + air which is more exothermic than the reaction in the presence of only air or CO_2. If only the hypothetical reaction occurred in

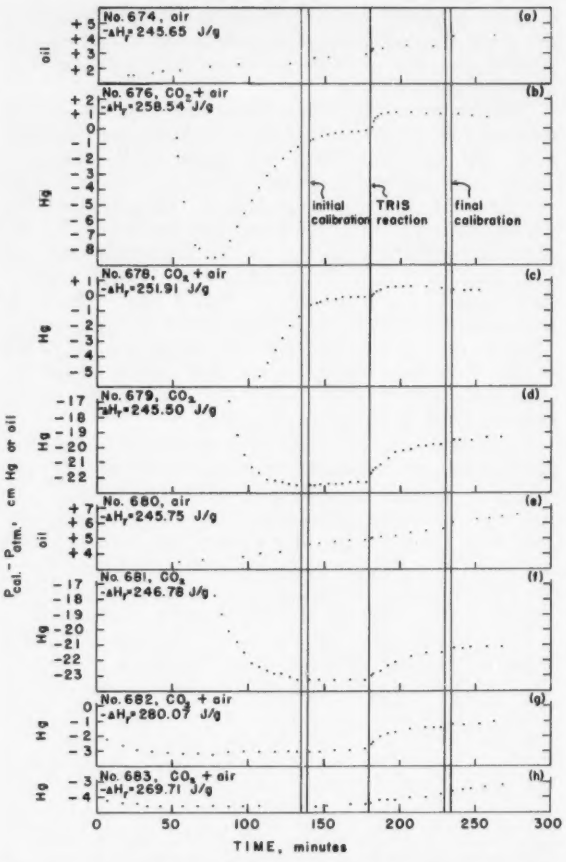

FIGURE 3. *Plots of observed pressures in the vapor space above the solutions during later* TRIS *experiments in a sealed calorimeter in atmospheres of air, air + CO_2, and CO_2.*

The scale for (a) and (e) is cm of oil, and cm of Hg for all others.

the system saturated with CO_2, a slightly smaller value for $-\Delta H_r$ would be expected because of the reduction in solubility of CO_2 at the higher temperature. However, the effect of the change in composition of the solution on the CO_2 solubility is not known. Quantitative and qualitative analyses of the solutions and gases, and more accurate pressure measurements would be necessary if the side reaction is to be fully described.

Variations in the enthalpy of reaction may be expected, especially in constant volume systems, unless care is taken to exclude CO_2 from the system. If CO_2 is absent from the system, the enthalpy value may be slightly lower than the certified value, where the solutions are in equilibrium with air which contains 0.03 percent CO_2.

3.2 Supplemental Measurements

Our enthalpy calculations are based on the assumption that the energy equivalents at the mean tempera-

TABLE 2. *Measurements of electrical energy equivalents at various temperatures for initial and final systems in the* TRIS *reaction with* 0.1 N HCl

Expt.	Initial system			Final system		
No.	ΔT	$\bar{T}$	*EEE*	ΔT	$\bar{T}$	*EEE*
	K	*K*	$J \cdot K^{-1}$	*K*	*K*	$J \cdot K^{-1}$
*477	1.28279	295.72	1730.35	1.28096	301.09	1733.07
	1.28262	297.01	1730.33	1.28064	302.37	1733.40
	1.28347	298.57	1729.50	1.28080	303.66	1733.29
	1.28242	299.58	1730.81	1.28050	304.95	1733.57
		(Mean)	1730.25		(Mean)	1733.33
693	0.22025	297.46	1727.35	0.22008	298.38	1730.15
	.22010	297.69	1727.26	.22021	298.61	1729.73
	.22028	297.93	1727.32	.22009	298.85	1729.90
		(Mean)	1727.31		(Mean)	1729.93
695	0.57543	296.53	1727.87	0.57436	298.53	1729.15
	.57471	297.12	1727.80	.57390	299.12	1728.78
	.57385	297.71	1726.97	.57423	299.71	1728.54
		(Mean)	1727.55		(Mean)	1728.82

*The temporary quartz thermometer used in this experiment had a different heat capacity than the new quartz-oscillator used in the other two experiments; this accounts for the difference in the *EEE*.

ture of the chemical reaction are the same as those at the mean temperatures of the electrical calibrations. Therefore, multiple electrical calibrations of the initial and final systems for the TRIS reaction in 0.1 *N* HCl were measured to determine whether the energy equivalents changed significantly with temperature. The results of these measurements in three experiments are given in table 2. The earlier quartz thermometer system (discussed in sec. 2.3) was used in Expt. No. 477 and the corrected temperature rise, ΔT, was 1.28 K for each of the four electrical calibrations of the initial and final systems. There was no consistent change in the electrical energy equivalents, EEE, with temperature and the maximum departure from the mean of the group was 0.04 percent. Although EEE of the initial systems would change by about 0.02 percent per deg (from known heat capacity data), this trend was considered negligible in relation to our measurements of the TRIS reaction because the difference between the mean temperature of the calibration and that of the reaction was less than 0.3 K. In Expt. Nos. 693 and 695 the temperatures were measured with the later quartz-oscillator system (discussed in sec. 2.3) and the temperature rises during the calibrations were 0.22 K and 0.57 K, respectively. There was no evidence of a change in the energy equivalents with temperature in this range and the stated assumption was justified.

There are small differences in the electrical energy equivalents for different experiments because of small variations in the mass of solutions used. The energy equivalents actually measured for each system are used in the calculations of heat evolved or absorbed. However, the differences in the energy equivalents do not reflect the precision of the measurement of the electrical energy equivalents. In order to obtain a factor for correcting the energy equivalents to a standard mass of solution, measurements were made on systems containing 5 percent more and 5 percent less than the standard mass of HCl solution (302.7 g) and of TRIS (1.50 g); these results are given in table 3. In these four experiments the temperature was measured with the platinum resistance thermometer and the system was vented to the atmosphere, arrangement (3) described in section 2.4. The vapor space above the solution in the vessel was nearly eliminated in Expt. Nos. 530 and 531, and was less than 40 cm^3 in volume in Expt. Nos. 532 and 533. Arvidsson and Westrum measured the heat capacity of TRIS as $Cp(298.15\ K) = 39.96$ cal $\cdot$ $mol^{-1} \cdot K^{-1}$ or 0.1394 $J \cdot g^{-1} \cdot \Omega^{-1}$ [14]. The corrections to the energy equivalents here were less than 0.02 $J \cdot \Omega^{-1}$ for the differences from the standard mass of TRIS: these corrections were neglected. The factors for correcting to the standard mass of HCl solution

TABLE 3. *Electrical energy equivalents of initial and final systems for the* TRIS *reaction in* 0.1 N HCl *using more and less than the standard mass of* HCl *solution and of* TRIS

Expt. No.	Mass of HCl soln.	Electrical energy equivalents	
		Initial	Final
	g	$J \cdot \Omega^{-1}$	$J \cdot \Omega^{-1}$
5% more than the standard mass of HCl and TRIS:			
530	317.68	17,730.6	17,756.4
531	317.71	17,731.9	17,764.0
(Mean)	317.70	17,731.2	17,760.2
5% less than the standard mass of HCl and TRIS:			
532	287.68	16,498.1	16,516.9
533	287.77	16.505.7	16,527.4
(Mean)	287.72	16,501.9	16,522.2

Factors: 41.00 $J \cdot \Omega^{-1} \cdot g^{-1}$ for initial system
41.29 $J \cdot \Omega^{-1} \cdot g^{-1}$ for final system

TABLE 4. *Corrections to the measured electrical energy equivalents (table 5) and the energy equivalents corrected to a standard mass of* HCl *solution for initial and final systems of the* TRIS *reaction in* 0.1 N NCl

Expt. No.	Mass of TRIS	Mass of HCl soln.	Correction to 302.70g HCl		Energy equivalent corrected	
			Initial	Final	Initial	Final
	g	*g*	$J \cdot \Omega^{-1}$	$J \cdot \Omega^{-1}$	$J \cdot \Omega^{-1}$	$J \cdot \Omega^{-1}$
521	1.49696	302.76	−2.5	−2.5	17,117.6	17,146.7
522	1.49214	302.73	−1.2	−1.2	17,115.3	17,149.3
523	1.52248	302.72	−0.8	−0.8	17,122.5	17,141.8
524	1.53278	302.69	+0.4	+0.4	17,116.1	17,142.1
527	1.50880	302.69	+0.4	+0.4	17,116.7	17,142.3
(Mean)					17,117.6	17,144.4
(sdm)					±1.3	±1.5
					(0.008%)	(0.009%)
528	1.52958	302.74	−1.6	−1.6	17,117.4	17,137.3
529	1.52074	302.72	−0.8	−0.8	17,116.1	17,139.2
532	1.45790	287.68	+615.8	+620.2	17,113.9	17,137.1
533	1.43550	287.77	+612.1	+616.4	17,117.8	17,143.8
534	1.52143	302.73	−1.2	−1.2	17,115.6	17,144.0
(Mean)					17,116.2	17,140.3
(sdm)					±0.7	±1.5
					(0.004%)	(0.009%)

given at the bottom of table 3 were obtained from the two means for mass of HCl solution and for the energy equivalents for the initial and final systems. These factors were used to obtain corrections to the energy equivalents for TRIS experiments to be described in the next section, 3.3, and the pertinent data are given in table 4. In each group the standard deviation from the mean of the corrected energy equivalent was less than ± 0.01 percent which is an indication of the precision of the calorimetry.

3.3 ΔHr of SRM 724a in HCl (aq)

Some of our measurements of the enthalpy of reaction of SRM 724a in 0.1 *N* HCl using the platinum resistance thermometer system previously described [2] are given in table 5. The masses of TRIS and of the HCl solution for these experiments were listed in table 4. The electrical energy equivalents given in table 5 are the values actually measured (not corrected to a standard mass of HCl solution). The "Stirring energy correction" is the net result of the extrapolations from the mid-points of the initial and final rating periods to the time of starting the reaction; it was subtracted from the difference between the temperatures at the mid-points of the rating periods to obtain the corrected temperature rise, ΔRc reaction. The enthalpy of solution at the temperature of reaction is $\Delta H(T) = -[\overline{EEE}\ (\Delta Rc)]$/(mass of TRIS), where $\overline{EEE}$ is the mean of the initial and final electrical energy equivalents. The enthalpy of reaction, ΔH(298.15 K), is the sum of $\Delta H(T)$ and the correction obtained from $\Delta Cp = 1.435$ $J \cdot g^{-1} \cdot K^{-1}$ which will be discussed later in this section.

The first five experiments given in table 5 were vented to the manometer containing mineral oil, arrangement (2) described in section 2.4, and are in good agreement with the vented experiments given in table 1 where the quartz-oscillator thermometer was used. The last five experiments listed in table 5 were vented to the atmosphere, arrangement (3) in section 2.4. Here the mean enthalpy of reaction was slightly smaller and the precision of the measurements was significantly improved as compared to the first five experiments. Thus, it appears that even the seemingly insignificant confinement by the open-end manometer of the vapor space above the solution may have affected the enthalpy of solution.

In table 5, the values for $-\Delta H$(298.15 K) which are marked with an asterisk were measured in a solution which was initially CO_2-free; the unmarked values were in solutions always in equilibrium with air. The CO_2-free solution was prepared in a Pyrex glass Erlenmeyer flask. The distilled water was boiled approximately 30 min to remove CO_2. Immediately after removing the flask from the heat, the concentrated HCl solution was added. Then the flask was sealed by a rubber stopper containing a glass siphon tube with a stopcock on the outer end. The air intake for the flask was guarded by a tube containing $MgClO_4$ and a CO_2 absorber. After cooling, the solution was analysed as 0.0984 *N* by titration with 0.1 *N* standard sodium hydroxide solution using a pH recording electrometer. All portions of the HCl solution were dispensed through the glass stopcock into a polyethylene bottle for weighing the calorimetric solutions. The weight of the solution was adjusted and the solution was poured into the cup of the calorimeter vessel which was quickly attached to the cover. Thus, although the HCl solution was initially CO_2-free, the calorimetric solutions were exposed to the atmosphere during weighing and transfer to the vessel as well as during the experiment since the calorimeter was not gas-tight. It is therefore not surprising that no significant difference was observed between the enthalpy values for experiments using solutions initially CO_2-free and those using solutions always in

TABLE 5. *Calorimetric data for reaction of SRM 724a in* 0.1 N HCl *solution*

The last five experiments are the basis for the certified enthalpy value

Expt. No.	Electrical energy equivalents		Stirring energy correction	ΔRc reaction	$\bar{T}$ reaction	Corr. to 298.15 K	$-\Delta H$(298.15 K)
	Initial	Final					
	$J \cdot \Omega^{-1}$	$J \cdot \Omega^{-1}$	Ω	Ω	K	$J \cdot g^{-1}$	$J \cdot g^{-1}$
Vented to manometer:							
521	17,120.1	17,149.2	0.000522	0.021514	297.946	−0.29	*245.96
522	17,116.5	17,145.2	.000497	.021454	297.945	− .29	246.01
523	17,123.3	17,142.6	.000495	.021882	298.147	.00	*246.24
524	17,115.7	17,141.7	.000494	.021993	298.146	.00	245.77
527	17,116.3	17,141.9	.000474	.021660	298.144	−.01	*245.90
						(Mean)	245.97
						(sdm)	±0.08
							(0.03%)
Vented to atmosphere:							
528	17,119.0	17,138.9	0.000474	0.021941	298.143	−0.01	245.70
529	17,116.9	17,140.0	.000479	.021826	298.143	−.01	*245.82
532	16,498.1	16,516.8	.000518	.021677	298.358	+.30	245.75
533	16,505.7	16,527.4	.000519	.021333	298.358	+.30	*245.75
534	17,116.8	17,145.2	.000554	.021856	297.952	−.28	*245.81
						(Mean)	245.76
						(sdm)	±0.02
							(0.01%)

*Initially solutions were CO_2-free.

equilibrium with air. The analysis of the latter stock solution was 0.1003 *N*.

A value of ΔCp for the reaction of TRIS in 0.1 *N* HCl was obtained from a least squares fit of the data in table 6 to a linear equation. A quadratic equation was also fitted by least squares and this indicated that the data did not justify a quadratic term. ΔCp for the reaction is 1.435 ± 0.023 $J \cdot g^{-1} \cdot K^{-1}$ or 41.54 ± 0.67 $cal \cdot mol^{-1} \cdot K^{-1}$ (the uncertainty is the standard error). This is in excellent agreement with the value of 1.437 $J \cdot g^{-1} \cdot K^{-1}$ reported by Hill et al. [15].

The certified value for the enthalpy of reaction of SRM 724a in 0.1 *N* HCl solution is

$$\Delta H(298.15\ K) = -245.76 \pm 0.26\ J \cdot g^{-1} \qquad (1)$$

and is based on the last 5 experiments in table 5. The conditions which apply to this value are as follows:

(1) The standard reference material should be used without further crushing or heating.
(2) The concentration should be 5 g of the sample per dm^3 of 0.100 *N* HCl solution.
(3) The sample and the calorimetric solution should be in equilibrium with air at atmospheric pressure.
(4) Measurements should be made at constant pressure.

The overall uncertainty (0.11%) assigned to the certified enthalpy value is the square root of the sum of the squares of the following uncertainties: the experimental precision at the 95 percent confidence level, 0.03 percent; inhomogeniety in the sample, 0.01 percent; and other possible systematic errors, 0.10 percent. The latter is larger than would have been assigned if the anomalous effects of venting and CO_2 were unknown. Until these effects can be fully explained and the conditions of the reaction more precisely defined, a smaller uncertainty can not be assigned.

TABLE 6. *Data used in obtaining the relationship of temperature and the enthalpy of reaction of* TRIS *in 0.1 N* HCl

Expt. No.	$\bar{T}$ reaction	$-\Delta H(T)$
	K	$J \cdot g^{-1}$
536	293.628	252.25
537	293.706	252.32
534	297.952	246.09
528	298.143	245.71
529	298.143	245.83
532	298.358	245.45
533	298.358	245.45
535	303.088	239.15
538	303.098	238.36

The following possible errors and corrections to the ΔH_{soln} were considered for the worst conditions and found to be negligible:

(1) Heater lead corrections, −0.004 percent;
(2) Factor switch on potentiometer, −0.004 percent;
(3) Vaporization correction for air in sample holder, <0.05 *J* or <0.02 percent.

The first two corrections are opposite in sign to the third resulting in a net correction of about 0.01 percent in the worst case.

3.4. ΔHr of SRM 724a in NaOH(aq)

The platinum resistance thermometer was used to measure the calorimeter temperature in all experiments in this section. The NaOH solutions were prepared and analysed as described in section 2.2.

The enthalpy of reaction of TRIS in aqueous NaOH is dependent on the NaOH concentration. In 11 preliminary experiments we measured the enthalpy of reaction of SRM 724 at various concentrations of NaOH as given in table 7. The mass of the samples was between 1.7 and 2.1 g and the mass of the solutions was 307 to 308 g. The correction to 298.15 K was obtained from $\Delta Cp = 1.03\ J \cdot g^{-1} \cdot K^{-1}$ (eq (3) discussed later in this section). A least squares fit of the NaOH concentration and enthalpy of reaction data in tables 7 and 8 resulted in the following equation (in $J \cdot g^{-1}$):

$$\Delta H(298.15\ K) = 146.03 - 87.8(N) + 43.2(N)^2,\ N < 1.0 \quad (2)$$

where N is the normality of the NaOH solution. The standard error of the estimate is $0.19\ J \cdot g^{-1}$. This equation agrees with the values reported by Hill et al. [15], within the uncertainties of the NaOH analyses.

In tables 8 and 9 are the data for 9 more recent experiments with SRM 724a which are the basis for the certified value for the enthalpy of reaction in 0.0500 N NaOH. The electrical energy equivalents for the initial and final systems are given and the stirring energy correction was described in section 3.3. (In Expt. 541 there was a malfunction of the electronic counter and an estimated value was used for the electrical energy equivalent of the final system.) The observed temperature rise, ΔRc net, is the result of the endothermic chemical reaction plus the electrical energy added to prevent a drop in the calorimeter temperature. (Without the addition of electrical energy, adiabatic conditions could not be maintained because the adiabatic shield would be warmer than the vessel.) Details of these electrical energy measurements are given in table 9.

After initiating the electrical heating, a time lag of 10 to 20 s occurs before there is a noticeable rise in the calorimeter temperature, however, the endothermic TRIS reaction in NaOH rapidly absorbs heat as soon as the sample holder is opened. Therefore it was necessary to delay initiation of the reaction until the calorimeter temperature was rising from electrical heating to prevent a drop in the calorimeter temperature. The time interval between the start of electrical heating

TABLE 7. *Data used in obtaining the relationship of* NaOH *concentration and the enthalpy of reaction of* TRIS *in* NaOH(aq)

Expt. No.	Normality of NaOH	$\bar{T}$ reaction	$\Delta H(T)$	Correction to 298.15 K	ΔH(298.15 K)	
	$mol \cdot dm^{-3}$	K	$J \cdot g^{-1}$	$J \cdot g^{-1}$	$J \cdot g^{-1}$	$kJ \cdot mol^{-1}$
264	0.005	297.974	145.47	0.18	145.65	17.644
265	.005	297.933	145.33	.23	145.56	17.632
274	.049	297.741	141.33	.42	141.75	17.171
275	.049	297.792	141.20	.37	141.57	17.149
272	.051	297.740	141.14	.43	141.57	17.149
273	.051	297.744	141.17	.42	141.59	17.152
276	.051	297.735	141.19	.43	141.62	17.156
270	.144	297.923	133.76	.22	133.98	16.230
271	.144	297.936	134.38	.22	134.60	16.306
268	.944	297.978	101.53	.18	101.71	12.321
269	.944	297.932	101.32	.23	101.54	12.300

TABLE 8. *Calorimetric data for experiments which are the basis for the certified enthalpy value for the reaction of SRM 724a in* 0.0500 N NaOH

Expt. No.	Electrical energy equivalents		Stirring energy correction	ΔRc net	Q reaction	Sample mass	NaOH conc.	Corr. to 0.0500 N NaOH	$\bar{T}$ reaction	Corr. to 298.15 K	ΔH(298.15 K)
	Initial	Final									
	$J \cdot \Omega^{-1}$	$J \cdot \Omega^{-1}$	Ω	Ω	J	g	$mol \cdot dm^{-3}$	$J \cdot g^{-1}$	K	$J \cdot g^{-1}$	$J \cdot g^{-1}$
539	17,360.8	17,382.2	0.000731	0.068443	−214.20	1.50772	0.0487	−0.11	298.174	−0.02	141.93
540	17,361.8	17,379.1	.000805	.068278	−216.74	1.52355	.0487	− .11	298.171	−0.02	*142.13
541	17,360.7	(17,380)	.000766	.055982	−214.61	1.51584	.0487	− .11	298.135	+0.02	141.48
542	17,364.4	17,382.6	.000664	.056105	−212.09	1.49550	.0487	− .11	298.113	+0.04	*141.75
543	17,364.6	17,379.3	.000801	.055751	−213.70	1.50330	.0487	− .11	298.312	−0.17	141.88
544	17,360.4	17,376.8	.000843	.055720	−215.58	1.51776	.0487	− .11	298.318	−0.17	*141.76
545	17,356.8	17,380.6	.000779	.055804	−213.35	1.50277	.0489	− .09	298.314	−0.17	141.71
547	17,364.4	17,383.2	.000715	.056145	−215.37	1.52006	.0489	− .09	298.120	+0.03	141.62
548	17,361.8	17,377.6	.000576	.060575	−215.27	1.51439	.0489	− .09	298.298	−0.15	141.91
										Mean=	141.80
										sdm =	±0.06

*Vented to manometer.

TABLE 9. *Data for electrical energy added during the reaction of SRM 724a in* 0.0500 N NaOH

Expt. No.	Reaction delay	E	I	t	$\frac{E}{I} = R$	EIt
	s	V	A	s	Ω	J
539	75	18.65942	0.1926715	390.2940	96.8458	1403.16
540	75	18.65945	.1926707	390.1824	96.8463	1402.76
541	75	18.65707	.1926458	330.2647	96.8465	1187.04
542	75	18.65649	.1926397	330.2258	96.8465	1186.82
543	75	18.63263	.1923931	329.7832	96.8467	1182.20
544	135	18.62740	.1923397	330.2887	96.8464	1183.35
545	135	18.62060	.1922698	330.3186	96.8462	1182.60
547	75	18.68088	.1928915	330.4768	96.8466	1190.83
548	45	28.57851	.2951283	150.2719	96.8342	1267.44

and the opening of the sample holder is the "Reaction delay" given in table 9; the variations shown here did not affect the enthalpy of reaction.

The voltage drop across the calorimeter heater, E, the current through the heater, I, and the time of heating, t, are also given in table 9. The resistance of the calorimeter heater, E/I, indicates the precision of the electrical energy measurements. In Expt. No. 548 the voltage was increased by 10 V; the heater resistance decreased by 0.01 percent. The total electrical energy added during the chemical reaction period, EIt, is subtracted from the product of ΔRc net and the mean electrical energy equivalent to obtain Q reaction (table 8). The enthalpy of reaction at the reaction temperature, $\Delta H(T)$, is $-Q$ reaction/(sample mass). A correction for condensation in the vapor space above the solution was estimated to be about 0.001 J in the worst case and was neglected.

Equation (2) was used for the corrections to 0.0500 N NaOH (table 8). Similar corrections were made to $\Delta H(T)$ in four additional experiments used in obtaining ΔCp for the reaction. The results of these experiments are as follows:

Expt. No.	$\bar{T}$ reaction	$\Delta H(\bar{T})$
	K	$J \cdot g^{-1}$
549	303.130	146.74
550	295.443	139.17
551	295.559	139.17
552	303.069	147.12

A least squares fit of the data for the mean temperature of reaction, $\bar{T}$ reaction, and for $\Delta H(T)$ in 0.0500 N NaOH from these experiments and those in table 8 gave the following equation for the range, 295 to 303 K (in $J \cdot g^{-1}$):

$$\Delta H(T) = 141.80 + 1.025(T - 298.15\ \text{K}) \qquad (3)$$

The standard errors of the constants are 0.05 and 0.025, respectively, and the standard error of the estimate is 0.19 $J \cdot g^{-1}$. Thus, $\Delta Cp = 1.025 \pm 0.025$ $J \cdot g^{-1}$ or 29.7 ± 0.7 $cal \cdot mol^{-1}$. This value was used for the corrections to 298.15 K in table 8.

The enthalpy values in table 8 which are marked with an asterisk were obtained in systems vented to the manometer containing mineral oil (see sec. 2.4) and all others were vented to the atmosphere; there appears to be no significant difference in the results.

In a group of earlier experiments (Nos. 272–277 made in March 1969) the conditions were similar to those in tables 8 and 9 except that the SRM 724 reaction was started only a few seconds after beginning the electrical heating. Because of the heater lag the calorimeter temperature dropped and there was a relatively large difference between the temperatures of the vessel and the shield; a correction (described in [2]) for the heat transferred to the vessel was about 0.03 percent of the heat absorbed by the reaction. The mean of these six experiments was $\Delta H(298.15\ \text{K}) = 141.63 \pm 0.03(\text{sdm})$ $J \cdot g^{-1}$. Although the mean enthalpy is within the combined experimental imprecision (2 sdm) of that given in table 8, the latter is probably a better value since no corrections were necessary for departures from adiabatic conditions. The standard deviation of the mean for the earlier experiments was smaller than that for the experiments in table 8 because conditions were reproduced in all six experiments. The fact that there were variations in Reaction delay, E, and t (as shown in table 9) suggests that the larger imprecision is more realistic.

Based on the experiments in table 8, the certified value for the enthalpy of solution of NBS Standard Reference Material 724a in 0.0500 N NaOH solution at a concentration of 5 g per dm^3 of solution is

$$\Delta H(298.15\ \text{K}) = 141.80 \pm 0.19\ J \cdot g^{-1}.$$

The sample should be used without further heating or crushing, and it should be with air at atmospheric pressure in the sample container. Air at atmospheric pressure should be above the calorimetric solution.

The overall uncertainty (0.19 $J \cdot g^{-1}$ or 0.13%) assigned to the certified value is the square root of the sum of the squares of the following uncertainties: the experimental imprecision at the 95 percent confidence level (2.31 sdm), 0.15 $J \cdot g^{-1}$; analysis of sodium hydroxide solutions, 0.10 $J \cdot g^{-1}$; and other possible systematic errors, 0.07 $J \cdot g^{-1}$.

4. Other Values Reported

Most measurements of the enthalpies of the TRIS reactions have been reported in the literature as an indication of the calorimetric accuracy and precision applicable to some other primary study. Consequently, these TRIS values are not indexed and are essentially lost to the usual literature searching procedures. We have made an effort to collect as many results as possible of TRIS measurements in various calorimeters using different procedures. Some of these are as unpublished data for which more detailed information is available from the authors.

The endothermic reaction of TRIS in 0.05 *N* NaOH has been measured by only one other group, Hill, Öjelund and Wadsö [15]. Their value of $\Delta H(298.15\ \mathrm{K}) = 141.90 \pm 0.04$ (sdm) $\mathrm{J \cdot g^{-1}}$ is in good agreement with our value, 141.80 ± 0.06 (sdm) $\mathrm{J \cdot g^{-1}}$ given in section 3.4.

In table 10 is a summary of measurements of the enthalpy of the TRIS reaction in 0.1 *N* HCl using samples other than the Standard Reference Material, and in table 11 is a similar summary where SRM 724 was used (SRM 724a was used in [39] and this work). These tables are a reasonably complete summary and show the range of values obtained as well as the precision of various measurements.

The first two columns in tables 10 and 11 give the reference, the authors, and the year when the enthalpy values were reported either by publication or by private communication; the order is chronological. The next column describes the calorimeter in code[6] and with a reference which describes the calorimeter used. A majority of the calorimeters are the constant pressure, isoperibol, and glass type; only two are constant volume, six are metal, and one is adiabatic. The last columns list the enthalpy values at 298.15 K, the number of experiments averaged, and the un-

[6] *Code* — *Type of calorimeter*
- *H* — Constant pressure
- *U* — Constant volume
- *I* — Isoperibol
- *A* — Adiabatic
- *G* — Glass
- M — Metal
- *C* — A commercial calorimeter which must pass an acceptance test based in part upon the value obtained for the TRIS reaction.

TABLE 10. *Summary of values reported for the enthalpy of reaction of* TRIS *in 0.1* N HCl *using samples other than the standard reference material (SRM 724 or 724a)*

Reference No.	Author(s) and year reported	Calorimeter[a]	$-\Delta H(298.15\ \mathrm{K})$		Number averaged	Uncertainty	
						2 sdm	Other
			$\mathrm{cal \cdot mol^{-1}}$	$\mathrm{J \cdot g^{-1}}$		$\mathrm{J \cdot g^{-1}}$	$\mathrm{J \cdot g^{-1}}$
[1]	Irving and Wadsö (1964)	H,I,G,[43]	7105	245.40	8	0.28	.....
			7099	245.19	5	0.41	.....
			7106	245.44	5	0.34	.....
			7100	245.23	6	0.28	.....
			7105	245.40	7	0.28	.....
			7106	245.44	5	0.28	.....
			[b]7104	245.37	Mean	.....	.....
[16]	Gunn (1965)	U,I,M,[16]	7107.0	245.47	7	0.03	.....
			7107.1	245.47	6	0.03	.....
[17]	Held and Criss (1965)	H,I,G,[17]	7113	245.68	5	.....	1.00
[18]	Sunner and Wadsö (1966)	H,I,G,[18],C	[c]7112	245.64	.....	.....	.....
			7111	245.61	6	0.07	.....
[19]	Becker, Lindenbaum, and Boyd (1966)	H,I,G,[44]	7118	245.85	.....	.....	0.62
[20]	Finch, Gardner, and Sen Gupta (1966)	H,I,G,[45]	7150	247.0	7	.....	1.7
[21]	Vacca and Arenare (1967)	H,I,G,[46]	7109	245.54	5	0.03	.....
[22]	Wilson and Worrall (1967)	H,I,G,[47]	7110	245.6	3	.....	1.7
[23]	Wood, et al (1967)	H,I,G,[23]	7117	245.8	3	1.2	.....
[24]	Kanbour and Joncich (1967)	H,I,G,[24]	7123	246.02	6	0.45	.....
[25]	Curnutt (1968)	H,I,G,[25]	7115.8	245.76	7	0.14	.....
[26]	Richards and Woolf (1968)	H,I,M,[48]	7120	245.92	.....	.....	0.52
		H,I,G,[26]	7100	245.23	.....	.....	0.69
[35]	Hansen (1969)	H,I,G,[49]	7125	246.1	9	1.2	.....
[27]	Cunningham, House, and Powell (1970)	H,I,G,[50]	7144	246.7	4	2.5	.....
[28]	Beck, Wood, and Greenwood (1970)	H,I,G,[23]	7108	245.5	10	1.4	.....
[29]	Cook, Davies, and Staveley (1971)	H,I,G,[18],C	7110.7	245.60	3	0.04	.....
[30]	Cassel and Wen (1972)	H,I,G,[30]	7109	245.54	7	0.28	.....
[31]	Vanderzee and King (1972)	H,I,G,[51]	7110	245.57	26	0.14	.....
[32]	Olofson (1972)	U,I,M,[32]	7120	245.92	10	0.68	.....
[33]	Somsen and de Visser (1972)	H,I,G,[18],C	7104	245.37	8	0.10	.....
[10]	Gardner (1972)	H,I,G,	7118	245.85	7	0.34	.....

[a] See footnote 6 in text for explanation of code.
[b] This value was later changed to 7107 (245.47 $\mathrm{J \cdot g^{-1}}$) to correct a computational error.
[c] This is reported as the "best" value for this commercial calorimeter.

TABLE 11. *Summary of values reported for the enthalpy of reaction of* TRIS *in* 0.1 N HCl *using SRM 724 and 724a*

Reference No.	Author(s) and year reported	Calorimeter [a]	$-\Delta H$(298.15 K)		Number averaged	Uncertainty	
						2 sdm	Other
			cal · mol^{-1}	*J · g*$^{-1}$		*J · g*$^{-1}$	*J · g*$^{-1}$
[34]	Fitzgibbon and Holley (1968)	H,I,M,[52]	7110.7	245.60	7	0.34	0.5
[15]	Hill, Öjelund, and Wadsö (1969)	H,I,G[18],C	7109.0	245.54	6	0.05	.....
[35]	Hansen (1969)	H,I,G,[49]	7125	246.1	9	0.6	.....
			7108	245.5	9	0.6	.....
[36]	Johnson and Hubbard (1969)	H,I,G,[18],C	7108	245.51	.....	.....	0.21
[37]	Kreis and Wood (1969)	H,I,G,[23]	7123	246.0	3	.....	.....
[3]	Gunn (1970)	U,I,M,[16]	7107.0	245.47	5	0.02	.....
[38]	O'Hare, Johnson, and Appelman (1970)[b]	H,I,G,[18],C	7109.6	245.56	7	0.04	.....
[39]	Brunetti, Prosen, and Goldberg (1971)	H,I,G,[39]	7120.2	245.93	9	0.09	.....
[40a]	Tso and Criss (1972)	H,I,G,[17]	7110	245.57	8	0.35	.....
[40b]	Tsai and Criss (1972)	H,I,G,[17]	7113	245.68	5	0.35	.....
[40c]	Chang and Criss (1972)	H,I,G,[17]	7111	245.61	9	0.35	.....
				245.62	[40] Mean	.....	.....
[9]	Duer (1972)	H,I,G	7128	246.19	5	0.25	.....
[41]	Baker, et al (1972)	H,I,G,[41]	7080	244.5	.....	.....	0.69
[42]	Navratil and Oetting (1972)	H,I,G,[42]	7108	245.50	8	0.17	.....
[11]	Robie and Hemingway (1972)	H,I,M,[12]	7111.8	245.64	5	.....	0.24
[53]	Christensen, Kimball, and Izatt (1973)	H,I,G,[54]	7104	245.3	8	0.3	.....
	This work	H,A,M,[2]	7115.4	245.76	5	0.04	0.26

[a] See footnote 6 in text for explanation of code.

[b] Results reported at Second International Conference on Calorimetry and Thermodynamics at Orono, Main (July 1971) and published in [39].

certainty. The uncertainty is given as 2 sdm where it was specifically defined, and as "other" where it was not defined. In two cases where 2 sdm is also given, "other" refers to the estimated overall uncertainty assigned.

The spread of the data in tables 10 and 11 is essentially the same, there is no significant difference between the maximum and minimum values. There appears to be little difference in the results from a single calorimeter of measurements using samples of different origins [1, 16, 3, 18, 15]; this has also been our experience in measurements not given here.

Gunn [16] found that the enthalpy of reaction in 0.2 *N* HCl was about 0.4 J · g^{-1} (12 cal · mol^{-1}) higher than in 0.1 *N* HCl at a concentration of 6 g of TRIS per dm^3 of solution. Doubling the TRIS concentration in 0.2 *N* HCl increased the enthalpy about 0.07 J · g^{-1} (2 cal · mol^{-1}) and tripling the TRIS concentration increased the enthalpy about 0.21 J · g^{-1} (6 cal · mol^{-1}). Held and Criss [17] found no concentration dependence in the enthalpy using 0.25 to 0.076 mmol samples in 80 cm^3 of 0.1 *N* HCl (0.38 to 0.12 g · dm^{-3}). Criss et al. [40a, b, c], measured the reaction in dilute solutions (ranging from 0.002 to 0.01 molal or 0.2 to 1.0 g · dm^{-3}) with apparently no significant difference from the values obtained at the recommended concentration of 5 g · dm^{-3} or 0.04 molal.

We have found no difference in the enthalpy values obtained at various stirring speeds. However, Olofson [32] has suspected that the reaction is sensitive to insufficient mixing in the calorimeter, and Gardner [10] measured 7118 ± 5(sdm) cal · mol^{-1} at 700 rpm and 7109 ± 6(sdm) cal · mol^{-1} at 470 rpm. This difference may not be significant, but it is a factor to be investigated if low enthalpy values are obtained in a calorimeter.

Christensen et al. [53], reported low enthalpy values when glass ampoules sealed with a flame were used. This was believed to be the result of partial decomposition of the sample.

The experimental precision of data, such as that given in tables 10 and 11, is sometimes mistakenly used as a gauge of the accuracy of the measurements. To a certain extent this reasoning is justified by the fact that those who strive for high precision are usually simultaneously concerned with achieving high accuracy, but the latter is more difficult to determine absolutely. Some of the values reported in the tables are obviously measured in calorimeters designed for applications where relative enthalpies are of interest rather than absolute enthalpies, and high precision and accuracy are of little concern. Therefore, in order to separate the measurements in calorimeters where an effort was apparently made to achieve high precision and accuracy, we have listed in table 12, in ascending order of the $-\Delta H$(298.15 K), only those values in which the standard deviation of the mean was 0.1 percent (2 sdm = 0.5 J · g^{-1}) or less. In cases where more than one value was reported using a single calorimeter, the value of highest precision is given in the table. Also, the calorimeters marked with "C" in tables 10 and 11 are considered as a single value because the measurements were made in a commercial calorimeter and are subject to a bias because of its acceptance test. The overall uncertainty assigned to this work, 0.26 J · g^{-1} (see sec. 3.3), includes all of the values in table 12 within their experimental uncertainties (2 sdm).

5. Discussion and Conclusions

The overall uncertainties assigned to the certified values for the enthalpies of the exothermic and endothermic reactions of the Standard Reference Material 724a should be small enough for greatest significance but large enough to include conceivable future adjustments in the mean enthalpy values as more information is acquired about calorimetry and the chemical behavior of the reactions. The values given in table 12 are measured in calorimeters capable of relatively high precision, and yet the spread of the results is nearly 0.4 percent (or 0.89 $J \cdot g^{-1}$), which indicates the presence of errors beyond the experimental imprecision. Some time will probably elapse before the spread of these values can be explained and the overall uncertainty in the certified value reduced accordingly.

This work provided the only value in table 12 which was measured in an adiabatic calorimeter; this eliminates the heat transfer corrections necessary in isoperibol calorimeters, but may conceivably introduce some errors of which we are not aware in the present state of adiabatic calorimetry. Gunn [3, 16] has measured the reaction in a constant-volume, rocking-bomb system; the fact that his value falls near the lower end of the values in table 12 suggests a possible need for a P–V–T correction which is not presently known. Wadsö and co-workers [1, 15, and 18] have made relatively extensive studies of the TRIS reactions using various samples and highly reproducible calorimetric procedures. The emphasis in our work has been to measure the reaction under various conditions in an effort to find possible explanations for the unexpected, large spread in the enthalpy values reported.

TABLE 12. *Summary of the measurements of highest precision for various calorimeters (from tables 10 and 11)*

Ref. No.	Authors	$-\Delta H$(298.15 K)	2 sdm[a]
		$J \cdot g^{-1}$	$J \cdot g^{-1}$
[53]	Christensen, et al.	245.3	0.3
[1]	Irving and Wadsö	245.47	0.3
[3]	Gunn	245.47	0.02
[42]	Navratil and Oetting	245.50	0.2
[21]	Vacca and Arenare	245.54	0.03
[30]	Cassel and Wen	245.54	0.3
[31]	Vanderzee and King	245.57	0.1
[34]	Fitzgibbon and Holley	245.60	0.3
[40]	Criss, et al.	245.62	0.4
[11]	Robie and Hemingway	245.64	0.2
[18]	Sunner and Wadsö	245.64	0.1
	This work	245.76	0.04
[25]	Curnutt	245.76	0.1
[10]	Gardner	245.85	0.3
[39]	Brunetti, et al.	245.93	0.1
[24]	Kanbour and Joncich	246.02	0.5
[9]	Duer	246.19	0.3

[a] The uncertainties are rounded to the nearest 0.1 $J \cdot g^{-1}$ unless they are less than 0.05 $J \cdot g^{-1}$.

All calorimeters represented in table 12 were lined primarily with glass except two which were lined with gold (Gunn, and Robie and Hemingway), and two which were lined with platinum (Fitzgibbon and Holley, and this work). Thus, the material lining the calorimeters does not account for extreme values.

It is possible that the venting effect described in section 3.1a is responsible for some of the high values, and that inadequate stirring is responsible for some of the low values; however, we are reasonably certain that these are not sources of error in our work. The variations in samples, concentrations, and CO_2 in the HCl solutions (see sec. 3.1b) are not likely to cause errors beyond the experimental imprecision. Electrical energy and calorimeter temperature measurements are always a source of possible error (see [39]); we have thoroughly checked these systems which have been described in detail for this calorimeter [2].

The relatively large overall uncertainty assigned to the certified values for the enthalpy of reaction of SRM 724a in 0.1 N HCl has been a disappointment to some. However, very few calorimetrists are concerned with accuracy and precision of measurements beyond the assigned uncertainty of ± 0.11 percent. Measured enthalpy values can be expected to fall within these limits providing the conditions described in section 3.3 are met. Perhaps in the future after further studies have been made of the chemistry of the reaction and the effects of various conditions on the enthalpy of reaction, it will be possible to define more specifically conditions for the reaction in 0.1 N HCl and to provide a certified value to which a smaller overall uncertainty can be assigned.

There is good agreement between the two values reported ([15] and sec. 3.4) for the endothermic reaction of the Standard Reference Material in 0.05 N NaOH, and the uncertainty assigned to the certified value is approximately as expected. Because of the calorimetric problems with endothermic reactions, the CO_2 reaction with dilute NaOH solutions, and the sensitivity of the enthalpy of reaction to NaOH concentrations, it was expected that the uncertainty would be larger than that for the exothermic reaction.

The Standard Reference Material 724a is useful not only for comparing the accuracy of calorimetric measurements, but for checking the relative performance of a calorimeter from time to time. It provides a method for checking quickly and easily whether modifications in a calorimeter have produced changes in the precision or absolute values of measurements. However, it is recommended that the TRIS reactions not be used instead of the usual electrical energy measurements to calibrate calorimeters. Although the search must continue for a reaction which can be certified with less uncertainty, for the present, SRM 724a is the best available.

We wish to thank those who have given us permission to use their unpublished data in this paper.

6. References

[1] Irving, A. J., and Wadsö, I., Acta Chem. Scand. **18,** 195 (1964).
[2] Prosen, E. J., and Kilday, M. V., J. Res. Nat. Bur. Stand. (U.S.) **77A** (Phys. and Chem.) No. 2, 179–203 (1973).
[3] Gunn, S. R., J. Chem. Thermodynamics **2,** 535 (1970).
[4] Marinenko, G., and Champion, C. E., Coulometric Analysis, Nat. Bur. Stand. (U.S.), Tech. Note 425, 42 (Oct. 1967).
[5] Marinenko, G., Coulometry, Nat. Bur. Stand. (U.S.), Tech. Note 543, 56 (Nov. 1970).
[6] Commission on Atomic Weights, Pure and Applied Chem. **21,** 91 (1970).
[7] Rose, H. A., and van Camp, A. V., Anal. Chem. **27,** 1356 (1955).
[8] Nuttall, R. L., Laufer, A. H., and Kilday, M. V., J. Chem. Thermodynamics **3,** 167 (1971).
[9] Duer, W. C., Univ. of Florida, Gainesville, private communications (April 21, 1972, and August 23, 1972). This work was done at the Univ. of Missouri, Rolla, Missouri.
[10] Gardner, P. J., Royal Holloway College, Surrey, United Kingdom, private communication (August 15, 1972). This work was done in 1971–1972 at the University of Otago, Dunedin, New Zealand.
[11] Robie, R. A., and Hemingway, B. S., Geological Survey, U.S. Deaprtment of Interior, private communication, (May 24, 1972).
[12] Robie, R. A., and Hemingway, B. S., Calorimeters for heat of solution and low-temperature heat capacity measurements, Geological Survey Professional Paper 755, U.S. Government Printing Office, Washington, D.C. (1972).
[13] Wagman, D. D., and Kilday, M. V., J. Res. Nat. Bur. Stand. (U.S.) **77A** (Phys. and Chem.) No. 5, 569 (1973).
[14] Arvidsson, K., and Westrum, E. F. Jr., J. Chem. Thermodynamics **4,** 449 (1972).
[15] Hill, J. O., Öjelund, G., and Wadsö, I., J. Chem. Thermodynamics **1,** 111 (1969).
[16] Gunn, S. R., J. Phys. Chem. **69,** 2902 (1965).
[17] Held, R. P., and Criss, C. M., J. Phys. Chem. **69,** 2611 (1965).
[18] Sunner, S., and Wadsö, I., Science Tools **13,** 1 (1966).
[19] Becker, K. E., Lindenbaum, S., and Boyd, G. E., J. Phys. Chem. **70,** 3834 (1966).
[20] Finch, A., Gardner, P. J., and Sen-Gupta, K. K., J. Chem. Soc. (A), 1367 (1966).
[21] Vacca, A., and Arenare, D., J. Phys. Chem. **71,** 1495 (1967).
[22] Wilson, J., and Worrall, I. J., J. Chem. Soc. (A), 392 (1967).
[23] Wood, R. H., Anderson, H. L., Beck, J. D., France, J. R., de Vry, W. E., and Soltzberg, L. J., J. Phys. Chem. **71,** 2149 (1967).
[24] Kanbour, F., and Joncich, M. J., Rev. Sci. Instr. **38,** 913 (1967).
[25] Curnutt, J. L., Ph.D. Thesis, University of Nebraska (July, 1968).
[26] Richards, G. W., and Woolf, A. A., J. Chem. Soc. (A), 470 (1968).
[27] Cunningham, A. J., House, D. A., and Powell, H. K. J., Aust. J. Chem. **23,** 2375 (1970).
[28] Beck, J. D., Wood, R. H., and Greenwood, N. N., Inorg. Chem. **9,** 86 (1970).
[29] Cook, R. O., Davies, A., and Staveley, L. A. K., J. Chem. Thermodynamics **3,** 907 (1971).
[30] Cassel, R. B., and Wen, W.-Y., J. Phys. Chem. **76,** 1369 (1972).
[31] Vanderzee, C. E., and King, D. L., J. Chem. Thermodynamics **4,** 675 (1972).
[32] Olofson, G., Thermochemical Center, University of Lund, Sweden, private communication (March 20, 1972); Olofsson, G., Sunner, S., Efimov, M., and Leynez, J., J. Chem. Thermodynamics **5** (2), 199 (1973).
[33] Somsen, G., and de Visser, C., Vrije University, Amsterdam, private communication (October 19, 1972).
[34] Fitzgibbon, G. C., and Holley, C. E. Jr., Los Alamos Scientific Laboratory, New Mexico, private communication (August 6, 1968).
[35] Hansen, L. D., University of New Mexico, Albequerque, New Mexico, private communication (March 25, 1969).
[36] Johnson, G. K., and Hubbard, W. N., J. Chem. Thermodynamics **1,** 459 (1969).
[37] Kreis, R. W., and Wood, R. H., J. Chem. Thermodynamics **1,** 523 (1969).
[38] O'Hare, P. A. G., Johnson, G. K., and Appleman, E. H., Inorg. Chem. **9,** 332 (1970).
[39] Brunetti, A. P., Prosen, E. J., and Goldberg, R. N., J. Res. Nat. Bur. Stand. (U.S.) **77A** (Phys. and Chem.), No. 5, 599 (1973).
[40] Criss, C. M., University of Miami, Coral Gables, Florida, private communication (March 23, 1972): (a) Tso, M. W., and Criss, C. M.; (b) Tsai, Y. A., and Criss, C. M.; and (c) Chang, S., and Criss, C. M.
[41] Baker, F. B., Fitzgibbon, G. C., Pavone, D., Holley, C. E. Jr., Hansen, L. D., and Lewis, E. A., J. Chem. Thermodynamics **4,** 621 (1972).
[42] Navratil, J. D., and Oetting, F. L., Dow Chemical Co., Golden, Colorado, RFP–1976 (March 12, 1973).
[43] Wadsö, I., Acta Chem. Scand. **16,** 479 (1962).
[44] Boyd, G. E., Vaslow, F., and Lindenbaum, S., J. Phys. Chem. **68,** 590 (1964).
[45] Finch, A., and Gardner, P. J., J. Chem. Soc. **1964,** 2985 (1964).
[46] Paoletti, P., Usenza, R., and Vacca, A., Ric. Sci. **35** (II–A), 201 (1965).
[47] Greenwood, N. N., and Perkins, P. G., J. Inorg. Nuclear Chem. **4,** 291 (1957).
[48] Richards, G. W., and Woolf, A. A., J. Chem. Soc. (A), 1118 (1967).
[49] Hansen, L. D., West, B. D., Baca, E. J., and Blank, C. L., J. Am. Chem. Soc. **90,** 6588 (1968).
[50] Powell, H. K. J., and Curtis, N. F., J. Chem. Soc. (B), 1205 (1966).
[51] Vanderzee, C. E., and Myers, R. A., J. Phys. Chem. **65,** 153 (1961).
[52] Fitzgibbon, G. C., and Holley, C. E. Jr., J. Phys. Chem. **69,** 2464 (1965).
[53] Christensen, J. J., Kimball, G. L., and Izatt, R. M., Thermochimica Acta **5,** 293 (1973).
[54] Hale, J. D., Izatt, R. M., and Christensen, J. J., J. Phys. Chem. **67,** 2605 (1963).

(Paper 77A5–785)

JOURNAL OF RESEARCH of the National Bureau of Standards—A. Physics and Chemistry
Vol. 77A, No. 5, September–October 1973

The Enthalpy of Reaction of Tris(hydroxymethyl)-aminomethane With Hydrochloric Acid

Anthony P. Brunetti,* Edward J. Prosen, and Robert N. Goldberg

Institute for Materials Research, National Bureau of Standards, Washington, D.C. 20234

(June 22, 1973)

The enthalpy of reaction of tris(hydroxymethyl)aminomethane with 0.1 *N* HCl has been measured using an isoperibol solution calorimeter, employing a modified quartz thermometer and an automatic digital data acquisition system. The enthalpy value obtained at 298.15 K is 245.93 ± 0.26 J · g^{-1}. Particular attention was given to possible sources of systematic error in the electrical calibrations.

Key words: Enthalpy of reaction; solution calorimetry; standard reference material; tris(hydroxymethyl)aminomethane; thermochemistry.

1. Introduction

This study was undertaken to establish the precision and accuracy of measurements that can be made with an isoperibol (isothermal jacket) solution calorimeter constructed for future work on the thermochemistry of calcium phosphates. The test reaction selected for this purpose was the reaction of tris(hydroxymethyl)-aminomethane (hereafter referred to as TRIS) with 0.1 *N* HCl. The samples of TRIS employed in the test reaction were parts of the preparation issued as NBS Standard Reference Material No. 724a (NBS–SRM 724a).

A summary [1][1] of values of high precision for the TRIS–HCl reaction reports interlaboratory variations in the enthalpy for this test reaction greater than 0.4 percent. The majority of these values have been measured in isoperibol solution calorimeters and are slightly lower than the value reported in this work. The results of this study are in close agreement with those obtained in an adiabatic calorimeter used in the certification of NBS–SRM 724a [1].

2. Materials

SRM 724a was used in all experiments. Prior to filling the sample ampoules, the TRIS was stored in a desiccator over a saturated aqueous solution of magnesium nitrate which gives 50 percent relative humidity. This procedure follows the recommendations of the NBS Standard Reference Material Certificate [7].

The HCl solutions were prepared using ACS reagent grade concentrated hydrochloric acid (37–38%) which was diluted to the desired concentration with freshly boiled distilled water. No special precautions were taken to exclude carbon dioxide during the filling of the calorimeter. The acid concentrations were determined by titrating the HCl solutions with sodium hydroxide solutions that were standardized with potassium acid phthalate (SRM 84h) using phenolphthalein as the end point indicator. The acid concentrations were 0.0996 *N* (Expt. Nos. 9 to 12) and 0.1011 *N* (Expt. Nos. 13 to 18).

The TRIS sample was introduced *via* a small glass funnel into cylindrical glass ampoules with very thin-walled ends. The ampoules hold a volume of 1.0 cm^3 and are manufactured by the LKB Company.[2] Before filling, the ampoules were rinsed with ACS reagent grade acetone followed by distilled water and then dried in an oven. After filling, the ampoule was closed with a small rubber stopper which had been presoaked in HCl, rinsed with distilled water and dried. The stopper was sealed with warm beeswax and the ampoule submerged in 0.1 *N* HCl to check for leakage. It was then rinsed, dried and mounted on the stirrer-ampoule holder of the calorimeter.

3. Calorimetric Apparatus and Procedure

The calorimeter vessel, jacket and constant temperature water bath were manufactured by the LKB Company [2]. However, all auxiliary equipment, including the electrical energy and temperature meas-

* Research Associate of the American Dental Association Research Unit at the National Bureau of Standards, Washington, D.C. 20234. Supported in part by Research Grant DE00572 to the American Dental Association from the National Institute of Dental Research.

[1] Figures in brackets indicate literature references at the end of this paper.

[2] Certain commercial materials are identified in this paper in order to adequately specify the experimental procedures. Such identification does not imply recommendation or endorsement by the National Bureau of Standards.

uring apparatus, were assembled from other sources and are described below. As this investigation proceeded several changes were made in various components of the apparatus and these will be described as well.

3.1. The Calorimeter

The isothermal jacket of the calorimeter, a can of nickel-plated brass, is immersed in a stirred-water bath whose temperature is regulated by means of a proportional controller. A test of the temperature stability of the bath, as measured at one point in the well-stirred bath, indicated that it was maintaining a constant temperature to within ±0.0015 K over a 15 hour period.

The first calorimeter vessel was constructed of thin-walled glass and held a volume of 100 cm^3. As received from the manufacturer the vessel contained three glass wells. One of the wells was specially added for installation of a quartz-oscillator probe. The other two glass wells held the electrical calibrating heater and a thermistor; the thermistor was not used in this work. The vessel is suspended from the lid of the submarine jacket by means of a screw connection and O-ring-seat at the top of its glass neck. The original glass vessel was broken in an accident following Expt. No. 11 and a second calorimeter vessel was constructed in the NBS glass blowing shop. It differed from the original in that its volume was 110 cm^3 and it was more nearly spherical than the original cylindrical vessel. The thermistor well was omitted and the walls of the heater and thermometer wells were made of thinner glass. The use of the new vessel (Expt. Nos. 12 to 18) had no observable effect on the value of the calorimeter heat leak modulus, the value of which was approximately 1.03×10^{-4} s^{-1}. A photograph of the second vessel is shown in figure 1.

Venting in the original calorimeter was only through the stirrer shaft bearings and housing. Since adequate venting of the calorimeter was desired, following Expt. No. 15, additional venting was provided by drilling a 1-mm diam hole through the bottom and the top of the housing for the stirring shaft and inserting a syringe needle through these two holes. This needle provided direct venting from above the calorimetric liquid to the atmosphere.

The gold-plated combination stirrer-ampoule holder was driven at a constant speed of approximately 300 rpm by a synchronous motor through an O-ring belt and pulley arrangement. This replaced the original cable drive system.

3.2. The Calibrating Heater

The original heater consisted of 50-Ω of manganin wire wound bifilarly on a phenolic form located in the bottom of the heater well of the vessel. A light oil covered the heater. Insulated copper leads were soldered to the manganin wire and were passed through two thin polytetrafluoroethylene (PTFE) disks that were separated with a layer of Wood's metal. The Wood's metal provided thermal tempering of the leads

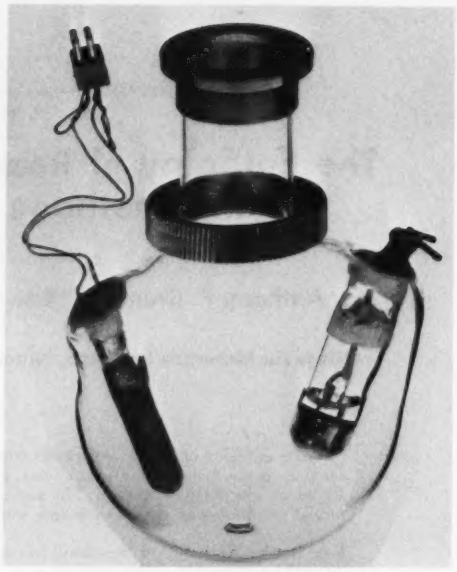

FIGURE 1. *Calorimeter Reaction Vessel.*

Calibration heater in left well and quartz-probe in right well, central glass pin is for breaking ampoules.

to the vessel. The copper leads, after passing through a second layer of Wood's metal, terminated at the top of the well where they were soldered to two small gold-plated connectors imbedded in an epoxy cement that sealed the heater well. Two short copper wire leads went from the connectors at the top of the heater well to a two-pin connector in the jacket lid. Current and potential leads were attached to each pin of the jacket connector.

After the original vessel was broken, the original heater was installed in the new vessel following the above method employed by the manufacturer as closely as possible and used in experiments 15 and 16. However, a new heater was constructed prior to Expt. No. 17. It was bifilarly wound with 82Ω of enamel-insulated manganin wire (#40 AWG) onto a piece of thin-walled stainless steel tubing that had been coated with insulating varnish and baked. Approximately six inches of PTFE-insulated copper wire (#30 AWG) was soldered to the manganin wire and then coiled and pushed down into the heater well. As in the original heater, a light mineral oil covered the heater and the thermal tempering and the sealing of the leads to the well of the calorimeter vessel was the same as described earlier. However, the two copper leads (#26 AWG, Formvar insulated) soldered to the PTFE-coated wire went directly to a four-pin connector. The four pins of the connector were shorted pair-wise at the connector to form the branch points for the current and potential leads (see fig. 1). The "thermal stationing" of the heater leads at the jacket was modified by removing the original connector and fitting a brass plug with a smaller hole, and placing a small four-pin feed-through connector into this hole.

3.3. Electrical Energy Measurements

A schematic diagram of the electrical calibration circuit is shown in figure 2. The current through the heater and the potential drop across the heater were obtained from measurements of the potential drop across the 1-Ω standard resistor and across a 2-kΩ resistor in the 20-kΩ volt box. Appropriate corrections were made for the current through the volt box and the leads connecting it to the branch points of the heater. As indicated in figure 2, the circuit was always grounded only at one point, namely, at the power supply (Princeton Model 602R) which was operated in the constant voltage mode. (Note that the measuring resistors are near ground potential. Otherwise the circuit was found to be isolated from ground by at least 100-MΩ.) Voltages were measured on a Leeds and Northrup type K5 potentiometer (error limit of $\pm 0.005\% + 0.03$ μV) which was standardized against a Weston unsaturated standard cell. The standard cell was periodically compared with a bank of NBS certified Weston saturated cells and all measuring equipment was calibrated and compared with other standards in this laboratory. Time measurements were made by inserting a timing circuit, consisting of an electronic counter (HP 5325 B) with a resolution of 1 ms, parallel to the electrical calibration circuit (point A in fig. 2). Current flowing through this parallel circuit has no effect on the measurement of the heater current and voltage since it is outside of the measuring circuit.

The above circuit and apparatus were used in Expt. Nos. 13 to 18. In Expt. Nos. 9 through 12 a completely separate electrical circuit was used. It differed from the above in that (1) there was no volt box across the heater, (2) a digital voltmeter (Hewlett Packard 3450A; input resistance $>10^{10}\Omega$, sensitivity of $\pm$ 1μV) was used to measure the potential drops across the heater and a standard resistor (0.1Ω) in series with the heater, (3) a different power supply (Princeton 602CR) was used, and (4) a mercury relay was used to switch between the ballast resistor and the heater side of the circuit.

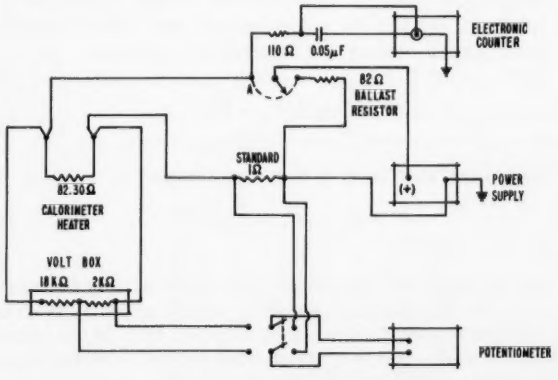

FIGURE 2. *Diagram of circuit used for electrical energy equivalent determinations.*

The total electrical energy was calculated from the product of the current through the heater, voltage across the heater and time interval of heating. It was assumed that the heat generated in the heater leads between the calorimeter vessel and jacket was apportioned one-half to the calorimeter vessel and the other half to the jacket. The resistance of the leads between the jacket and the calorimeter vessel was 0.04 percent of the resistance of the calibration heater; therefore, a correction of 0.02 percent was applied to the measured electrical energy for the heat lost to the jacket.

It was observed that the heater resistance, as determined from the current and potential measurements, was dependent on the power level applied to the heater. This effect is attributable to the change in resistance of the heater wire as the temperature in the well rises, and became significant at power levels approaching 2 W. Power input during the TRIS experiments was maintained below this level and by measurement of the current through and the potential drop across the heater under load conditions, any change in heater resistance was automatically accounted for in the electrical calibrations.

The power input was 1.18 W, in Expt. Nos. 9 through 16, 0.95 W in Expt. No. 17, and 0.13 W in Expt. No. 18. The time interval of electrical heating was varied from approximately 100 to 1000 s.

In order to test for possible errors associated with the electrical calibrations, a second, temporary heater with a resistance of 87Ω was placed directly into the water of the solution vessel. This heater was coated with Apiezon "W" wax and no electrical leakage was detectable using the high impedance scale of a volt-ohm meter (the electrical resistance was estimated to be greater than 100 MΩ). Several centimeters of the leads from this heater were coiled and submerged with it in the water to insure good thermal tempering. The two current leads were then passed through the 1-mm vent holes of the housing for the stirrer shaft, and were stationed at the top of the shaft-housing where potential leads were attached. Repeated determinations of the calorimeter electrical energy equivalent, alternating between the permanent heater in the well and the temporary heater in the water of the solution vessel, gave a difference between the means of three determinations with each heater of 0.006 percent, with none of the deviations from each of the means being greater than 0.009 percent. In calculating the heater-lead correction for the temporary heater the calorimeter boundary was chosen to be one-half the distance between the surface of the water in the vessel and the jacket lid. The heater lead correction was approximately equal to that for the permanent heater.

3.4. Thermometry and Data Acquisition

The temperature of the calorimeter vessel was determined by means of a Hewlett-Packard quartz-oscillator thermometer [3]. The TO–5 transistor case containing the temperature-sensitive quartz crystal was removed from its original stainless steel capsule,

508-076 O - 73 - 3

placed in the bottom of the glass well in the solution vessel, and covered with light mineral oil. The leads from the quartz crystal were thermally stationed to the calorimeter vessel by passing them through a layer of dental amalgam which was contained between two thin PTFE disks. At the top of the well the leads were soldered to two small, gold-plated pin connectors which were imbedded in the epoxy cement that sealed the well (see fig. 1).

The temperature dependence of the frequency of the quartz probe is nominally 1000 $Hz \cdot K^{-1}$ [3], and by counting for 100-s, a temperature resolution of 10 μK is obtained. In order for this resolution to be meaningful, it is necessary that the reference oscillator in the quartz thermometer chassis be stable to within 3 parts in 10^{10} during an experiment. It was found by one of us (EJP) that this stability was obtained by replacing the ceramic trimmer-capacitor in the oscillator circuit of the reference oscillator with an air capacitor. To check this stability the reference oscillator frequency was monitored against a standard frequency available at NBS which is reproducible to 1 part in 10^{11}.

The digital output from the quartz thermometer and from a digital clock with 0.1-s resolution, went to a digital coupler and then to a teletype where the time and temperature data were logged both on punched paper tape and in typed form.

The absolute temperature of the quartz thermometer from 295 to 303 K was obtained to within ±0.003 K by comparison with a platinum resistance thermometer that had been calibrated by NBS (IPTS 1948). In performing the comparison, the platinum thermometer was placed in the stirred-water jacket of the calorimeter and its temperature was compared with the quartz oscillator temperature by measurement of the voltage of a differential copper-constantan thermocouple between the vessel and the jacket. One of the thermocouple junctions was cemented to a thin, insulated silver tab cemented to the side of the solution vessel, the other wax-coated junction was located in the bath near the platinum thermometer. Throughout this procedure the water in the solution vessel was stirred and the calorimeter was maintained near its convergence temperature to minimize the temperature difference between the calorimeter and the jacket.

3.5. Experimental Procedure

All weighings were done on a single-pan microbalance with a sensitivity of one microgram. The balance was calibrated against a set of Class M metric weights that had been calibrated by the Mass Section of NBS. Corrections to vacuum were made using a density of 1.35 $g \cdot cm^{-3}$ for TRIS. The density of air was determined by daily observations of the temperature, pressure and humidity and corrections were applied as described by Bowman et al. [4]. Care was taken, employing uranyl nitrate in the balance chamber, to avoid electrostatic charge effects that might interfere with the weighings. A molecular weight of 121.1369 $g \cdot mol^{-1}$ TRIS was assigned on the basis of the 1969 table of atomic weights [5].

Each calorimetric experiment included three parts, an electrical calibration, the TRIS–HCl reaction, and finally a second electrical calibration. Each part consisted of approximately 30 data points (each point being recorded at 101.6-s intervals) which included an initial rating period, a main period, and a final rating period. Following each part, dried, cold air (introduced *via* a stainless steel tube temporarily inserted through a hole in the lid of the jacket) was blown over the exterior surface of the vessel in order to cool it. The electrical heatings and chemical reaction were thus carried out over the same temperature interval (within a few hundredths of a kelvin). In all experiments the final temperature of the calorimetric vessel was 0.05 to 0.17 K below the convergence temperature.

4. Calculations

4.1. Corrected Temperature Rise

The following treatment to obtain the corrected temperature rise was developed with the help of R. L. Nuttall, NBS Thermochemistry Section.

The corrected temperature rise (ΔT_{corr}) was calculated [6a] using eq (1),

$$\Delta T_{corr} = (T_f - T_i) - k \int_{t_i}^{t_f} (T_\infty - T)\,dt, \qquad (1)$$

where T_i and T_f are, respectively, the temperatures at t_i, a time during the initial rating period, and t_f, a time during the final rating period. In eq (1), k is the calorimeter heat leak modulus or cooling constant, and T_∞ is the convergence temperature. The time, t_i, was chosen as the time just before heat, either electrical or chemical, was introduced into the calorimeter; the time, t_f, was chosen as any one of several points in the final rating period. The quartz thermometer is an integrating device and will automatically evaluate a part of the integral in eq (1), as indicated below in eq (10). To utilize this feature of the quartz thermometer over the entire main period the times t_i and t_f must be, and were, chosen at the end points of integration periods of observed quartz thermometer readings. During the rating periods the rate of temperature change is given by eq (2).

$$\frac{dT}{dt} = k(T_\infty - T). \qquad (2)$$

The integrated form of this equation is

$$T = T_\infty - (T_\infty - T_0)e^{-k(t-t_0)}, \qquad (3)$$

where T_0 is temperature at the time t_0, any selected time in the particular rating period used. It is convenient to select t_0 in eq (3) as equal to t_i in the initial period and equal to t_f in the final period. This has been done in eqs (7) and (8) below.

Since the quartz thermometer is an integrating device the reading, θ, displayed by the quartz ther-

mometer is the time-average temperature over the integration interval, λ, as given by eq (4) and was referenced to the midtime of the interval:

$$\theta=\frac{1}{\lambda}\int_{t-\lambda/2}^{t+\lambda/2} T dt. \tag{4}$$

Substitution of T from eq (3) into eq (4), results in the following expression for θ during rating periods:

$$\theta=T_\infty-(T_\infty-T_0)\,e^{-k(t-t_0)}\left[\frac{e^{\frac{k\lambda}{2}}-e^{\frac{-k\lambda}{2}}}{k\lambda}\right]. \tag{5}$$

By defining two new constants, $\theta_\infty=T_\infty$ and

$$\theta_0=T_\infty-(T_\infty-T_0)\left[\frac{e^{\frac{k\lambda}{2}}-e^{\frac{-k\lambda}{2}}}{k\lambda}\right]$$

we get:

$$\theta=\theta_\infty-(\theta_\infty-\theta_0)\,e^{-k(t-t_0)}. \tag{6}$$

Thus, we have for the initial and final rating periods, respectively, the following equations:

$$\theta_r=\theta_\infty-(\theta_\infty-\theta_i)e^{-k(t_r-\lambda/2-t_i)} \tag{7}$$

$$\theta_r=\theta_\infty-(\theta_\infty-\theta_f)e^{-k(t_r-\lambda/2-t_f)} \tag{8}$$

where t_r's are the times at the end of the thermometer-integration periods at which time the readings θ_r appear on the read-out, t_i is the time at the end of the initial period, and t_f is the time at the start of the final period. Equations (7) and (8) were fitted to the time-quartz thermometer data (θ_r, t_r) of the initial and final rating periods as a single set of data by using a nonlinear least squares procedure [8]. From this fit the parameters k, θ_∞, θ_i, and θ_f are obtained. The observed temperature rise, T_f-T_i, can then be shown to be given by

$$T_f-T_i=(\theta_f-\theta_i)\left[\frac{k\lambda}{e^{\frac{k\lambda}{2}}-e^{\frac{-k\lambda}{2}}}\right]. \tag{9}$$

The last factor in eq (9) depends on k and λ. In this calorimeter $k\cong 0.0001$ s^{-1} and $\lambda\cong 100$ s. Thus the factor has the value 0.999996 and can almost be neglected.

The correction to the observed temperature rise, i.e., the integral in eq (1), can be written as

$$k\int_{t_i}^{t_f}(T_\infty-T)dt=kT_\infty(t_f-t_i)-k\int_{t_i}^{t_f}T dt. \tag{10}$$

The integral on the right side of eq (10) was evaluated in two parts: (1) an integral over the thermometer integration time which, for the nth time interval is equal to $\lambda\theta_n$; (2) an integral over the dead time (the fraction of a second during which the counter is transmitting data to the coupler) which is evaluated by assuming a linear temperature change between adjacent data points.

Equation (1) can also be written in the form,

$$\Delta T_{corr}=(T_f-T_i)-u(t_f-t_i)-k\int_{t_i}^{t_f}(T_j-T)dt \tag{11}$$

where T_j is the constant jacket temperature, and u represents energy contributions from constant power sources such as stirring and the temperature sensor. Values of u were calculated from the relationship, $u=k(\theta_\infty-\theta_j)$ and are listed in table 1 with θ_∞, θ_j, and k for the TRIS-HCl reaction portion of each experiment. It was found that u was negative and thus contributed a positive correction to the observed temperature rise. Since the energy dissipated by the quartz-probe oscillator is small, 10 μW [3], u would then be primarily a function of the stirring energy, but its contribution is also positive. However, negative contributions to u could arise from evaporation of liquid from the top of the vessel, or heat conduction up the stirrer shaft to the cooler room environment.

In an attempt to limit evaporation electrical heating experiments were conducted with a light film of oil on the surface of the calorimetric liquid. Negative values of u were still observed. We presume, therefore, that heat leakage *via* the stirring shaft results in a small negative power contribution to u. Although a positive value of u is desirable, the values of u in table 1 are seen to be small and reasonably constant, thus indicating that no inconsistency exists that would adversely bias the calorimetric measurement in any way.

The behavior of the u was evaluated in a more direct manner by plotting values of $d\theta/dt$ (the average slope

TABLE 1. *Calorimetric parameters for the* TRIS-HCl *experiments*

Expt. No.	$k\cdot 10^4$	T_j	T_∞	$-u\times 10^4$	$-u(t_f-t_i)\times 10^4$	$k\int_{t_i}^{t_f}(T_\infty-T)dt$
	s^{-1}	°C	°C	$K\cdot min^{-1}$	K	K
9	1.027	25.0449	25.0272	1.399	18.863	0.010388
10	1.031	25.0513	25.0289	1.379	16.088	.010275
11	1.035	25.0486	25.0274	1.317	17.856	.012646
12	1.045	25.2225	25.1913	1.956	29.813	.013539
13	1.019	25.2070	25.1873	1.199	16.246	.012193
15	1.019	25.2064	25.1849	1.314	22.264	.014371
16	1.045	25.2198	25.2006	1.204	20.396	.012241
17	1.042	25.2155	25.1968	1.169	15.840	.010955
18	1.033	25.2163	25.1976	1.164	21.687	.012027

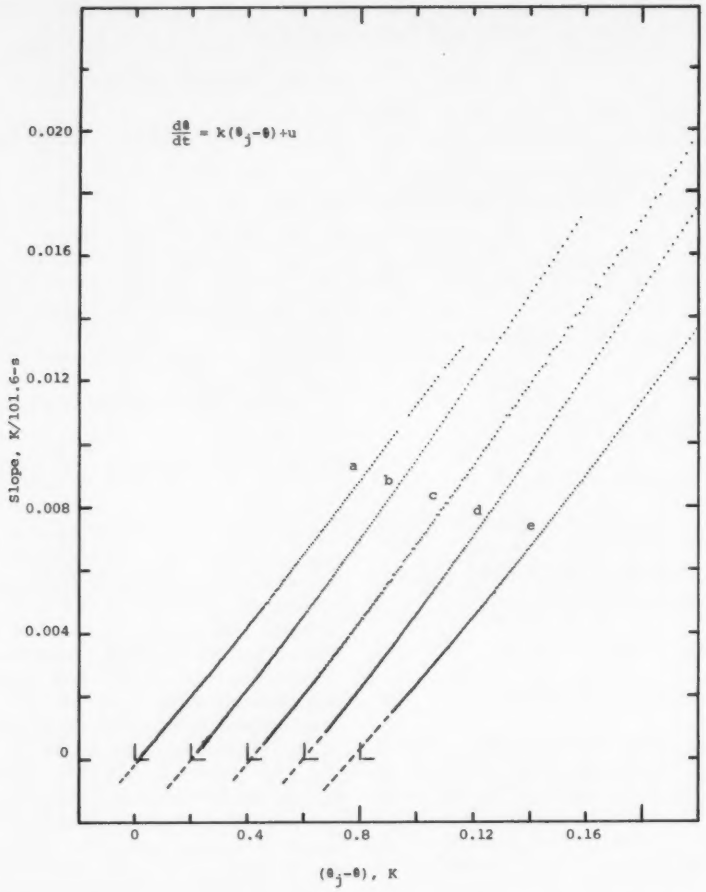

FIGURE 3. *Characterization of the calorimeter parameters* u *and* k *by plotting* s, *the average slope between adjacent data points, versus* $(\theta_j - \theta)$, *as the calorimeter temperature approaches* θ_∞.

θ_j was taken as a constant using the jacket temperature observed at the end of the experiment. *X*-axis origin displaced 0.2 °C for each successive plot as indicated. For curve a, b, c, d, and e respectively: θ_j(°C) = 28.19, 25.15, 25.15, 25.15, 25.15; RPM = 300, 300, 101, 300, 800; u(°C/101 sec) = −0.00020, 0.00000, −0.00015, 0.00000, 0.00030; oil was on the surface of the calorimetric liquid during d and e.

between adjacent data points) *versus* $(\theta_j - \theta)$, employing eq (12),

$$d\theta/dt = k\,(\theta_j - \theta) + u. \qquad (12)$$

Temperature and time data were recorded at 101.6-s intervals for periods up to fourteen hours, as the calorimeter temperature approached θ_∞. This procedure was repeated for various jacket temperatures and stirring speeds. From the intercepts and slopes of the plots (see fig. 3) values of u and k, respectively, were obtained. At stirring speeds and jacket temperatures similar to those used in the TRIS experiments, zero or small, negative intercept values were obtained for u. Higher stirring speeds gave larger, positive values, as did the lower stirring rates after bending the paddle blades of the stirrer-ampoule holder to increase stirring efficiency. These results confirmed the view that low stirring energies were more than compensated by cooling effects, resulting in small, negative values of u, as previously calculated from normal rating period data. The above procedure was found to be very useful in characterizing the various operational parameters of the calorimeter.

As a means of guarding against possible systematic errors in the calculation of the corrected temperature rise, a comparison was made between the results obtained with the computer program we used and a program also written specifically for quartz thermometry by S. R. Gunn.[3] For three values of ΔT_{corr}, calcu-

[3] Lawrence Radiation Laboratory, University of California, Livermore, Calif. 94550.

TABLE 2. *Calorimetric data for the reaction of* TRIS *with* 0.1 N HCl

Expt. No.	Electrical energy equivalent		Mass of TRIS in vacuum	Corrected temperature rise	Q reaction	$-Q$ vaporization	Assigned reaction temperature	$-\Delta H$(298.15 K)
	Initial	Final						
	$J \cdot K^{-1}$	$J \cdot K^{-1}$	g	K	J	J	°C	$J \cdot g^{-1}$
9 a	443.839	444.609	0.500758	0.277398	123.227	0.030	24.789	245.836
10 a	444.373	444.977	.505858	.279860	124.447	.030	24.785	245.758
11 a	446.939	446.793	.505409	.278566	124.482	.028	24.779	246.032
12 b	491.951	492.334	.558259	.279037	137.326	.024	24.951	245.962
13 c	492.932	493.531	.557665	.277890	137.064	.022	24.962	245.767
15 d	491.587	491.693	.537582	.269113	132.307	.023	24.967	246.109
16 d	492.310	492.839	.562404	.280911	138.370	.022	24.971	246.030
17 e	493.010	494.116	.560898	.279550	137.976	.022	24.986	246.009
18 e	493.129	493.693	.543787	.270891	133.661	.023	24.994	245.829
								Mean = 245.926
								Sdm = 0.043

Experiment Nos. 1 to 8 were the first measurements made with the solution calorimeter facility. Difficulties were experienced due to erratic stirring energy and a malfunctioning timer. Expt. No. 14 was not completed. Therefore these experiments were not included in table 2.

a Original vessel, digital voltmeter employed in calibration circuit.
b Second vessel, original heater installed.
c As b, but potentiometer now in calibration circuit.
d As c, with calorimeter venting increased.
e As d, with new calibration heater in vessel.

lated from the data of a typical TRIS experiment, two of the values agreed to within 0.002 percent, and the third to within 0.011 percent, clearly minimizing the probability of error from the method of data treatment.

4.2. Enthalpy of Reaction

The enthalpy of the TRIS–HCl reaction at the mean reaction temperature, T_m, was calculated from eq (13)

$$-\Delta H(T_m) = \overline{EE} \times \Delta T_{corr} \qquad (13)$$

where $\overline{EE}$ is the average of the initial and final state electrical energy equivalents. This enthalpy is equivalent to the isothermal enthalpy at the mean reaction temperature [6b], assuming no significant change in heat capacity over the temperature range of the measurement.

The measured enthalpy was corrected for the following effects: (1) the heat of vaporization of a small amount of water into the increased vapor space that resulted from breaking the sample ampoule (0.016 to 0.025%), and (2) the correction of the measured enthalpy to 298.15 K (0.004 to 0.130%). In applying the latter correction, ΔCp for the TRIS–HCl reaction was taken to be 1.435 $J \cdot K^{-1} \cdot g^{-1}$ [1]. No correction was made for the heat of breaking the ampoule. Several sealed ampoules, both empty and with a drop of water added, were broken in 0.1 N HCl. However, the analysis of drift data in experiments in which sample ampoules were and were not broken showed that the heat effect (0.015J) associated with breaking the ampoules is less than the uncertainty of the temperature rise calculation.

5. Results and Discussion

5.1. Experimental Results

The results of nine TRIS–HCl experiments are listed in table 2. Inspection of the calculated values of the reaction enthalpy indicates no apparent differences due to the various experimental parameters that were changed during the course of the investigation. Namely, the changes made in the calibrating instruments, heaters, solution vessel, and venting did not affect the results. In view of this, the nine results were averaged to give a value of -245.93 $J \cdot g^{-1}$ (29791 $J \cdot mol^{-1}$) with a standard deviation of the mean of 0.043 $J \cdot g^{-1}$ (5.2 $J \cdot mol^{-1}$).

5.2. Estimate of Uncertainty

In table 3 we estimate reasonable upper limits for possible sources of systematic errors in our experiments. If all of the listed sources of systematic error were in the same direction, the results would be in error by 0.07 percent.

A reasonable assignment of uncertainty would be twice the standard deviation of the mean (±0.035%), if we were to assume that all of our measurement errors were random errors. However, in view of possible sources of systematic error, we have added our estimate of possible systematic errors to the random error and assigned an overall uncertainty of ±0.10 percent to the TRIS–HCl reaction enthalpy and obtain a value of -245.93 ± 0.26 $J \cdot g^{-1}$ at 298.15 K.

5.3. Conclusion

The enthalpy reported in this paper for the TRIS–HCl reaction is one of the higher values that have been

TABLE 3. *Judgement of possible sources of systematic error*

Source of error	Estimate of Error (percent)
Electrical power measurements	0.005
Time interval measurements	.003
Mass measurements	.005
Heater lead correction	.010
Assigned reaction temperature	.010
Vapor space correction	.003
Heat of bulb breaking	.010
Non-equivalence of heat sources	.020
Total	0.066

reported [1], the range of values of high precision being from 245.3 to 246.2 $J \cdot g^{-1}$. It is uncertain at present whether this spread represents difficulties inherent in the solution calorimetry, or is due to anomalies in the test reaction itself. The value reported in this paper agrees within the assigned uncertainties of the NBS certificate value of 245.76 ± 0.26 $J \cdot g^{-1}$ [7].

We thank Ralph L. Nuttall for his advice and assistance with the calculations of the corrected temperature rise, Stuart Gunn for making a comparison test of the computer calculation, and Marthada Kilday for helpful comments during the preparation of this paper.

6. References

[1] Prosen, E. J., and Kilday, M. V., J. Res. Nat. Bur. Stand. (U.S.), **77A** (Phys. and Chem.), No. 5, 581 (1973).
[2] Sunner, S., and Wadsö, I., Science Tools **13**, 1 (1966).
[3] Hammond, D. L., and Benjaminson, A., Instru. Control Systems **38** (10) 115 (1965).
[4] Bowman, H. A., Schoonover, R. M., and Jones, M. W., J. Res. NBS 71C, 179 (1967).
[5] Commission on Atomic Weights, Pure and Applied Chemistry, **21**, 91 (1970).
[6a] Coops, J., Jessup, R. S., Van Ness, K., Chapter 3, Experimental Thermochemistry, Vol. **1**, edited by F. D. Rossini (Interscience Publishers, New York, 1956).
[6b] Rossini, F. D., Chapter 1, ibid.
[7] Nat. Bur. Stand. Certificate, Standard Reference Material 724 for Solution Calorimetry, tris(hydroxymethyl)aminomethane, Washington, D.C. 20234, April 14, 1972.
[8] Deming, W. E., Chapter 9, Statistical Adjustment of Data (Dover Publications, Inc., New York, 1964).

(Paper 77A5–786)

JOURNAL OF RESEARCH of the National Bureau of Standards—A. Physics and Chemistry
Vol. 77A, No. 5, September–October 1973

Theory of Disclinations: IV. Straight Disclinations

Roland deWit

Institute for Materials Research, National Bureau of Standards, Washington, D.C. 20234

(May 31, 1973)

The general theory of disclinations developed earlier is applied to the special case of a straight disclination line. First the geometrical fields are found, such as the defect loop densities which correspond to Mura's new concepts of "plastic distortion" and "plastic rotation," the basic plastic fields (strain and bend-twist), the defect densities (dislocation and disclination), the characteristic vectors (Burgers and Frank), and the incompatibility. Then the static fields are found for the isotropic case, such as the displacement, total distortion, basic elastic fields, and the stress. It is shown that the disclination axis is moved by adding a dislocation to the disclination line. All these special results for the straight disclination line are shown to satisfy the general equations of the theory. As corollaries the following topics are also treated:

1. The finite and infinitesimal straight disclination dipole, which can be biaxial or uniaxial. It resembles the straight dislocation line.
2. The dislocation models of the straight disclination line and of the finite disclination dipole. They are terminating dislocation walls (tilt and twist).
3. The compensated disclination line and the bent dislocation wall.
4. Finally we show analytically a special case of a dislocation ending on a disclination.

Key words: Burgers vector; continuum mechanics; defect; dipole; disclination; dislocation; distortion; Green's tensor; incompatibility; loop; plasticity; strain; Volterra.

Contents

	Page
1. Introduction	608
2. Volterra's equations	609
3. Review of the straight dislocation	610
3.1 Geometry	610
3.2 Isotropic statics	612
4. Geometry of straight disclinations	616
5. Isotropic statics of the straight disclination	621
6. Movement of the disclination axis	626
6.1 Geometry	626
6.2 Statics	627
7. The infinitesimal disclination dipole	628
7.1 The biaxial dipole	628
7.2 The uniaxial dipole	629
8. The "Dislocation model" of the straight disclination	631
8.1 Geometry	631
8.2 Statics	633
9. The finite disclination dipole	635
9.1 The biaxial dipole	635
a. Geometry	635
b. Statics	636
9.2 The uniaxial dipole	639

Page
10. The compensated disclination line..... 640
11. The bent dislocation wall..... 642
12. Example of a terminating dislocation line..... 643
13. Summary..... 645
14. Appendix A. Evaluation of the delta function on a straight line and a semi-infinite plane..... 646
15. Appendix B. Generalized derivatives of cylindrical coordinates..... 649
16. Appendix C. Derivation of static fields of a straight defect from the general theory..... 651
17. References..... 658

1. Introduction

In previous papers [1, 2, 3][1] we have developed the general linear theory of stationary disclinations in an anisotropic or isotropic body. In the present paper we wish to specialize some of these results to the case of discrete straight disclination lines.

In 1907 Volterra [4] gave the elastic fields of straight hollow core dislocations and disclinations running along the axis of a long isotropic cylinder. He called these defects "distortions." Later Love [5] ventured to call them "dislocations." This name has been widely accepted, but its meaning has been narrowed to translational dislocations, because of the early importance of this type of defect in plastic deformation. Therefore Frank [6] introduced the new name "disinclination," later changed to *disclination*, to describe the rotational dislocation. Furthermore the word "distortion" has since come to stand for the gradient of the displacement, and it would therefore lead to confusion if we still tried to ascribe to it Volterra's original meaning as the combination of dislocations and disclinations. Still it would be useful to have a name for this combination, and we have adopted the word *defect* for that purpose. In this terminology, then, the present paper deals with discrete straight defect lines. This word usage does not exclude the consideration of "point defects," because they can be regarded as combinations of discrete dislocation loops [3].

We would here also like to point out that it has become customary to refer to "disclination theory" when really "defect theory" is meant (i.e., the theory of dislocations *and* disclinations). We have done this in our paper titles to emphasize the fact that the new results in defect theory are obtained because disclinations have been introduced.

Furthermore there are at least three independent ways of defining the two types of defects, i.e., in terms of (1) continuous distributions, (2) discrete lines, or (3) infinitesimal loops, which lead to essentially different descriptions of the disclination. This means, for example, that a discrete disclination line contains a certain amount of dislocation density, or a certain different amount of dislocation loop density. In this paper we shall identify these quantities for the case of straight disclinations.

In section 2 we recall that Volterra also summarized the characteristic terms in the displacement fields for straight defects. These results have to be slightly modified to obtain equilibrium everywhere.

Section 3 reviews straight dislocations to show the approach used in specializing the general theory. It also serves as a reference for the later sections.

In section 4 we apply the general results of [2] to our special case of discrete straight disclinations. We find the defect loop densities which are Mura's "plastic distortion" and "plastic rotation." Then we identify the basic plastic fields from which all other results follow. We find the defect densities and show that they satisfy the necessary general relations. The Burgers and Frank vectors are examined, and we conclude with relations for the incompatibility tensor.

Section 5 treats the isotropic statics of straight disclinations. From the given displacement we derive the basic elastic fields, and show that they satisfy the field equations with the defect densities. Then we find the stress and show that it maintains equilibrium.

[1] Figures in brackets indicate the literature references at the end of this paper.

In section 6 we find how the fields are modified when the disclination axis is moved away from the origin. We show that it is equivalent to adding a dislocation to the disclination.

Section 7 treats the infinitesimal straight disclination dipole line.

In section 8 we give the dislocation model of the straight disclination. We show that it is a terminating dislocation wall (in general tilt and twist). It has the same displacement, elastic strain and stress as the corresponding disclination line. In terms of the dislocation model we find more precise interpretations of Mura's new concepts.

Section 9 treats the finite straight disclination dipole line. We show that it reduces to the infinitesimal case of section 7 when the width approaches zero.

In section 10 we derive the results for the straight compensated disclination line, using two different defect surfaces.

In section 11 we apply the results of section 10 to the bent dislocation wall, which is made up of two semi-infinite dislocation walls meeting at right angles.

Section 12 shows analytically how a dislocation can end on a disclination.

Throughout the paper we assume that the body is infinitely extended. The geometric results are valid for the anisotropic case, but we have obtained the static fields only for the isotropic body.

We shall freely refer to the results of the three previous papers [1, 2, 3], which will be denoted in the present paper as I, II, and III.

2. Volterra's Equations

Weingarten's theorem [1, 2] states: On following around an irreducible circuit in a multiply-connected body, the displacement and rotation change by an amount that represents a rigid body motion, if and only if the classical elastic compatibility conditions are satisfied throughout the body.

This theorem led Volterra to conceive of the defects he called "distortions." They have subsequently also been called the most general Weingarten-Volterra dislocations. Volterra then proceeded to calculate the properties of such straight defects lying along the z axis. He first found the terms in the displacement fields that characterize such defects. Nabarro [7] considered these so important to dislocation theory that he quoted them directly in his book (eq (2.20)):

$$
\begin{aligned}
2\pi u_x &= (b_x - d_{zz}z + d_{xy}y)\,\tan^{-1}(y/x) + \tfrac{1}{2}\,(-b_y - d_{yz}z - \alpha d_{xy}x)\ln(x^2+y^2),\\
2\pi u_y &= (b_y - d_{xy}x + d_{yz}z)\,\tan^{-1}(y/x) + \tfrac{1}{2}\,(b_x - d_{zz}z - \alpha d_{xy}y)\ln(x^2+y^2),\\
2\pi u_z &= (b_z - d_{yz}y + d_{zz}x)\,\tan^{-1}(y/x) + \tfrac{1}{2}\,(d_{yz}x + d_{zz}y)\ln(x^2+y^2),
\end{aligned}
\tag{2.1}
$$

where α is an elastic constant. These displacements maintain equilibrium under no body forces except at the z axis. It will be recognized that the terms with coefficients b represent possible displacements for dislocations. The terms with coefficients d will be seen to be possible displacements for straight discrete disclinations.

These equations have to be modified to obtain equilibrium under no body forces also at the z axis. This can be done in several ways. One method is to calculate the body force from (2.1) by the usual equations of elasticity. It is found to be singular at the z axis. Then the displacement field of an equal but opposite force along the z axis is derived, and added to (2.1) to get the desired result. We do not show the details in this paper. Another method is to use the general expressions from III. Even though straight defects do not satisfy the necessary boundary conditions used there, it is still possible to find the correct functional dependence of the fields from the general expressions. The details are given in appendix C.

Once a set of displacement functions is found "by hook or crook," it is easy to verify that they are a solution by showing that they maintain equilibrium everywhere, including at singular points, and that they include the characteristic Volterra terms (2.1). Equilibrium is checked simply by deriving the stress and showing that it satisfies the equilibrium equation.

The development in this paper can also be put in terms of the following general question: Given the displacement as an empirical function of the coordinates representing experimental data, what is the system of defects that would produce such a displacement? To answer this question we have to determine how to divide the resulting fields into elastic and plastic parts. For a discrete defect this will be simple to do, because the most logical candidates for the basic plastic fields are the terms that are singular on a particular surface, as we shall see for the dislocation in section 3.2 and for the disclination in section 5. However, by another division we can also find a different system of defects that will give the same displacement, as we shall also see for the "dislocation model" of the straight disclination in section 8.

3. Review of the Straight Dislocation

In this section we apply the general results of section II 3.2* to the special case of a straight dislocation.

3.1. Geometry

The plastic distortion for a constant displacement across a surface S and the dislocation density for the corresponding discrete dislocation along the line L are given by the general expressions, (II3.21, II3.23),*

$$\beta^P_{kl}(\mathbf{r}) = -\delta_k(S)b_l, \tag{3.1}$$

$$\alpha_{pl}(\mathbf{r}) = \delta_p(L)b_l, \tag{3.2}$$

where L is the closed boundary of S, $\delta_k(S)$ and $\delta_p(L)$ are the Dirac delta functions on the surface S and the curve L, respectively, defined by (A11–12) in appendix A, and b_l is constant, identified as the Burgers vector of the discrete dislocation line. For the special case of this paper we wish to take L as a straight line and S as a semi-infinite plane bounded by L. In particular, let L run along the x_3 axis and S be the part of the x_1x_3 plane for negative x_1. To satisfy the right-hand rule we take the normal of S in the negative x_2 direction. These relationships are illustrated in figure 1. Then the only nonvanishing components of (3.1−2) become

$$\beta^P_{2l} = b_l H(-x_1)\delta(x_2), \tag{3.3}$$

$$\alpha_{3l} = b_l \delta(x_1)\delta(x_2), \tag{3.4}$$

according to (A15–16). The plastic distortion is singular on the plane S, and the dislocation density is concentrated on the x_3 axis. The three different cases for $l = 1, 2, 3$ are illustrated in figures 2–4. In figures 2 and 4 the plane S is also the slip plane, because it contains the Burgers vector.

For consistency we see that these results satisfy the definition, (I5.2), (II3.4),

$$\alpha_{pl} \equiv -\epsilon_{pmk}\beta^P_{kl,\,m}, \tag{3.5}$$

by (A6). We see also that (3.4) satisfies the continuity condition, (I5.4), (II3.24),

$$\alpha_{pl,\,p} = 0. \tag{3.6}$$

Now take for a Burgers circuit λ a circle of radius a in the x_1x_2 plane centered at the origin (fig. 1).

*Section II 3.2 refers to section 3.2 in reference [2], and the symbol (II3.21) refers to eq (3.21) in reference [2].

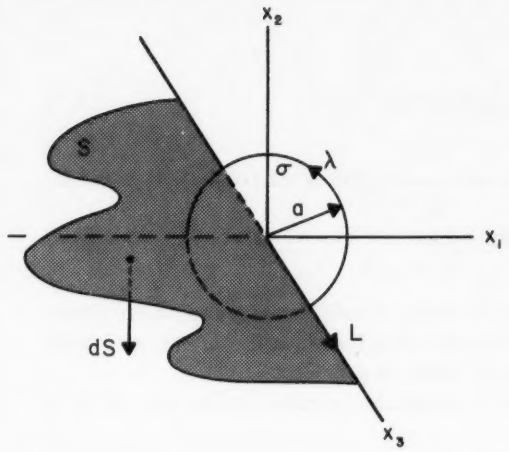

FIGURE 1. *Geometry of the discrete straight defect line in the Cartesian coordinate system* $x_1x_2x_3$.

The defect line L is along the x_3 axis and the defect surface S is the semi-infinite part of the x_1x_3 plane for which x_1 is a negative, with a normal in the negative x_2 direction. For the Burgers circuit λ, which links L, and the Burgers surface σ, which is pierced by L, we have chosen a circle of radius a in the x_1x_2 plane centered at the origin.

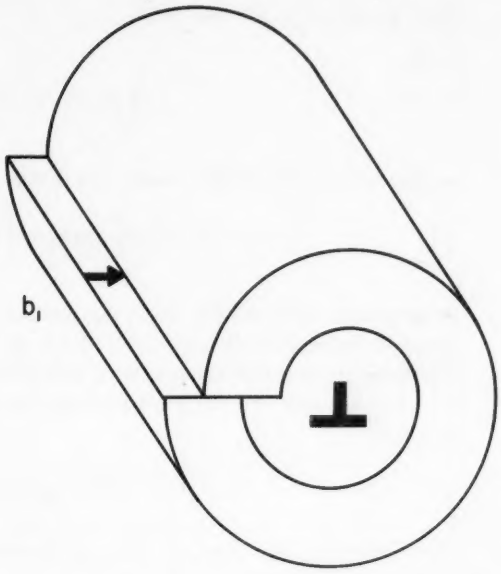

FIGURE 2. *Edge dislocation described by the dislocation density* $\alpha_{31}=b_1\delta(x_1)\delta(x_2)$.

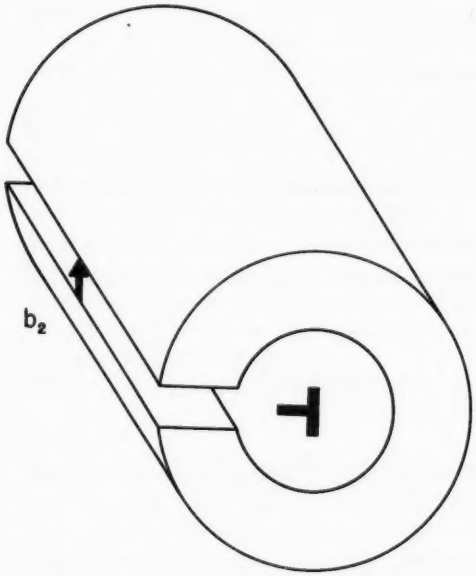

FIGURE 3. *Edge dislocation described by the dislocation density* $\alpha_{32}=b_2\delta(x_1)\delta(x_2)$.

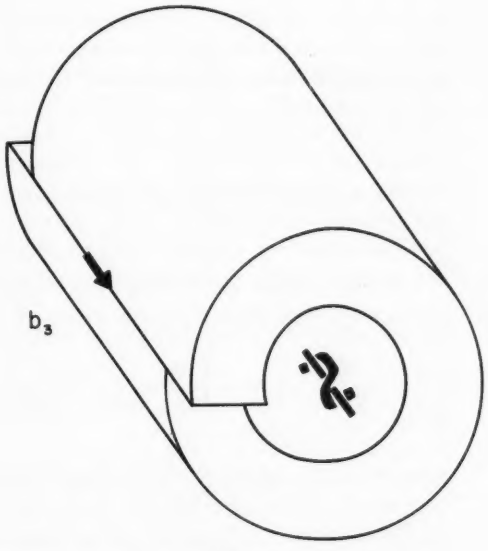

FIGURE 4. *Screw dislocation described by the dislocation density* $\alpha_{33}=b_3\delta(x_1)\delta(x_2)$.

Then we have by (3.3) and (A23)

$$-\oint_\lambda \beta^p_{kl}\, dL_k = -\oint_\lambda b_l H(-x_1)\delta(x_2)\, dL_2 = b_l, \tag{3.7}$$

in agreement with (II3.22), confirming that b_l is the Burgers vector. We also have by (3.4) and (A22)

$$\int_\sigma \alpha_{pl} dS_p = \int_\sigma b_l \delta(x_1)\delta(x_2)\, dS_3 = b_l, \tag{3.8}$$

in agreement with (II3.25). So in this section we have found the special forms of the plastic distortion and dislocation density (3.3–4) for a straight dislocation running along the x_3 axis, and these equations are in complete agreement with all the general results for geometry.

We conclude this section with expressions for the incompatibility tensor. It is in general given by, (I5.3),

$$\eta_{pq} = -(\epsilon_{qnl}\alpha_{pl,\,n})_{(pq)}. \tag{3.9}$$

For our special case the only nonvanishing components are

$$\eta_{13} = -\tfrac{1}{2} b_3 \delta(x_1)\delta'(x_2), \tag{3.10a}$$

$$\eta_{23} = \tfrac{1}{2} b_3 \delta'(x_1)\delta(x_2), \tag{3.10b}$$

$$\eta_{33} = b_1 \delta(x_1)\delta'(x_2) - b_2 \delta'(x_1)\delta(x_2), \tag{3.10c}$$

from (3.4). We note that they satisfy the continuity condition, (I4.2),

$$\eta_{pq,\,p} = 0. \tag{3.11}$$

The results in this section apply to an infinitely extended body, whether isotropic or anisotropic.

3.2. Isotropic Statics

In this section we find the static fields for a straight dislocation in an infinitely extended isotropic body. The displacement is given by (appendix C)

$$u^T_1 = b_1\left[\frac{\varphi}{2\pi} + \frac{x_1x_2}{4\pi(1-\nu)\rho^2}\right] + \frac{b_2}{4\pi(1-\nu)}\left[(1-2\nu)\ln\rho + \frac{x_2^2}{\rho^2}\right], \tag{3.12a}$$

$$u^T_2 = -\frac{b_1}{4\pi(1-\nu)}\left[(1-2\nu)\ln\rho + \frac{x_1^2}{\rho^2}\right] + b_2\left[\frac{\varphi}{2\pi} - \frac{x_1x_2}{4\pi(1-\nu)\rho^2}\right], \tag{3.12b}$$

$$u^T_3 = \frac{b_3\varphi}{2\pi}, \tag{3.12c}$$

where ν is Poisson's ratio. These expressions are well-known for a dislocation line of Burger vector b_l running along the x_3 axis. We have used a cartesian coordinate system $x_1x_2x_3$, as shown in figure 1. The cylindrical coordinates ρ and ϕ are defined in appendix B and shown in figure 5. By restricting the angle ϕ to the range $(-\pi, \pi)$ it becomes discontinuous on the semi-infinite plane S shown in figure 1, which then becomes the natural plastic displacement surface of section 3.1. Note that we have labeled (3.12) as the total displacement. In the literature these expressions are

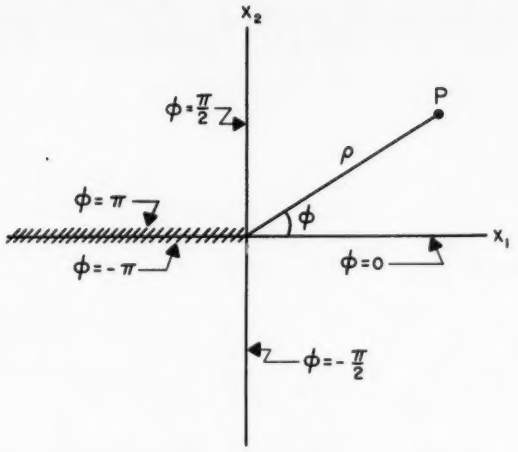

FIGURE 5. *Relation between Cartesian coordinates* x_1 *and* x_2 *and cylindrical coordinates* ρ *and* ϕ.

The angle ϕ has the range $(-\pi, \pi)$, assumes the values shown at the ordinates, and has a jump of 2π across the negative x_1 axis.

usually regarded as the elastic displacement which is then taken to be multiple-valued on account of the angle ϕ. In the framework of the present theory, however, it would not be correct to regard (3.12) as the elastic displacement. For, if the elastic displacement is prescribed, then there can be no dislocations (c.f. I2.1, I2.2, and I5.6, c.f. also footnote 10 in II). But if the total displacement is given the dislocations are still unspecified. We see from (3.5) that they are specified when we determine how the total distortion is split into an elastic and a plastic part. Intuitively we can see that it is unreasonable to split the displacement into an elastic and a plastic part in the present special case because of the fact that the angle ϕ cannot be split into a continuous and a discrete part. In general we shall contend that if a total field quantity of a straight defect contains the angle ϕ, it is unreasonable to split it into an elastic and plastic part. This idea will also be applied in section 5. The results (3.12) show a logarithmic dependence for the displacement at large distances from the dislocation line, in agreement with table II3.

The total distortion is defined in terms of the total displacement and consists of an elastic and plastic part, (I2.1), (II3.9),

$$\beta^T_{kl} \equiv u^T_{l,k} = \beta_{kl} + \beta^P_{kl}. \tag{3.13}$$

On differentiating the displacement (3.12), the terms containing ϕ will produce expressions singular on S, by (B4). These expressions correspond exactly to the plastic distortion (3.3) found in the previous section. This apparent coincidence is of course achieved by our special choice of S and the range of ϕ. These terms occur only because we chose the angle ϕ to be discontinuous rather than multiple-valued. Alternatively, if we had no a priori knowledge of the plastic distortion, we could assign the singular terms to it. These terms intuitively represent a surface along which a plastic displacement has taken place, as discussed in section 3.1. So we find for the elastic distortion of the straight dislocation

$$\beta_{11} = -\frac{b_1}{4\pi(1-\nu)}\left[(1-2\nu)\frac{x_2}{\rho^4} + 2\frac{x_1^2 x_2}{\rho^4}\right] + \frac{b_2}{4\pi(1-\nu)}\left[(1-2\nu)\frac{x_1}{\rho^2} - \frac{x_1 x_2^2}{\rho^4}\right], \tag{3.14a}$$

$$\beta_{21} = \frac{b_1}{4\pi(1-\nu)}\left[(3-2\nu)\frac{x_1}{\rho^2} - 2\frac{x_1x_2^2}{\rho^4}\right] + \frac{b_2}{4\pi(1-\nu)}\left[(1-2\nu)\frac{x_2}{\rho^2} + 2\frac{x_1^2x_2}{\rho^4}\right], \tag{3.14b}$$

$$\beta_{31} = 0, \tag{3.14c}$$

$$\beta_{12} = -\frac{b_1}{4\pi(1-\nu)}\left[(1-2\nu)\frac{x_1}{\rho^2} + 2\frac{x_1x_2^2}{\rho^4}\right] - \frac{b_2}{4\pi(1-\nu)}\left[(3-2\nu)\frac{x_2}{\rho^2} - 2\frac{x_1^2x_2}{\rho^4}\right], \tag{3.14d}$$

$$\beta_{22} = -\frac{b_1}{4\pi(1-\nu)}\left[(1-2\nu)\frac{x_2}{\rho^2} - 2\frac{x_1^2x_2}{\rho^4}\right] + \frac{b_2}{4\pi(1-\nu)}\left[(1-2\nu)\frac{x_1}{\rho^2} + 2\frac{x_1x_2^2}{\rho^4}\right], \tag{3.14e}$$

$$\beta_{32} = 0, \tag{3.14f}$$

$$\beta_{13} = -\frac{b_3x_2}{2\pi\rho^2}, \tag{3.14g}$$

$$\beta_{23} = \frac{b_3x_1}{2\pi\rho^2}. \tag{3.14h}$$

$$\beta_{33} = 0, \tag{3.14i}$$

using (B3–7). By contrast with the plastic distortion (3.3), we see that the elastic distortion consists of functions that are continuous everywhere except at the x_3 axis. This is reasonable to expect for an elastic field. To check the consistency of our results, it is easily shown that the elastic distortion and the dislocations density (3.4) satisfy the field equation, (I5.6), (II3.10),

$$\epsilon_{pmk}\beta_{kl,\,m} = \alpha_{pl}, \tag{3.15}$$

by (B8–10). This result then confirms that (3.14) represents the elastic distortion of a discrete dislocation line running along the x_3 axis.

Next we want to show that equilibrium is maintained everywhere. We first find the elastic strain, which is in general given by, (II3.13),

$$e_{kl} = \beta_{(kl)}. \tag{3.16}$$

Hence we have from (3.14) for the elastic strain of a straight dislocation

$$e_{11} = -\frac{b_1}{4\pi(1-\nu)}\left[(1-2\nu)\frac{x_2}{\rho^2} + 2\frac{x_1^2x_2}{\rho^4}\right] + \frac{b_2}{4\pi(1-\nu)}\left[(1-2\nu)\frac{x_1}{\rho^2} - 2\frac{x_1x_2^2}{\rho^4}\right], \tag{3.17a}$$

$$e_{22} = -\frac{b_1}{4\pi(1-\nu)}\left[(1-2\nu)\frac{x_2}{\rho^2} - 2\frac{x_1^2x_2}{\rho^4}\right] + \frac{b_2}{4\pi(1-\nu)}\left[(1-2\nu)\frac{x_1}{\rho^2} + 2\frac{x_1x_2^2}{\rho^4}\right], \tag{3.17b}$$

$$e_{33} = 0, \tag{3.17c}$$

$$e_{12} = \frac{b_1}{4\pi(1-\nu)}\left[\frac{x_1}{\rho^2} - 2\,\frac{x_1 x_2^2}{\rho^4}\right] - \frac{b_2}{4\pi(1-\nu)}\left[\frac{x_2}{\rho^2} - 2\,\frac{{}^2_1 x_2}{\rho^4}\right], \tag{3.17d}$$

$$e_{23} = \frac{b_3 x_1}{4\pi\rho^2} \tag{3.17c}$$

$$e_{31} = -\frac{b_3 x_2}{4\pi\rho^2}, \tag{3.17f}$$

The dilatation $e = e_{kk}$ is

$$e = -\frac{1-2\nu}{2\pi(1-\nu)\rho^2}\,(b_1 x_2 - b_2 x_1). \tag{3.17g}$$

At large distances from the dislocation line the elastic strain varies inversely with the distance, in agreement with table II3. Hooke's law for an isotropic body is in general given by, (III3.2),

$$\sigma_{kl} = 2G\left(e_{kl} + \frac{\nu}{1-2\nu}\,e\,\delta_{kl}\right). \tag{3.18}$$

Hence we find for the stress of the straight dislocation

$$\sigma_{11} = -\frac{Gb_1}{2\pi(1-\nu)}\left[\frac{x_2}{\rho^2} + 2\,\frac{x_1^2 x_2}{\rho^4}\right] + \frac{Gb_2}{2\pi(1-\nu)}\left[\frac{x_1}{\rho^2} - 2\,\frac{x_1 x_2^2}{\rho^4}\right], \tag{3.19a}$$

$$\sigma_{22} = -\frac{Gb_1}{2\pi(1-\nu)}\left[\frac{x_2}{\rho^2} - 2\,\frac{x_1^2 x_2}{\rho^4}\right] + \frac{Gb_2}{2\pi(1-\nu)}\left[\frac{x_1}{\rho^2} + 2\,\frac{x_1 x_2^2}{\rho^4}\right], \tag{3.19b}$$

$$\sigma_{33} = -\frac{G\nu}{2\pi(1-\nu)}\left(2\,\frac{b_1 x_2}{\rho^2} - 2\,\frac{b_2 x_1}{\rho^2}\right), \tag{3.19c}$$

$$\sigma_{12} = \frac{Gb_1}{2\pi(1-\nu)}\left[\frac{x_1}{\rho^2} - 2\,\frac{x_1 x_2^2}{\rho^4}\right] - \frac{Gb_2}{2\pi(1-\nu)}\left[\frac{x_2}{\rho^2} - 2\,\frac{x_1^2 x_2}{\rho^4}\right], \tag{3.19d}$$

$$\sigma_{23} = \frac{Gb_3 x_1}{2\pi\rho^2}, \tag{3.19e}$$

$$\sigma_{31} = -\frac{Gb_3 x_2}{2\pi\rho^2}. \tag{3.19f}$$

These expressions are also well-known in the literature. Finally, the equation of equilibrium are, (II2.1),

$$f_l = -\sigma_{kl,k}, \tag{3.20}$$

where f_l is the body force per unit volume. From (3.19) and (B8–10) we find

$$f_l = 0 \tag{3.21}$$

everywhere, including at the x_3 axis where (3.19) is singular. So the above fields maintain equilib-

rium without body forces, including at the x_3 axis. The displacement (3.12) contains the characteristic Volterra terms (2.1) for a dislocation. Therefore, as discussed in section 2, we may conclude that (3.12) correctly represents the displacement of a dislocation.

We conclude this section with expressions for the elastic rotation of the dislocation, which is in general given by (III4.6),

$$\omega_q = \tfrac{1}{2}\epsilon_{klq}\beta_{kl}, \tag{3.22}$$

or, from (3.14), for our special case by

$$\omega_1 = \frac{b_3 x_1}{4\pi\rho^2}, \tag{3.23a}$$

$$\omega_2 = \frac{b_3 x_2}{4\pi\rho^2}, \tag{3.23b}$$

$$\omega_3 = -\frac{b_1 x_1}{2\pi\rho^2} - \frac{b_2 x_2}{2\pi\rho^2}. \tag{3.23c}$$

In this section we have summarized the well-known expressions for the displacement and the elastic fields of a straight dislocation in an infinite isotropic body.

4. Geometry of Straight Disclinations

In this section we shall apply the general geometrical results of section II5.2 to the special case of a straight disclination. For a discrete defect along the line L, which has been formed by plastic displacement across the surface S, the dislocation and disclination loop densities are in general given by, (II5.12–13),

$$\beta^*_{kl}(\mathbf{r}) = -\delta_k(S)\{b_l + \epsilon_{lqr}\Omega_q(x_r - x^0_r)\}, \tag{4.1}$$

$$\varphi^*_{kq}(\mathbf{r}) = -\delta_k(S)\Omega_q, \tag{4.2}$$

where b_l is the dislocation Burgers vector, Ω_q the Frank vector, x^0_r a point through which the disclination axis passes, and $\delta_k(S)$ is the Dirac delta function on the surface S, defined by (A12) in appendix A. The quantities (4.1–2) were introduced by Mura [9], who called them the "plastic distortion" and "plastic rotation." For our special case of a straight disclination running along the x_3 axis, we take S to be the semi-infinite x_1x_3 plane for negative x_1 with normal in the negative x_2 direction, as illustrated in figure 1, and set $b_l = 0$. Furthermore, for simplicity at this point, we let the axis of rotation pass through the origin, so that $x^0_r = 0$. The effect of *moving* the axis will be investigated in section 6. Then the only nonvanishing components of (4.1–2) become

$$\beta^*_{2l} = \epsilon_{lqr}\Omega_q x_r H(-x_1)\delta(x_2), \tag{4.3}$$

$$\varphi^*_{2q} = \Omega_q H(-x_1)\delta(x_2), \tag{4.4}$$

according to (A16). For convenience, we write these results out in full

$$\beta^*_{21} = \Omega_2 x_3 H(-x_1)\delta(x_2), \tag{4.3a}$$

$$\beta^*_{22} = (\Omega_3 x_1 - \Omega_1 x_3)H(-x_1)\delta(x_2), \tag{4.3b}$$

$$\beta^*_{23} = -\Omega_2 x_1 H(-x_1)\delta(x_2), \tag{4.3c}$$

$$\varphi_{21}^{*}=\Omega_1 H(-x_1)\delta(x_2), \tag{4.4a}$$

$$\varphi_{22}^{*}=\Omega_2 H(-x_1)\delta(x_2), \tag{4.4b}$$

$$\varphi_{23}^{*}=\Omega_3 H(-x_1)\delta(x_2), \tag{4.4c}$$

where we have used (A8). The basic plastic fields (plastic strain and bend-twist) are in general given by, (II5.14–15),

$$e_{kl}^{P}=\beta_{(kl)}^{*}, \tag{4.5}$$

$$\kappa_{mq}^{P}=\tfrac{1}{2}\epsilon_{klq}\beta_{kl,m}^{*}+\varphi_{mq}^{*}. \tag{4.6}$$

For our special case we easily find the only nonvanishing components for the plastic strain

$$e_{12}^{P}=\tfrac{1}{2}\Omega_2 x_3 H(-x_1)\delta(x_2), \tag{4.7a}$$

$$e_{22}^{P}=(\Omega_3 x_1-\Omega_1 x_3)H(-x_1)\delta(x_2), \tag{4.7b}$$

$$e_{23}^{P}=-\tfrac{1}{2}\Omega_2 x_1 H(-x_1)\delta(x_2), \tag{4.7c}$$

from (4.3), and by (4.6) we find that the components of the plastic bend-twist are

$$\kappa_{11}^{P}=-\tfrac{1}{2}\Omega_2 H(-x_1)\delta(x_2), \tag{4.8a}$$

$$\kappa_{21}^{P}=-\tfrac{1}{2}\Omega_2 x_1 H(-x_1)\delta'(x_2)+\Omega_1 H(-x_1)\delta(x_2), \tag{4.8b}$$

$$\kappa_{31}^{P}=0, \tag{4.8c}$$

$$\kappa_{12}^{P}=0, \tag{4.8d}$$

$$\kappa_{22}^{P}=\Omega_2 H(-x_1)\delta(x_2), \tag{4.8e}$$

$$\kappa_{32}^{P}=0. \tag{4.8f}$$

$$\kappa_{13}^{P}=\tfrac{1}{2}\Omega_2 x_3\delta(x_1)\delta(x_2), \tag{4.8g}$$

$$\kappa_{23}^{P}=-\tfrac{1}{2}\Omega_2 x_3 H(-x_1)\delta'(x_2)+\Omega_3 H(-x_1)\delta(x_2), \tag{4.8h}$$

$$\kappa_{33}^{P}=-\tfrac{1}{2}\Omega_2 H(-x_1)\delta(x_2), \tag{4.8i}$$

from (4.3–4), where we have used (A6). The defect loop densities (4.3–4) and the basic plastic fields (4.7–8) are singular on the plane S, figure 1. This is the plane on which a discrete amount of plastic displacement has taken place to create the disclination line along the x_3 axis.

The general expressions for the dislocation and disclination densities are given by, (II5.19–20),

$$\alpha_{pl}(\mathbf{r})=\delta_p(L)\{b_l+\epsilon_{lqr}\Omega_q(x_r-x_r^0)\}, \tag{4.9}$$

$$\theta_{pq}(\mathbf{r})=\delta_p(L)\Omega_q, \tag{4.10}$$

where $\delta_p(L)$ is the Dirac delta function on the curve L, defined by (A11). For our special case, with $b_l=x_r^0=0$, the only nonvanishing components of the defect densities are

$$\alpha_{3l}=\epsilon_{lqr}\Omega_q x_r\delta(x_1)\delta(x_2), \tag{4.11}$$

508-076 O - 73 - 4

$$\theta_{3q}=\Omega_q\delta(x_1)\delta(x_2), \tag{4.12}$$

by (A15). Again, for convenience, we write these results out in full

$$\alpha_{31}=\Omega_2 x_3\delta(x_1)\delta(x_2), \tag{4.11a}$$

$$\alpha_{32}=-\Omega_1 x_3\delta(x_1)\delta(x_1), \tag{4.11b}$$

$$\alpha_{33}=0, \tag{4.11c}$$

$$\theta_{31}=\Omega_1\delta(x_1)\delta(x_2), \tag{4.12a}$$

$$\theta_{32}=\Omega_2\delta(x_1)\delta(x_2), \tag{4.12b}$$

$$\theta_{33}=\Omega_3\delta(x_1)\delta(x_2), \tag{4.12c}$$

where we have used (A8). The defect densities are concentrated on the x_3 axis. We illustrate the three different types of disclinations for $q=1, 2, 3$ in figures 6–8. Figures 6–7 represent twist disclinations because the Frank vectors Ω_1 and Ω_2 are normal to the disclination line, whereas figure 8 represents a wedge disclination because the Frank vector Ω_3 is parallel to the disclination line. From (4.12) we see that the twist disclinations correspond to the off-diagonal components of the disclination density, whereas the wedge disclination corresponds to the diagonal component (see table III). Note also that the discrete straight twist disclination contains a certain amount of dislocation density, given by (4.11a–b). The significance of these expressions can be interpreted as follows. Consider a slice of material parallel to the x_1x_2 plane at the point x_3. Locally near the

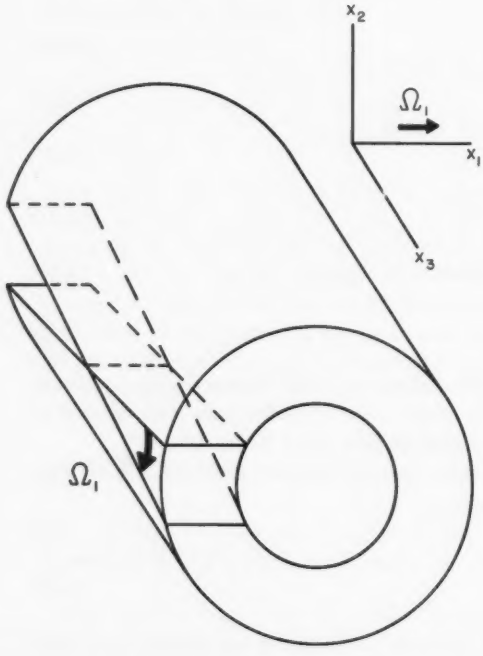

FIGURE 6. *Twist disclination with Frank vector* Ω_1.

It is described by the defect densities $\alpha_{32}=-\Omega_1 x_3\delta(x_1)\delta(x_2)$ and $\theta_{31}=\Omega_1\delta(x_1)\delta(x_2)$.

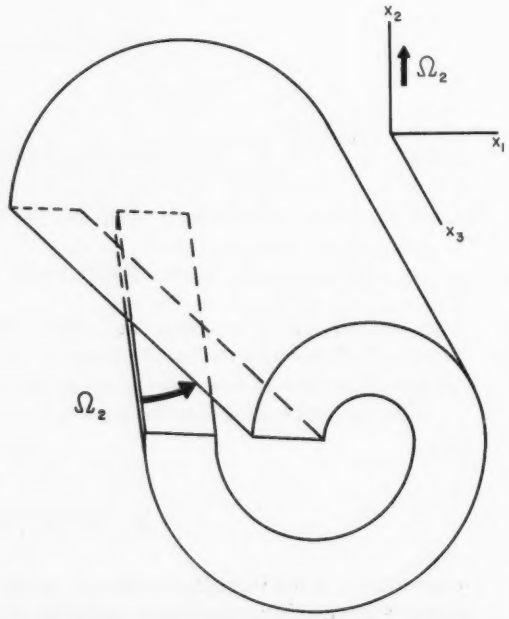

FIGURE 7. *Twist disclination with Frank vector* Ω_2.

It is described by the defect densities $\alpha_{31}=\Omega_2 x_3\delta(x_1)\delta(x_2)$ and $\theta_{32}=\Omega_2\delta(x_1)\delta(x_2)$.

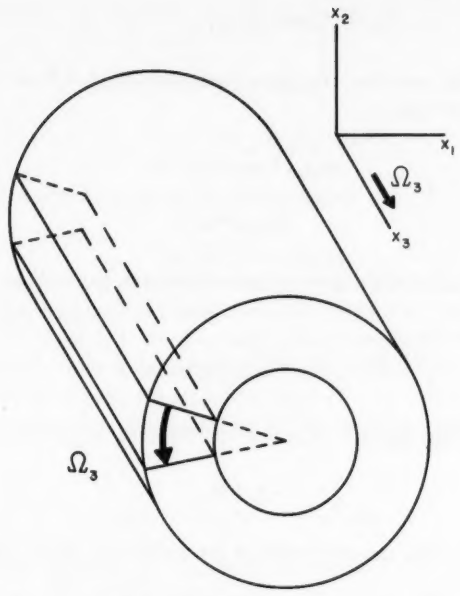

FIGURE 8. *Wedge disclination with Frank vector* Ω_3.

It is described by the disclination density $\theta_{33}=\Omega_3\delta(x_1)\delta(x_2)$.

x_3 axis the displacement jump of the disclination cannot be distinguished from that of a dislocation, even though there is a rotation jump. In figure 6 the deformation and the displacement jump near the point x_3 is similar to that of the dislocation in figure 3 with the density given by (4.11b). Similarly in figure 7 the deformation near the disclination line is similar to that of the dislocation in figure 2 with the density given by (4.11a). From this point of view it is therefore quite reasonable to regard the discrete disclination line as consisting of a mixture of dislocation and disclination density. This is a particular illustration of the general assertation we have already made in II. Note that the dislocation density implies a dislocation line with changing Burgers vector.

By contrast Anthony [10] does not regard (4.11) as a dislocation density, but as an integral part of the disclination density. The advantage of this approach is that the disclination is unambiguously defined, whether it is described in terms of continuous distribution of defects, or a discrete line. However, this approach becomes cumbersome when we try to describe a terminating dislocation as in section 12. Anthony has also treated several special cases of straight disclinations. For the wedge disclination his equations (27–28) and (30) correspond to our equations (4.12c) and (4.11c). We shall compare his results for the twist disclination with ours in section 6.

For consistency it is straightforward to verify that the basic plastic fields (4.7–8) and the defect densities (4.11–12) satisfy the general definitions, (I6.3, I6.1), (II4.1–2),

$$\alpha_{pl} \equiv -\epsilon_{pmk}\left(e^P_{kl,\,m}+\epsilon_{klq}\kappa^P_{mq}\right), \tag{4.13}$$

$$\theta_{pq} \equiv -\epsilon_{pmk}\kappa^P_{kq,\,m}, \tag{4.14}$$

by (A6) and (A8). Furthermore, it is easy to verify the general relations (II6.27–28) between the loop densities (4.3–4) and the defect densities (4.11–12)

$$\alpha_{pl} = -\epsilon_{pmk}\left(\beta^*_{kl,\,m}+\epsilon_{klq}\varphi^*_{mq}\right), \tag{4.15}$$

$$\theta_{pq} = -\epsilon_{pmk}\varphi^*_{kq,\,m}, \tag{4.16}$$

also by (A6) and (A8). We also see that the defect densities (4.11–12) satisfy the general continuity conditions, (I6.8, I6.2), (II5.27–28),

$$\alpha_{pl,\,p} + \epsilon_{lpq}\theta_{pq} = 0, \tag{4.17}$$

$$\theta_{pq,\,p} = 0. \tag{4.18}$$

We next wish to calculate the total Burgers vector which is in general defined in terms of the basic plastic fields by, (II4.5),

$$B_l = -\oint_\lambda (e^p_{kl} - \epsilon_{lqr}\kappa^p_{kq}x_r)dL_k, \tag{4.19}$$

where λ is the Burgers circuit, figure 1. For our special case we find from (4.7–8) by a somewhat tedious calculation that

$$B_l = 0, \tag{4.20}$$

where we have used (A8–9). The general relation for a discrete defect line is, (II5.17),

$$B_l = b_l - \epsilon_{lqr}\Omega_q x^0_r \tag{4.21}$$

and with our special assumption that $b_l = x^0_r = 0$ this reduces to (4.20). The total Burgers vector B_l measures the displacement jump at the origin, which vanishes in figures 6–8. The total Burgers vector can in general also be expressed in terms of the defect loop densities, (II6.31), or the defect densities, (II4.7),

$$B_l = -\oint_\lambda (\beta^*_{kl} - \epsilon_{lqr}\varphi^*_{kq}x_r)dL_k \tag{4.22}$$

$$= \int_\sigma (\alpha_{pl} - \epsilon_{lqr}\theta_{pq}x_r)dS_p, \tag{4.23}$$

where σ is the Burgers surface, figure 1. From (4.3–4) and (4.11–12) it easily follows that these equations lead to the same result as (4.20). Now we take for the Burgers circuit λ a circle of radius a in the x_1x_2 plane centered at the origin (fig. 1). Then we have by (4.8) and (A19–21)

$$-\oint_\lambda \kappa^p_{kq}dL_k = \Omega_q, \tag{4.24}$$

in agreement with (II5.18), confirming that Ω_q is the Frank vector. We also have by (4.4) and (A23)

$$-\oint_\lambda \varphi^*_{kq}dL_k = -\oint_\lambda \Omega_q H(-x_1)\delta(x_2)dL_2 = \Omega_q, \tag{4.25}$$

in agreement with (II6.32), and by (4.12) and (A22)

$$\int_\sigma \theta_{pq}dS_p = \int_\sigma \Omega_q\delta(x_1)\delta(x_2)dS_3 = \Omega_q, \tag{4.26}$$

in agreement with (II5.30). The jump in displacement across the surface S is in general given by,

(II5.1, II5.5),

$$[u_l(\mathbf{r})] = B_l + \epsilon_{lqr}\Omega_q x_r \tag{4.27}$$

$$= b_l + \epsilon_{lqr}\Omega_q(x_r - x_r^0). \tag{4.28}$$

In our special case with $b_l = x_r^0 = 0$, or by (4.20), this reduces to

$$[u_l(\mathbf{r})] = \epsilon_{lqr}\Omega_q x_r. \tag{4.29}$$

This jump agrees with those depicted in figures 6–8. So, in this section we have found the special forms of the defect loop densities (4.3–4), the basic plastic fields (4.7–8), and the defect densities (4.11–12), for a straight disclination running along the x_3 axis, and these equations are in complete agreement with all the general results for geometry from II.

We conclude this section with expressions for the incompatability tensor. It is in general given by, (I6.6), (II4.12),

$$\eta_{pq} = -(\epsilon_{qnl}\alpha_{pl,n} + \theta_{pq})_{(pq)}. \tag{4.30}$$

For our special case we find the only nonvanishing components from (4.11–12)

$$\eta_{13} = -\Omega_1\delta(x_1)\delta(x_2), \tag{4.31a}$$

$$\eta_{23} = -\Omega_2\delta(x_1)\delta(x_2) \tag{4.31b}$$

$$\eta_{33} = \Omega_1 x_3\delta'(x_1)\delta(x_2) + \Omega_2 x_3\delta(x_1)\delta'(x_2) - \Omega_3\delta(x_1)\delta(x_2), \tag{4.31c}$$

by (A9). We note that these results satisfy the continuity condition, (I4.2), (II4.13),

$$\eta_{pq,p} = 0. \tag{4.32}$$

The results in this section apply to an infinitely extended body, whether isotropic or anisotropic.

5. Isotropic Statics of the Straight Disclination

In this section we find the elastostatic fields for a straight disclination in an infinitely extended isotropic body. If the Volterra expressions (2.1) are properly modified to maintain equilibrium everywhere, then the displacement is given by (appendix C)

$$u_1^T = -\frac{\Omega_1 x_3}{4\pi(1-\nu)}\left[(1-2\nu)\ln\rho + \frac{x_2^2}{\rho^2}\right] + \Omega_2 x_3\left[\frac{\varphi}{2\pi} + \frac{x_1 x_2}{4\pi(1-\nu)\rho^2}\right] - \Omega_3\left[\frac{x_2\varphi}{2\pi} - \frac{1-2\nu}{4\pi(1-\nu)}x_1(\ln\rho - 1)\right], \tag{5.1a}$$

$$u_2^T = -\Omega_1 x_3\left[\frac{\varphi}{2\pi} - \frac{x_1 x_2}{4\pi(1-\nu)\rho^2}\right] - \frac{\Omega_2 x_3}{4\pi(1-\nu)}\left[(1-2\nu)\ln\rho + \frac{x_1^2}{\rho^2}\right] + \Omega_3\left[\frac{x_1\varphi}{2\pi} + \frac{1-2\nu}{4\pi(1-\nu)}x_2(\ln\rho - 1)\right], \tag{5.1b}$$

$$u_3^T = \Omega_1\left[\frac{x_2\varphi}{2\pi} - \frac{1-2\nu}{4\pi(1-\nu)}x_1(\ln\rho - 1)\right] - \Omega_2\left[\frac{x_1\varphi}{2\pi} + \frac{1-2\nu}{4\pi(1-\nu)}x_1(\ln\rho - 1)\right], \tag{5.1c}$$

where ν is Poisson's ratio. We have used a Cartesian coordinate system x_1, x_2, x_3, as shown in figure 1, and the cylindrical coordinates ρ and ϕ, as defined in appendix B and shown in figure 2. This is the displacement field of a straight disclination line running along the x_3 axis, with Frank vector Ω_q. By restricting the angle ϕ to the range $(-\pi, \pi)$ we shall find that the semi-infinite plane S becomes the natural plastic displacement surface of section 4. The asymptotic dependence of the displacement (5.1) goes as $\rho \ln \rho$, in agreement with table II3.

The total distortion is in general defined in terms of the displacement by, (I2.1), (II3.9),

$$\beta^T_{kl} \equiv u^T_{l,k}. \tag{5.2}$$

In performing these differentiations in the displacement (5.1) we shall regard three-dimensional space to consist of the product of the two-dimensional x_1x_2 plane and the independent one-dimensional x_3 line. For x_1 and x_2 we use the results for generalized derivatives of appendix B. Since x_3 appears only linearly in (5.1) the classical and generalized derivatives with respect to x_3 coincide. So we find for the total distortion, using (B3–7),

$$\beta^T_{11} = -\frac{\Omega_1 x_3}{4\pi(1-\nu)}\left[(1-2\nu)\frac{x_1}{\rho^2} - 2\frac{x_1x_2^2}{\rho^4}\right] - \frac{\Omega_2 x_3}{4\pi(1-\nu)}\left[(1-2\nu)\frac{x_2}{\rho^2} + 2\frac{x_1^2x_2}{\rho^4}\right] + \frac{\Omega_3}{4\pi(1-\nu)}\left[(1-2\nu)\ln\rho + \frac{x_2^2}{\rho^2}\right], \tag{5.3a}$$

$$\beta^T_{21} = -\frac{\Omega_1 x_3}{4\pi(1-\nu)}\left[(1-2\nu)\frac{x_2}{\rho^2} + 2\frac{x_1^2x_2}{\rho^4}\right] + \frac{\Omega_2 x_3}{4\pi(1-\nu)}\left[(3-2\nu)\frac{x_1}{\rho^2} - 2\frac{x_1x_2^2}{\rho^4}\right] + \Omega_2 x_3 H(-x_1)\delta(x_2) - \Omega_3\left[\frac{\varphi}{2\pi} + \frac{x_1x_2}{4\pi(1-\nu)\rho^2}\right], \tag{5.3b}$$

$$\beta^T_{31} = -\frac{\Omega_1}{4\pi(1-\nu)}\left[(1-2\nu)\ln\rho + \frac{x_2^2}{\rho^2}\right] + \Omega_2\left[\frac{\varphi}{2\pi} + \frac{x_1x_2}{4\pi(1-\nu)\rho^2}\right], \tag{5.3c}$$

$$\beta^T_{12} = \frac{\Omega_1 x_3}{4\pi(1-\nu)}\left[(3-2\nu)\frac{x_2}{\rho^2} - 2\frac{x_1^2x_2}{\rho^4}\right] - \frac{\Omega_2 x_3}{4\pi(1-\nu)}\left[(1-2\nu)\frac{x_1}{\rho^2} + 2\frac{x_1x_2^2}{\rho^4}\right] + \Omega_3\left[\frac{\varphi}{2\pi} - \frac{x_1x_2}{4\pi(1-\nu)\rho^2}\right], \tag{5.3d}$$

$$\beta^T_{22} = -\frac{\Omega_1 x_3}{4\pi(1-\nu)}\left[(1-2\nu)\frac{x_1}{\rho^2} + 2\frac{x_1x_2^2}{\rho^4}\right] - \Omega_1 x_3 H(-x_1)\delta(x_2) - \frac{\Omega_2 x_3}{4\pi(1-\nu)}\left[(1-2\nu)\frac{x_2}{\rho^2} - 2\frac{x_1^2x_2}{\rho^4}\right] + \frac{\Omega_3}{4\pi(1-\nu)}\left[(1-2\nu)\ln\rho + \frac{x_1^2}{\rho^2}\right] + \Omega_3 x_1 H(-x_1)\delta(x_2), \tag{5.3e}$$

$$\beta^T_{32} = -\Omega_1\left[\frac{\varphi}{2\pi} - \frac{x_1x_2}{4\pi(1-\nu)\rho^2}\right] - \frac{\Omega_2}{4\pi(1-\nu)}\left[(1-2\nu)\ln\rho + \frac{x_1^2}{\rho^2}\right], \tag{5.3f}$$

$$\beta^T_{13} = -\frac{\Omega_1}{4\pi(1-\nu)}\left[(1-2\nu)\ln\rho + \frac{x_2^2}{\rho^2}\right] - \Omega_2\left[\frac{\varphi}{2\pi} - \frac{x_1x_2}{4\pi(1-\nu)\rho^2}\right], \tag{5.3g}$$

$$\beta^T_{23} = \Omega_1\left[\frac{\varphi}{2\pi} + \frac{x_1x_2}{4\pi(1-\nu)\rho^2}\right] - \frac{\Omega_2}{4\pi(1-\nu)}\left[(1-2\nu)\ln\rho + \frac{x_1^2}{\rho^2}\right] - \Omega_2 x_1 H(-x_1)\delta(x_2), \tag{5.3h}$$

$$\beta^T_{33} = 0. \tag{5.3i}$$

Note that the total distortion contains terms which are singular on S and which correspond exactly to the dislocation loop density β^*_{kl} given by (4.3). This result is in agreement with the general equation (II5.34). Therefore we may be tempted to regard these terms as the plastic distortion β^P_{kl} and consequently find the elastic distortion from (3.13). This is the point of view taken by Mura [9]. We shall investigate the consequences of this approach in section 8. Strictly speaking we are at liberty to split the total distortion in any way we wish into an elastic and a plastic part. However, the present theory then implies that there are no disclinations. We note, though, that the total distortion (5.3) still contains the angle ϕ, in contrast to the dislocation case. Since ϕ is discontinuous at the surface S, it is not possible to split it into a part that is continuous everywhere except at the x_3 axis, and a part that is localized only on the surface S. Therefore the total distortion cannot be split into an elastic part that should be continuous everywhere except at the x_3 axis and a plastic part that is localized on the surface S of plastic displacement. We shall find, however, that the basic total fields no longer contain the angle ϕ and so it will be easy to find an intuitively reasonable way to split them into an elastic and plastic part.

We first consider the total strain which is the symmetric part of the total distortion and consists of an elastic and plastic part, (II4.14),

$$e^T_{kl} \equiv \beta^T_{(kl)} = e_{kl} + e^P_{kl}. \tag{5.4}$$

If we use (5.3) in this expression we shall find that the terms which are singular on S correspond exactly to the plastic strain e^P_{kl} given by (4.7). So we find for the elastic strain of the straight disclination

$$e_{11} = -\frac{\Omega_1 x_3}{4\pi(1-\nu)}\left[(1-2\nu)\frac{x_1}{\rho^2} - 2\frac{x_1 x_2^2}{\rho^4} \right] - \frac{\Omega_2 x_3}{4\pi(1-\nu)}\left[(1-2\nu)\frac{x_2}{\rho^2} + 2\frac{x_1^2 x_2}{\rho^4} \right] + \frac{\Omega_3}{4\pi(1-\nu)}\left[(1-2\nu)\ln\rho + \frac{x_2^2}{\rho^2} \right], \tag{5.5a}$$

$$e_{22} = -\frac{\Omega_1 x_3}{4\pi(1-\nu)}\left[(1-2\nu)\frac{x_1}{\rho^2} + 2\frac{x_1 x_2^2}{\rho^4} \right] - \frac{\Omega_2 x_3}{4\pi(1-\nu)}\left[(1-2\nu)\frac{x_2}{\rho^2} - 2\frac{x_1^2 x_2}{\rho^4} \right] + \frac{\Omega_3}{4\pi(1-\nu)}\left[(1-2\nu)\ln\rho + \frac{x_1^2}{\rho^2} \right], \tag{5.5b}$$

$$e_{33} = 0, \tag{5.5c}$$

$$e_{12} = \frac{\Omega_1 x_3}{4\pi(1-\nu)}\left[\frac{x_2}{\rho^2} - 2\frac{x_1^2 x_2}{\rho^4} \right] + \frac{\Omega_2 x_3}{4\pi(1-\nu)}\left[\frac{x_1}{\rho^2} - 2\frac{x_1 x_2^2}{\rho^4} \right] - \frac{\Omega_3 x_1 x_2}{4\pi(1-\nu)\rho^2}, \tag{5.5d}$$

$$e_{23} = \frac{\Omega_1 x_1 x_2}{4\pi(1-\nu)\rho^2} - \frac{\Omega_2}{4\pi(1-\nu)}\left[(1-2\nu)\ln\rho + \frac{x_1^2}{\rho^2} \right], \tag{5.5e}$$

$$e_{31} = -\frac{\Omega_1}{4\pi(1-\nu)}\left[(1-2\nu)\ln\rho + \frac{x_2^2}{\rho^2} \right] + \frac{\Omega_2 x_1 x_2}{4\pi(1-\nu)\rho^2}, \tag{5.5f}$$

The dilatation $e = e_{kk}$ is

$$e = -\frac{(1-2\nu)x_3}{2\pi(1-\nu)\rho^2}(\Omega_1 x_1 + \Omega_2 x_2) + \frac{\Omega_3}{4\pi(1-\nu)}[2(1-2\nu)\ln\rho - 1]. \tag{5.5g}$$

The elastic strain consists of functions that are continuous everywhere except at the x_3 axis, which is reasonable to expect for an elastic field. These expressions also show a logarithmic dependence

for the elastic strain at large distances from the disclination line, in agreement with table II3.

To find the total bend-twist we first find the total rotation which is in general given by, (III5.11),

$$\omega_q^T = \tfrac{1}{2}\epsilon_{klq}\beta_{kl}^T, \tag{5.6}$$

or, from (5.3), for our special case by

$$\omega_1^T = \frac{\Omega_1\varphi}{2\pi} - \frac{1}{2}\Omega_2 x_1 H(-x_1)\delta(x_2), \tag{5.7a}$$

$$\omega_2^T = \frac{\Omega_2\varphi}{2\pi}, \tag{5.7b}$$

$$\omega_3^T = \frac{\Omega_1 x_2 x_3}{2\pi\rho^2} - \frac{\Omega_2 x_1 x_3}{2\pi\rho^2} - \frac{1}{2}\Omega_2 x_3 H(-x_1)\delta(x_2) + \frac{\Omega_3\varphi}{2\pi}. \tag{5.7c}$$

These expressions still contain the angle ϕ, which prevents us from splitting the total rotation into an elastic and plastic part in a reasonable way. The total bend-twist is in general defined in terms of the total rotation and can be split into an elastic and plastic part, (II4.15),

$$\kappa_{kq}^T \equiv \omega_{q,k}^T = \kappa_{kq} + \kappa_{kq}^P \tag{5.8}$$

In carrying out this differentiation on the functions in (5.7) we shall find that the resulting terms singular on S correspond exactly to the plastic bend-twist κ_{kq}^P given by (4.8). So we find for the elastic bend-twist, using also (A6), (B3–4), and (B8),

$$\kappa_{11} = -\frac{\Omega_1 x_2}{2\pi\rho^2}, \tag{5.9a}$$

$$\kappa_{21} = \frac{\Omega_1 x_1}{2\pi\rho^2}, \tag{5.9b}$$

$$\kappa_{31} = 0, \tag{5.9c}$$

$$\kappa_{12} = -\frac{\Omega_2 x_2}{2\pi\rho^2}, \tag{5.9d}$$

$$\kappa_{22} = \frac{\Omega_2 x_1}{2\pi\rho^2}, \tag{5.9e}$$

$$\kappa_{32} = 0, \tag{5.9f}$$

$$\kappa_{13} = -\frac{\Omega_1 x_1 x_2 x_3}{\pi\rho^4} - \frac{\Omega_2 x_3}{2\pi}\left[\frac{1}{\rho^2} - 2\frac{x_1^2}{\rho^4} + \pi\delta(\boldsymbol{\rho})\right] - \frac{\Omega_3 x_2}{2\pi\rho^2}, \tag{5.9g}$$

$$\kappa_{23} = \frac{\Omega_1 x_3}{2\pi}\left[\frac{1}{\rho^2} - 2\frac{x_2^2}{\rho^4} + \pi\delta(\boldsymbol{\rho})\right] + \frac{\Omega_2 x_1 x_2 x_3}{\pi\rho^4} + \frac{\Omega_3 x_1}{2\pi\rho^2} \tag{5.9h}$$

$$\kappa_{33} = \frac{\Omega_1 x_2}{2\pi\rho^2} - \frac{\Omega_2 x_1}{2\pi\rho^2}. \tag{5.9i}$$

The elastic bend-twist, like the elastic strain, no longer contains the angle ϕ and is continuous everywhere except at the x_3 axis. Alternatively, if we had no a priori knowledge of the basic plastic fields (4.7–8), we could assign to them the terms in the basic total fields that are singular on S, because these surface singularities intuitively show where the plastic displacement has taken place. In this manner we would then also have been able to obtain the basic elastic fields (5.5) and (5.9), starting only with the expressions for the displacement (5.1), as discussed at the end of section 2.

To check the consistency of our results, it can be verified that the basic elastic fields (5.5) and (5.9) and the defect densities (4.11–12) satisfy the field equations, (I6.3, I6.1), (II4.17–18),

$$\epsilon_{pmk}(e_{kl,\,m}+\epsilon_{klq}\kappa_{mq})=\alpha_{pl}, \tag{5.10}$$

$$\epsilon_{pmk}\kappa_{kq,\,m}=\theta_{pq}, \tag{5.11}$$

by (B8–12). These results then confirm that (5.5) and (5.9) represent the basic elastic fields of a discrete disclination line running along the x_3 axis. Furthermore it can be verified that the elastic strain (5.5) and the incompatibility tensor (4.31) satisfy the field equation, (II4.22),

$$-\epsilon_{pmk}\epsilon_{qnl}e_{kl,\,mn}=\eta_{pq}, \tag{5.12}$$

by (B8–12).

Next we want to show that equilibrium is maintained everywhere. We first find the stress from Hookes' law (3.18) and the elastic strain (5.5)

$$\sigma_{11}=-\frac{G\Omega_1x_3}{2\pi(1-\nu)}\left[\frac{x_1}{\rho^2}-2\frac{x_1x_2^2}{\rho^4}\right]-\frac{G\Omega_2x_3}{2\pi(1-\nu)}\left[\frac{x_2}{\rho^2}+2\frac{x_1^2x_2}{\rho^4}\right]$$
$$+\frac{G\Omega_3}{2\pi(1-\nu)}\left[\ln\rho+\frac{x_2^2}{\rho^2}+\frac{\nu}{1-2\nu}\right], \tag{5.12a}$$

$$\sigma_{22}=-\frac{G\Omega_2x_3}{2\pi(1-\nu)}\left[\frac{x_1}{\rho^2}+2\frac{x_1x_2^2}{\rho^4}\right]-\frac{G\Omega_2x_3}{2\pi(1-\nu)}\left[\frac{x_2}{\rho^2}-2\frac{x_1^2x_2}{\rho^4}\right]$$
$$+\frac{G\Omega_3}{2\pi(1-\nu)}\left[\ln\rho+\frac{x_1^2}{\rho^2}+\frac{\nu}{1-2\nu}\right], \tag{5.12b}$$

$$\sigma_{33}=-\frac{G\nu x_3}{\pi(1-\nu)\rho^2}(\Omega_1x_1+\Omega_2x_2)+\frac{G\Omega_3}{2\pi(1-\nu)}\left[2\nu\ln\rho+\frac{\nu}{1-2\nu}\right], \tag{5.12c}$$

$$\sigma_{12}=\frac{G\Omega_1x_3}{2\pi(1-\nu)}\left[\frac{x_2}{\rho^2}-2\frac{x_1^2x_2}{\rho^4}\right]+\frac{G\Omega_2x_3}{2\pi(1-\nu)}\left[\frac{x_1}{\rho^2}-2\frac{x_1x_2^2}{\rho^4}\right]-\frac{G\Omega_3x_1x_2}{2\pi(1-\nu)\rho^2}, \tag{5.12d}$$

$$\sigma_{23}=\frac{G\Omega_1x_1x_2}{2\pi(1-\nu)\rho^2}-\frac{G\Omega_2}{2\pi(1-\nu)}\left[(1-2\nu)\ln\rho+\frac{x_1^2}{\rho^2}\right], \tag{5.12e}$$

$$\sigma_{31}=-\frac{G\Omega_1}{2\pi(1-\nu)}\left[(1-2\nu)\ln\rho+\frac{x_2^2}{\rho^2}\right]+\frac{G\Omega_2x_1x_2}{2\pi(1-\nu)\rho^2}. \tag{5.12f}$$

If we substitute these results into the equations of equilibrium (3.20) we find by (B5–10) that

$$f_l=0, \tag{5.13}$$

everywhere, so that the above fields maintain equilibrium without body forces, including at the x_3 axis. The displacement (5.1) contains the characteristic Volterra terms (2.1) for a disclination.

Therefore, as discussed in section 2, we may conclude that (5.1) correctly represents the displacement of a straight disclination line.

In this section we have presented the static fields, i.e., the displacement, total distortion, basic elastic fields (strain and bend-twist), and stress, of a straight disclination line in an infinite isotropic body.

6. Movement of the Disclination Axis

If we do not restrict the disclination axis from passing through the origin as in sections 4–5 we obtain more general results. These can be found by removing the restriction $x_r^0=0$, which was used in those sections to find the explicit formulas from the general expressions of II. In this section we shall discuss a few selected expressions which are of particular interest. They will show that the effect of moving the disclination axis is equivalent to adding a dislocation, as was already pointed out in II.

6.1. Geometry

The general expression for the dislocation density of a discrete defect line is given by (4.9). We shall now consider the special case of a discrete disclination line lying along the x_3 axis, but whose rotation axis passes through the general point x_r^0. Then the only nonvanishing components of the dislocation density become by (A15), setting $b_l=0$,

$$\alpha_{3l}=\epsilon_{lqr}\Omega_q(x_r-x_r^0)\delta(x_1)\delta(x_2), \tag{6.1}$$

instead of (4.11). On the other hand, the disclination density of our discrete disclination line with its axis shifted from the origin remains the same as (4.12). When written out in full we have for (6.1)

$$\alpha_{31}=[\Omega_2(x_3-x_3^0)+\Omega_3x_2^0]\delta(x_1)\delta(x_2), \tag{6.1a}$$

$$\alpha_{32}=[-\Omega_3x_1^0-\Omega_1(x_3-x_3^0)]\delta(x_1)\delta(x_2), \tag{6.1b}$$

$$\alpha_{33}=[-\Omega_1x_2^0+\Omega_2x_1^0]\delta(x_1)\delta(x_2), \tag{6.1c}$$

where we had used (A8). These results of course reduce to (4.11) when $x_r^0=0$. In the present case we find that the total Burgers vector no longer vanishes,

$$B_l=-\epsilon_{lqr}\Omega_qx_r^0, \tag{6.2}$$

from (4.21) with $b_l=0$. So the displacement jump across the surface S for our special case becomes

$$[u_l(\mathbf{r})]=\epsilon_{lqr}\Omega_q(x_r-x_r^0), \tag{6.3}$$

from (4.27–28), or, when written out in detail

$$[u_1(\mathbf{r})]=\Omega_2(x_3-x_3^0)-\Omega_3(x_2-x_2^0), \tag{6.3a}$$

$$[u_2(\mathbf{r})]=\Omega_3(x_1-x_1^0)-\Omega_1(x_3-x_3^0), \tag{6.3b}$$

$$[u_3(\mathbf{r})]=\Omega_1(x_2-x_2^0)-\Omega_2(x_1-x_1^0). \tag{6.3c}$$

The total Burgers vector (6.2) is the displacement jump at the origin. Anthony [10] has treated the special case of the twist disclination, Ω_1, for the case when the axis passes through the point $x_2^0=x_2(Z)$, $x_3^0=0$. To find the results for his case we set $\Omega_2=\Omega_3=0$ in the above equations. The

only nonvanishing components of (4.12), (6.1), and (6.3) then are

$$\theta_{31}=\Omega_1\delta(x_1)\delta(x_2), \tag{6.4}$$

$$\alpha_{32}=-\Omega_1 x_3\delta(x_1)\delta(x_2), \tag{6.5a}$$

$$\alpha_{33}=-\Omega_1 x_2(Z)\delta(x_1)\delta(x_2), \tag{6.5b}$$

$$[u_2]=-\Omega_1 x_3(P_0), \tag{6.6a}$$

$$[u_3]=\Omega_1(x_2(P_0)-x_2(Z)), \tag{6.6b}$$

where we have set $x_2=x_2(P_0)$, $x_3=x_3(P_0)$. These results correspond to Anthony's equations (31), (33), and (34). Hence our results are in complete agreement with Anthony.

If we compare (6.1) with (4.11) we see that the axis has been moved from the origin to the point x_r^0 by adding the dislocation density

$$\alpha_{3l}=-\epsilon_{lqr}\Omega_q x_r^0\delta(x_1)\delta(x_2) \tag{6.7}$$

to the disclination line of section 4. This is in agreement with (II5.24). From (3.4) this corresponds to adding a dislocation line with Burgers vector

$$b_l=-\epsilon_{lqr}\Omega_q x_r^0 \tag{6.8}$$

to the disclination line, in agreement with (II5.23). In detail (6.8) is

$$b_1=-\Omega_2 x_3^0+\Omega_3 x_2^0, \tag{6.8a}$$

$$b_2=-\Omega_3 x_1^0+\Omega_1 x_3^0, \tag{6.8b}$$

$$b_3=-\Omega_1 x_2^0+\Omega_2 x_1^0. \tag{6.8c}$$

So the disclination axis is moved from the origin to x_r^0 by simply adding a dislocation with Burgers vector (6.8) to it.

6.2. Statics

The fields of a straight discrete disclination along the x_3 axis whose rotation axis passes through the point x_r^0 can be obtained by adding the fields of the dislocation line in section 3.2 with the Burgers vector given by (6.8) to the fields of the disclination line in section 5. For example, the displacement is obtained by substituting (6.8) into (3.12) and adding it to (5.1)

$$u_1^T=-\frac{\Omega_1(x_3-x_3^0)}{4\pi(1-\nu)}\left[(1-2\nu)\ln\rho+\frac{x_2^2}{\rho^2}\right]+\Omega_2(x_3-x_3^0)\left[\frac{\varphi}{2\pi}+\frac{x_1x_2}{4\pi(1-\nu)\rho^2}\right]$$
$$+\frac{\Omega_3(x_1-x_1^0)}{4\pi(1-\nu)}\left[(1-2\nu)\ln\rho+\frac{x_2^2}{\rho^2}\right]-\Omega_3(x_2-x_2^0)\left[\frac{\varphi}{2\pi}+\frac{x_1x_2}{4\pi(1-\nu)\rho^2}\right]-\Omega_3\frac{1-2\nu}{4\pi(1-\nu)}x_1, \tag{6.9a}$$

$$u_2^T=-\Omega_1(x_3-x_3^0)\left[\frac{\varphi}{2\pi}-\frac{x_1x_2}{4\pi(1-\nu)\rho^2}\right]-\frac{\Omega_2(x_3-x_3^0)}{4\pi(1-\nu)}\left[(1-2\nu)\ln\rho+\frac{x_1^2}{\rho^2}\right]$$
$$+\Omega_3(x_1-x_1^0)\left[\frac{\varphi}{2\pi}-\frac{x_1x_2}{4\pi(1-\nu)\rho^2}\right]+\frac{\Omega_3(x_2-x_2^0)}{4\pi(1-\nu)}\left[(1-2\nu)\ln\rho+\frac{x_1^2}{\rho^2}\right]-\Omega_3\frac{1-2\nu}{4\pi(1-\nu)}x_2, \tag{6.9b}$$

$$u_3^T=\Omega_1\left[\frac{(x_2-x_2^0)\varphi}{2\pi}-\frac{1-2\nu}{4\pi(1-\nu)}x_1(\ln\rho-1)\right]-\Omega_2\left[\frac{(x_1-x_1^0)\varphi}{2\pi}+\frac{1-2\nu}{4\pi(1-\nu)}x_2(\ln\rho-1)\right]. \tag{6.9c}$$

This is the displacement of a straight disclination line running along the x_3 axis, with a rotation axis that passes thru the point x_r^0. Other field quantities can be calculated in the same way, or can be derived from (6.9) by the same method as used in section 5.

7. The Infinitesimal Disclination Dipole

In this section we wish to apply the general expressions of section II7 to the special case of a straight disclination dipole line. The biaxial dipole is obtained by moving the whole basic straight disclination (line and axis) by an infinitesimal distance ξ_m. The uniaxial dipole is obtained by moving only the line and keeping the axis fixed. In both cases the negative of the basic disclination is left at the x_3 axis.

7.1. The Biaxial Dipole

In general the defect densities of a biaxial dipole are given by, (II7.1–2),

$$\alpha_{pl}^D=-\xi_m\alpha_{pl,\,m}, \tag{7.1}$$

$$\theta_{pq}^D=-\xi_m\theta_{pq,\,m}, \tag{7.2}$$

where α_{pl} and θ_{pq} are the defect densities of the corresponding basic defect. For the special case of a *discrete straight biaxial disclination dipole line* the basic defect densities are given by (4.11–12). So for the conjugate dipole the only nonvanishing components of (7.1–2) are

$$\alpha_{3l}^D=-\epsilon_{lqr}\Omega_q[x_r\xi_m\delta_{,m}(\boldsymbol{\rho})+\xi_r\delta(\boldsymbol{\rho})], \tag{7.3}$$

$$\theta_{3q}^D=-\Omega_q\xi_m\delta_{,m}(\boldsymbol{\rho}), \tag{7.4}$$

where $\delta(\boldsymbol{\rho})$ is the two-dimensional Dirac delta function defined by (B9). These results could of course also be found from (II7.3–4) and (A15). In these expressions the tensor $\Omega_q\xi_m$ represents the strength of the dipole. When written out in full (7.3–4) become

$$\alpha_{31}^D=-\Omega_2[x_3\xi_1\delta'(x_1)\delta(x_2)+x_3\xi_2\delta(x_1)\delta'(x_2)+\xi_3\delta(x_1)\delta(x_2)], \tag{7.3a}$$

$$\alpha_{32}^D=\Omega_1[x_3\xi_1\delta'(x_1)\delta(x_2)+x_3\xi_2\delta(x_1)\delta'(x_2)+\xi_3\delta(x_1)\delta(x_2)], \tag{7.3b}$$

$$\theta_{31}^D=-\Omega_1[\xi_1\delta'(x_1)\delta(x_2)+\xi_2\delta(x_1)\delta'(x_2)], \tag{7.4a}$$

$$\theta_{32}^D=-\Omega_2[\xi_1\delta'(x_1)\delta(x_2)+\xi_2\delta(x_1)\delta'(x_2)], \tag{7.4b}$$

$$\theta_{33}^D=-\Omega_3[\xi_1\delta'(x_1)\delta(x_2)+\xi_2\delta(x_1)\delta'(x_2)], \tag{7.4c}$$

where we have used (A8–9).

In general the displacement of the biaxial dipole is given by, (II7.5),

$$u_n^D=-\xi_m u_{n,\,m}^T, \tag{7.5}$$

where u_n^T is the displacement of the corresponding basic defect. For our special case the distortion of the basic straight disclination line is given by (5.3), and so the displacement of the conjugate

dipole is

$$u_1^D=\frac{\Omega_1\xi_1x_3}{4\pi(1-\nu)}\left[(1-2\nu)\frac{x_1}{\rho^2}-2\frac{x_1x_2^2}{\rho^4}\right]-\frac{\Omega_2\xi_2x_3}{4\pi(1-\nu)}\left[(3-2\nu)\frac{x_1}{\rho^2}-2\frac{x_1x_2^2}{\rho^4}\right]$$

$$+\frac{(\Omega_1\xi_2+\Omega_2\xi_1)x_3}{4\pi(1-\nu)}\left[(1-2\nu)\frac{x_2}{\rho^2}+2\frac{x_1^2x_2}{\rho^4}\right]-(\Omega_2\xi_3-\Omega_3\xi_2)\left[\frac{\varphi}{2\pi}+\frac{x_1x_2}{4\pi(1-\nu)\rho^2}\right]$$

$$-\frac{\Omega_3\xi_1-\Omega_1\xi_3}{4\pi(1-\nu)}\left[(1-2\nu)\ln\rho+\frac{x_2^2}{\rho^2}\right], \tag{7.6a}$$

$$u_2^D=-\frac{\Omega_1\xi_1x_3}{4\pi(1-\nu)}\left[(3-2\nu)\frac{x_2}{\rho^2}-2\frac{x_1^2x_2}{\rho^4}\right]+\frac{\Omega_2\xi_2x_3}{4\pi(1-\nu)}\left[(1-2\nu)\frac{x_2}{\rho^2}-2\frac{x_1^2x_2}{\rho^4}\right]$$

$$+\frac{(\Omega_1\xi_2+\Omega_2\xi_1)x_3}{4\pi(1-\nu)}\left[(1-2\nu)\frac{x_1}{\rho^2}+2\frac{x_1x_2^2}{\rho^4}\right]+\frac{\Omega_2\xi_3-\Omega_3\xi_2}{4\pi(1-\nu)}\left[(1-2\nu)\ln\rho+\frac{x_1^2}{\rho^2}\right]$$

$$-(\Omega_3\xi_1-\Omega_1\xi_3)\left[\frac{\varphi}{2\pi}-\frac{x_1x_2}{4\pi(1-\nu)\rho^2}\right], \tag{7.6b}$$

$$u_3^D=\frac{\Omega_1\xi_1}{4\pi(1-\nu)}\left[(1-2\nu)\ln\rho+\frac{x_2^2}{\rho^2}\right]+\frac{\Omega_2\xi_2}{4\pi(1-\nu)}\left[(1-2\nu)\ln\rho+\frac{x_1^2}{\rho^2}\right]$$

$$-(\Omega_1\xi_2-\Omega_2\xi_1)\left[\frac{\varphi}{2\pi}-\frac{x_1x_2}{4\pi(1-\nu)\rho^2}\right], \tag{7.6c}$$

where we have ignored the terms in (5.3) which are concentrated on the surface S. We presume that the displacement is not a state quantity because it contains the angle ϕ. The displacement has a logarithmic dependence at large distances from the dipole line, in agreement with table II3.

7.2. The Uniaxial Dipole

To derive the relations for the uniaxial disclination dipole we first find the results of moving the axis of the basic disclination line by an infinitesimal distance ξ_m, keeping the disclination line fixed. The dislocation density of this defect is given by, (II7.7),

$$\alpha_{pl}^A=\xi_m\partial\alpha_{pl}/\partial x_m^0, \tag{7.7}$$

whereas the disclination density vanishes, $\theta_{pq}^A=0$. For our special case of a straight disclination line we find from (6.1) that the only nonvanishing components of (7.7) are

$$\alpha_{3l}^A=-\epsilon_{lqr}\Omega_q\xi_r\delta(\boldsymbol{\rho}), \tag{7.8}$$

in agreement with (II7.9) and (A15). The displacement of the above defect is, (II7.11),

$$u_n^A=\xi_m\partial u_n^T/\partial x_m^0, \tag{7.9}$$

which, for our special case, becomes

$$u_1^A=-(\Omega_2\xi_3-\Omega_3\xi_2)\left[\frac{\varphi}{2\pi}+\frac{x_1x_2}{4\pi(1-\nu)\rho^2}\right]-\frac{\Omega_3\xi_1-\Omega_1\xi_3}{4\pi(1-\nu)}\left[(1-2\nu)\ln\rho+\frac{x_2}{\rho^2}\right], \tag{7.10a}$$

$$u_2^A=\frac{\Omega_2\xi_3-\Omega_3\xi_2}{4\pi(1-\nu)}\left[(1-2\nu)\ln\rho+\frac{x_1^2}{\rho^2}\right]-(\Omega_3\xi_1-\Omega_1\xi_3)\left[\frac{\varphi}{2\pi}-\frac{x_1x_2}{4\pi(1-\nu)\rho^2}\right], \tag{7.10b}$$

$$u_3^A=-(\Omega_1\xi_2-\Omega_2\xi_1)\frac{\varphi}{2\pi}, \tag{7.10c}$$

from (6.9). If we compare (7.8) and (7.10) with (3.4) and (3.12) we see that the above results are the dislocation density and displacement of a discrete straight dislocation line with a Burgers vector given by

$$b_l=-\epsilon_{lqr}\Omega_q\xi_r, \tag{7.11}$$

in agreement with (II7.13).

We now find the relations for the *discrete straight uniaxial disclination dipole line.* In general they are given by the difference between those in section 7.1 and the above. For example, the dislocation density is found from, (II7.14),

$$\alpha_{pl}^L=\alpha_{pl}^D-\alpha_{pl}^A. \tag{7.12}$$

Hence from (7.3) and (7.8) we find that the only nonvanishing components of (7.12) are

$$\alpha_{3l}^L=-\epsilon_{lqr}\Omega_qx_r\xi_m\delta_{,m}(\boldsymbol{\rho}), \tag{7.13}$$

in agreement with (II7.15) and (A15). When written out in full this expression becomes

$$\alpha_{31}^L=-\Omega_2x_3[\xi_1\delta'(x_1)\delta(x_2)+\xi_2\delta(x_1)\delta'(x_2)]-\Omega_3\xi_2\delta(x_1)\delta(x_2), \tag{7.13a}$$

$$\alpha_{32}^L=\Omega_1x_3[\xi_1\delta'(x_1)\delta(x_2)+\xi_2\delta(x_1)\delta'(x_2)]+\Omega_3\xi_1\delta(x_1)\delta(x_2), \tag{7.13b}$$

$$\alpha_{33}^L=(\Omega_1\xi_2-\Omega_2\xi_1)\delta(x_1)\delta(x_2), \tag{7.13c}$$

where we have used (A8–9). The disclination density of the uniaxial dipole is the same as for the biaxial dipole, $\theta_{pq}^L=\theta_{pq}^D$, given by (7.4). The displacement of the uniaxial dipole is given by, (II7.16),

$$u_n^L=u_n^D-u_n^A. \tag{7.14}$$

By (7.6) and (7.10) this becomes for our special case

$$u_1^L=\frac{\Omega_1\xi_1x_3}{4\pi(1-\nu)}\left[(1-2\nu)\frac{x_1}{\rho^2}-2\frac{x_1x_2^2}{\rho^4}\right]-\frac{\Omega_2\xi_2x_3}{4\pi(1-\nu)}\left[(3-2\nu)\frac{x_1}{\rho^2}-2\frac{x_1x_2^2}{\rho^4}\right]$$
$$+\frac{(\Omega_1\xi_2+\Omega_2\xi_1)x_3}{4\pi(1-\nu)}\left[(1-2\nu)\frac{x_2}{\rho^2}+2\frac{x_1^2x_2}{\rho^4}\right], \tag{7.15a}$$

$$u_2^L=-\frac{\Omega_1\xi_1x_3}{4\pi(1-\nu)}\left[(3-2\nu)\frac{x_2}{\rho^2}-2\frac{x_1^2x_2}{\rho^4}\right]+\frac{\Omega_2\xi_2x_3}{4\pi(1-\nu)}\left[(1-2\nu)\frac{x_2}{\rho^2}-2\frac{x_1^2x_2}{\rho^4}\right]$$
$$+\frac{(\Omega_1\xi_2+\Omega_2\xi_1)x_3}{4\pi(1-\nu)}\left[(1-2\nu)\frac{x_1}{\rho^2}+2\frac{x_1x_2^2}{\rho^4}\right], \tag{7.15b}$$

$$u_3^L=\frac{\Omega_1\xi_1}{4\pi(1-\nu)}\left[(1-2\nu)\ln\rho+\frac{x_2^2}{\rho^2}\right]+\frac{\Omega_2\xi_2}{4\pi(1-\nu)}\left[(1-2\nu)\ln\rho+\frac{x_1^2}{\rho^2}\right]$$

$$+(\Omega_1\xi_2-\Omega_2\xi_1)\frac{x_1x_2}{4p(1-\nu)\rho^2}. \tag{7.15c}$$

We note that these expressions no longer contain the angle φ, and so u_n^L is a state quantity. The asymptotic dependence at large distances is the same as the biaxial dipole, and shown in table II3.

Furthermore the displacement of the uniaxial dipole u_n^L does not contain any contribution from the wedge disclination, i.e., Ω_3 is missing from (7.15). We may therefore conclude that it is possible to find the displacements of an edge dislocation from those of a biaxial wedge disclination dipole. Specifically if we set

$$\Omega_1=\Omega_2=0, \tag{7.16}$$

we find for (7.11)

$$b_1=\Omega_3\xi_2, \tag{7.17a}$$

$$b_2=-\Omega_3\xi_1. \tag{7.17b}$$

If these results are substituted in (7.6 a–b) we find (3.12 a–b). This method of obtaining the edge dislocation displacements was first pointed out by Eshelby [11].

8. The "Dislocation Model" of the Straight Disclination

8.1. Geometry

As discussed in section II9 the dislocation model of a discrete defect line along the curve L is obtained by eliminating the disclination loop density (II9.1)

$$\varphi_{kq}^*=0, \tag{8.1}$$

from the corresponding defect surface S that spans L. We shall illustrate this for our special case and so find the dislocation model of a straight disclination. There are of course many possible choices for the surface S, but we consider only the one used in the previous sections and illustrated in figure 1.

The dislocation loop density remains the same as before, (4.3), and becomes the plastic distortion, (II9.2). So it has the only nonvanishing components

$$\beta_{2l}^P=\beta_{2l}^*=\epsilon_{lqr}\Omega_q x_r H(-x_1)\delta(x_2), \tag{8.2}$$

or, when written out in full

$$\beta_{21}^P=\beta_{21}^*=\Omega_2x_3H(-x_1)\delta(x_2), \tag{8.2a}$$

$$\beta_{22}^P=\beta_{22}^*=(\Omega_3x_1-\Omega_1x_3)H(-x_1)\delta(x_2), \tag{8.2b}$$

$$\beta_{23}^P=\beta_{23}^*=-\Omega_2x_1H(-x_1)\delta(x_3). \tag{8.2c}$$

The dislocation density of the dislocation model is in general given by, (II9.7),

$$\alpha_{pl}(\mathbf{r}) = \delta_p(L)\{b_l + \epsilon_{lqr}\Omega_q(x_r - x_r^0)\} + \delta_l(S)\Omega_p - \delta_{pl}\delta_k(S)\Omega_k. \tag{8.3}$$

For our special case, with $b_l = x_r^0 = 0$, this reduces to

$$\alpha_{11} = \Omega_2 H(-x_1)\delta(x_2), \tag{8.4a}$$

$$\alpha_{21} = 0, \tag{8.4b}$$

$$\alpha_{31} = \Omega_2 x_3 \delta(x_1)\delta(x_2), \tag{8.4c}$$

$$\alpha_{12} = -\Omega_1 H(-x_1)\delta(x_2), \tag{8.4d}$$

$$\alpha_{22} = 0, \tag{8.4e}$$

$$\alpha_{32} = -\Omega_1 x_3 \delta(x_1)\delta(x_2) - \Omega_3 H(-x_1)\delta(x_2), \tag{8.4f}$$

$$\alpha_{13} = 0, \tag{8.4g}$$

$$\alpha_{23} = 0, \tag{8.4h}$$

$$\alpha_{33} = \Omega_2 H(-x_1)\delta(x_2), \tag{8.4i}$$

where we have used (A15–16) and (A8). The dislocation model consists of two parts, the same dislocation density along L as for the corresponding discrete disclination, given by (4.11), and a constant distribution over the surface S, given by the terms with the Heaviside function. We have sketched the three different type of dislocation models for Ω_1, Ω_2, and Ω_3 in figures 9–11. Rather than the constant dislocation distribution over S implied by (8.4), which is somewhat difficult to draw, we have shown the discrete distribution that most closely approximates it, and is somewhat easier to visualize. These figures represent the dislocation models of the straight disclinations shown in figures 6–8. Figures 9 and 11 represent terminating tilt walls and figure 10 a terminating twist wall. The disclination density of course vanishes, (II9.8),

$$\theta_{pq} = 0. \tag{8.5}$$

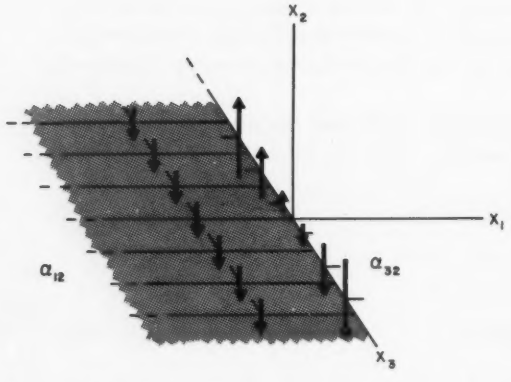

FIGURE 9. *Dislocation model of the twist disclination in figure 6.*

The tilt wall on the surface S (fig. 1), which terminates at the x_3 axis, is represented by a set of parallel edge dislocations. The arrows are Burgers vectors and the attached short lines show the orientation of the extra half planes. This defect is described by the dislocation densities $\alpha_{12} = -\Omega_1 H(-x_1)\delta(x_2)$ and $\alpha_{32} = -\Omega_1 x_3 \delta(x_1)\delta(x_2)$.

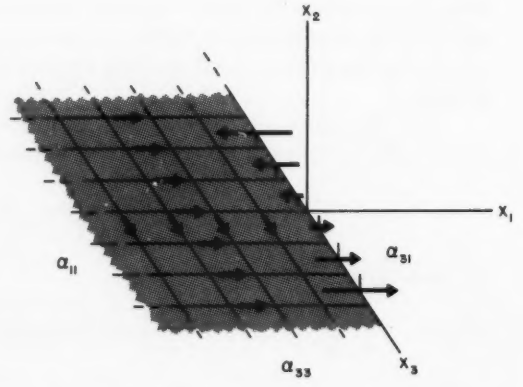

FIGURE 10. *Dislocation model of the twist disclination in figure 7.*

The twist wall on the surface S, which terminates at the x_3 axis, is represented by a crossed grid of screw dislocations. The arrows are Burgers vectors and the attached short lines show the orientation of the extra half planes for the edge dislocations. This defect is described by the dislocation densities $\alpha_{11} = \alpha_{33} = \Omega_2 H(-x_1)\delta(x_2)$ and $\alpha_{31} = \Omega_2 x_3 \delta(x_1)\delta(x_2)$.

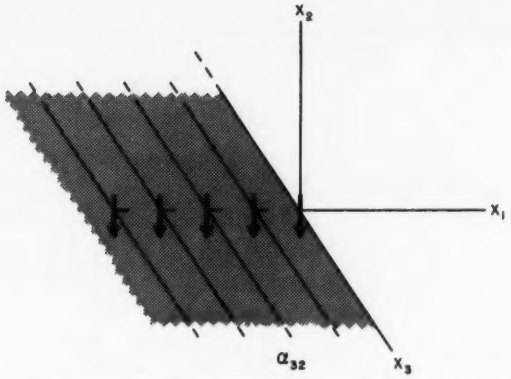

FIGURE 11. *Dislocation model of the wedge disclination in figure 8.*

The tilt wall on the surface S, which terminates at the x_3 axis, is represented by a set of parallel edge dislocations. The arrows are Burgers vectors and the attached short lines show the orientation of the extra half planes. This defect is described by the dislocation density $\alpha_{32}=-\Omega_3 H(-x_1)\delta(x_2)$.

For consistency it is easily verified that (8.2) and (8.4) satisfy the definition (3.5). It is also easily checked that the continuity condition (3.6) is satisfied by (8.4), in agreement with (II9.9).

We conclude this section with expressions for the incompatibility tensor. If we substitute (8.4) into (3.9) we find the only nonvanishing components

$$\eta_{13}=-\Omega_1\delta(x_1)\delta(x_2), \tag{8.6a}$$

$$\eta_{23}=-\Omega_2\delta(x_1)\delta(x_2), \tag{8.6b}$$

$$\eta_{33}=\Omega_1 x_3\delta'(x_1)\delta(x_2)+\Omega_2 x_3\delta(x_1)\delta'(x_2)-\Omega_3\delta(x_1)\delta(x_2). \tag{8.6c}$$

These results are identical with the incompatibility tensor of the corresponding disclination given by (4.31). Since the incompatibility is the source of elastic strain, (II4.22) and (II4.31), this means that the dislocation model has the same elastic strain as the corresponding discrete disclination line.

8.2. Statics

According to (II9.11–12) the total displacement and distortion of the dislocation model are identical to those for the corresponding disclination line. They are therefore given by (5.1) and (5.3).

To determine the elastic fields it is necessary to know how to split up the total fields. The difference between a discrete disclination line and its dislocation model simply results from splitting the total fields up in a different way. For a discrete disclination we have argued that the total distortion cannot be split into an elastic and plastic part. In particular in section 5 we argued that for the straight disclination (5.3) cannot be split because it contains the angle φ. For the dislocation model, however, we ignore this point of view and say that the total distortion can be split into an elastic and plastic part. This approach leads to Mura's new concepts of "plastic distortion" and "elastic distortion" of a disclination line. In particular, for the straight disclination, we assert that (5.3) can be split. The logical terms for the plastic part are those that are concentrated on the surface S, which correspond exactly to (8.2), or the dislocation loop density of section 4. So we find the elastic distortion from (3.13), (5.3), and (8.2),

508-076 O - 73 - 5

$$\beta_{11} = -\frac{\Omega_1 x_3}{4\pi(1-\nu)}\left[(1-2\nu)\,\frac{x_1}{\rho^2} - 2\,\frac{x_1 x_2^2}{\rho^4}\right] - \frac{\Omega_2 x_3}{4\pi(1-\nu)}\left[(1-2\nu)\,\frac{x_2}{\rho^2} + 2\,\frac{x_1^2 x_2}{\rho^4}\right] + \frac{\Omega_3}{4\pi(1-\nu)}\left[(1-2\nu)\,\ln\rho + \frac{x_2^2}{\rho^2}\right], \tag{8.7a}$$

$$\beta_{21} = -\frac{\Omega_1 x_3}{4\pi(1-\nu)}\left[(1-2\nu)\,\frac{x_2}{\rho^2} + 2\,\frac{x_1^2 x_2}{\rho^4}\right] + \frac{\Omega_2 x_3}{4\pi(1-\nu)}\left[(3-2\nu)\,\frac{x_1}{\rho^2} - 2\,\frac{x_1 x_2^2}{\rho^4}\right] - \Omega_3\left[\frac{\varphi}{2\pi} + \frac{x_1 x_2}{4\pi(1-\nu)\rho^2}\right], \tag{8.7b}$$

$$\beta_{31} = -\frac{\Omega_1}{4\pi(1-\nu)}\left[(1-2\nu)\,\ln\rho + \frac{x_2^2}{\rho^2}\right] + \Omega_2\left[\frac{\varphi}{2\pi} + \frac{x_1 x_2}{4\pi(1-\nu)\rho^2}\right], \tag{8.7c}$$

$$\beta_{12} = \frac{\Omega_1 x_3}{4\pi(1-\nu)}\left[(3-2\nu)\,\frac{x_2}{\rho^2} - 2\,\frac{x_1^2 x_2}{\rho^4}\right] - \frac{\Omega_2 x_3}{4\pi(1-\nu)}\left[(1-2\nu)\,\frac{x_1}{\rho^2} + 2\,\frac{x_1 x_2^2}{\rho^4}\right] + \Omega_3\left[\frac{\varphi}{2\pi} - \frac{x_1 x_2}{4\pi(1-\nu)\rho^2}\right], \tag{8.7d}$$

$$\beta_{22} = -\frac{\Omega_1 x_3}{4\pi(1-\nu)}\left[(1-2\nu)\,\frac{x_1}{\rho^2} + 2\,\frac{x_1 x_2^2}{\rho^4}\right] - \frac{\Omega_2 x_3}{4\pi(1-\nu)}\left[(1-2\nu)\,\frac{x_2}{\rho^2} - 2\,\frac{x_1^2 x_2}{\rho^4}\right] + \frac{\Omega_3}{4\pi(1-\nu)}\left[(1-2\nu)\,\ln\rho + \frac{x_1^2}{\rho^2}\right], \tag{8.7e}$$

$$\beta_{32} = -\Omega_1\left[\frac{\varphi}{2\pi} - \frac{x_1 x_2}{4\pi(1-\nu)\rho^2}\right] - \frac{\Omega_2}{4\pi(1-\nu)}\left[(1-2\nu)\,\ln\rho + \frac{x_1^2}{\rho^2}\right], \tag{8.7f}$$

$$\beta_{13} = -\frac{\Omega_1}{4\pi(1-\nu)}\left[(1-2\nu)\,\ln\rho + \frac{x_2^2}{\rho^2}\right] - \Omega_2\left[\frac{\varphi}{2\pi} - \frac{x_1 x_2}{4\pi(1-\nu)\rho^2}\right], \tag{8.7g}$$

$$\beta_{23} = \Omega_1\left[\frac{\varphi}{2\pi} + \frac{x_1 x_2}{4\pi(1-\nu)\rho^2}\right] - \frac{\Omega_2}{4\pi(1-\nu)}\left[(1-2\nu)\,\ln\rho + \frac{x_1^2}{\rho^2}\right], \tag{8.7h}$$

$\beta_{33} = 0.$

This is the elastic distortion of the "dislocation model" of the straight disclination line. It also represents Mura's "elastic distortion" of the straight disclination line. Note that these expressions still contain the angle ϕ. For consistency it is straightforward to check that (8.7) and (8.4) satisfy the field equation (3.15). From the elastic distortion we can then find all the other elastic fields of the dislocation model.

The elastic strain is obtained by substituting (8.7) into (3.16) and the result is identical to (5.5). Thus the elastic strain and hence stress of the dislocation model is identical to that of the corresponding discrete disclination, as we already discussed in section II9.

The elastic rotation is found from (3.22) and (8.7)

$$\omega_1 = \frac{\Omega_1 \varphi}{2\pi}, \tag{8.8a}$$

$$\omega_2 = \frac{\Omega_2 \varphi}{2\pi}, \tag{8.8b}$$

$$\omega_3 = \frac{\Omega_1 x_2 x_3}{2\pi\rho^2} - \frac{\Omega_2 x_1 x_3}{2\pi\rho^2} + \frac{\Omega_3 \varphi}{2\pi}. \tag{8.8c}$$

In general the elastic bend-twist is given by, (II3.14),

$$\kappa_{kq} = \omega_{q,k}. \tag{8.9}$$

For our special case (8.8) we find the components

$$\kappa_{11} = -\frac{\Omega_1 x_2}{2\pi\rho^2}, \tag{8.10a}$$

$$\kappa_{21} = \frac{\Omega_1 x_1}{2\pi\rho^2} + \Omega_1 H(-x_1)\delta(x_2), \tag{8.10b}$$

$$\kappa_{31} = 0, \tag{8.10c}$$

$$\kappa_{12} = -\frac{\Omega_1 x_2}{2\pi\rho^2}, \tag{8.10d}$$

$$\kappa_{22} = -\frac{\Omega_2 x_1}{2\pi\rho^2} + \Omega_2 H(-x_1)\delta(x_2), \tag{8.10e}$$

$$\kappa_{32} = 0, \tag{8.10f}$$

$$\kappa_{13} = -\frac{\Omega_1 x_1 x_2 x_3}{\pi\rho^4} - \frac{\Omega_2 x_3}{2\pi}\left[\frac{1}{\rho^2} - 2\frac{x_1^2}{\rho^4} + \pi\delta(\boldsymbol{\rho})\right] - \frac{\Omega_3 x_2}{2\pi\rho^2}, \tag{8.10g}$$

$$\kappa_{23} = \frac{\Omega_1 x_3}{2\pi}\left[\frac{1}{\rho^2} - 2\frac{x_2^2}{\rho^4} + \pi\delta(\boldsymbol{\rho})\right] + \frac{\Omega_2 x_1 x_2 x_3}{\pi\rho^4} + \frac{\Omega_3 x_1}{2\pi\rho^2} + \Omega_3 H(-x_1)\delta(x_2), \tag{8.10h}$$

$$\kappa_{33} = \frac{\Omega_1 x_2}{2\pi\rho^2} - \frac{\Omega_2 x_1}{2\pi\rho^2}, \tag{8.10i}$$

where we have used (B3–4) and (B8). The elastic bend-twist of the dislocation model consists of the sum of the elastic bend-twist of the corresponding disclination line, (5.9), and the disclination loop density or Mura's "plastic rotation," (4.4). For consistency it can easily be verified that (8.10) and (8.5) satisfy the field equation (5.11), by (B8) and (B11–12).

Mura's new concepts therefore have a clear interpretation in terms of the dislocation model. Mura's "plastic and elastic distortion" of the disclination line are the plastic and elastic distortion of the corresponding dislocation model. Mura's "plastic rotation" is the excess elastic bend-twist of the dislocation model over the corresponding disclination line.

9. The Finite Disclination Dipole

The results for a finite dipole can be derived simply by combining the fields of a positive and negative basic disclination which are a finite distance apart. We choose the positive disclination to pass through the point $(L, 0, 0)$ and the negative one through $(-L, 0, 0)$, both parallel to the x_3 axis.

9.1. The Biaxial Dipole

a. Geometry

We find the defect densities for the *finite straight biaxial disclination dipole* from the basic defect densities of the discrete straight disclination line, given by (4.11–12), using the above pro-

cedure. The only nonvanishing components are

$$\alpha_{31}^{D} = \Omega_2 x_3[\delta(x_1 - L) - \delta(x_1 + L)]\,\delta(x_2), \tag{9.1a}$$

$$\alpha_{32}^{D} = -\Omega_1 x_3[\delta(x_1 - L) - \delta(x_1 + L)]\delta(x_2), \tag{9.1b}$$

$$\theta_{3q}^{D} = \Omega_q[\delta(x_1 - L) - \delta(x_1 + L)]\,\delta(x_2). \tag{9.2}$$

It is interesting also to find the dislocation model for this defect since it has exactly the same total displacement, total distortion, elastic strain, and stress. The defect densities for the dislocation model of the finite biaxial disclination dipole can be found from the basic defect densities of the dislocation model of the discrete straight disclination line, given by (8.4–5). Using the same procedure again, we find

$$\alpha_{11}^{D} = -\Omega_2[H(x_1 - L) - H(x_1 + L)]\delta(x_2), \tag{9.3a}$$

$$\alpha_{21}^{D} = 0, \tag{9.3b}$$

$$\alpha_{31}^{D} = \Omega_2 x_3[\delta(x_1 - L) - \delta(x_1 + L)]\,\delta(x_2), \tag{9.3c}$$

$$\alpha_{12}^{D} = \Omega_1[H(x_1 - L) - H(x_2 + L)]\,\delta(x_2), \tag{9.3d}$$

$$\alpha_{22}^{D} = 0, \tag{9.3e}$$

$$\alpha_{32}^{D} = -\Omega_1 x_3[\delta(x_1 - L) - \delta(x_1 + L)]\,\delta(x_2) + \Omega_3[H(x_1 - L) - H(x_1 + L)]\,\delta(x_2), \tag{9.3f}$$

$$\alpha_{13}^{D} = 0, \tag{9.3g}$$

$$\alpha_{23}^{D} = 0, \tag{9.3h}$$

$$\alpha_{33}^{D} = -\Omega_2[H(x_1 - L) - H(x_1 + L)]\,\delta(x_2), \tag{9.3i}$$

$$\theta_{pq}^{D} = 0. \tag{9.4}$$

The dislocation model consists of two parts: the same dislocation density as for the corresponding defect, given by (9.1), and a constant distribution over the surface strip between $(-L, 0, 0)$ and $(L, 0, 0)$. We have illustrated this case in figures 12–14. The dislocation model of the biaxial wedge disclination dipole, figure 14, was examined by Li [12], who called it a "dislocation wall."

b. Statics

The fields of the finite straight biaxial disclination dipole can be found from the fields of the corresponding basic defect, i.e., the straight disclination line, given in section 5, by the same procedure as used above. We shall illustrate this by two examples. We first find the total displacement of the biaxial disclination dipole from (5.1)

$$u_1^D = -\frac{\Omega_1 x_3}{4\pi(1-\nu)}\left[\frac{1}{2}(1-2\nu)\ln\frac{(x_1-L)^2+x_2^2}{(x_1+L)^2+x_2^2} + \frac{x_2^2}{(x_1-L)^2+x_2^2} - \frac{x_2^2}{(x_1+L)^2+x_2^2}\right]$$
$$+ \frac{\Omega_2 x_3}{2\pi}\left[\varphi(x_1-L, x_2) - \varphi(x_1+L, x_2) + \frac{x_2}{2(1-\nu)}\left\{\frac{x_1-L}{(x_1-L)^2+x_2^2} - \frac{x_1+L}{(x_1+L)^2+x_2^2}\right\}\right]$$

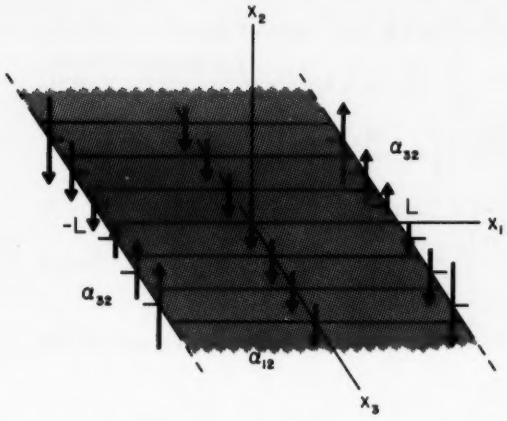

FIGURE 12. *Dislocation model of the finite twist disclination dipole (biaxial and uniaxial), corresponding to figures 6 and 9.*

The dislocation densities are $\alpha^D_{12}=\Omega_1[H(x_1-L)-H(x_1+L)]\delta(x_3)$ and $\alpha^D_{32}=-\Omega_1 x_3[\delta(x_1-L)-\delta(x_1+L)]\delta(x_3)$.

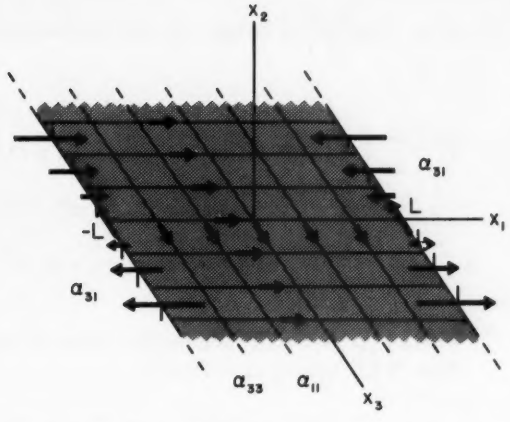

FIGURE 13. *Dislocation model of the finite twist disclination dipole, corresponding to figures 7 and 10.*

The dislocation densities for the biaxial dipole are $\alpha^D_{11}=\alpha^D_{33}=-\Omega_3[H(x_1-L)-H(x_1+L)]\delta(x_3)$ and $\alpha^D_{31}=\Omega_3 x_3[\delta(x_1-L)-\delta(x_1+L)]\delta(x_3)$. For the uniaxial dipole we have to add the dislocation density $\alpha^A_{32}=-\Omega_3 L[\delta(x_1-L)+\delta(x_1+L)]\delta(x_3)$, which is indicated by the two Burgers vectors at L and $-L$.

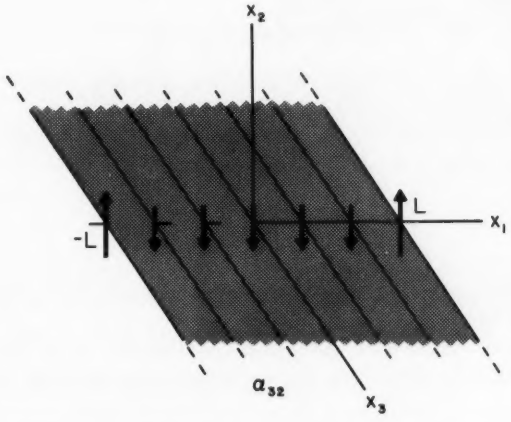

FIGURE 14. *Disclination model of the finite wedge disclination dipole, corresponding to figures 8 and 11.*

The dislocation density for the biaxial dipole is $\alpha^D=\Omega_3[H(x_1-L)-H(x_1+L)]\delta(x_3)$. For the uniaxial dipole we have to add the dislocation density $\alpha^A_{32}=\Omega_3 L[\delta(x_1-L)+\delta(x_1+L)]\delta(x_3)$, which is indicated by the two large Burgers vectors at L and $-L$.

$$-\frac{\Omega_3}{2\pi}\left[x_2\{\varphi(x_1-L,x_2)-\varphi(x_1+L,x_2)\}-\frac{1-2\nu}{2(1-\nu)}\left\{\frac{1}{2}x_1\ln\frac{(x_1-L)^2+x_2^2}{(x_1+L)^2+x_2^2}\right.\right.$$
$$\left.\left.-\frac{1}{2}L\ln\left((x_1-L)^2+x_2^2\right)\left((x_1+L)^2+x_2^2\right)+2L\right\}\right], \qquad (9.5a)$$

$$u_2^D=-\frac{\Omega_1 x_3}{2\pi}\left[\varphi(x_1-L,x_2)-\varphi(x_1+L,x_2)-\frac{x_2}{2(1-\nu)}\left\{\frac{x_1-L}{(x_1-L)^2+x_2^2}-\frac{x_1+L}{(x_1+L)^2+x_2^2}\right\}\right]$$
$$-\frac{\Omega_2 x_3}{4\pi(1-\nu)}\left[\frac{1}{2}(1-2\nu)\ln\frac{(x_1-L)^2+x_2^2}{(x_1+L)^2+x^2}+\frac{(x_1-L)^2}{(x_1-L)^2+x_2^2}-\frac{(x_1+L)^2}{(x_1+L)^2+x_2^2}\right]$$

$$+\frac{\Omega_3}{2\pi}\left[x_1\{\varphi(x_1-L,x_2)-\varphi(x_1+L,x_2)\}-\frac{1}{2}\{\varphi(x_1-L,x_2)+\varphi(x_1+L,x_2)\}\right.$$
$$\left.+\frac{1-2\nu}{2(1-\nu)}x_2\frac{1}{2}\ln\frac{(x_1-L)^2+x_2^2}{(x_1+L)^2+x_2^2}\right], \tag{9.5b}$$

$$u_3^D=\frac{\Omega_1}{2\pi}\left[x_2\{\varphi(x_1-L,x_2)-\varphi(x_1+L,x_2)\}-\frac{1-2\nu}{2(1-\nu)}\left\{\frac{1}{2}x_1\ln\frac{(x_1-L)^2+x_2^2}{(x_1+L)^2+x_2^2}\right.\right.$$
$$\left.\left.-\frac{1}{2}L\ln\left((x_1-L)^2+x_2^2\right)\left((x_1+L)^2+x_2^2\right)+2L\right\}\right]-\frac{\Omega_2}{2\pi}\left[x_1\{\varphi(x_1-L,x_2)-\varphi(x_1+L,x_2)\}\right.$$
$$\left.-L\{\varphi(x_1-L,x_2)+\varphi(x_1+L,x_2)\}+\frac{1-2\nu}{2(1-\nu)}x_2\frac{1}{2}\ln\frac{(x_1-L)^2+x_2^2}{(x_1+L)^2+x_2^2}\right], \tag{9.5c}$$

where $\varphi(x_1, x_2)$ is defined by (B2). Second we find the stress of the biaxial wedge disclination dipole from (5.12), setting $\Omega_1=\Omega_2=0$,

$$\sigma_{11}^D=\frac{G\Omega_3}{2\pi(1-\nu)}\left[\frac{1}{2}\ln\frac{(x_1-L)^2+x_2^2}{(x_1+L)^2+x_2^2}+\frac{x_2^2}{(x_1-L)^2+x_2^2}-\frac{x_2^2}{(x_1+L)^2+x_2^2}\right], \tag{9.6a}$$

$$\sigma_{22}^D=\frac{G\Omega_3}{2\pi(1-\nu)}\left[\frac{1}{2}\ln\frac{(x_1-L)^2+x_2^2}{(x_1+L)^2+x_2^2}+\frac{(x_1-L)^2}{(x_1-L)^2+x_2^2}-\frac{(x_1+L)^2}{(x_1+L)^2+x_2^2}\right], \tag{9.6b}$$

$$\sigma_{33}^D=\frac{G\Omega_3\nu}{2\pi(1-\nu)}\ln\frac{(x_1-L)^2+x_2^2}{(x_1+L)^2+x_2^2}, \tag{9.6c}$$

$$\sigma_{12}^D=-\frac{G\Omega_3x_2}{2\pi(1-\nu)}\left[\frac{x_1-L}{(x_1-L)^2+x_2^2}-\frac{x_1+L}{(x_1+L)^2+x_2^2}\right], \tag{9.6d}$$

$$\delta_{23}^D=0, \tag{9.6e}$$

$$\sigma_{31}^D=0. \tag{9.6f}$$

These results agree with the stress at large distances from a finite dislocation wall found by Li [12], except for a 90° rotation of the x_1x_2 plane.

Finally, to compare the finite with the infinitesimal dipole, we let the two basic disclinations approach each other. When $L\to 0$ in (9.5) the displacement of the finite dipole approaches

$$u_1^D\to\frac{2L\Omega_1x_3}{4\pi(1-\nu)}\left[(1-2\nu)\frac{x_1}{\rho^2}-2\frac{x_1x_2^2}{\rho^4}\right]+\frac{2L\Omega_2x_3}{4\pi(1-\nu)}\left[(1-2\nu)\frac{x_2}{\rho^2}+2\frac{x_1^2x_2}{\rho^4}\right]$$
$$-\frac{2L\Omega_3}{4\pi(1-\nu)}\left[(1-2\nu)\ln\rho+\frac{x_2^2}{\rho^2}\right], \tag{9.7a}$$

$$u_2^D\to-\frac{2L\Omega_2x_3}{4\pi(1-\nu)}\left[(1-2\nu)\frac{x_2}{\rho^2}-2\frac{x_1^2x_2}{\rho^4}\right]+\frac{2L\Omega_2x_3}{4\pi(1-\nu)}\left[(1-2\nu)\frac{x_1}{\rho^2}+2\frac{x_1x_2^2}{\rho^4}\right]$$
$$-2L\Omega_3\left[\frac{\varphi}{2\pi}-\frac{x_1x_2}{4\pi(1-\nu)\rho^2}\right], \tag{9.7b}$$

$$u_3^D\to\frac{2L\Omega_1}{4\pi(1-\nu)}\left[(1-2\nu)\ln\rho+\frac{x_2^2}{\rho^2}\right]+2L\Omega_3\left[\frac{\varphi}{2\pi}-\frac{x_1x_2}{4\pi(1-\nu)\rho^2}\right]. \tag{9.7c}$$

These results agree with the displacement of the infinitesimal dipole (7.6) if we put $\xi_r=(2L, 0, 0)$. This was to be expected since this dipole is built up by confining the translation of the basic

disclination to the x_1 axis. Next we let $L \to 0$ in (9.6) and find that the stress of the finite wedge dipole approaches

$$\sigma_{11}^D \to -\frac{2L\,G\,\Omega_3}{2\pi(1-\nu)}\left[\frac{x_1}{\rho^2} - 2\,\frac{x_1 x_2^2}{\rho^4}\right], \tag{9.8a}$$

$$\sigma_{22}^D \to -\frac{2L\,G\,\Omega_3}{2\pi(1-\nu)}\left[\frac{x_1}{\rho^2} + 2\,\frac{x_1 x_2^2}{\rho^4}\right], \tag{9.8b}$$

$$\sigma_{33}^D \to -\frac{2L\,G\,\Omega_3 \nu}{2\pi(1-\nu)}\,2\,\frac{x_1}{\rho^2}, \tag{9.8c}$$

$$\sigma_{12}^D \to \frac{2L\,G\,\Omega_3}{2\pi(1-\nu)}\left[\frac{x_2}{\rho^2} - 2\,\frac{x_1^2 x_2}{\rho^4}\right]. \tag{9.8d}$$

These results should agree with the stress of the infinitesimal biaxial wedge disclination dipole, which we did not calculate in section 7. However, we noted there that the fields of such a dipole are the same as those of an edge dislocation. If we substitute the translation found above, $\xi_r = (2L, 0, 0)$, into (7.17) we find $b_l = (0, -2L\Omega_3, 0)$. Now (9.8) agrees with (3.19) with this particular value for the Burgers vector.

9.2 The Uniaxial Dipole

We find the *finite straight uniaxial disclination dipole* by moving the axis of each basic disclination in section 9.1 back to the x_3 axis. We shall sketch out how to get results for this case. In general the axis of a discrete disclination line is translated from the point x_r^0 to the point $x_r^{0'}$ by adding to it a discrete dislocation line whose dislocation density is given by, (II5.24),

$$\alpha_{pl}(\mathbf{r}) = \delta_p(L)\epsilon_{lqr}\Omega_q(x_r^0 - x_r^{0'}). \tag{9.9}$$

In our special case $x_r^{0'} = 0$, because we move the axis to the origin. For the positive disclination passing through $(L, 0, 0)$ and the negative through $(-L, 0, 0)$ parallel to the x_3 axis we find that the only nonvanishing components of $\delta_p(L)$ are

$$\delta_3(L) = \delta(x_1 - L)\;\delta(x_2), \text{ at } x_r^0 = (L, 0, 0), \tag{9.10a}$$

$$\delta_3(L) = \delta(x_1 + L)\;\delta(x_2), \text{ at } x_r^0 = (-L, 0, 0). \tag{9.10b}$$

by a coordinate translation of (A15). Hence, we find that the only nonvanishing components of the additional dislocations (9.9) are

$$\alpha_{32}^A = \Omega_3 L[\delta(x_1 - L) + \delta(x_1 + L)]\delta(x_2), \tag{9.11a}$$

$$\alpha_{33}^A = -\Omega_2 L[\delta(x_1 - L) + \delta(x_1 + L)]\delta(x_2). \tag{9.11b}$$

We now find the dislocation density from

$$\alpha_{pl}^L = \alpha_{pl}^D + \alpha_{pl}^A\,. \tag{9.12}$$

Note the change in sign between this relation and (7.12). Relation (9.12) gives the dislocation density of the finite uniaxial disclination dipole if α_{pl}^D is given by (9.1), but also of the corresponding dislocation model if α_{pl}^D is given by (9.3). The disclination density of the uniaxial dipole remains the

same as for the biaxial dipole, (9.2) or (9.4). The additional dislocations (9.11) are also illustrated in figures 13–14.

The static fields of the uniaxial dipole can be found simply by adding the fields of the dislocations (9.11) to the fields of the biaxial dipole in section 9.1. The procedure is straightforward and we leave the details to the reader.

10. The Compensated Disclination Line

As discussed in section II10 the compensated disclination line is obtained by eliminating the dislocation loop density, (II10.1),

$$\beta^*_{kl}=0, \tag{10.1}$$

from the defect surface S that spans the disclination line L. We shall illustrate this for our special case of a straight disclination. There are of course many possible choices for the surface S. We shall choose two of them, first the one already used and illustrated in figure 1, and second the semi-infinite x_2x_3 plane for positive x_2.

From (10.1) and (4.5) we see that the plastic strain also vanishes, (II10.3),

$$e^P_{kl}=0. \tag{10.2}$$

With the choice for S as in figure 1 the disclination loop density remains the same as before, (4.4), and becomes the plastic bend-twist, (II10.4). So it has the only nonvanishing components

$$\kappa^P_{2q}=\varphi^*_{2q}=\Omega_q H(-x_1)\delta(x_2). \tag{10.3}$$

The defect densities of the compensated disclination are in general given by, (II10.5),

$$\alpha_{pl}(\mathbf{r})=\delta_{pl}\delta_k(S)\Omega_k-\delta_l(S)\Omega_p, \tag{10.4}$$

$$\theta_{pq}(\mathbf{r})=\delta_p(L)\Omega_q. \tag{10.5}$$

For our special case we find the only nonvanishing components

$$\alpha_{11}=-\Omega_2 H(-x_1)\delta(x_2), \tag{10.6a}$$

$$\alpha_{12}=\Omega_1 H(-x_1)\delta(x_2), \tag{10.6b}$$

$$\alpha_{32}=\Omega_3 H(-x_1)\delta(x_2), \tag{10.6c}$$

$$\alpha_{33}=-\Omega_2 H(-x_1)\delta(x_2), \tag{10.6d}$$

$$\theta_{3q}=\Omega_q\delta(x_1)\delta(x_2), \tag{10.7}$$

where we have used (A15–16). The compensated disclination consists of the same disclination line along L as the corresponding discrete disclination, given by (4.12), and a constant dislocation distribution over the surface S, which is opposite to that of the dislocation model, given by (8.4). The latter distribution is a simple rotation wall, as we saw. The components α_{12} and α_{32} represent tilt walls, while the components α_{11} and α_{33} represent a twist wall.

For consistency it can be verified that (10.1–3) and (10.6–7) satisfy the definitions (4.13–14), as well as the relations (4.15–16). It is also easily verified that the continuity conditions (4.17–18) are satisfied by (10.6–7), in agreement with (II10.7–8).

The incompatibility tensor is found by substituting (10.6–7) into (4.30) and we find

$$\eta_{pq}=0. \tag{10.8}$$

In general we know that the total displacement and elastic strain vanish for the compensated disclination line, (II10.11–12),

$$u_n^T=0, \tag{10.9}$$

$$e_{kl}=0. \tag{10.10}$$

The last result (10.10) is consistent with (10.8), because the incompatibility is the source of elastic strain. Since the elastic strain vanishes we see by Hookes' law that the stress also vanishes. The only elastic field that does not vanish is the elastic bend-twist. It is in general given by, (II10.13),

$$\kappa_{kq}=-\kappa_{kq}^P, \tag{10.11}$$

and for our special case has the only non-vanishing components

$$\kappa_{2q}=-\Omega_q H(-x_1)\,\delta(x_2), \tag{10.12}$$

by (10.3).

We note that if we add the results of the compensated disclination to those of the dislocation model in section 8 we get the results for the disclination line in sections 4–5, as we already pointed out for the general case in section II10. For example, we have, symbolically, (10.1) + (8.2) = (4.3), (10.3) + (8.1) = (4.4), (10.6) + (8.4) = (4.11), (10.7) + (8.5) = (4.12), (10.8) + (8.6) = (4.31), and (10.12) + (8.10) = (5.9).

We now investigate the other choice for the surface S, namely the semi-infinite plane lying in the x_2x_3 plane for positive x_2 and with a normal in the negative x_1 direction. This geometry can easily be obtained by rotating the plane S of figure 1 clockwise by 90°. Then the only nonvanishing component of $\delta_p(S)$ becomes

$$\delta_1(S)=-\delta(x_1)\,H(x_2), \tag{10.13}$$

instead of (A16). Hence from (4.2) the only nonvanishing components of the plastic bend-twist and disclination loop densities become

$$\kappa_{1q}^P=\varphi_{1q}^*=\Omega_q\,\delta(x_1)\,H(x_2), \tag{10.14}$$

instead of (10.3). Furthermore from (10.4) the only nonvanishing components of the dislocation density now become

$$\alpha_{21}=\Omega_2\,\delta(x_1)\,H(x_2), \tag{10.15a}$$

$$\alpha_{31}=\Omega_3\,\delta(x_1)\,H(x_2), \tag{10.15b}$$

$$\alpha_{22}=-\Omega_1\,\delta(x_1)\,H(x_2), \tag{10.15c}$$

$$\alpha_{33}=-\Omega_1\delta(x_1)\,H(x_2), \tag{10.15d}$$

instead of (10.6). Finally the elastic bend-twist is also changed according to (10.11) and (10.14). All other relations remain the same for either choice of the surface S.

11. The Bent Dislocation Wall

In section 10 we found the fields of the compensated disclination for two different choices of the defect surface S. If we take the difference between the results for these two geometries all the fields vanish, except the plastic and elastic bend-twist, the disclination loop density, and the dislocation density. The latter becomes from (10.6) and (10.15)

$$\alpha_{11} = \Omega_2 H(-x_1)\, \delta(x_2), \tag{11.1a}$$

$$\alpha_{21} = \Omega_2 \delta(x_1)\, H(x_2), \tag{11.1b}$$

$$\alpha_{31} = \Omega_3 \delta(x_1)\, H(x_2), \tag{11.1c}$$

$$\alpha_{12} = -\Omega_1 H(-x_1)\, \delta(x_2), \tag{11.1d}$$

$$\alpha_{22} = -\Omega_1 \delta(x_1)\, H(x_2), \tag{11.1e}$$

$$\alpha_{32} = -\Omega_3 H(-x_1)\, \delta(x_2), \tag{11.1f}$$

$$\alpha_{13} = 0, \tag{11.1g}$$

$$\alpha_{23} = 0, \tag{11.1h}$$

$$\alpha_{33} = -\Omega_1 \delta(x_1)\, H(x_2) + \Omega_2 H(-x_1)\, \delta(x_2). \tag{11.1i}$$

What kind of defect is this? It represents two semi-infinite dislocation walls that meet at the x_3 axis, i.e., it is bent dislocation wall. It has no long range stress or elastic strain. The three different cases are illustrated in figures 15–17, where for clarity we have shown the discrete rather than the constant dislocation distribution. Figures 15–16 show the geometry that has been observed by Schober and Baluffi [13], their figures 6 and 7.

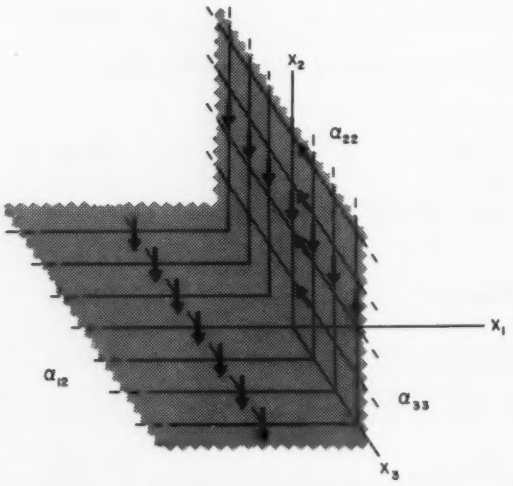

FIGURE 15. *The bent dislocation wall with Ω_1 rotation, described by the dislocation density $\alpha_{12} = -\Omega_1 H(-x_1)\, \delta(x_2)$ and $\alpha_{22} = \alpha_{33} = -\Omega_1 \delta(x_1) H(x_2)$.*

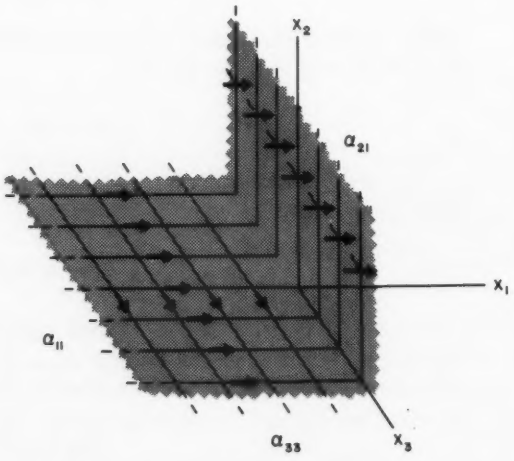

FIGURE 16. *The bent dislocation wall with Ω_2 rotation, described by the dislocation density $\alpha_{11} = \alpha_{33} = \Omega_2 H(-x_1)\, \delta(x_2)$ and $\alpha_{21} = \Omega_2 \delta(x_1) H(x_2)$.*

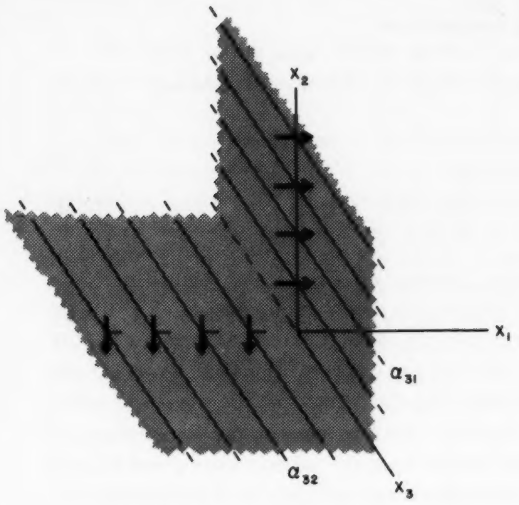

FIGURE 17. *The bent dislocation wall with Ω_3 rotation, described by the dislocation density $\alpha_{31}=\Omega_3\delta(x_1)H(x_2)$ and $\alpha_{32}=-\Omega_3 H(-x_1)\delta(x_2)$.*

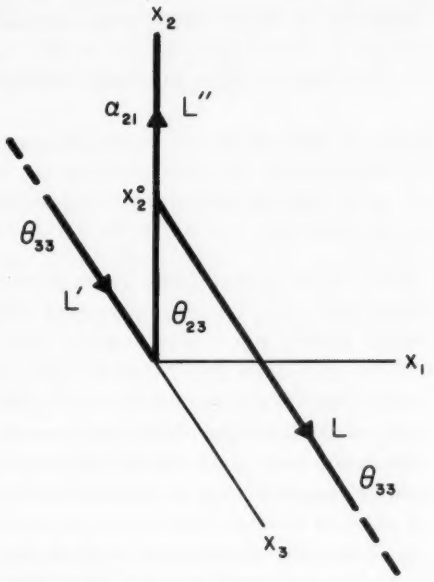

FIGURE 18. *Edge dislocation terminating at a jog on a wedge disclination.*

12. Example of a Terminating Dislocation

In a recent publication [14] we gave a concrete example of a discrete edge dislocation terminating on a jog in a discrete wedge disclination. We claimed that example illustrated the continuity equation (4.17). In this section we give a detailed analysis of the geometry of this example. Then we can verify the continuity equation for this case explicitly.

We have already derived the general expressions for a discrete dislocation terminating on a discrete disclination. The defect densities are given by, (II5.25–26),

$$\alpha_{pl}(\mathbf{r})=\delta_p(L)\{b_l+\epsilon_{lqr}\Omega_q(x_r-x_r^0)\}+\delta_p(L')\{b_l+\epsilon_{lqr}\Omega_q(x_r-x_r^{0\prime})\}+\delta_p(L'')\epsilon_{lqr}\Omega_q(x_r^0-x_r^{0\prime}.), \tag{12.1}$$

$$\theta_{pq}(\mathbf{r})=\delta_p(L+L')\Omega_q. \tag{12.2}$$

Here the disclination line lies along the closed curve L and L', and the dislocation line lies along the connecting link L''.

We choose the special case illustrated in figure 18. We set $b_l=x_r^{0\prime}.=0$, and for Ω_q and x_r^0 we choose the only nonvanishing components Ω_3 and $x_2^0>0$. Furthermore we choose for L a line parallel to the positive x_3 axis passing through the point $(0, x_2^0, 0)$, for L' the negative x_3 axis and the small jog on the positive x_2 axis, running from the origin to x_2^0, and for L'' the rest of the positive x_2 axis beyond x_2°. Then the only nonvanishing components of the delta functions in (12.1–2) are

$$\delta_3(L)=\delta(x_1)\delta(x_2-x_2^0)H(x_3), \tag{12.3a}$$

$$\delta_2(L')=\delta(x_1)H(x_2)H(x_2^0-x_2)\delta(x_3), \tag{12.3b}$$

$$\delta_3(L')=\delta(x_1)\delta(x_2)H(-x_3), \tag{12.3c}$$

$$\delta_2(L'')=\delta(x_1)H(x_2-x_2^0)\delta(x_3). \tag{12.3d}$$

Therefore we find for (12.1–2) the only nonvanishing components

$$\alpha_{21} = -\Omega_3 x_2\, \delta(x_1)\, H(x_2)\, H(x_2^0 - x_2)\, \delta(x_3) - \Omega_3 x_2^0\, \delta(x_1)\, H(x_2 - x_2^0)\, \delta(x_3), \tag{12.4}$$

$$\theta_{23} = \Omega_3\, \delta(x_1)\, H(x_2)\, H(x_2^0 - x_2)\, \delta(x_3), \tag{12.5a}$$

$$\theta_{33} = \Omega_3\, \delta(x_1)\, \delta(x_2 - x_2^0)\, H(x_3) + \Omega_3\, \delta(x_1)\, \delta(x_2)\, H(-x_3). \tag{12.5b}$$

where we have used (A8). These relations represent a wedge disclination with a jog near the origin from which an edge dislocation emerges. Specifically, the disclination consists of a straight wedge disclination approaching the origin along the negative x_3 axis, (the second term in (12.5b)), a small jog of twist disclination running along the x_2 axis from the origin to x_2^0, (12.5a), and a straight wedge disclination running parallel to the positive x_3 axis from the point x_2^0 on the x_2 axis, (the first term of (12.5b)). The dislocation consists of the following: The first term of (12.4) represents a dislocation that grows linearly in strength along the x_2 axis from the origin to the point x_2^0, and can be regarded as an integral part of the element of discrete twist disclination. The second term of (12.4) is an edge dislocation running along the positive x_2 axis starting from the point x_2^0. From (12.4) this edge dislocation has the Burgers vector

$$b_1 = -\Omega_3 x_2^0. \tag{12.6}$$

Note that the effect of the terminating dislocation is to move the disclination as well as its axis from $x_2 = 0$ for L' to $x_2 = x_2^0$ for L.

Now we shall show that (12.4–5) satisfy the continuity equations (4.17–18)

$$\alpha_{pl,p} + \epsilon_{lpq}\theta_{pq} = 0, \tag{12.7}$$

$$\theta_{pq,p} = 0. \tag{12.8}$$

We need only consider the cases $l = 1$ in (12.7) and $q = 3$ in (12.8), for all other cases are identically satisfied. We have for (12.7)

$$\begin{aligned}\alpha_{21,2} + \theta_{23} = &-\Omega_3\delta(x_1)\, H(x_2)\, H(x_2^0 - x_2)\, \delta(x_3) + \Omega_3 x_2\, \delta(x_1)\, H(x_2)\, \delta(x_2^0 - x_2)\, \delta(x_3) \\ &- \Omega_3 x_2^0\, \delta(x_1)\, \delta(x_2 - x_2^0)\, \delta(x_3) + \Omega_3\, \delta(x_1)\, H(x_2)\, H(x_2^0 - x_2)\, \delta(x_3) \\ = &\ 0,\end{aligned}$$

by (A6–7) and the assumption that $x_2^0 > 0$. We have for (12.8)

$$\begin{aligned}\theta_{23,2} + \theta_{33,3} = &\ \Omega_3\delta(x_1)\, \delta(x_2)\, H(_2^0 - x_2)\, \delta(x_3) - \Omega_3\delta(x_1)\, H(x_2)\, \delta(x_2^0 - x_2)\, \delta(x_3) \\ &+ \Omega_3\delta(x_1)\, \delta(x_2 - x_2^0)\, \delta(x_3) - \Omega_3\delta(x_1)\, \delta(x_2)\, \delta(x_3) \\ = &\ 0,\end{aligned}$$

similarly. So we have shown here by a detailed analysis that a dislocation can terminate on a disclination, and that this is consistent with the continuity equations.

13. Summary

We have specialized results derived for the general theory to the special case of straight disclination lines. First we recalled the work of Volterra and reviewed the straight dislocation to introduce the subject.

We derived the geometry of straight disclination lines. We found the defect loop densities which are the same as Mura's "plastic distortion" and "plastic rotation." They are concentrated on the defect surface, which is a semi-infinite plane terminating at the disclination line. Then we identified the basic plastic fields (plastic strain and bend-twist) which are also concentrated on the defect surface. We found the defect densities (dislocation and disclination) which are singular along the disclination line. We noted that there is a finite dislocation density for the discrete disclination line, and we gave it an intuitively reasonable interpretation. Our results agree completely with Anthony's. We checked the consistency of our specific results by showing that they satisfy the necessary general equations: the definitions of the defect densities in terms of the basic plastic fields, the relations between defect loops and densities, and the continuity conditions. We illustrated the significance of the total Burgers vector as the displacement jump at the origin by showing that it vanishes for our special choice, whereas the displacement jump condition gives a result that is intuitively clear from the illustrations. The incompatibility tensor was found and shown to satisfy its continuity condition.

Then we found the isotropic static results for straight disclinations. The displacements of a straight disclination were written down. Our point of departure was to regard these expressions as an educated guess. By differentiating we found the total distortion. From this total distortion the basic total fields (strain and bend-twist) can be derived. They consist of two types of terms: the first terms are singular on the defect surface and correspond exactly to the basic plastic fields derived independently above and the second terms are continuous away from the singular disclination line. This then provides a natural separation of the basic fields into elastic and plastic parts. In this manner we found the elastic strain and bend-twist of a straight disclination line. We showed that they satisfied the field equations with the defect densities. The stress followed from Hooke's law. It satisfied the equilibrium equations, including at the singular defect line, thus confirming that the original displacements were correct.

Then we showed how the fields were modified when the disclination axis was moved away from the origin. The dislocation density and total Burgers vector were changed whereas the disclination density and Frank vector remained the same. The results can be interpreted by saying that the axis is moved by adding a dislocation to the disclination line. This observation facilitates finding the static fields of the disclination with the new axis. The fields are found by adding those for a dislocation to those for a disclination with its axis thru the origin.

We derived results for the infinitesimal disclination dipole, which can be biaxial or uniaxial. We found the defect densities and displacements of both types and the relations between them. We noted that the displacement of the straight uniaxial dipole does not contain a wedge component. Therefore the static fields of the straight biaxial wedge disclination dipole are the same as those of a straight edge dislocation, confirming a result published by Eshelby.

The dislocation model of a straight disclination was found to be a terminating dislocation wall (tilt and twist). We found that the dislocation model and its corresponding disclination line have the same incompatibility tensor, displacement, total distortion, elastic strain, and stress. The total distortion contains terms that are singular on the defect surface, which correspond exactly to the dislocation loop density derived independently before. If these terms are identified as the plastic distortion, as Mura did, the dislocation model follows. In this way we found the interpretation of Mura's "elastic distortion" of the discrete disclination as the elastic distortion of the corresponding dislocation model. Finally we interpreted Mura's "plastic rotation" as the difference in bend-twist between the disclination and its dislocation model.

Next we found the defect densities of the finite disclination dipole. It was also possible to construct the dislocation model for this defect. The displacement of the biaxial dipole was found. It

approaches the displacement of the infinitesimal dipole when the width of the dipole approaches zero. The stress of the biaxial wedge disclination dipole was found to correspond to an earlier calculation of Li for the finite dislocation wall.

We found the defect densities for the compensated disclination line, using two different defect surfaces. From these results we constructed the bent dislocation wall, which has been observed by Schober and Baluffi. These defects have no displacement, elastic strain, or stress.

Finally we showed in analytical detail how a discrete edge dislocation can end on a jog in a discrete wedge disclination. The jog is a small segment of twist disclination line, which contains a finite amount of dislocation density. We showed that the analytic results satisfy the continuity conditions.

In appendix A we show how the general Dirac delta functions for a curve and a surface, which are defined for and occur in the general theory, are specialized to the case of a straight line and a semi-infinite plane. It is essential to know this type of specialization in order to apply the general theory to particular geometries. We also calculate some useful Burgers circuit integrals.

In appendix B we show how to take the generalized derivatives of the cylindrical coordinates. We carefully define the cylindrical angle φ in terms of the Cartesian Coordinates x_1 and x_2, restricting it to the range $(-\pi, \pi)$. Its derivative is regarded as a generalized derivative and contains a delta function. Also functions whose degree of homogeneity is -1 or less will have generalized functions in their generalized derivatives. The usefulness of these generalized function techniques is that they allow us to carry through the traditional field operations, such as differentiation, even at singular lines and surfaces, in the field theoretic framework that is traditionally set up for continuous well-behaved functions only. This simplifies the work for discrete defects considerably, since we can apply straightforward mathematical techniques at the singularities, instead of intuitive notions as is done classically.

In appendix C we show how the isotropic general results of III can be used to find the functional dependence of the static fields for straight discrete defects.

14. Appendix A. Evaluation of the Delta Function on a Straight Line and a Semi-Infinite Plane

The Dirac delta function $\delta(x)$ is defined by, (IIB1),

$$\int_a^b \delta(x-x')\varphi(x')\,dx' = \begin{cases} 0, & \text{if } x < a, \\ \varphi(x), & \text{if } a < x < b, \\ 0, & \text{if } b < x. \end{cases} \tag{A1}$$

This relation is illustrated by the following special cases

$$\int_{-\infty}^{\infty} \delta(x-x')\,dx' = 1, \tag{A2}$$

$$\int_0^{\infty} \delta(x-x')\,dx' = H(x), \tag{A3}$$

$$\int_{-\infty}^{0} \delta(x-x')\,dx' = H(-x), \tag{A4}$$

where we have introduced the Heaviside function defined by

$$H(x) \equiv \begin{cases} 0, & \text{if } x < 0, \\ 1, & \text{if } 0 < x. \end{cases} \tag{A5}$$

The derivative of the Heaviside function is easily found from (A3) by a partial integration

$$
\begin{aligned}
H'(x) &= \frac{\partial H(x)}{\partial x} \\
&= \int_0^\infty \frac{\partial}{\partial x}\delta(x-x')\,dx' \\
&= -\int_0^\infty \frac{\partial}{\partial x'}\delta(x-x')\,dx' \\
&= -[\delta(x-x')]_0^\infty \\
&= \delta(x),
\end{aligned} \tag{A6}
$$

since $\delta(x)=0$ whenever $x\neq 0$. From (A1) we see that we also have

$$
\delta(x-x')\varphi(x')=\delta(x-x')\varphi(x). \tag{A7}
$$

A particular case of this relation is

$$
(x-x')\delta(x-x')=0. \tag{A8}
$$

By differentiating this relation we find

$$
(x-x')\delta'(x-x')=-\delta(x-x'). \tag{A9}
$$

The three-dimensional Dirac delta function $\delta(\mathbf{r})$ is defined by, (IIB2),

$$
\delta(\mathbf{r}-\mathbf{r}') \equiv \delta(x_1-x_1')\delta(x_2-x_2')\delta(x_3-x_3'). \tag{A10}
$$

The Dirac delta functions for a curve L and a surface S are defined by, (IIB4–5),

$$
\delta_i(L) \equiv \int_L \delta(\mathbf{r}-\mathbf{r}')\,dL_i', \tag{A11}
$$

$$
\delta_i(S) \equiv \int_S \delta(\mathbf{r}-\mathbf{r}')\,dS_i'. \tag{A12}
$$

We want to evaluate these quantities for the special case when L is the straight line lying along the x_3 axis and S is the semi-infinite plane lying in the x_1x_3 plane for negative x_1 and with a normal in the negative x_2 direction, as illustrated in figure 1. Then we have in particular for L

$$
\begin{aligned}
dL_i' &= (0, 0, dL_3') = (0, 0, dx_3'), \\
\mathbf{r}' &= (0, 0, x_3'),
\end{aligned} \tag{A13}
$$

and for S

$$
\begin{aligned}
dS_i' &= (0, dS_2', 0) = (0, -dx_1'dx_3', 0), \\
\mathbf{r}' &= (x_1', 0, x_3').
\end{aligned} \tag{A14}
$$

We find that the only nonvanishing components of (A11–12) are

$$
\delta_3(L)=\int_{-\infty}^{\infty}\delta(x_1)\delta(x_2)\delta(x_3-x_3')dx_3'
$$

$$= \delta(x_1)\delta(x_2), \tag{A15}$$

$$\delta_2(S) = -\int_{-\infty}^{\infty}\int_{-\infty}^{0} \delta(x_1 - x_1')\delta(x_2)\delta(x_3 - x_3')dx_1'dx_3'$$
$$= -H(-x_1)\delta(x_2), \tag{A16}$$

where we have used (A2) and (A4). We note that these results satisfy Stokes' theorem, (IIB26),

$$\epsilon_{ijk}\delta_{i,j}(S) = -\delta_k(L), \tag{A17}$$

by (A6). This was to be expected since L is the boundary of S. Next we want to consider some integrals along a curve λ that links L. We take the special case where λ is a circle of radius a in the x_1x_2 plane centered at the origin, also illustrated in figure 1. Then we have

$$x_1^2 + x_2^2 = a^2 \tag{A18}$$

on λ. We wish to evaluate three typical closed line integrals on λ involving generalized functions. The first one is

$$\oint_\lambda f(x_1)\delta(x_2)dL_1 = -\oint_\lambda f(x_1)\delta(x_2)x_2(a^2 - x_2^2)^{-1/2}dL_2$$
$$= 0, \tag{A19}$$

where we have used (A18) to change the variable of integration, and (A8). The second one is

$$\oint_\lambda f(x_1)\delta(x_2)dL_2 = \int_{-a}^{a} f([a^2 - x_2^2]^{1/2})\ \delta(x_2)dx_2 + \int_{a}^{-a} f(-[a^2 - x_2^2]^{1/2})\delta(x_2)dx_2$$
$$= f(a) - f(-a), \tag{A20}$$

where we have used (A18) and (A1). The third one is

$$\oint_\lambda f(x_1)\delta'(x_2)dL_2 = -\oint_\lambda f'(x_1)\delta(x_2)dL_1$$
$$= 0, \tag{A21}$$

by a partial integration and (A19). Finally, for the sake of consistency we wish to show that the results (A15–16) satisfy (IIB15). Let σ be the circular plane bounded by λ (fig. 1). Then we have from (A15)

$$\int_\sigma \delta_3(L)dS_3 = \int\int \delta(x_1)\delta(x_2)dx_1dx_2$$
$$= 1, \tag{A22}$$

by (A1). Next we have from (A16)

$$\oint_\lambda \delta_2(S)dL_2 = -\oint_\lambda H(-x_1)\delta(x_2)dL_2$$
$$= -H(-a) + H(a)$$
$$= 1, \tag{A23}$$

by (A20) and (A5). So these results agree with (IIB15).

15. Appendix B. Generalized Derivatives of Cylindrical Coordinates

The expressions that are differentiated in the text contain the cylindrical coordinates ρ and φ. The geometric relation of these coordinates to the Cartesian Coordinates x_1 and x_2 is illustrated in figure 5. The functional relation for ρ is

$$\rho(x_1, x_2) = (x_1^2 + x_2^2)^{1/2}. \tag{B1}$$

The relation for φ is customarily given as $\tan^{-1}(x_2/x_1)$. However, this leads to some ambiguity for two reasons: (1) The arctangent is usually taken to be restricted to its principal value, lying in the range $(-\pi/2, \pi/2)$, especially in integral formulas. (2) The angle φ is usually regarded to be multiple-valued, a procedure that conflicts with the assumption of uniqueness for the functions that occur in the general defect theory. Therefore we shall arbitrarily restrict φ to the range $(-\pi, \pi)$, so that it is uniquely defined everywhere, but possesses a discontinuity of 2π across the negative x_1 axis, as shown in figure 5. This choice is convenient for the calculations in the text, for then the discontinuity occurs at the semi-infinite plane S of appendix A (fig. 1). So the functional relation for φ is

$$\varphi(x_1, x_2) = \tan^{-1}(x_2/x_1) + \pi H(-x_1)[H(x_2) - H(-x_2)], \tag{B2}$$

where the arctangent is restricted to its principal value and the Heaviside function H is defined by (A5). We see that φ, so defined, assumes the values indicated in figure 5.

In order to maintain the necessary uniqueness when differentiating the discontinuous function φ, it becomes necessary to take the generalized derivative. The discontinuity will then lead to a generalized function, the Dirac delta function. We refer to Gel'fand and Shilov [8], chapter 1, section 2.2, for the detailed procedure on taking this generalized derivative. The result is

$$\varphi_{,1} = -x_2/\rho^2, \tag{B3}$$

$$\varphi_{,2} = x_1/\rho^2 + 2\pi H(-x_1)\delta(x_2). \tag{B4}$$

Intuitively, these results could have been anticipated. They contain the ordinary derivatives of the arctangent function plus a term having a delta function across the negative x_1 axis, which originates from the discontinuity of φ.

By contrast the generalized derivatives of ρ and $\ln \rho$ are the same as the straightforward classical ones. For the latter we have

$$(\ln \rho)_{,1} = x_1/\rho^2, \tag{B5}$$

$$(\ln \rho)_{,2} = x_2/\rho^2. \tag{B6}$$

Another function whose generalized and classical derivatives coincide is the following

$$\left(\frac{x_\alpha x_\beta}{\rho^2}\right)_{,\gamma} = -2\frac{x_\alpha x_\beta x_\gamma}{\rho^4} + \frac{x_\alpha \delta_{\beta\gamma} + x_\beta \delta_{\gamma\alpha}}{\rho^2}, \quad (\alpha, \beta, \gamma = 1, 2), \tag{B7}$$

where we have used the convention that Greek subscripts have the range 1, 2. When written out in full these equations are

$$\left(\frac{x_1^2}{\rho^2}\right)_{,1} = 2\frac{x_1 x_2^2}{\rho^4}, \qquad \left(\frac{x_1^2}{\rho^2}\right)_{,2} = -2\frac{x_1^2 x_2}{\rho^4},$$

$$\left(\frac{x_1 x_2}{\rho^2}\right)_{,1} = -2\frac{x_1^2 x_2}{\rho^4} + \frac{x_2}{\rho^2}, \qquad \left(\frac{x_1 x_2}{\rho^2}\right)_{,2} = -2\frac{x_1 x_2^2}{\rho^4} + \frac{x_1}{\rho^2},$$

508-076 O - 73 - 6

$$\left(\frac{x_2^2}{\rho^2}\right)_{,1} = -2\frac{x_1x_2^2}{\rho^4}, \qquad \left(\frac{x_2^2}{\rho^2}\right)_{,2} = 2\frac{x_1^2x_2}{\rho^4}.$$

The above derivatives (B5–7) are all locally integrable in the x_1x_2 plane, including the singularity at the origin. This is the reason why the generalized and classical functions coincide.

However, if we take further derivatives of (B7), the results (having a ρ^{-2} dependence) will no longer be locally integrable at the origin, because then the algebraic singularity has the same strength as the dimension of the space (i.e., 2). To maintain uniqueness it becomes again necessary to take the generalized derivative. We refer also to Gel'fand and Shilov [8], chapter III, section 3.3, for the detailed procedure on taking this type of generalized derivative. The results will contain expressions homogeneous of degree -2 (such as ρ^{-2}), which have to be regarded as generalized functions. One result is

$$\left(\frac{x_\alpha}{\rho^2}\right)_{,\beta} = \frac{\delta_{\alpha\beta}}{\rho^2} - 2\frac{x_\alpha x_\beta}{\rho^4} + \pi\delta_{\alpha\beta}\delta(\boldsymbol{\rho}), \tag{B8}$$

where we have defined the two-dimensional Dirac delta function

$$\delta(\boldsymbol{\rho}) = \delta(x_1)\delta(x_2). \tag{B9}$$

When (B8) is written out in full we have

$$\left(\frac{x_1}{\rho^2}\right)_{,1} = \frac{1}{\rho^2} - 2\frac{x_1^2}{\rho^4} + \pi\delta(\boldsymbol{\rho}), \qquad \left(\frac{x_1}{\rho^2}\right)_{,2} = -2\frac{x_1x_2}{\rho^4},$$
$$\left(\frac{x_2}{\rho^2}\right)_{,1} = -2\frac{x_1x_2}{\rho^4}, \qquad \left(\frac{x_2}{\rho^2}\right)_{,2} = \frac{1}{\rho^2} - 2\frac{x_2^2}{\rho^4} + \pi\delta(\boldsymbol{\rho}).$$

Another result is

$$\left(\frac{x_\alpha x_\beta x_\gamma}{\rho^4}\right)_{,\delta} = -4\frac{x_\alpha x_\beta x_\gamma x_\delta}{\rho^6} + \frac{x_\alpha x_\beta\delta_{\gamma\delta} + x_\alpha\delta_{\beta\delta}x_\gamma + \delta_{\alpha\delta}x_\beta x_\gamma}{\rho^4} + \frac{\pi}{4}(\delta_{\alpha\beta}\delta_{\gamma\delta} + \delta_{\gamma\alpha}\delta_{\beta\delta} + \delta_{\beta\gamma}\delta_{\alpha\delta})\delta(\boldsymbol{\rho}),$$

or, when written out in full

$$\left(\frac{x_1^3}{\rho^4}\right)_{,1} = -4\frac{x_1^4}{\rho^6} + 3\frac{x_1^2}{\rho^4} + \frac{3\pi}{4}\delta(\boldsymbol{\rho}), \qquad \left(\frac{x_1^3}{\rho^4}\right)_{,2} = -4\frac{x_1^3x_2}{\rho^6},$$
$$\left(\frac{x_1^2x_2}{\rho^4}\right)_{,1} = -4\frac{x_1^3x_2}{\rho^6} + 2\frac{x_1x_2}{\rho^4}, \qquad \left(\frac{x_1^2x_2}{\rho^4}\right)_{,2} = -4\frac{x_1^2x_2^2}{\rho^6} + \frac{x_1^2}{\rho^4} + \frac{\pi}{4}\delta(\boldsymbol{\rho}),$$
$$\left(\frac{x_1x_2^2}{\rho^4}\right)_{,1} = -4\frac{x_1^2x_2^2}{\rho^6} + \frac{x_2^2}{\rho^4} + \frac{\pi}{4}\delta(\boldsymbol{\rho}), \qquad \left(\frac{x_1x_2^2}{\rho^4}\right)_{,2} = -4\frac{x_1x_2^3}{\rho^6} + 2\frac{x_1x_2}{\rho^4},$$
$$\left(\frac{x_2^3}{\rho^4}\right)_{,1} = -4\frac{x_1x_2^3}{\rho^6}, \qquad \left(\frac{x_2^3}{\rho^4}\right)_{,2} = -4\frac{x_2^4}{\rho^6} + 3\frac{x_2^2}{\rho^4} + \frac{3\pi}{4}\delta(\boldsymbol{\rho}).$$

Further generalized derivatives can be taken similarly, leading to homogeneous generalized functions of degree -3. Two results we need are

$$\left(\frac{1}{\rho^2}\right)_{,\alpha} = -2\frac{x_\alpha}{\rho^4} - \pi\delta_{,\alpha}(\boldsymbol{\rho}), \tag{B11}$$

$$\left(\frac{x_\alpha x_\beta}{\rho^4}\right)_{,\alpha}=-4\frac{x_\alpha x_\beta x_\gamma}{\rho^6}+\frac{x_\alpha\delta_{\beta\gamma}+x_\beta\delta_{\gamma\alpha}}{\rho^4}-\frac{\pi}{4}(\delta_{\alpha\beta}\delta_{,\gamma}(\boldsymbol{\rho})+\delta_{\beta\gamma}\delta_{,\alpha}(\boldsymbol{\rho})+\delta_{\gamma\alpha}\delta_{,\beta}(\boldsymbol{\rho})). \tag{B12}$$

The latter equation written out in full is

$$\left(\frac{x_1^2}{\rho^4}\right)_{,1}=-4\frac{x_1^3}{\rho^6}+2\frac{x_1}{\rho^4}-\frac{3\pi}{4}\delta_{,1}(\boldsymbol{\rho}),\qquad \left(\frac{x_1^2}{\rho^4}\right)_{,2}=-4\frac{x_1^2x_2}{\rho^6}-\frac{\pi}{4}\delta_{,2}(\boldsymbol{\rho}),$$

$$\left(\frac{x_1x_2}{\rho^4}\right)_{,1}=-4\frac{x_1^2x_2}{\rho^6}+\frac{x_2}{\rho^4}-\frac{\pi}{4}\delta_{,2}(\boldsymbol{\rho}),\qquad \left(\frac{x_1x_2}{\rho^4}\right)_{,2}=-4\frac{x_1x_2^2}{\rho^6}+\frac{x_1}{\rho^4}-\frac{\pi}{4}\delta_{,1}(\boldsymbol{\rho}),$$

$$\left(\frac{x_2^2}{\rho^4}\right)_{,1}=-4\frac{x_1x_2^2}{\rho^6}-\frac{\pi}{4}\delta_{,1}(\boldsymbol{\rho}),\qquad \left(\frac{x_2^2}{\rho^4}\right)_{,2}=-4\frac{x_2^3}{\rho^6}+2\frac{x_2}{\rho^4}-\frac{3\pi}{4}\delta_{,2}(\boldsymbol{\rho}).$$

16. Appendix C. Derivation of Static Fields of a Straight Defect from the General Theory

In III we derived general expressions for the static fields in an infinitely extended isotropic body. We showed there that a condition on the plastic strain for the integrals to converge is that $e_{ij}^P(\mathbf{r})$ approaches zero faster than r^{-1} as $r\to\infty$. This condition is not satisfied for straight defect lines, as can be seen from (3.3) and (4.7). However, it is still possible to find the functional dependence of the static fields from the general formulas by ignoring infinite terms that appear in the integrations. The correctness of the resulting static fields can then be assessed by checking them in the general field theory, as is done in the text.

The general expressions that we shall use are the following: For a dislocation line, the displacement, (III4.21),

$$u_i^T(\mathbf{r})=\frac{1}{8\pi}\int_S\left[R_{,jjk}b_kdS_i'+R_{,jkk}b_idS_j'-\frac{1}{1-\nu}R_{,ijk}b_kdS_j'+\frac{\nu}{1-\nu}R_{,ijj}b_kdS_k'\right], \tag{C1}$$

and the elastic distortion, (III4.23),

$$\beta_{ij}(\mathbf{r})=\frac{b_l}{8\pi}\oint_L\left[R_{,lnn}\epsilon_{ijk}dL_k'+R_{,knn}\epsilon_{ikl}dL_j'+\left(\frac{R_{,ijk}}{1-\nu}-\delta_{ij}R_{,knn}\right)\epsilon_{klm}dL_m'\right]. \tag{C2}$$

For a disclination line with its axis through the origin, the displacement, (III6.10),

$$u_i^T(\mathbf{r})=\frac{1}{8\pi}\int_S\epsilon_{kmn}\Omega_mx_n'\left[R_{,ijk}dS_j'+R_{,jli}\delta_{ik}dS_j'-\frac{1}{1-\nu}R_{,ijk}dS_j'+\frac{\nu}{1-\nu}R_{,ijj}dS_k'\right], \tag{C3}$$

and the basic elastic fields, i.e., the elastic strain, (III6.11),

$$e_{ij}(\mathbf{r})=\frac{1}{8\pi}\oint_L\left[\epsilon_{lpq}\Omega_px_q'\left\{R_{,knn}(\epsilon_{ikl}dL_j')_{(ij)}+\left(\frac{R_{ijk}}{1-\nu}-\delta_{ij}R_{,knn}\right)\epsilon_{klm}dL_m'\right\}+R_{,nn}(\Omega_jdL_i')_{(ij)}\right.$$

$$\left.+\left(\frac{R_{,ij}}{1-\nu}-\delta_{ij}R_{,nn}\right)\Omega_mdL_m'\right], \tag{C4}$$

and the elastic bend-twist, (III6.14),

$$\kappa_{ij}(\mathbf{r})=\frac{1}{8\pi}\oint_L\left[\epsilon_{kpq}\Omega_px_q'\ \{R_{,klnn}dL_j'-\tfrac{1}{2}R_{,jlnn}dL_k'\}-R_{,knn}\epsilon_{ikl}\Omega_jdL_l'\right], \tag{C5}$$

508-076 O - 73 - 7

where

$$R=(X_iX_i)^{1/2}, \tag{C6}$$

$$X_i=x_i-x_i'. \tag{C7}$$

The expressions (C1–5) are line and surface integrals. For the special geometry of figure 1 the curve L is given by (A13)

$$dL_i'=(0,\,0,\,dL_3')=(0,\,0,\,dx_3'),\ \mathbf{r}'=(0,\,0,\,x_3'). \tag{C8}$$

Hence we have

$$R=(\rho^2+X_3^2)^{1/2}, \tag{C9}$$

$$\rho=(x_1^2+x_2^2)^{1/2}, \tag{C10}$$

by (B1). The surface S is given by (A14)

$$dS_i'=(0,\,dS_2',\,0)=(0,\,-dx_1'\,dx_3',\,0),\ \mathbf{r}'=(x_1',\,0,\,x_3'). \tag{C11}$$

Hence

$$R=(X_1^2+x_2^2+X_3^2)^{1/2}. \tag{C12}$$

We shall first investigate the line integrals. All the necessary results can in general be derived from differentiating the basic integrals $\int R dL_i'$ and $\int x_i' R dL_j'$. From (C8) the only non-vanishing components of these integrals are $\int R dL_3$ and $\int x_3' R dL_3'$. Since these integrals are along an infinite straight line they will diverge. So we first find the finite integral

$$\begin{aligned}\int_{-L+x_3}^{L+x_3} R dx_3' &= \int_{-L}^{L} R dX_3\\ &= [\tfrac{1}{2}\rho^2 \ln (X_3+R)+\tfrac{1}{2}x_3 R]_{-L}^{L}\\ &= \rho^2 \ln \frac{L+(\rho^2+L^2)^{1/2}}{\rho}+L(\rho^2+L^2)^{1/2}.\end{aligned} \tag{C13}$$

The integral we want is obtained when $L\to\infty$, but then the terms in (C13) containing L will also approach infinity. However, these terms can be regarded as constants in the subsequent differentiations. Therefore they do not contribute to the fields and we can ignore them for practical purposes. So the functional dependence of the desired integral goes as

$$\int_L R dL_3' \to q, \tag{C14}$$

where we have defined the function

$$q\equiv -\rho^2 \ln \rho. \tag{C15}$$

The justification for this procedure can also be given as follows: A sufficiently high derivative of (C13) will converge for $L\to\infty$ to a finite function of ρ. The same derivative of (C15) will give the

same finite function. Now the relations (C1–5) contain only derivatives of integrals such as $\int R dL_i$. Therefore we can use (C14–15) in them directly. We find the functional dependence of the other integral in the same way. First we find the finite integral

$$\int_{-L+x_3}^{L+x_3} x_3' R dx_3' = \int_{-L}^{L} (x_3 - X_3) R dX_3$$

$$= \left[\tfrac{1}{2} x_3 \rho^2 \ln (X_3 + R) + \tfrac{1}{2} x_3 X_3 R - \tfrac{1}{3} R^3 \right]_{-L}^{L}, \tag{C16}$$

and hence, comparing with (C13),

$$\int_L x_3' R dx_3' \to x_3 q. \tag{C17}$$

We now consider the surface integrals. All the necessary results can in general be obtained from $\int R dS_i'$ and $\int x_i' R dS_j'$. From (C11) the only nonvanishing components are $\int R dS_2'$, $\int x_1' R dS_2'$, and $\int x_3' R dS_2'$. The derivation of the first integral may be indicated as follows

$$\int_S R dS_2' \to -\int_{-L}^{L} \int_{-L}^{0} R dx_1' dx_3' \to \int_{-L}^{0} (X_1^2 + x_2^2) \ln (X_1^2 + x_2^2)^{1/2} dx_1' \to \int_{x_1}^{L} (X_1^2 + x_2^2) \ln (X_1^2 + x_2^2)^{1/2} dX_1$$

$$= \left[(\tfrac{1}{3} X_1^3 + X_1 x_2^2) \ln (X_1^2 + x_2^2)^{1/2} - \tfrac{2}{3} x_2^3 \tan^{-1} \frac{x_2}{x_1} - (\tfrac{1}{9} X_1^3 + \tfrac{2}{3} X_1 x_2^2) \right]_{x_1}^{L} \tag{C18}$$

Here the first result follows from the geometry of the surface S in figure 1, the second by integration over x_3' which goes through the same as above but with R given by (C12) instead of (C9), and the third by a change of variable. So the functional dependence becomes

$$\int_S R dS_2' \to g, \tag{C19}$$

where we have defined the function

$$g \equiv -(\tfrac{1}{3} x_1^3 + x_1 x_2^2) \ln \rho + \tfrac{2}{3} x_2^3 \varphi + (\tfrac{1}{9} x_1^3 + \tfrac{2}{3} x_1 x_2^2). \tag{C20}$$

The next integral goes as

$$\int_S x_1' R dS_2' \to \int_{-L}^{0} x_1' (X_1^2 + x_2^2) \ln (X_1^2 + x_2^2)^{1/2} dx_1'$$

$$\to \int_{x_1}^{L} (x_1 - X_1) (X_1^2 + x_2^2) \ln (X_1^2 + x_2^2)^{1/2} dX_1. \tag{C21}$$

This leads to the functional dependence

$$\int_S x_1' R dS_2' \to h, \tag{C22}$$

where we have defined the function

$$h \equiv x_1 g + \tfrac{1}{4}\rho^4 \ln \rho + \tfrac{1}{16} x_1^4 - \tfrac{1}{8} x_1^2 x_2^2. \tag{C23}$$

The last integral goes as

$$\int_S x_3' R dS_2' \to -\int_{-L}^{L} \int_{-L}^{0} x_3' R dx_1' dx_3' \to x_3 g. \tag{C24}$$

The functions q, g, and h depend only on x_1 and x_2. The derivatives of q that we shall need are the following

$$q_{,11} = -2 \ln \rho - 1 - 2 \frac{x_1^2}{\rho^2}, \tag{C25a}$$

$$q_{,12} = -2 \frac{x_1 x_2}{\rho^2}, \tag{C25b}$$

$$q_{,22} = -2 \ln \rho - 1 - 2 \frac{x_2^2}{\rho^2} \tag{C25c}$$

$$q_{,\alpha\alpha} = -4 (\ln \rho + 1), \tag{C25d}$$

$$q_{,111} = -2 \frac{x_1}{\rho^2} - 4 \frac{x_1 x_2^2}{\rho^4}, \tag{C25e}$$

$$q_{,112} = -2 \frac{x_2}{\rho^2} + 4 \frac{x_1^2 x_2}{\rho^4}, \tag{C25f}$$

$$q_{,122} = -2 \frac{x_1}{\rho^2} + 4 \frac{x_1 x_2^2}{\rho^4}, \tag{C25g}$$

$$q_{,222} = -2 \frac{x_2}{\rho^2} - 4 \frac{x_1^2 x_2}{\rho^4}, \tag{C25h}$$

$$q_{,1\alpha\alpha} = -4 \frac{x_1}{\rho^2}, \tag{C25i}$$

$$q_{,2\alpha\alpha} = -4 \frac{x_2}{\rho^2}, \tag{C25j}$$

$$q_{,11\alpha\alpha} = -4 \left(\frac{1}{\rho^2} - 2 \frac{x_1^2}{\rho^4} + \pi \delta(\boldsymbol{\rho}) \right), \tag{C25k}$$

$$q_{,12\alpha\alpha} = 8 \frac{x_1 x_2}{\rho^4}, \tag{C25l}$$

$$q_{,22\alpha\alpha} = -4 \left(\frac{1}{\rho^2} - 2 \frac{x_2^2}{\rho^4} + \pi \delta(\boldsymbol{\rho}) \right). \tag{C25m}$$

Here the Greek indices range only over 1 and 2. The results (C25k–m) follow from (B8). The other derivatives we shall need are

$$g_{,112} = -2 \frac{x_1 x_2}{\rho^2}, \tag{C26a}$$

$$g_{,122}=-2\left(\ln\rho+\tfrac{1}{2}+\frac{x_2^2}{\rho^2}\right), \tag{C26b}$$

$$g_{,222}=4\varphi+2\frac{x_1x_2}{\rho^2}, \tag{C26c}$$

$$g_{,1\alpha\alpha}=-4(\ln\rho+1), \tag{C26d}$$

$$g_{,2\alpha\alpha}=4\varphi, \tag{C26e}$$

$$h_{,122}=-2x_1\ln\rho+4x_2\varphi-\tfrac{3}{2}x_1, \tag{C27a}$$

$$h_{,222}=6x_2\ln\rho+4x_1\varphi+6x_2+\tfrac{1}{2}x_2, \tag{C27b}$$

$$h_{,1\alpha\alpha}=-4x_1\ln\rho+4x_2\varphi-x_1, \tag{C27c}$$

$$h_{,2\alpha\alpha}=4x_2\ln\rho+4x_1\varphi+6x_2-\tfrac{1}{2}x_2. \tag{C27d}$$

The displacement of the dislocation (C1) now reduces to

$$u_i^T=\frac{1}{8\pi}\left[g_{,\alpha\alpha\beta}b_\beta\delta_{i2}+g_{,2\alpha\alpha}b_i-\frac{1}{1-\nu}g_{,i2\alpha}b_\alpha+\frac{\nu}{1-\nu}g_{,i\alpha\alpha}b_2\right]. \tag{C28}$$

The individual components are

$$u_1^T=-\frac{b_1}{8\pi}\left[\frac{1}{1-\nu}g_{,112}-g_{,2\alpha\alpha}\right]-\frac{b_2}{8\pi}\left[\frac{1}{1-\nu}g_{,122}-\frac{\nu}{1-\nu}g_{,1\alpha\alpha}\right], \tag{C29a}$$

$$u_2^T=-\frac{b_1}{8\pi}\left[\frac{1}{1-\nu}g_{,122}-g_{,1\alpha\alpha}\right]-\frac{b_2}{8\pi}\left[\frac{1}{1-\nu}g_{,222}-\frac{2-\nu}{1-\nu}g_{,2\alpha\alpha}\right], \tag{C29b}$$

$$u_3^T=\frac{b_3}{8\pi}g_{,2\alpha\alpha}, \tag{C29c}$$

which give (3.12) by (C26), except for some trivial constants. The elastic distortion of the dislocation (C2) reduces to

$$\beta_{\alpha\beta}=\frac{b_\lambda}{8\pi}\left[\epsilon_{\alpha\beta}q_{,\lambda\nu\nu}+\epsilon_{\kappa\lambda}\left(\frac{q_{\alpha\beta\kappa}}{1-\nu}-\delta_{\alpha\beta}q_{,\kappa\nu\nu}\right)\right], \tag{C30a}$$

$$\beta_{\alpha 3}=\frac{b_3}{8\pi}\epsilon_{\alpha\beta}q_{,\beta\lambda\lambda}, \tag{C30b}$$

$$\beta_{3j}=0, \tag{C30c}$$

where $\epsilon_{\alpha\beta}$ is the two dimensional permutation symbol, i.e., $\epsilon_{11}=\epsilon_{22}=0$, $\epsilon_{12}=-\epsilon_{21}=1$. The non-vanishing components of (C30) are

$$\beta_{11}=-\frac{b_1}{8\pi}\left[\frac{q_{,112}}{1-\nu}-q_{,2\nu\nu}\right]+\frac{b_2}{8\pi}\left[\frac{q_{,111}}{1-\nu}-q_{,1\nu\nu}\right], \tag{C31a}$$

$$\beta_{21}=-\frac{b_1}{8\pi}\left[\frac{q_{,122}}{1-\nu}+q_{,1\nu\nu}\right]+\frac{b_2}{8\pi}\left[\frac{q_{,112}}{1-\nu}-q_{,2\nu\nu}\right], \tag{C31b}$$

$$\beta_{12}=-\frac{b_1}{8\pi}\left[\frac{q_{,122}}{1-\nu}-q_{,1\nu\nu}\right]+\frac{b_2}{8\pi}\left[\frac{q_{,112}}{1-\nu}+q_{,2\nu\nu}\right], \tag{C31c}$$

$$\beta_{22}=-\frac{b_1}{8\pi}\left[\frac{q_{,222}}{1-\nu}-q_{,2\nu\nu}\right]+\frac{b_2}{8\pi}\left[\frac{q_{,122}}{1-\nu}-q_{,1\nu\nu}\right], \tag{C31d}$$

$$\beta_{13}=\frac{b_3}{8\pi}q_{,2\nu\nu}, \tag{C31e}$$

$$\beta_{23}=-\frac{b_3}{8\pi}q_{,1\nu\nu}, \tag{C31f}$$

which give (3.14) by (C25). The displacement of the disclination (C3) reduces to

$$u_i^T=\frac{\Omega_3}{8\pi}\left[h_{,2\alpha\alpha}\delta_{i2}-\frac{1}{1-\nu}h_{,i22}+\frac{\nu}{1-\nu}h_{,i\alpha\alpha}\right]+\frac{\Omega_j}{8\pi}\epsilon_{ijl}h_{,2\alpha\alpha}$$

$$+\frac{\epsilon_{\alpha\beta}\Omega_\beta}{8\pi}\left[x_3g_{,\alpha\gamma\gamma}\delta_{i2}+x_3g_{,2\gamma\gamma}\delta_{i\alpha}-\frac{1}{1-\nu}(x_3g)_{,i2\alpha}+\frac{\nu}{1-\nu}(x_3g)_{,i\gamma\gamma}\delta_{\alpha 2}\right]. \tag{C32}$$

The individual components are

$$u_1^T=\frac{\Omega_1x_3}{8\pi}\left[\frac{1}{1-\nu}g_{,122}-\frac{\nu}{1-\nu}g_{,1\gamma\gamma}\right]-\frac{\Omega_2x_3}{8\pi}\left[\frac{1}{1-\nu}g_{,112}-g_{,2\gamma\gamma}\right]$$

$$-\frac{\Omega_3}{8\pi}\left[\frac{1}{1-\nu}h_{,122}-\frac{\nu}{1-\nu}h_{,1\alpha\alpha}\right], \tag{C33a}$$

$$u_2^T=\frac{\Omega_1x_3}{8\pi}\left[\frac{1}{1-\nu}g_{,222}-\frac{2-\nu}{1-\nu}g_{,2\gamma\gamma}\right]-\frac{\Omega_2x_3}{8\pi}\left[\frac{1}{1-\nu}g_{,122}-g_{,1\gamma\gamma}\right]$$

$$-\frac{\Omega_3}{8\pi}\left[\frac{1}{1-\nu}h_{,222}-\frac{2-\nu}{1-\nu}h_{,2\alpha\alpha}\right], \tag{C33b}$$

$$u_3^T=\frac{\Omega_1}{8\pi}\left[\frac{1}{1-\nu}g_{,22}-\frac{\nu}{1-\nu}g_{,\gamma\gamma}\right]-\frac{\Omega_2}{8\pi}\left[\frac{1}{1-\nu}g_{,12}+h_{,2\alpha\alpha}\right], \tag{C33c}$$

which give (5.1) by (C26–27), except for some trivial linear terms. The elastic strain of the disclination (C4) reduces to

$$e_{\alpha\beta}=-\frac{1}{8\pi}\left[\Omega_\gamma x_3\left(\frac{q_{,\alpha\beta\gamma}}{1-\nu}-\delta_{\alpha\beta}q_{,\gamma\nu\nu}\right)+\Omega_3\left(\frac{q_{,\alpha\beta}}{1-\nu}-\delta_{\alpha\beta}q_{,\nu\nu}\right)\right], \tag{C34a}$$

$$e_{\alpha 3}=\frac{1}{8\pi}\left[\Omega_\alpha q_{,\beta\beta}-\frac{1}{1-\nu}\Omega_\beta q_{,\alpha\beta}\right], \tag{C34b}$$

$$e_{33}=0. \tag{C34a}$$

The individual components are

$$e_{11}=-\frac{\Omega_1x_3}{8\pi}\left[\frac{q_{,111}}{1-\nu}-q_{,1\nu\nu}\right]-\frac{\Omega_2x_3}{8\pi}\left[\frac{q_{,112}}{1-\nu}-q_{,2\nu\nu}\right]+\frac{\Omega_3}{8\pi}\left[\frac{q_{,11}}{1-\nu}-q_{,\nu\nu}\right], \tag{C35a}$$

$$e_{22}=-\frac{\Omega_1 x_3}{8\pi}\left[\frac{q_{,122}}{1-\nu}-q_{,1\nu\nu}\right]-\frac{\Omega_2 x_3}{8\pi}\left[\frac{q_{,222}}{1-\nu}-q_{,2\nu\nu}\right]+\frac{\Omega_3}{8\pi}\left[\frac{q_{,22}}{1-\nu}-q_{\nu\nu}\right], \tag{C35b}$$

$$e_{33}=0, \tag{C35c}$$

$$e_{12}=-\frac{\Omega_1 x_3}{8\pi}\frac{q_{,112}}{1-\nu}-\frac{\Omega_2 x_3}{8\pi}\frac{q_{,122}}{1-\nu}+\frac{\Omega_3}{8\pi}\frac{q_{,12}}{1-\nu}, \tag{C35d}$$

$$e_{23}=-\frac{\Omega_1}{8\pi}\frac{q_{,12}}{1-\nu}-\frac{\Omega_2}{8\pi}\left[\frac{q_{,22}}{1-\nu}-q_{,\nu\nu}\right], \tag{E35e}$$

$$e_{31}=-\frac{\Omega_1}{8\pi}\left[\frac{q_{,11}}{1-\nu}-q_{,\nu\nu}\right]-\frac{\Omega_2}{8\pi}\frac{q_{,12}}{1-\nu}, \tag{C35f}$$

which give (5.5) by (C25), except for some trivial constant terms. The elastic bend-twist of the disclination (C5) reduces to

$$\kappa_{\alpha\gamma}=\frac{\Omega_\gamma}{8\pi}\epsilon_{\alpha\beta}q_{,\beta\nu\nu}, \tag{C36a}$$

$$\kappa_{\alpha 3}=\frac{1}{8\pi}\left[\Omega_\gamma x_3\epsilon_{\beta\gamma}q_{,\alpha\beta\nu\nu}+\Omega_3\epsilon_{\alpha\beta}q_{,\beta\nu\nu}\right], \tag{C36b}$$

$$\kappa_{3\gamma}=0. \tag{C36c}$$

The individual components are

$$\kappa_{11}=\frac{\Omega_1}{8\pi}q_{,2\nu\nu}, \tag{C37a}$$

$$\kappa_{21}=-\frac{\Omega_1}{8\pi}q_{,2\nu\nu}, \tag{C37b}$$

$$\kappa_{31}=0, \tag{C37c}$$

$$\kappa_{12}=\frac{\Omega_2}{8\pi}q_{,2\nu\nu}, \tag{C37d}$$

$$\kappa_{22}=-\frac{\Omega_2}{8\pi}q_{,1\nu\nu} \tag{C37e}$$

$$\kappa_{32}=0, \tag{C37f}$$

$$\kappa_{13}=-\frac{\Omega_1 x_3}{8\pi}q_{,12\nu\nu}+\frac{\Omega_2 x_3}{8\pi}q_{,11\nu\nu}+\frac{\Omega_3}{8\pi}q_{,2\nu\nu}, \tag{C37g}$$

$$\kappa_{23}=-\frac{\Omega_1 x_3}{8\pi}q_{,22\nu\nu}+\frac{\Omega_2 x_3}{8\pi}q_{,12\nu\nu}-\frac{\Omega_3}{8\pi}q_{,1\nu\nu}, \tag{C37h}$$

$$\kappa_{33}=-\frac{\Omega_1}{8\pi}q_{,2\nu\nu}+\frac{\Omega_2}{8\pi}q_{,1\nu\nu}, \tag{C37i}$$

which give (5.9) by (C25).

17. References

[1] de Wit, R., in Fundamental Aspects of Dislocation Theory (NBS Spec. Publ. 317), Ed. by J. A. Simmons, R. de Wit, and R. Bullough (U.S. Government Printing Office, Washington, 1970), p. 651. In this paper referred to as I.
[2] de Wit, R., J. Res. Nat. Bur. Stand. (U.S.), **77A** (Phys. and Chem.), No. 1, 49–100 (Jan.–Feb. 1973). In this paper referred to as II.
[3] de Wit, R., J. Res. Nat. Bur. Stand. (U.S.), **77A** (Phys. and Chem.), No. 3, 359–368 (May–June 1973). In this paper referred to as III.
[4] Volterra, V., Annls. scient. Ec. norm. sup., Paris [3], **24**, 400 (1907).
[5] Love, A. E. H., A Treatise on the Mathematical Theory of Elasticity, 3rd ed. (Cambridge U. P., 1920).
[6] Frank, F. C., Disc. Faraday Soc. **25**, 19 (1958).
[7] Nabarro, F. R. N., Theory of Crystal Dislocations (Clarendon Press, Oxford, 1967).
[8] Gel'fand, I. M., and Shilov, G. E., Generalized Functions, Vol. **I** (Academic Press, New York, 1964).
[9] Mura, T., Arch. Mech. Stos. **24**, 449 (1972).
[10] Anthony, K. H., Arch. Rat. Mech. Anal. **39**, 43 (1970).
[11] Eshelby, J. D., Brit. J. Appl. Phys. **17**, 1131 (1966).
[12] Li, J. C. M., Acta Met. **8**, 563 (1960).
[13] Schober, T., and Baluffi, R. W., phys. stat. sol. (b) **44**, 115 (1971).
[14] de Wit, R., J. Appl. Phys. **42**, 3304 (1971).

(Paper 77A5–787)

JOURNAL OF RESEARCH of the National Bureau of Standards—A. Physics and Chemistry
Vol. 77A, No. 5, September–October 1973

Optical Properties of *U* Centers in Alkali Halides and Alkaline Earth Fluorides

Herbert S. Bennett

Institute for Materials Research, National Bureau of Standards, Washington, D.C. 20234

(May 1, 1973)

The two-electron orbitals for the *U* center have been computed numerically from the Hartree-Fock-Slater (HFS) equations in the point-ion lattice potential. The lattice relaxation of the nearest-neighbor ions is included in the model. The five lowest-lying *U*-center states for NaCl, KCl, CdF_2, CaF_2, SrF_2, and BaF_2 are given. The low-lying singlet states have the following order for increasing values of the energy: $^1S(1s, 1s)$, $^1P(1s, 2p)$, and $^1S(1s, 2p)$. The energy levels for the triplet states $^3S(1s, 2s)$, and $^3P(1s, 2p)$ lie between the energy levels for the $^1S(1s, 1s)$ and $^1P(1s, 2p)$ states. The ordering of the triplet states depends upon the host crystal and the lattice relaxation. The predictions based upon the numerical HFS wave functions are compared with the predictions based upon past variational wave functions and with experiment.

Key words: BaF_2; CaF_2; ionic polarization; KCl; Mollwo-Ivey relations; NaCl; point-ion potential; SrF_2; *U* centers.

1. Introduction

The *U* center in ionic crystals consists of a negative-hydrogen ion H^-, located substitutionally at an anion site. Because the H^- ion has a different mass, polarizability, and interaction with its neighboring ions than has the anion which it replaces, the *U* center changes both the phonon spectrum and the optical properties of its host crystal. Changes in the phonon spectrum include new features at energies substantially greater than the energies of the optic phonons of the host lattice [1–11].[1] Changes in the optical properties include a characteristic electronic absorption band, the *U* band, in the ultraviolet region [12–20] and are the concerns of this paper.

The author continues in this paper his calculations, reported in part in [21], on the several states of the *U* center in the two alkali halides, NaCl and KCl, and in the four alkaline earth fluorides, CdF_2, CaF_2, SrF_2, and BaF_2. Reference [21] contains discussions which stress the *U* band transition energies between the singlet ground and first excited states. The author now reports his results on the spatial extent of the *U*-center orbitals, on the transition energies between the first and second excited singlet states, and on the transition energies between the two lowest-lying truplet states. A point-ion lattice model is used which incorporates the Hartree-Fock-Slater (HFS) procedure to compute numerically the defect electron orbitals. The model includes estimates for the correlation energy of the singlet states [22], for the exchange energy of the triplet states [23], and for the lattice relaxation of the nearest-neighbor ions. The model also obeys completely the Franck-Condon principle that the lattice relaxation does not respond to rapid changes in the electronic state of the *U* center when the *U* center undergoes an optical transition. This means that all low-lying *U*-center states should have spatially compact electron orbitals, if the predictions of the model are to be internally consistent with its assumptions.

The present point-ion model has some limitations. Its numerical wave functions are not orthogonal to the electronic states of neighboring ions and thereby do not account properly for the finite size of the neighboring ions, particularly when the lattice relaxes. An extended-ion model which uses numerical wave functions instead of variational wave functions for the defect electron orbitals has not been reported. Such a calculation would require an amount of com-

[1] Figures in brackets indicate the literature references at the end of this paper.

puter time which is substantially greater than that required by Wood and Opik [18]. These authors solved extended-ion models by using trial wave functions with two variational parameters and by devising accurate approximations for efficiently computing Coulomb and exchange integrals. Their methods use Slater-type functions and are not applied readily to the present numerical procedures.

Keeping the above limitations in mind, we shall calculate here within the framework of the above model the energy levels of the three lowest-lying singlet states and the two lowest-lying triplet states. In some cases, these triplet states are degenerate or very nearly degenerate.

Because expressions for the change in energy of a classical point-ion lattice with lattice relaxation of the neighboring ions and expressions for the total energy of the U center when the two electrons are in singlet and triplet states appear in sections 2 and 3 of [21], they are not repeated here. In section 2 of the present paper, the equations for absorption are given. Section 3 contains a discussion of the results and some remarks on the validity of point-ion models. Finally, the appendix contains a summary of the many assumptions upon which the HFS equations are based.

2. Absorption

Because no emission bands have been associated with the U center [18], we shall study only the optical absorption which the defect electrons may undergo.

The initial state of an optical transition is a relaxed state, $|\eta_i;\ \sigma_i>$. The symbol η denotes an electronic configuration of the two defect electrons which transforms as one of the following states, $^1S(1s,\ 1s)$, $^3S(1s,\ 2s)$, $^3P(1s,\ 2p)$, $^1P(1s,\ 2p)$, and $^1S(1s,\ 2s)$. The quantity σ characterizes the lattice relaxation; i.e., the n nearest-neighbor ions of the U center may move radially to the sites $\vec{r}_\nu' = \vec{r}_\nu\ (1-\sigma)$ for $1 \leq \nu \leq n$. All other ions remain at their perfect lattice sites $\vec{r}_\nu$. We minimize $E_T(\eta_i;\ \sigma)$ with respect to the lattice relaxation σ to obtain the energy of the initial state $E_i = E_T(\eta_i;\ \sigma_i)$. The value σ_i is that value of σ for which $E_T(\eta_i;\ \sigma_i)$ attains its minimum value. The U center then undergoes an optical transition to an unrelaxed state $|\eta_f;\ \sigma_i>$, which has an electronic wave function calculated for the same distortion σ_i as that for the initial state $|\eta_i;\ \sigma_i>$. The total energy of the final state is $E_f = E_T(\eta_f;\ \sigma_i)$. The optical absorption energy for a transition from state i to state f is

$$E(i,f) = E_T(\eta_f;\ \sigma_i) - E_T(\eta_i;\ \sigma_i), \tag{1}$$

where each term on the right-hand side of eq (1) is a negative number.

The expectation value of a given power of the radial coordinate r gives us information on the spatial extent of the two-defect-electron wave functions. As a measure of the spatial extent, the author chooses to consider the first and third powers of r for each of the orbitals; namely,

$$r_{nl}[s,\ \eta(nl;\ n'l');\ \sigma] = \bar{r_1}^s \int R_{nl}(r) r^s R_{nl}(r) 4\pi r^2 dr \tag{2}$$

and

$$r_{n'l'}[s;\ \eta(nl;\ n'l');\ \sigma] = \bar{r_1}^s \int R_{n'l'}(r) r^s R_{n'l'}(r) 4\pi r^2 dr, \tag{3}$$

where $s=1$ or $s=3$ and r_1 is the nearest-neighbor distance of the perfect lattice. The principal and orbital quantum numbers for the radial wave functions $R_{nl}(r)$ are respectively n and l. The ratio,

$$r_e(nl) = [r_{nl}(s=3)/r_{nl}(s=1)], \tag{4}$$

also indicates to what extent the radial functions have extended tails. The values of $r_e < 1$ indicate compact states, and values of $r_e > 1$ indicate diffuse states.

3. Results and Conclusions

In this section, the results of the point-ion model with lattice relaxation are reported. Table 1 contains the values of the input data which have been used.

TABLE 1. Input data for the point-ion model of the U center with ionic polarization, exchange energy, and Coulomb-correlation energy. The Pauling factor of the νth and μth ions is $\beta_{\nu\mu}$. The ionic radius of the cation is ρ_+ and the anion is ρ_-. The quantity ρ, having the units of length, is the stiffness factor in the empirical Born-Mayer exponential form which characterizes the repulsive energy between the νth and μth ions. The Madelung potential constant at the anion site is α_M. The quantity $\bar{r}_1$ is the nearest-neighbor distance (anion-cation) for the NaCl structure and is the lattice constant (cation-cation) for the CaF_2 structure. The series coefficients C_4, C_6, and C_8 appear in the expansion in powers of the lattice distortion σ for the change in electrostatic energy E_1 which occurs when a cation moves in the background of a perfect point-ion lattice potential; namely, $E_1 = -(n/\bar{r}_1)\ (C_4\sigma^4 + C_6\sigma^6 + C_8\sigma^8 + \ldots)$, where n is the number of nearest-neighbor cations to an anion. The quantities β_{++}, β_{+-}, and β_{--}, and α_M are dimensionless. All other quantities are expressed in terms of atomic units (1 a.u. of energy = 27.2 eV = 4.36 attojoules and 1 a.u. of length = 0.0529 nm).

	NaCl	KCl	CdF_2	CaF_2	SrF_2	BaF_2
β_{++}	1.25	1.25	1.50	1.50	1.50	1.50
β_{+-}	1.00	1.00	1.125	1.125	1.125	1.125
β_{--}	0.75	0.75	0.75	0.75	0.75	0.75
ρ	[a] 0.599	[a] 0.637	0.582	[b] 0.546	[b] 0.560	[b] 0.582
ρ_+	[a] 2.21	[a] 2.77	2.76	[c] 2.21	[c] 2.48	[c] 2.76
ρ_-	[a] 3.00	[a] 3.00	1.98	[c] 1.98	[c] 1.98	[c] 1.98
α_M	1.748	1.748	4.071	4.071	4.071	4.071
$\bar{r}_1$	[a] 5.31	[a] 5.93	10.21	[c] 10.32	[c] 10.95	[c] 11.71
C_4	[d] 3.579	[d] 3.579	[e] 1.865	[e] 1.865	[e] 1.865	[e] 1.865
C_6	[d] 0.9895	[d] 0.9895				
C_8	[d] 2.942	[d] 2.942				

[a] M. P. Tosi, in Solid State Physics, edited by F. Seitz and D. Turnbull (Academic Press Inc., New York, 1964), Vol. XVI, p. 52.
[b] A. D. Franklin (private communication).
[c] G. C. Benson and E. Dempsey, Proc. Roy. Soc. (London) A266, 344 (1962).
[d] A. Scholz, Phys, Status Solidi 7, 973 (1964).
[e] H. S. Bennett, J. Res. Nat. Bur. Stand. (U.S.), 72A (Phys. and Chem.), No. 5, 471-474 (Sept.–Oct. 1968).

The numerical procedures give the energy eigenvalues to an accuracy of $|\Delta E/E| \approx 0.001$. They also give the self-consistent potential which appears in the HFS equations to an accuracy of $|\Delta V/V| \approx 0.01$, within the context of the point-ion model. The quantities ΔE and ΔV are, respectively, the changes in the trial eigenvalue and self-consistent potential which occur between two successive iterations in the numerical itegration procedure. The numerical details on the spatial extent of the five lowest-lying states of the U center are reported only for KCl and CaF_2 with no lattice relaxation. These two crystals are quantitatively representative of the remaining four crystals examined in this paper and illustrate respectively most of the salient features common to the NaCl-type and CaF_2-type structures. Succeeding tables do contain, however, the energy levels for the five lowest-lying states in all six crystals. The computed data for the case in which the lattice relaxation and the electron orbitals are determined in a self-consistent manner are to within about 30 percent qualitatively similar to the computed data presented in tables 2 and 3. The only exception to this is that the orbitals tend to be more compact when $\sigma > 0$ and that the orbitals tend to be more diffuse when $\sigma < 0$ than they are when $\sigma = 0$ (no lattice relaxation). Tables 2 and 3 contain the numerical predictions of the point-ion model for U centers in KCl and CaF_2 when the lattice relaxation is zero ($\sigma = 0$). These two tables show that the ordering of the singlet energy levels with increasing energy is $^1S(1s, 1s)$, $^1P(1s, 2p)$, and $^1S(1s, 2s)$. They also show that the energies of the triplet states $^3S(1s, 2s)$ and $^3P(1s, 2p)$ lie between the ground singlet state energy and the first-excited-singlet state energy. The energies of these two low-lying triplet states lie close together and may be nearly degenerate as in the case for KCl. In addition the ordering of these two triplet energy levels depends upon the crystal and upon the lattice relaxation. The results of [17] for the alkali halides predict the same ordering for the singlet energy levels. They also predict that the triplet $^3S(1s, 2s)$ and $^3P(1s, 2p)$ energy levels lie between the $^1S(1s, 1s)$ and $^1P(1s, 2p)$ energy levels. However, contrary to the present results, the results of [17] predict that the $^3S(1s, 2s)$ energy level lies below and is well spearated from the $^3P(1s, 2p)$ energy level. These differences among the ordering of variational states and numerical triplet states may be explained by either or both of two possibilities: First, the authors of [17] have estimated the exchange terms in a different manner than the present author. And second, the numerical wave functions are more "flexible" than two-parameter-variational wave functions. One measure of the flexibility of a wave function is its second order-spatial derivative. The latter is proportional to the kinetic energy. Variational functions introduce artificial bounds on the kinetic energy and for some self-consistent potentials predict lower energy levels and different orderings of the states than numerical functions.

Table 4 gives for the six crystals the predicted energy levels, U-band transition energies, the U-band oscillator strengths, and the lattice relaxation of the nearest-neighbor ions. The oscillator strengths f in

TABLE 2. The five lowest-lying states for KCl of the U center in the perfect point-ion lattice ($\sigma = 0$) with exchange energy and Coulomb correlation energy. For convenience, the states $^1S(1s, 1s)$, $^3P(1s, 2p)$, $^3S(1s, 2s)$, $^1P(1s, 2p)$, and $^1S(1s, 2s)$ are labeled A, B, C, D, and E, respectively, in this table. The total energy of state X is $E_T(X; \sigma = 0)$, where $X = A, B, C, D$, or E. The transition energy from state X to state Y is $E(X, Y)$. The quantities n and l are the principal and angular-momentum quantum numbers for the symmetry of the one-electron orbitals from which the U-center configuration is made. The spatial extent quantities $r_{nl}(s)$ and $r_e(nl)$ are dimensionless and the energies are expressed in terms of atomic units. (1 a.u. of energy = 27.2 eV = 4.36 attojoules.)

State	*A*	*B*	*C*	*D*	*E*
E_T	−1.015	−0.953	−0.957	−0.878	−0.856
$r_{nl}(1)$	0.565	.281	.285	.479	.531
$r_{nl}(3)$	.334	.057	.059	.234	.293
$r_e(nl)$	.590	.202	.208	.490	.551
$r_{n'l'}(1)$	.565	.857	.882	.881	.956
$r_{n'l'}(3)$	.334	.868	1.005	.929	1.915
$r_e(n'l')$	.590	1.012	1.140	1.054	2.002
$E(A, D)$	.137				
$E(D, E)$	.022				
$E(B, C)$	.004				

TABLE 3. The five lowest-lying states for CaF_2 of the U center in the perfect point-ion lattice ($\sigma = 0$) with exchange energy and Coulomb correlation energy. The notation in this table is the same as the notation given in table 2.

State	*A*	*B*	*C*	*D*	*E*
E_T	−1.204	−1.072	−1.047	−0.999	−0.960
$r_{nl}(1)$	0.626	0.374	0.372	.559	.553
$r_{nl}(3)$	.435	.123	.120	.340	.330
$r_e(nl)$	.694	.328	.323	.607	.597
$r_{n'l'}(1)$	.626	.940	1.079	.986	1.516
$r_{n'l'}(3)$	.435	1.268	2.180	1.455	1.608
$r_e(n'l')$	.694	1.350	2.021	1.476	4.012
$E(A, D)$	.205				
$E(D, E)$	.039				
$E(B, C)$	.025				

TABLE 4. Energy levels and U-band transition energies for absorption from the $^1S(1s, 1s)$ state to the $^1P(1s, 2p)$ state for the U center. The lattice relaxation and Coulomb correlation are included. The initial state is $^1S(1s, 1s)$ and $\sigma = \sigma_i$. The value of σ remains the same for the final state $^1P(1s, 2p)$. For convenience, the states $^1S(1s, 1s)$ and $^1P(1s, 2p)$ are labeled A and D, respectively, in this table. The total energy of the state X is $E_T(X; \sigma)$, where $X = A$ or D. The U-band energy is $E(A, D)$. The experimental value for the U-band energy is $E(A, D;$ expt). The theoretical oscillator strength is f. The quantities σ_i and f are dimensionless. All other quantities are in atomic units. (1 a.u. of energy = 27.2 eV = 4.36 attojoules.)

Substance	σ_i	f	$E_T(A, \sigma_i)$	$E_T(D; \sigma_i)$	$E(A, D)$	$E(A, D,$ expt)
NaCl	0.041	1.90	−1.087	−0.914	0.173	[a] 0.238
KCl	.060	1.90	−1.023	−.870	.153	[a] .213
CdF_2	.050	1.94	−1.221	−.987	.234	
CaF_2	.060	1.94	−1.221	−.985	.236	[b] .281
SrF_2	.057	1.94	−1.177	−.960	.217	[b] .259
BaF_2	.065	1.94	−1.138	−.937	.201	[b] .221

[a] J. W. Schulman and W. D. Compton, Color Centers in Physics (The Macmillan Company, New York, 1962).
[b] J. H. Beaumont et al., J. of Physics C **3**, L153 (1970).

table 4 agree reasonably well with other theoretical calculations [1, 16, 21].

Referring to tables 4 and 5, we observe that including the lattice relaxation of the nearest-neighbor ions increases the predicted U-band transition energies. Nevertheless, the point-ion model with lattice relaxation still yields values for the U-band energies which are smaller than the observed values. Table 6 shows that these results are consistent with the other results predicted by point-ion models based upon variational wave functions.

One possible explanation for the energy levels of the singlet states in the present work lying above the corresponding energy levels in variational theories is given in [21].

Tables 7 and 8 give the energy levels and transition energies for absorption respectively from the $^1P(1s, 2p)$ state to the $^1S(1s, 2s)$ state and from the $^3P(1s, 2p)$ state to the $^3S(1s, 2s)$ state.

TABLE 5. Energy levels and U-band transition energies for absorption from the $^1S(1s, 1s)$ state to the $^1P(1s, 2p)$ state for the U center with no ionic polarization. Because $\sigma = 0$, the lattice relaxation is zero. The Coulomb correlation is included. The initial state is $^1S(1s, 1s)$ and $\sigma = \sigma_i = 0$. For convenience, the states $^1S(1s, 1s)$ and $^1P(1s, 2p)$ are labeled A and D, respectively, in this table. The total energy of the state X is $E_T(X; \sigma)$, where $X = A$ or D. The U-band energy is $E(A, D)$. The experimental value for the U-band energy is $E(A, D;$ expt). The quantity σ_i is dimensionless. All other quantities are in atomic units. (1 a.u. of energy = 27.2 eV = 4.36 attojoules.)

Substance	σ_i	$E_T(A; \sigma_i)$	$E_T(D; \sigma_i)$	$E(A, D)$	$E(A, D;$ expt)
NaCl	0.0	−1.082	−0.921	0.161	[a] 0.238
KCl	.0	−1.015	−.878	.137	[a] 0.213
CdF_2	.0	−1.211	−1.003	.208	
CaF_2	.0	−1.204	−0.999	.205	[b] 0.281
SrF_2	.0	−1.162	−0.972	.190	[b] 0.259
BaF_2	.0	−1.117	−0.943	.174	[b] 0.221

[a] J. W. Schulman and W. D. Compton, Color Centers in Physics (The Macmillan Company, New York, 1962).
[b] J. H. Beaumont et al., J. of Physics C **3**, L153 (1970).

TABLE 6. Comparisons among various theoretical values and experimental values for the U-band transition energies. This is the transition from the $^1S(1s, 1s)$ state to the $^1P(1s, 2p)$ state. All energies are in atomic units (1 a.u. of energy = 27.2 eV = 4.36 attojoules).

Substance	Experiment	Ref. a	Ref. b	Ref. c	Ref. d	Ref. e	Present work (Table 4)
NaCl	[f] 0.238			0.203	0.202		0.173
KCl	[f] .213	0.205	0.219	.178	.178		153
CdF_2							.234
CaF_2	[g] .281					0.251	.236
SrF_2	[g] .259					.234	.217
BaF_2	[g] .221					.217	.201

[a] R. F. Wood and U. Öpik, Phys. Rev. **162**, 736 (1967); first model.
[b] R. F. Wood and U. Öpik, Phys. Rev. **162**, 736 (1967); second model.
[c] H. N. Spector et al., J. Chem. Phys. **46**, 2676 (1967).
[d] B. S. Gourary, Phys. Rev. **112**, 337 (1958).
[e] R. S. Singh et al., J. Chem. Phys. **52**, 2341 (1970).
[f] J. W. Schulman and W. D. Compton, Color Centers in Physics (The Macmillan Company, New York, 1962).
[g] J. H. Beaumont et al., J. of Physics C **3**, L153 (1970).

TABLE 7. Energy levels and second singlet transition energies for absorption from the $^1P(1s, 2p)$ state to the $^1S(1s, 2s)$ state for the U center. The lattice relaxation and Coulomb correlation are included. The initial state is $^1P(1s, 2p)$ and $\sigma = \sigma_i$. The value of σ remains the same for the final state $^1S(1s, 2s)$. For convenience, the states $^1P(1s, 2p)$ and $^1S(1s, 2s)$ are labeled D and E, respectively. The total energy of the state X is $E_T(X; \sigma)$, where $X = D$ or E. The second singlet transition energy is $E(D, E)$. The quantity σ_i is dimensionless. All other quantities are in atomic units. (1 a.u. of energy = 27.2 eV = 4.36 attojoules.)

Substance	σ_i	$E_T(D; \sigma_i)$	$E_T(E; \sigma_i)$	$E(D, E)$
NaCl	−0.011	−0.921	−0.894	0.028
KCl	.000	−.878	−0.856	0.022
CdF_2	−.082	−1.010	−1.010	0.000
CaF_2	.000	−0.999	−0.960	0.039
SrF_2	.001	−.972	−0.935	0.037
BaF_2	.024	.945	−0.904	0.042

TABLE 8. Energy levels and first triplet transition energies for transitions from the $^3P(1s, 2p)$ state to the $^3S(1s, 2s)$ state for the U center. The lattice relaxation and exchange energy are included. The initial state is $^3P(1s, 2p)$ and $\sigma = \sigma_i$. The value of σ remains the same for the final state $^3S(1s, 2s)$. These states are labeled B and C, respectively, for convenience. The total energy of the state X is $E_T(X, \sigma)$, where $X = B$ or C. The first triplet transition energy is $E(B, C)$. The quantity σ_i is dimensionless. All other quantities are in atomic units. (1 a.u. of energy = 27.2 eV = 4.36 attojoules.)

Substance	σ_i	$E_T(B; \sigma_i)$	$E_T(C; \sigma_i)$	$E(B, C)$
NaCl	−0.006	−0.996	−0.992	0.004
KCl	0.004	−0.953	−0.957	−0.004
CdF_2	−0.014	−1.077	−1.057	0.021
CaF_2	0.009	−1.072	−1.044	0.029
SrF_2	0.006	−1.046	−1.026	0.020
BaF_2	0.028	−1.020	−1.004	0.017

A Mollwo-Ivey relation [24].

$$E = \alpha a^{-n},$$

with $n \approx 1.1$ relates the observed energies E at the peak of the U-band in many alkali halides to the lattice spacing a. However, the observed energies of the U-band peaks in the alkaline earth fluorides do not fit a Mollwo-Ivey empirically-derived ralation [20]. A similar situation occurs for the F-band peaks. A Mollwo-Ivey relation with $n \approx 1.84$ predicts quite well the locations of the F-band peaks in many NaCl-type alkali halides. But, such a relation does not predict the observed F-band peaks in the alkaline earth fluorides [20].

Point-ion models for the U-band which do not include lattice relaxation yield U-band energies which follow Mollwo-Ivey relations. The variational-point-ion theory of [17] predicts U-band energies for NaCl-type crystals which obey a Mollwo-Ivey relation with $n \approx 1.14$. The similar variational theory of [1] gives U-band energies for the alkaline earth fluorides which follow reasonably well a Mollwo-Ivey relation with $n \approx 1.143$. The present point-ion model in which the lattice relaxation and the coulomb correlation term $W(r)$ are zero predicts that the Mollwo-Ivey exponents are 1.22 for U-bands in NaCl and KCl and 1.31 for U-bands in the fluorides CdF_2, CaF_2, SrF_2, and BaF_2. When the Coulomb correlation term $W(r)$ in a point-ion model with no lattice relaxation is included, the Mollwo-Ivey exponents become, respectively, 1.46 and 1.33. The predicted Mollwo-Ivey exponents for the alkali halides which are obtained by variational methods are closer to the experimental values than those exponents which are obtained by the present numerical methods. However, when the lattice relaxation is included, then the predicted U-band energies for both the alkali halides and the fluorides do not follow Mollwo-Ivey relations.

The above results show that solving the HFS equations for the point-ion model of the U center by numerical techniques leads to a greater disagreement between theory and experiment for the U-band energies than does solving the point-ion model by variational techniques. Also, the Mollwo-Ivey exponent obtained from the numerical HFS wave functions differs more from the observed exponent for U-bands in the alkali halides than does the exponent obtained from the variational wave functions. These greater disagreements between the predictions of the numerical HFS wave functions and predictions of the variational wave functions for the point-ion model suggest that the past successes of the point-ion model have been fortuitous. More generally, the disagreement among the observed and computed values reported in this paper lead one to conclude that the point-ion models do not represent satisfactorily the properties of the U-center. The present work also emphasizes a need for models containing more detailed treatment of ionic polarization, electronic polarization, and the finite extent of the neighboring ions. Examples of two such models for the alkali halides appear in [18].

Whenever both of the U-center electrons have compact wave functions, the U center (proton, anion vacancy and two electrons) is essentially neutral. In this case, it would produce only small, long-range polarizations, if any. The existence of these conditions then would justify treating all ions as point charges. Hence, the point-ion model is a reasonable approximation for the case in which most of the charge associated with the U-center electrons is localized about the proton-anion vacancy site and remains outside the neighboring ionic cores. The defect electrons then would experience a potential which scales with the lattice constant and the predicted U bands would vary with the lattice constant, to a good approximation, according to a Mollow-Ivey relation.

The observed U bands in the alkali halides satisfy a Mollwo-Ivey relation; those in the alkaline earth fluorides do not. The failure of the observed U bands in the alkaline earth fluorides to obey a Mollwo-Ivey relation suggests the speculation that extended ion effects are more important in the alkaline earth fluorides than they are in the alkali halides. Extended ion effects include exchange and overlap among the U-center electrons and the core electrons of neighboring ions. These effects probably do not depend smoothly upon the lattice constant. It is interesting to notice in table 6 that most of the predicted U bands in the alkaline earth fluorides are closer to the observed values than the predicted U bands in the alkali halides. Nevertheless, using a point-ion model to describe the U center in the alkaline earth fluorides is more questionable than using a point-ion model to describe the U center in the alkali halides because the former class of U centers fails to follow a Mollwo-Ivey relation.

The author thanks A. D. Franklin for many helpful discussions. He also thanks the personnel of the Aspen Center for Physics, where portions of the manuscript were written, for their kind hospitality.

4. Appendix. Assumptions Contained in the HFS Equations

Because the Schrödinger equation for the two-electron U center,

$$H_T(\mathbf{x}, \mathbf{y}; \sigma)\ \Psi_\eta(x, y) = E\Psi_\eta(x, y),$$

cannot be solved exactly, we use the self-consistent field method [Hartree-Fock (HF)] to calculate the wave functions of the U center. The wave functions for the self-consistent field approximation are antisymmetrized sums of products of one-electron functions $u_1(r)$ and $u_2(r)$:

$$\Psi_\eta(x, y) \approx \Psi_\eta(x, y; HF)$$
$$= 2^{-1/2}\ [u_1(x)u_2(y) - u_1(y)u_2(x)].$$

The functions u have a restricted-central-field representation given by

$$u_{nlms} = R_{nl}(r) y_{lm}(\theta, \phi) \alpha_s,$$

where $R_{nl}(r)$ is the radial function, Y_{lm} is a spherical harmonic function, and α_s is the spin function. The principal, orbital, magnetic, and spin quantum numbers are, respectively, n, l, m, and s. The radial functions $P_{nl}(r)$, $P_{nl}(r) = rR_{nl}(r)$, are normalized to the crystal volume $\int P_{nl}^2(r)\, dr = 1$. The spherically averaged total electronic charge density for both spins in terms of the radial functions becomes

$$\rho_{av}(r) = -e[\sigma(r)/4\pi r^2],$$

where the spherical density $\sigma(r)$ is

$$\sigma(r) = \sum_{nl} \omega_{nl} P_{nl}^2(r),$$

and the occupation number of the spatial orbital for both spins is ω_{nl}. The summation $\Sigma_{nl}\omega_{nl}$ equals 2 for the U center.

In terms of the above assumptions, the Coulomb potential $V_c(r)$ for the HFS equations then has the form:

$$V_c(r) = \frac{e^2}{r}\int_0^r \sigma(t)dt + e^2 \int_r^\infty \frac{\sigma(t)}{t}\, dt.$$

Slater [23] suggests that the essential features of the HF method are retained when a common exchange potential replaces the exchange potentials for each of the orbitals u_1 and u_2. Applying his suggestion to the triplet states of the U center, we assume that the common exchange potential $V_e(r)$ for the U center at the point r is equal to the exchange potential which a free-electron gas would have if its total electron charge density for both spins were equal to that of the nonuniform system (the two U-center defect electrons): namely,

$$V_e(r) = -3e^2\, [(3/8\pi)\, e^{-1} |\rho_{av}(r)|]^{1/3}.$$

Let us define $V_s(r) = V_c(r) + V_e(r)$ for future use. The self-Coulomb energy part of the total electronic Coulomb energy cancels exactly in the conventional HF method a corresponding energy in the total exchange energy. This cancellation does not occur in the HFS equations at large r. We alter the sum $V_s(r)$ so that it has the correct asymptotic behavior at large r. We define $V(r) = V_c(r) + V_e(r)$ for $r < r_0$ and $V(r) = e^2(\Sigma_{nl}\omega_{nl} - 1)/r$ for $r \geq r_0$. The radius r_0 is that value of r at which

$$V_s(r_0) = e^2 \left(\sum_{nl} \omega_{nl} = 1 \right) / r_0.$$

The HF method also does not include the spatial correlation in the motion of the two defect electrons produced by their instantaneous Coulomb repulsion $H_c(\mathbf{x}, \mathbf{x})$. The approximate HF wave function is the source of this Coulomb correlation problem because it does not depend upon the distance between the two electrons $|\mathbf{x} - \mathbf{y}|$. We define the correlation energy by the relation

$$E_c = \langle \Psi_\eta(x, y) | H_T | \Psi_\eta(x, y) \rangle - \langle \Psi^\eta(x, y; HF) | H_T | \Psi_\eta(x, y; HF) \rangle.$$

Let us assume also that a correlation operator $\epsilon_c(|\mathbf{x} - \mathbf{y}|)$ exists such that its expectation value in the approximate representation $\Psi_\eta(\mathbf{x}, \mathbf{y}; HF)$ is the correlation energy

$$E_c = \langle \Psi_\eta(x, y; HF | \epsilon_c(|\mathbf{x} - \mathbf{y}|) | \Psi_\eta(x, y; HF) \rangle.$$

We may introduce, then, the correlation potential $W_c(r)$ by the following operation:

$$W_c(r) = \int d^3x \Psi_\eta(x, r; HF) \epsilon_c(|\mathbf{x} - \mathbf{r}|) \Psi_\eta(x, r; HF).$$

Mitler [22] adapts to atomic helium the free-electron gas approximation for the correlation energy. He introduces in the HF equations an additional central "correlation" potential $W(r)$ to which pairs of electrons with opposite spin are subject. The approximate correlation potential $W(r)$ has the form [22]

$$W(r) = -e^2 \frac{0.288}{5.1\, a_0 + r_s(r)},$$

where a_0 is the Bohr radius and the local density of electrons is

$$e^{-1}|\rho(r)| = [(4\pi/3)\, r_s^3(r)]^{-1}.$$

We expect that the expression for $W(r)$ is a good estimate for the correlation potential $W_c(r)$. Mitler [22] applies the expression for $W(r)$ to the ground state for helium and obtaines by perturbation theory a ground state energy which agrees to within $\frac{1}{2}$ percent of the experimental value. Our prescription is, then, to replace $V_c(r)$ in the singlet HFS variational equations with $V_c(r) + W(r)$. Because the inequality

$$0 \leq W(r_s)/V_{\text{exch}}(r_s) \leq 0.314 r_s/(5.1\, a_0 + r_s) \leq 0.314 r_s$$

is obtained, we do not include the Coulomb correlation potential in the triplet HFS variational equations.

5. References

[1] Singh, R. S., et al., J. Chem. Phys. **52**, 4341 (1970).
[2] Dötsch, H., and Mitra, S. S., Phys. Rev. **178**, 1492 (1969).
[3] Schulman, J. H., and Compton, W. Dale, Color Centers in Solids (The Macmillan Company, New York, 1962).
[4] Klein, M. V., in Physics of Color Centers, edited by W. Beall Fowler (Academic Press, New York, 1968).
[5] Bilz, H., et al., J. Phys. Suppl. **27**, C2 (1966).

[6] Mitra, S. S., and Singh, R. S., Phys. Rev. Letters **16,** 694 (1966).
[7] Wood, R. F., and Gilbert, R. L., Phys. Rev. **162,** 746 (1967).
[8] Hayes W., and Mac Donald, H. F., Proc. Roy Soc. (London) **A297,** 503 (1967).
[9] Elliot, R. J., et al., Proc. Roy. Soc. (London) **A289,** 1 (1966).
[10] Harrington, J. A., et al., (unpublished).
[11] Hall, J. L., and Schumacher, R. T., Phys. Rev. **127,** 1892 (1962).
[12] Hilsch, R., and Pohl, R., Trans. Faraday Soc. **34,** 883 (1938).
[13] Martienssen, W., Z. Physik **131,** 488 (1952).
[14] Baldini, G., et al., Phys. Rev. **140,** A2094 (1965).
[15] Mitra, S. S., and Brada, Y., Phys. Rev. **145,** 626 (1966).
[16] Gourary, B. S., Phys. Rev. **112,** 337 (1958).
[17] Spector, H. N., et al., J. Chem. Phys. **46,** 2676 (1967).
[18] Wood, R. F., and Öpik, U., Phys. Rev. **162,** 736 (1967).
[19] Sennett, C. T., J. Phys. Chem. Solids **26,** 1097 (1965).
[20] Beaumont, J. H., et al., J. Phys. C **3,** 152 (L) (1970).
[21] Bennett, H. S., Phys. Rev. B **6,** 3936 (1972).
[22] Mitler, H., Phys. Rev. **99,** 1835 (1955).
[23] Slater, J. C., Phys. Rev. **81,** 385 (1951).
[24] Ivey, R. F., Phys. Rev. **72,** 341 (1947).

(Paper 77A5–788)

JOURNAL OF RESEARCH of the National Bureau of Standards—A. Physics and Chemistry
Vol. 77A, No. 5, September–October 1973

Air Flow Rate as a Test For Gage Block Wringing

L. A. Guildner, R. L. Anderson*, and R. E. Edsinger

Institute for Basic Standards, National Bureau of Standards, Washington, D.C. 20234

(June 11, 1973)

Gage blocks can be joined by "wringing" to produce a vacuum-tight joint. Hoke gage blocks have square gaging surfaces with a central hole connecting them. The quality of the joints between blocks can be tested by measuring the vacuum leak rates through the joints into the central hole. When two Hoke blocks are in contact at one edge but tilted at an angle ϕ, the vacuum leak rate into a chamber of 22 cm^3 produces a rate of pressure increase which can be represented by the following polynomial:

$$dp/dt = 0.42 \quad \phi^2 + 0.022 \quad \phi^3 \ \mu\text{m Hg/min},$$

where ϕ is in μrad. Hoke blocks in suitable condition to be joined by wringing can also be joined by alining them and evacuating the joint through the center hole.

Key words: End length standards; gage blocks; joining; wringing; wring test.

1. Introduction

The lapped surfaces of gage blocks are ordinarily joined by greasing them very lightly and then pressing them together with a twisting and sliding motion known as "wringing." A similar joint can be made with fused silica surfaces (without grease) by techniques known as "optical contacting." The closeness of two surfaces joined by wringing is more reproducible than that produced by any other means of positioning except optical contacting. For this reason, joints made by wringing are used extensively for assembling end length standards and for other precise assemblies.

When components with lapped surfaces are constrained, however, wringing may not be a practical means for joining them. Typically, components being joined by wringing are free to aline themselves, and the drag of their relative motion is a fairly reliable indication of the quality of the joint. For constrained components, the possible motions for wringing may be insufficient for good joining, and the sensing of the drag may well be misleading. This arrangement exists with the NBS precision manometer, where the height of the mercury column is determined by a column of Hoke gage blocks, joined between the cell boss and its pedestal [1][1]. Because it was difficult to perform wringing, it became important to develop other means to produce the joints and to sense their reliability.[2]

2. Experimental Method

A tightly wrung joint between continuous, optically flat metal surfaces is "vacuum tight." It was decided, therefore, to investigate the rate of air flow from the ambient atmosphere into an evacuated small volume through the center hole of a Hoke block, as a function of the dihedral angle between it and a fused silica optical flat.[3]

Hoke gage blocks are end length standards of square cross-section, 2.41 cm on a side with an axial hole 0.67 cm in diameter running between the gaging faces. As used for the manometer, the holes of the gage blocks served for vacuum lines and were connected to lines incorporated in the pedestals of the manometer base. The remainder of the measuring system included a group of valves and a thermocouple gage (see fig. 1), with a total volume of 22 cm^3, which was small enough to allow good responses for the tests.

To determine the angle of tilt, we observed the number of fringes of the cadmium green line (508.582 nm) produced by a Fizeau interferometer that was formed by a fused silica optical flat wrung to one edge

*Formerly a member of the staff of the Heat Division at NBS. Present address: Physikalisch Technische Bundesanstalt, 33 Braunschweig, Bundesallee 100, West Germany.

[1] Figures in brackets indicate the literature reference at the end of this paper.

[2] Based on earlier measurements, a brief discussion of the techniques to be presented in this paper has appeared in the manometer paper.

[3] Clearly such a test will be useless if the surface is either heavily greased or discontinuous.

TABLE 1.

(1) Fringes	(2) Meas. time (seconds)	(3) Pressure increase (μm Hg)	(4) dp/dt (μm Hg/min)	(5) Cal. by eq (2)	(6) Dev.	(7) Order of meas.
1.00	46.2 46.5	50	64.9 64.5	56.5 56.5	8.4 8.0	17
1.05	45.5 46.3 46.3	50	65.9 64.8 64.8	64.1 64.1 64.1	1.8 0.7 0.7	15
1.08	46.4	50	64.7	68.9	−4.2	4
1.2	36.8	50	81.5	90.6	−9.1	5
1.2	30.1 30.7	50	99.7 97.7	90.6 90.6	9.1 7.1	10
1.3	21.6 21.3	50	138.9 140.8	111.5 111.5	27.4 29.3	9
1.75	20.2 20.0	100	297.0 300.0	242.4 242.4	54.6 57.6	14
1.9	18.4 18.6	100	326.1 322.6	301.0 301.0	25.1 21.6	3
2.0	18.9 18.8	100	317.5 319.1	344.7 344.7	−27.2 −25.6	16
2.05	17.6 17.9	100	340.9 335.2	368.0 368.0	−27.1 −32.8	13
2.2	12.8 12.7	100	468.8 472.4	443.8 443.8	25.0 28.6	8
2.5	18.6 19.2	200	645 625	624 624	21 1	12
2.5	17.2 17.6	200	698 682	624 624	74 58	2
2.6	15.4 15.3	200	779 784	694 694	85 90	7
3.05	28.3 29.5	400	848 814	1067 1067	−219 −253	11
3.05	30.5 24.7		787 972	1067 1067	−280 −95	11
3.1	23.0 23.0	400	1043 1043	1115 1115	−73 −73	1
3.3	15.4 15.9 15.9	400	1558 1509 1509	1321 1321 1321	237 188 188	6
0	3600	1.5	0.024	0	0	18

of the Hoke block. The illumination was provided by the optical system of a Saunders interferograph [2], whereby the green line was separated by a constant deviation prism and projected normal to the face of the Hoke block. The time for the pressure to increase by a selected amount from air flow into the evacuated system was measured for angles producing 1 to 3 fringes, and for a tightly wrung joint (see table 1).

Once a technique of measurement to test for wringing was established, it was also desired, if possible, to find an alternative technique for making the joints. Very lightly greased, dirt-free surfaces that were aligned and vacuum pumped, showed very low leak rates, and proved to be tightly joined as sensed subsequently by resistance to motion. As is true for wringing, the blocks could not be joined by evacuation

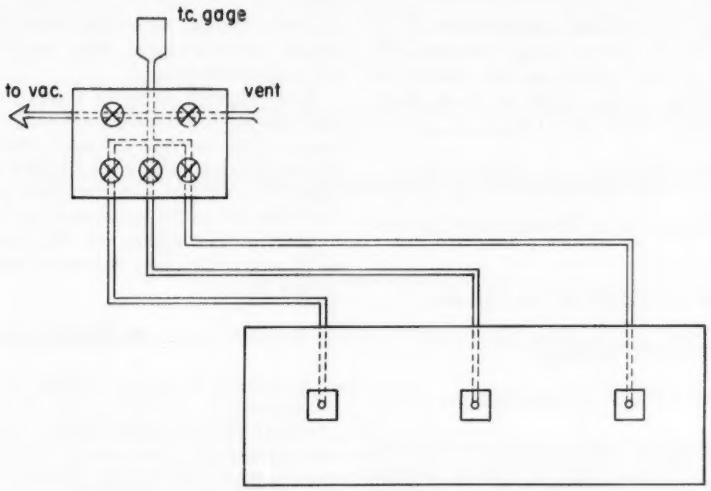

FIGURE 1. *Schematic drawing of vacuum system for leak rate test.*

when their surfaces were completely grease-free nor could a permanent joint be made with a film of volatile material.

3. Discussion

The data can be adequately represented by the polynomial expression $dp/dt = af^2 + bf^3$ μm Hg/min, where f is the fringe number. The constants determined by the method of least squares are

$$a = 32.22$$

$$b = 27.01 \qquad (1)$$

Because the phase change at the surface of the metal differs from that at the surface of the fused silica, the actual distance between the silica flat and the gage block surface may be less than would be inferred from the fringe count. The difference is estimated to be equivalent to 0.1 fringe or less, and depends upon the metal and the condition of its surface, as well as the wavelength. If the fringe number is uniformly reduced by 0.1, the constants of the polynomial become

$$a = 46.49$$

$$b = 25.78 \qquad (2)$$

The deviation, obs.–calc., is shown in table 1 for the second set of constants, and the percent deviation relative to the calculated value is shown versus fringe number in figure 2. Either equation suffices to represent the rate of pressure increase with about the same precision and the same estimate of the standard deviation of the mean.

As a test for wringing, we are interested in the leak rate for angles between gage blocks for $f \sim 0.1$. More important than whether $a = 32$ or 46 is what exponent of the fringe number should dominate the interpolation between 0 and 1 fringe. The flow of gas at large angles and high pressures takes place as Poiseuille flow, while at small angles and low pressures, the flow is of the "free molecule" type. It is to be expected that the gas flow in this experiment occurs over a large pressure range involving a combination of types of flow. The form of the polynomial which was used is consistent with classical theory [3, 4, 5, 6], and the constants are of such values as to be reasonable for the transition pressure range in which the concept of "slip distance" is employed. As theory demands, the experiment confirms that for small angles of tilt ($\phi < 5$ μrad) the interpolation follows an essentially quadratic function.

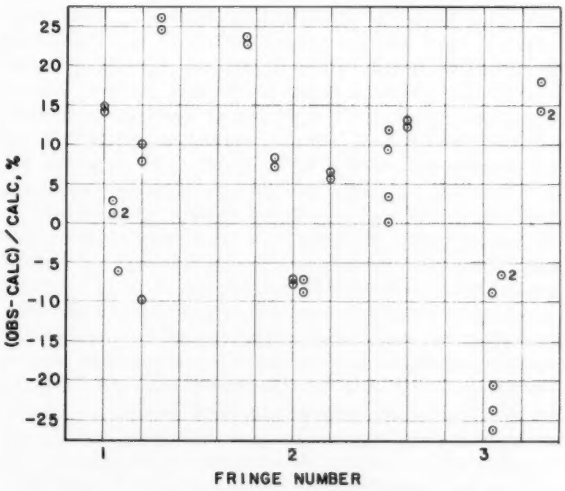

FIGURE 2. *Percent deviation versus fringe number.*

The controlling error is the reading of the fringes.

508-076 O - 73 - 8

Interference occurs for vertical separations of integral half-wavelengths, so that a fringe corresponds to a distance of 254.1 nm, which in our system is equivalent to an increase in the angle of 10.54 μrad. Expressed as a function of angle, eq (1) is

$$dp/dt = 0.2900\ \phi^2 + 0.02307\ \phi^3\ \mu\text{m Hg/min},$$

where ϕ is in μrad. Similarly, eq (2) expressed in μrad is

$$dp/dt = 0.4185\ \phi^2 + 0.02202\ \phi^3\ \mu\text{m Hg/min},$$

or with only significant figures retained,

$$dp/dt = 0.42\ \phi^2 + 0.022\ \phi^3\ \mu\text{m Hg/min}.$$

Thus we see that a vacuum leak rate of 0.3 to 0.4 μm Hg/min can be expected for an angle of 1 μrad and that the rate will vary as the square of the angle if the angle is < 5 μrad.

The values given for the relation between the angle of tilt and the vacuum leak rate were incorrect as quoted in the manometer paper [1]. They were derived using "white light fringes," which we now conclude was an idea (as we used it) without acceptable definition.

For angles around 10 μrad (1 fringe), degassing contributes a significant amount of the pressure rise unless the system has been evacuated at least 15 minutes. For smaller angles, the effect is relatively larger, so that no final evaluation of a good joint can be made until the system has been evacuated for a number of hours. After cleanup, we have observed vacuum leak rates as low as 3 to 5 μm Hg/hr for as many as 10 joints in the system, and thus were able to confirm by a single measurement that several gage blocks had been properly joined.

Even though a tilt of 1 μrad does not represent a good joint, it produces an error within an acceptable range of uncertainty for most purposes. The component of length along the gage block axis is not significantly affected, and the displacement, at the center, of 12 nm is about the same amount of uncertainty, or less, than typical uncertainties of flatness, calibration, phase shift, wringing film variation and lack of parallelism of the faces.

4. Conclusions

A vacuum leak rate method of estimating the extent of alinement of Hoke gage blocks has been demonstrated. The practical limits of error for the method are no greater than several others to be expected in the careful use of gage blocks. The same process of evacuation can be used to produce a joint between the gaging surfaces, when their alinement and surface conditions will permit joining.

5. References

[1] Guildner, L. A., Stimson, H. F., Edsinger, R. E., and Anderson, R. L., Metrologia **6**, 1 (1970).
[2] Saunders, J. B., J. Research N. B. S. **35**, 157 (1945) RP1668.
[3] Gaede, W., Ann. Physik **41**, 289 (1913).
[4] Kennard, E. H., Kinetic Theory of Gases, Chap. **VIII** (McGraw-Hill Book Co., Inc., New York, New York 1938).
[5] Clausing, P., Physica **9**, 65 (1929).
[6] Armand, G., Lapujoulade, J., and Paigne, J., Vacuum **14**, 53 (1964).

(Paper 77A5–789)

JOURNAL OF RESEARCH of the National Bureau of Standards—A. Physics and Chemistry
Vol. 77A, No. 5, September–October 1973

Low Frost-Point Humidity Generator*

Lewis Greenspan

Institute for Basic Standards, National Bureau of Standards, Washington, D.C. 20234

(June 25, 1973)

A low frost-point humidity generator has been developed at NBS to provide a capability for calibration, testing and research at very low levels of water vapor content in such gases as atmospheric air, carbon dioxide and nitrogen. The generator produces frost points from −30 to −100 °C at ambient pressures from 500 to 200,000 pascals (0.005 to 2 atm.). This is equivalent to mixing ratios of 4×10^{-6} to 51 grams of water vapor per kilogram of dry air and to vapor pressures of 1.4×10^{-3} to 38 pascals. The generated test gas can be fed to a test chamber with independent temperature control between +25 and −100 °C. The uncertainty of the frost point in the test chamber is estimated not to exceed 0.05 deg C. Intercomparisons with a frost-point hygrometer as well as two gravimetric checks gave results which in all cases agreed to within 0.2 deg C in frost-point temperature.

Key words: Calibration; frost-point; generator; humidity; water vapor.

1. Introduction

Measurements of trace quantities of water vapor are being made with increasing frequency in the sciences and in industrial and technological areas. For example, there has been a continual effort to determine the humidity of the stratosphere and the mesosphere; the measurement of the moisture content of planetary atmospheres, particularly that of Mars, continues to challenge astronomers and space scientists; processes in the chemical industry, such as butane isomerization, are affected by very low levels of humidity; and the water vapor content of helium in high temperature nuclear reactors requires close control. The sensors and instruments used for these and similar measurements are often empirical and require calibration. Even instruments based on fundamental principles are susceptible to systematic errors that may go undetected without test, calibration, or evaluation. It is therefore desirable, if not essential, that there be some method for the direct calibration of these devices, or for the calibration of transfer standards that, in turn, can be used to check these devices. To fulfill this need, the National Bureau of Standards has recently developed and put into operation a new calibration facility. The purpose of this paper is to describe this facility. With it, calibrations can be performed over a range of frost points from −30 to −100 °C, at ambient pressures from 500 to 200,000 pascals,[1] and at ambient temperatures from −100 to +25 °C.

2. Principle of Operation

This humidity calibration facility is a generator, which produces or generates a stream of gas of known moisture content. This stream is fed directly to the test instrument or, alternatively, to a test chamber into which the test instrument or sensor is placed. The test chamber is independently temperature-regulated.

A stream of dry gas first flows through a heat exchanger and then through a saturator that are both immersed in a constant-temperature liquid bath. The saturator is a long metal tube formed into a helical coil, the interior surface of which (about 1200 cm^2) is coated with a film of ice approximately one mm in thickness. During its traverse through the saturator no part of the test gas is farther than 4 mm from the ice surface. At a flow rate of 2 liters per minute the mean transit time through the saturator is about 7 s.

The heat exchanger brings the gas stream to bath temperature. Because the mass of water vapor required to saturate the gas stream is very small, the temperatures of the gas and inner ice surface are not perturbed significantly by the sublimation process. Furthermore, the saturator coil being of sufficient length, saturation is completed in the entrance portion of the coil. The remainder of the coil then serves solely as a final heat exchanger, since there is no significant pressure drop. The gas temperature at the exit end of the saturator is, therefore, the same or very close to the saturation temperature, that is, it is the value of the frost point of the gas stream. The pressure within the saturator can be set and regulated at any desired value from 500 to 200,000 pascals.

*This work was supported by the Viking Project Office of NASA.

[1] 1 Pascal = 1 newton/m^2 = 10^{-5} bar = 10^{-2} mb = 7.50062×10^{-3} mm Hg.

3. Description

The generator is schematically depicted in figure 1. It is constructed exclusively of stainless steel. The inner coil S is the saturator. It consists of a 16-foot length of 3/8-in tubing of 0.035-in wall thickness wound into a helix 5 1/2 in in o.d. and 8 in long. The outer coil, E, is a heat exchanger likewise constructed from a 16-foot length of similar tubing wound into a 10-in o.d. helix 4 1/2 in long. A vertical tube, F, of similar tubing is connected to the exit of the heat exchanger and to the entrance of the saturator.

Upstream of the heat exchanger is a 75-cm^3 collector cylinder, C_1, with an outside diameter of 1 1/2 in and a length of 4 1/2 in. The collector cylinder provides a surface for the freezing out of moisture in the entrance gas which might tend to block the heat exchanger. Downstream of the saturator is a similar saturator cylinder, C_2, with an exit port located 1 1/2 in below its top. At this same elevation and diametrically opposite to the exit port is a pressure tap to which is attached tubing of 1/8-in o.d. and 0.035-in wall thickness. This tubing leads to a sensitive quartz helix pressure gage, P. A temperature well 5/16-in o.d. and 0.035-in thick extends 2 in into the cylinder, C_2, from the top. A bakelite extension tube, T, 1/2-in o.d. is connected to the well.

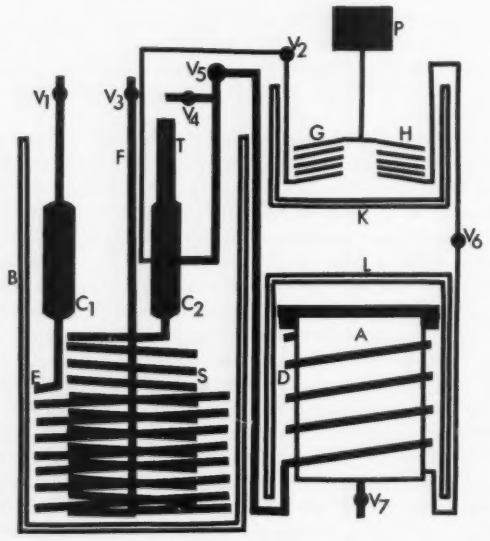

FIGURE 1. *Schematic diagram of low frost-point generator.*

B	Generator Dewar bath	G	Saturator pressure trap coil
C_1	Heat exchanger cylinder	H	Test chamber pressure trap coil
E	Heat exchanger coil	K	Pressure trap bath
F	Coating exit tube	V_1	Generator inlet valve
C_2	Saturator cylinder	V_2	Generator pressure valve
S	Saturator coil	V_3	Coating exit valve
T	Saturator temperature well	V_4	Coating inlet valve
A	Test chamber	V_5	Generator exit valve
D	Test chamber heat exchanger coil	V_6	Test chamber pressure valve
L	Test chamber Dewar cylinder	V_7	Test chamber exit valve
P	Pressure gage		

There are five valves, V_1, V_2, V_3, V_4, V_5, associated with the generator. All valves are of the welded bellows type. The lines controlled by these valves are shown in figure 1. Between valve V_2 and the pressure gage, P, is a coil, G, of 1/4-in o.d. tubing located within a glass Dewar K. With the exception of two pipe fittings in each of the cylinders, all generator connections are either welds or cone compression fittings.

Connected to the generator through valve V_5 is a test chamber, A. The chamber is constructed from a stainless steel cylinder 6-in o.d., 6-in long and 1/4-in thick. A 1/4-in thick stainless steel plate is welded to the bottom and an 8-in vacuum flange is welded to the top. The top of the chamber consists of an 8-in blank vacuum flange and is sealed to the chamber proper with a gold plated copper gasket. Welded into the wall of the test chamber are 12 pass-through electrical connections, six thermocouple wire connectors, a 3/8-in inlet tubing connection near the top, a 3/8-in outlet tubing connection at the bottom and a 1/4-in pressure tap connection near the bottom. Valves V_5, V_7, and V_6 respectively control the lines to each of these connections. Surrounding the test chamber is a four-turn helix of 3/8-in o.d. tubing which connects to the inlet and to valve V_5. Between valve V_6 and pressure gage P is a helical coil of 1/4-in o.d. tubing, H, within Dewar K. The entire inner surface of the test chamber including the cover is gold plated. The gold plating is used to reduce the amount of water vapor adsorbed on the walls of the test chamber and thereby reduce equilibration time.

The test chamber rests on expanded polystyrene and is covered with a vacuum-jacketed glass bell jar. All wires and tubing enter the test chamber area through individual holes in the styrofoam insulation. A spiral of 1/4-in o.d. copper tubing is located above the test chamber under the bell jar. This spiral is self-supported by a vertical section which extends through the styrofoam insulation. When the test chamber temperature is to be lowered, liquid nitrogen is forced through the spiral and evaporates into the space around the test chamber. The flow of liquid nitrogen is controlled by a solenoid valve which is actuated by an on-off temperature controller operating in conjunction with a thermistor in the space surrounding the test chamber.

The generator can be maintained at any desired temperature by a liquid bath. The generator is suspended from a metal frame above the bath. The bath sits on the platform of a hydraulic lift which can raise the bath until the generator is immersed so that the liquid level is about four inches above the top of the saturator cylinder C_2.

The bath is a 50-liter stainless steel Dewar cylinder, measuring 13 in i.d. and 23 in deep. Along the inner wall of the bath is a double helix of 3/8-in stainless steel tubing through which liquid nitrogen is fed for cooling the bath liquid. Between this tubing and the inner wall of the bath are two 8-foot, flexible rod, stainless steel heaters, capable of supplying 2,000 W of heating power.

The bath is filled with a fluid consisting of: methylene chloride 25.3 percent; chloroform 14.5 percent, ethyl bromide 33.4 percent, transdichloroethylene 10.4 percent, and trichloroethylene 16.4 percent by weight. This fluid remains liquid down to −130 °C and is nonflammable [1].[1]

Suspended from the rack (which supports the generator) are a stirrer and a nickel resistance thermometer which are immersed in the bath liquid when the bath is raised. This resistance thermometer actuates a proportional controller which controls both the heaters and the liquid nitrogen flow and thereby regulates bath temperature. The frost-point temperature is measured by a platinum resistance thermometer located in the temperature well of the saturator cylinder, C_2.

The generator is supplied with dry test gas which is cooled to the desired frost-point temperature before it is brought into contact with the ice, avoiding the possibility of condensate being carried through by the gas stream.

If saturation is achieved at the point of temperature and pressure measurement, the accuracy of the generator is dependent on the accuracy of temperature and pressure measurement and the absence of moisture sources or sinks downstream of this point.

4. Operational Procedure

The method of obtaining an ice surface in this generator forms the most important part of the operational procedure and will be described in detail. The method consists of the condensation of water vapor on the inner wall of the saturator tube at −100 °C. At this low temperature the condensate is in the form of ice. In order to obtain a uniform coating of ice, the entrance end of the saturator tube is first cooled, condensation occurring at the end. The cooling is then progressively moved along the saturator tube at a constant velocity providing a continuously new condensation surface until the entire tube is coated with ice.

Prior to coating, the interior of the entire generator is dried thoroughly by passing dry gas through the generator for long periods of time (weeks) at room temperature or for shorter periods of time with the generator in an air oven operating near 100 °C. During this period the bath is empty and remains below the generator. The bath is then filled with the cryogenic fluid, and a stream of moistened gas, at atmospheric pressure, is introduced into the saturator, S. Concurrently a stream of dry gas is introduced into the heat exchanger, E, in order to prevent any deposition of ice on its walls. The two streams join at the tee and emerge through vertical tube F.

The coating operation commences with a vacuum being applied to the outlet of valve V_3 and dry gas being fed into valve V_1. Valve V_1 is adjusted to provide a dry gas inlet flow of between one and two liters per minute. Valves V_2 and V_5 are closed during this operation. Valve V_4 is adjusted to allow an inlet flow of moist gas at approximately 20 liters per minute. Both the dry gas and the moist gas exit through valve V_3.

Atmospheric air, or any gas that does not react with water, is moistened so that the partial pressure of the water vapor is in excess of 1000 Pa and is heated to a temperature in excess of 100 °C. This gas enters the saturator cylinder C_2 through valve V_4.

The bath is raised under manual control to bring the surface of the liquid to the bottom of the saturator and then an automatic mechanism, which raises the bath at a constant rate of $^{15}/_{16}$ in per hour, is activated. The flow of moist gas and the elevation of the bath are continued until the liquid surface of the bath reaches the top of the saturator uppermost coil while the bath fluid is maintained at −100 °C. This process requires more than 7 h. The bath is then raised quickly until the lower half of saturator cylinder C_2 is immersed in the bath fluid. The bath liquid is now automatically maintained at this level. The gas flow is continued for an additional 15 to 30 min, then stopped.

The next step is to dry out the exit tubing from cylinder C_2. Valves V_3 and V_4 are closed and the vacuum source is removed from the exit of valve V_3. Heated dry air of approximately 100 °C is fed into the exit of the test chamber, A, and valve V_5 is opened. When the generator is above atmospheric pressure, valve V_3 is opened and the gas is allowed to exhaust into the room. The flow through valve V_5 is adjusted to approximately two liters per minute valve V_4 is cracked such that there is a small flow (a few cm^3 per min) exiting valve V_4 into the room. During this time the dry gas flow continues to flow into valve V_1. This condition is maintained for 12 to 16 h, after which time valves V_3 and V_4 are closed and the source of dry gas is removed from the exit of the test chamber. Although the above procedure dries out the exit tubing it removes a negligible amount of the ice in the saturator, due to the fact that the saturator is maintained at −100 °C.

The bath is now raised another $5^1/_2$ in bringing the surface of the liquid at least 3 in above the saturator cylinder, C_2. The bath K is filled with dry ice, causing coils G and H to become vapor traps, thereby minimizing any vapor diffusion between the pressure gage and the generator. The generator is now ready to produce atmospheres of known frost point, pressure and temperature. The generator bath temperature is set to the desired value and valve V_2 is opened. For operation below ambient pressure a vacuum source is connected to the test chamber outlet valve V_7 and by adjustment of this valve, the pressure in the saturator is set and controlled at the desired value. If temperatures other than ambient are desired in the test chamber, the vacuum jacket bell jar, L, is placed over the test chamber, the liquid nitrogen flow started and the test chamber temperature controller set.

After equilibrium at test conditions has been established, the frost-point temperature in the saturator is determined by measurement with the resistance thermometer in the temperature well T. Freon 11 is used

[1] Figures in brackets indicate the literature references at the end of this paper.

in this well as a heat transfer fluid. Readings of the pressure in the saturator are performed with valve V_2 open and valve V_6 closed and in the test chamber with valve V_6 open and valve V_2 closed. These pressure readings provide the data for calculating the difference in frost-point temperature in the test chamber from that measured in the saturator. These measurements also permit the mixing ratio to be computed. Measurement of the test chamber temperature by means of thermocouples provides the additional data for conversion of frost point to any of the common humidity units such as relative humidity. Fixed conditions are maintained for at least 16 h before measurements are attempted on instruments under test or calibration. Sixteen hours was selected to permit a change in conditions to be made everyday and yet allow adequate time for equilibration. The time necessary to achieve equilibration in the test chamber depends on the vapor pressure and temperature as well as flow rate. We estimate that 16 hours will be adequate for all operational conditions.

5. Validation

Reference [3] gives a theoretical analysis of the factors involved in obtaining saturation. Under the operating condition of a 2 liters per minute flow rate, the length of saturator necessary to reduce the degree of unsaturation by a factor of $1/e$ is 29 cm based on a diffusion constant of 0.1 cm/s which corresponds to the diffusion constant of water vapor into air at atmospheric pressure and −80 °C. The degree of unsaturation for the equipment at 2 liters per minute flow rate is about e^{-17}. At 10 liters per minute, saturation would be 97 percent and at 5 liters per minute, saturation would be 99.9 percent.

A more important consideration at 2 liters per minute is the pressure drop which amounts to approximately 0.025 mb within the saturator. As is shown in reference [3], the pressure drop has a limiting effect on the degree of saturation achievable, independent of the length of the saturator tube. At 2 liters per minute flow and atmospheric pressure, this limit is 99.9988 percent. At 10 liters per minute and atmospheric pressure, this limit would be approximately 99.9935 percent of the saturation at 0 pressure drop.

At reduced pressures, the diffusion constant is greater and the length required for the unsaturation to be reduced by a factor of $1/e$ is correspondingly less. But the pressure drop through the saturator is relatively independent of the absolute pressure and therefore the relative pressure drop $(\Delta P/P)$ is approximately inversely proportional to the absolute pressure. Since the length requirements at reduced pressure are also proportionately reduced this leads to the result that the pressure drop effect is essentially independent of absolute pressure. It may be of interest to note that a 0.1 percent error in saturation has about a 0.009 °C effect on the frost point at −30 °C and decreases to a 0.005 °C effect at a frost point of −100 °C. It is therefore concluded that errors in the degree of saturation are so small as to require no consideration at the operating flow rate of 2 liters per minute.

Estimates of uncertainty have been made based on the accuracies with which the temperature and pressure are measured and the uncertainties in the knowledge of the vapor pressure and the nonideal behavior of the gases.

The accuracy of an individual temperature measurement is ±0.01 °C but short term fluctuations of ±0.02 °C exist in operation. The determination of the frost point temperature might therefore be in error by as much as ±0.03 °C.

The accuracy of the pressure measurement is estimated at ±0.2 percent. The estimated uncertainty in the vapor pressure equation varies with temperature. At −30 °C it is estimated to be ±0.07 percent or ±0.007 °C in frost point and at −100 °C it is estimated to be ±0.54 percent or ±0.026 °C in frost point.

At 1 atm, it is estimated that the uncertainty in moisture content due to uncertainty of the nonideal behavior of moist air varies from ±0.3 percent at −30 °C to ±6 percent at −100 °C [2]. This uncertainty is proportional to pressure. At 5000 Pa, the uncertainty would range from ±0.015 percent at −30 °C to ±0.3 percent at −100 °C.

With regard to frost-point accuracy, only the temperature and pressure measurements are of consequence. With a ±0.2 percent uncertainty in the ratio of the saturation pressure to test pressure, the maximum uncertainty in frost point due to the pressure uncertainty would occur at −30 °C frost-point and be ±0.02 °C.

It is, therefore, estimated that the frost-point uncertainty due to both systematic and random errors does not exceed 0.05 °C.

When the moisture content, say mixing ratio, is desired, the uncertainty in the value of vapor pressure and in the correction for nonideal behavior of gases must be added to the uncertainty in frost point. Since the independence of these uncertainties is not established, we take the conservative approach and sum these uncertainties. These errors summed produce an estimated uncertainty in moisture content at 1 atm that varies from 0.9 percent at a frost point −30 °C to 7.4 percent at a frost point of −100 °C. Table 1 gives the estimated total uncertainty in moisture content of a test gas at atmospheric pressure and frost points from −30 to −100 °C. At lower absolute pressures, the uncertainties would be less.

In order to insure that this generator performs as predicted, it was considered essential that either the generator be checked or its performance verified by some independent means. Therefore, an intercomparison with a precision frost-point hygrometer was made over the frost point range of −30 to −78 °C. The results are given in table 2. This intercomparison is considered to be a nominal confirmation of performance and not a calibration.

Due to operating limitations on the frost-point hygrometer, comparisons could be made only at atmos-

TABLE 1. *Uncertainties in moisture content*

Frost-point temperature °C	Estimated maximum uncertainties in moisture content due to estimated uncertainties in:				
	Temperature measurement percent	Pressure measurement percent	Vapor pressure equation percent	Nonideal gas correction percent	Total percent
−30	0.31	0.2	0.07	0.30	0.88
−35	.32	.2	.08	.45	1.05
−40	.34	.2	.10	.60	1.24
−45	.36	.2	.12	.80	1.48
−50	.37	.2	.14	1.00	1.71
−55	.39	.2	.16	1.50	2.25
−60	.41	.2	.19	2.00	2.80
−65	.43	.2	.22	2.50	3.35
−70	.45	.2	.25	3.00	3.90
−75	.47	.2	.29	3.50	4.46
−80	.49	.2	.33	4.00	5.02
−85	.52	.2	.38	4.50	5.60
−90	.55	.2	.43	5.00	6.18
−95	.58	.2	.48	5.50	6.76
−100	.61	.2	.54	6.00	7.35

TABLE 2. *Comparison of low frost-point generator with frost-point hygrometer at atmospheric pressure*

Frost point	Mean difference (hygrometer-generator)	Standard deviation	Number of measurements
°C	°C	°C	°C
−30	−0.046	0.042	6
−50	−.047	.045	13
−58	−.048	.058	6
−69	+.023	.128	9
−78	−.116	.413	2

pheric pressure. It was felt that some verification of performance at reduced pressure was desirable in order to insure proper performance at reduced pressure.

This verification was obtained by making gravimetric moisture measurements at frost points of −49 and −55 °C.

Three absorption tubes arranged in series containing pelletized P_2O_5 were connected downstream of the test chamber. A vacuum pump was connected to the outlet of the absorption tubes. These tubes were weighed before and after the run in order to determine the total moisture produced by the generator during the run. The test gas was nitrogen supplied by a cylinder and dried. The nitrogen cylinder was weighed before and after the run to determine the amount of dry gas used during the run. The ratio of the mass of moisture to the mass of dry gas is the mixing ratio.

Although the volume flow in the generator was approximately 1.5 liters per minute throughout the run, the volume flow and pressure in the absorption tubes was not known. For this reason, we have no rigorous method of estimating the amount of moisture that may have passed through the absorption tubes without being absorbed nor do we have experience at these conditions which would dictate the correction to be applied due to third tube pick up.

Lacking data for making these corrections, the gravimetric mixing ratio was calculated without correction and the results are given in table 3.

The −49 °C frost-point run took 6 days and 21 h during which time temperature and pressure data were recorded every 10 min except during malfunctions in the data acquisition system. Such lack of data amounted to 8 percent of the total; however from the trends of the recorded data the values for the missing data were extracted and used in the computation. The −55 °C frost-point run took 8 days and 18 h, during which time 6 percent of the data was missing for which estimated values were used. An uncertainty equal to twice the estimated uncertainty of an individual determination has been assigned to the periods during which data was not collected.

The intercomparison with the frost-point hygrometer gave a maximum difference of 0.12 °C at −78 °C frost point. All other points were in agreement to better than 0.05 °C. The generated frost point at reduced pressure agreed with the gravimetric determinations to within 0.05 and 0.19 °C. The 0.05 °C is well within the estimated band of total uncertainty whereas the 0.19 °C exceeds the estimated band of total uncertainty by 0.01 °C. In all intercomparisons, agreement was better than 0.2 °C in frost point.

6. Discussion and Conclusions

The generator has been operated successfully to produce a wide range of humidities. Although humidities higher than −30 °C in frost point can be established, the ice film in the saturator will not last long

TABLE 3. Gravimetric comparisons

Generated values		Run A	Run B
Mean saturator temperature		−49.47 °C	−55.04 °C
Mean saturator pressure		4092. Pa	4630. Pa
Mean mixing ratio		0.71914 g/Kg	0.28989 g/Kg
Uncertainties		**Mixing ratio**	
Saturator temperature	±0.03 °C	$^{+0.00266}_{-0.00261}$ g/Kg	$^{+0.00113}_{-0.00112}$ g/Kg
	Percent		
Saturator pressure	±0.02	$^{+0.00146}_{-0.00141}$ g/Kg	±0.00058 g/Kg
Vapor pressure equation	±0.14	$^{+0.00103}_{-0.00098}$ g/Kg	
	±0.16		±0.00046 g/Kg
Enhancement factor	±0.05	$^{+0.00038}_{-0.00034}$ g/Kg	
	±0.08		±0.00023 g/Kg
Missing data		$^{+0.00059}_{-0.00046}$ g/Kg	±0.00015 g/Kg
Total		$^{+0.00612}_{-0.00518}$ g/Kg	$^{+0.00255}_{-0.00254}$ g/Kg
Gravimetric values			
Weight of collected water		0.7358±0.00044 g	0.36775±0.00044 g
Weight of expended nitrogen		1016.83±0.34 g	1299.78±0.34 g
Additional uncertainties			
Correction for 3d tube pickup		−0.00501 g	−0.00627 g
Weight of uncollected water		+0.0049 g	+0.0050 g
Comparison			
Generated mixing ratio		$0.71914^{+0.00612}_{-0.00580}$ g/Kg	$0.28989^{+0.00255}_{-0.00254}$ g/Kg
Gravimetrically measured Mixing ratio		$0.72362^{+0.00550}_{-0.00570}$ g/Kg	$0.28293^{+0.00426}_{-0.00523}$ g/Kg
Equivalent generated frost-point		−48.784±0.034 °C	−55.028±0.034 °C
Gravimetrically determined Frost-point		$-48.733^{+0.093}_{-0.097}$ °C	$-55.216^{+0.150}_{-0.178}$ °C

enough for most tests. Hence a −30 °C frost point is considered a practical upper limit. Frost points as low as −100 °C have been generated. It is possible to operate the liquid bath, in which the saturator is immersed, at temperature as low as −130 °C and to thereby produce equivalent frost points. However, it is likely that the time required to reach a steady state condition would be excessively long so as to make this impractical.

Any gas can be used as the carrier. Air, nitrogen, and carbon dioxide have been employed without any detectable change in performance. The generator has also been operated at total pressures as low as 500 Pa, again without any observable change in performance.

Two techniques were used to evaluate the performance of the generator: direct measurement of the frost point with a precision frost-point hygrometer and gravimetric measurement of the moisture content with a solid desiccant.

The excellent agreement achieved between the low frost-point generator and the frost-point hygrometer indicates that the generator behaves in a predictable fashion in accordance with the laws of physics, at least at atmospheric pressure in the range of frost points from −30 to −78 °C. There is no reason to suspect any

significant departure at lower frost points from predicted behavior. The gravimetric measurements were intended to disclose whether operation of the generator at reduced pressures introduced any unforeseen degradation in performance. It was difficult to design a suitable test for checking both at low frost point and at low absolute pressure. The gravimetric method was chosen because it has great inherent accuracy. Unfortunately at low moisture levels the sampling time is inordinately long and the experiment becomes as much a test of the durability of apparatus and equipment as it is of the humidity. Thus only two runs were made. The agreement achieved, particularly under the circumstances of the test procedure, was again excellent. There does not appear to be any reason for questioning the predicted behavior of the generator at reduced pressures—at least down to 50 mb. There appears to be no reason why the generator would not perform equally well down to 5 mb, the lower operational limit.

7. References

[1] Kanolt, C. W., Bureau of Standards Sci. Papers 520, Vol. **20**, p. 619 (1926).

[2] Wexler, Arnold, Calibration of Humidity Measuring Instruments at the National Bureau of Standards, in Analysis Instrumentation Vol. **6**, p. 161 (Plenum Press, 1969).

[3] Johnson, Daniel P., Note on diffusion of vapor into flowing gas, to be published.

(Paper 77A5–790)

JOURNAL OF RESEARCH of the National Bureau of Standards — A. Physics and Chemistry
Vol. 77A, No. 5, September-October 1973

Publications of the National Bureau of Standards*

Citations with Selected Abstracts

SP236, 1973 Edition. **NBS frequency and time broadcast services, radio stations WWV, WWVH, WWVB, and WWVL,** P. P. Viezbicke, Editor, Nat. Bur. Stand. (U.S.), Spec. Publ. 236, 1973 Edition, 19 pages (May 1973) 45 cents, SD Catalog No. C13.10:236, 1973 Edition.

Key words: Broadcast of standard frequencies; high frequency; low frequency; standard frequencies; time signals; very low frequency.

Detailed descriptions are given of the technical services provided by the National Bureau of Standards radio stations WWV, WWVH, WWVB, and WWVL. These services are: 1. Standard radio frequencies; 2. Standard audio frequencies; 3. Standard musical pitch; 4. Standard time intervals; 5. Time signals; 6. UTl corrections; and 7. Official announcements. In order to provide users with the best possible services, occasional changes in broadcasting schedules are required. This publication shows the schedules in effect on January 1, 1973. Annual revisions will be made. Current data relating to standard frequencies and time signals are available monthly in the Time and Frequency Services Bulletin. Advance notices of changes occurring between revisions will be sent to users of NBS broadcast services who request such notice on the basis of need. Supersedes NBS Special Publication 236, 1972 and previous editions.

SP371. **A supplementary bibliography of kinetic data on gas phase reactions of nitrogen, oxygen, and nitrogen oxides,** F. Westley, Nat. Bur. Stand. (U.S.), Spec. Publ. 371, 92 pages (Feb. 1973) $1.25, SD Catalog No. C13.10:371.

Key words: Bibliography; chemical kinetics; excited state; gas phase; nitrogen atom; nitrogen molecule; nitrogen oxides; oxygen atom; oxygen molecule; ozone.

A bibliography, a reaction-oriented list of references supplementing NBS publication COM-71-00841 (NBS-OSRDB-71-2, August 1971), is provided for published papers and reports containing rate data for reactions of N, N_2, N_3, N_2O, N_2O_2, N_2O_3, N_2O_4, N_2O_5, NO, NO_2, NO_3, NO_4, O, O_2 and O_3 with each other. It includes an extensive list of papers dealing with production and reactions of molecular oxygen in excited singlet state ($a^1\Delta_g$, $b^1\Sigma_g^+$, $c^1\Sigma_u$). In addition, two lists of critical reviews dealing with the above reactions are included. About 500 papers are listed. The period covered extends from 1900 through January 1972.

SP380. **Photonuclear reaction data, 1973,** E. G. Fuller, H. M. Gerstenberg, H. Vander Molen, and T. C. Dunn, Nat. Bur. Stand. (U.S.), Spec. Publ. 380, 131 pages (Mar. 1973) $2.10, SD Catalog No. C13.10:380.

Key words: Bibliography; data index; data summary; elements; isotopes; nuclear physics; photonuclear giant resonance; photonuclear reaction.

A brief summary is given of the available data on the gross features of the photonuclear giant resonance. Data are presented in tabular form for all nuclei where measurements have been made. In addition, a comprehensive, annotated data index and bibliography are given which cover experimental data for the field of photonuclear reactions published in scientific and technical journals in the period from 1955 through 1972. Organized by element and isotope, each entry in the index is for a specific reaction reported in a given reference. Information is given on the type of measurement, excitation energies studied, source type and energies, detector type and angular ranges covered for each reaction entry. This publication supersedes NBS Miscellaneous Publication 277 and NBS Special Publication 322 which also embraced Supplement 1 to Misc. Publ. 277. All information contained in these publications has been combined and merged with new data to form the Photonuclear Data Index and Bibliography contained in this publication.

BSS44. **Full scale test on a two-story house subjected to lateral load,** F. Y. Yokel, G. Hsi, and N. F. Somes, Nat. Bur. Stand. (U.S.), Bldg. Sci. Ser. 44, 26 pages (Nov. 1972) 50 cents, SD Catalog No. C13.29/2:44.

TN270-7. **Selected values of chemical thermodynamic properties. Tables for the lanthanide (rare earth) elements (elements 62 through 76 in the standard order of arrangement),** R. H. Schumm, D. D. Wagman, S. Bailey, W. H. Evans, and V. B. Parker, Nat. Bur. Stand. (U.S.), Tech. Note 270-7, 93 pages (Apr. 1973) $1.25, SD Catalog No. C13.46:270-7.

Key words: Cerium compounds; dysprosium compounds; enthalpy; entropy; erbium compounds; europium compounds; gadolinium compounds; Gibbs energy of formation; holium compounds; lanthanides; lanthanum compounds; lutetium compounds; neodymium compounds; praseodymium compounds; promethium compounds; rare-earth elements; samarium compounds; terbium compounds; thulium compounds; ytterbium compounds.

Contains tables of values for the standard heats and Gibbs (free) energies of formation, entropies and enthalpies at 298.15 K and heats of formation at 0 K for compounds of the rare-earth elements (the lanthanides; lutetium through lanthanum; elements 62 through 76 in the Standard Order of Arrangement). These tables are a continuation of the comprehensive revision of NBS Circular 500.

TN594-4. **Optical Radiation Measurements: The impact of radiometry and photometry and the role of NBS,** B. Steiner, Nat. Bur. Stand. (U.S.), Tech. Note 594-4, 56 pages (Mar. 1973) 80 cents, SD Catalog No. C13.46:594-4.

Key words: Agriculture; clinical analysis; economic impact; energy crisis; meteorology; photometry; phototherapy; pollution; radiometry; remote sensing.

Serious measurement discrepancies universally plague quantitative measurement in the electro-optics industry. The impact of the resulting problems is reviewed and the role of NBS explored. The measurement discrepancies arise chiefly through the recent explosive expansion of this industry. The growth has precipitated a complex development in the variety and accuracy of measurements required. The impact of problems in optical radiation measurement falls in many areas. One is the increasing Federal responsibility for public life defined in recent legislation. Another is the influence of good optical radiation measurement on the technical development of the electro-optics industry. The impact of these measurements on a

number of public issues is reviewed: public health, public safety, the energy crisis, meteorology, pollution, agriculture, crime prevention, and surveillance from air and space. The economic impact of improved measurement both on a fair domestic market and on the balance of payments operates through unit production cost, quality control, product improvement, and innovation. Leadership by NBS has been urged by the industry not only in fulfillment of its legislative responsibility but also to permit the focus of elaborate and impartial resources on the complex problem of optical radiation measurement. In keeping with its mission to help improve industrial technology and the competitiveness of American industry, NBS has an opportunity of major proportions in the electro-optics industry. Leaders of this industry are calling for NBS initiatives to resolve many of the measurement problems now hindering further progress.

TN628. **On the utility of the m-6-8 potential function,** H. J. M. Hanley and M. Klein, Nat. Bur. Stand. (U.S.), Tech. Note 628, 77 pages (Nov. 1972) 70 cents, SD Catalog No. C13.46:628.

Key words: Dispersion coefficients; m-6-8 potential; parameter selection; second virial coefficients; transport properties.

The calculation of transport and equilibrium properties of simple gases with the m-6-8 potential function is discussed. Properties referred to specifically are the viscosity, diffusion, thermal conductivity and second virial coefficients, and the thermal diffusion factor. Gases referred to are argon, krypton, xenon, nitrogen, oxygen, carbon dioxide and methane. We also discuss in detail the general behavior of a model potential with respect to the fitting of data and the selection of potential parameters. The m-6-8 appears to be the simplest model potential which can satisfactorily be used to fit data over a wide temperature range. The relationship of the potential to independent theory is briefly examined.

TN632. **Frequency stability specification and measurement: High frequency and microwave signals,** J. H. Shoaf, D. Halford, and A. S. Risley, Nat. Bur. Stand. (U.S.), Tech. Note 632, 70 pages (Jan. 1973) 65 cents, SD Catalog No. C13.46:632.

Key words: Allan variance; frequency stability measurements; measurement system description; phase noise, spectral density; stability definitions; terminology standards.

This report gives concise definitions for specifying stability for measurements in the frequency domain and time domain. Standards of terminology and of measurement techniques are recommended. Measurement systems in the high frequency and microwave regions are described in adequate detail so that the systems may be duplicated.

TN634. **Lorenz ratios of technically important metals and alloys,** J. G. Hust and L. L. Sparks, Nat. Bur. Stand. (U.S.), Tech. Note 634, 133 pages (Feb. 1973) $1.25, SD Catalog No. C13.46:634.

Key words: Alloys; compilation; cryogenic; electrical resistivity; Lorenz ratio; metals; thermal conductivity.

A comprehensive review and compilation of the world literature on Lorenz ratio of technically important metals and alloys is presented. Lorenz ratio, electrical resistivity, thermal conductivity and characterization data are compiled in tabular form and the Lorenz ratio data are presented in graphical form as well. Data are included here only if the research reported both thermal conductivity and electrical resistivity of the specimens. No attempt has been made to smooth data or present recommended values.

TN636. **Modeling of atomic clock performance and detection of abnormal clock behavior,** W. A. Ganter, Nat. Bur. Stand. (U.S.), Tech. Note 636, 39 pages (Mar. 1973) 50 cents, SD Catalog No. C13.46:636.

Key words: Atomic clock model; detection; flicker noise; sequential test; time scale.

We have assumed that the nominal performance of an atomic clock can be well characterized by (1) a noise amplitude and (2) a mix of white and flicker pure noise processes. A number of specific kinds of changes are assumed that a clock might encounter. We assume that these changes can occur with either sign and with varying magnitudes. The changes considered are a noise amplitude different from nominal, a flicker component in the noise mix which is different from nominal, a step jump in the time counts for a clock and a linear (frequency jump) or quadratic (frequency drift) trend in the time counts for a clock.

Detection of a change is accomplished with a multiple sequential test having compound limits. The test is designed to respond quickly to an actual change but to make few incorrect detections (identify the wrong change) or false detections (when no change from nominal operation has occurred). When a change is detected for a clock, the laboratory time scale can be adjusted accordingly for this condition.

TN756. **A user's guide to the OMNITAB command "STATISTICAL ANALYSIS",** H. H. Ku, Nat. Bur. Stand. (U.S.), Tech. Note 756, 44 pages (Mar. 1973) 75 cents, SD Catalog No. C13.46:756.

Key words: Computing, statistical; documentation for users; OMNITAB; statistics.

This Technical Note is the first of a series of interpretive notes for a number of commands in the OMNITAB system that have the automatic printout feature. Others planned in the series include commands FIT and POLYFIT, TWOWAY analysis, ONEWAY analysis, and CORRELATION.

These notes aim to be self-contained so that users may have sufficient information on hand for the understanding of the statistics computed and to use them for their immediate applications. Computation formulas are given in the text, and a number of statistical tables are reproduced in the Appendix for the convenience of users.

TN758. **NBS reactor: Summary of activities October 1971 to September 1972,** R. S. Carter, Editor, Nat. Bur. Stand. (U.S.), Tech. Note 758, 140 pages (Mar. 1973) $2.10, SD Catalog No. C13.46:758.

Key words: Activation analysis; crystal structure; diffraction; isotopes; molecular dynamics; neutron; nuclear reactor; radiation.

This report summarizes all those programs which depend on the NBS reactor. It covers the period from October 1971 through September 1972. The programs range from the use of neutron beams to study the structure and dynamics of materials through nuclear physics and neutron standards to sample irradiations for activation analysis, isotope production, and radiation effects studies.

TN760. **Description of the magnetic tape version of the Bulletin of Thermodynamics and Thermochemistry, No. 14 (1971),** R. McClenon, W. H. Evans, D. Garvin, and B. C. Duncan, Nat. Bur. Stand. (U.S.), Tech. Note 760, 51 pages (Mar. 1973) 75 cents, SD Catalog No. C13.46:760.

Key words: Bibliography; chemical thermodynamics; extended character codes; information retrieval; magnetic tape.

The substance-property index and bibliography sections of the Bulletin of Thermodynamics and Thermochemistry, No. 14 (May 1971) have been converted to a magnetic tape version designed for computerized searching written in an extended form of the American National Standard Code for Information Interchange (X3.4-1968). In this version each substance-property entry has been supplemented by a searching key. This report describes the magnetic tape version.

TN761. **Project SOAP: A systems approach to biomedical research program management—A case study,** R. S. Cutler, Nat. Bur. Stand. (U.S.), Tech. Note 761, 75 pages (Apr. 1973) 95 cents, SD Catalog No. C13.46:761.

Key words: Biomedical research; "health relevance"; program

planning and budgeting; R&D management; systems analysis; systems approach.

This case study describes the activities of an interagency task group that applied systems analysis to improve management controls within a biomedical research agency of the federal government. The results were the formulation and implementation of a discipline for program management, which explicitly makes use of multiple criteria in arriving at resource allocation decisions.

The text details the necessary preliminary analysis describing operational activities, information flows, and key decision points within the organization. It goes on to identify the techniques employed and the difficulties encountered while attempting to improve the decision-making process for selecting research projects, under conditions of reduced funding. In particular, a comparison is made between: (1) the agency's traditional single-criterion "peer review" judgment for determining budget priorities, and (2) the multiple-criteria judgments required to effect more positive management control. The systematic use of separate "scientific merit" and "health relevance" ratings is compared with the organization's actual experience. The criteria used by various participants in the decision process are analyzed, and a dollar allocation "investment" procedure based on these findings is developed.

A procedure which organizes relevant information for research program planning and evaluation is presented, and extension of this recommended procedure to wider use by science administrators elsewhere in government is discussed.

TN762. **Tabulation of voluntary standards and certification programs for consumer products,** S. J. Chumas, Nat. Bur. Stand. (U.S.), Tech. Note 762, 119 pages (Mar. 1973) $1.25, SD Catalog No. C13.46:762.

Key words: Certification programs; consumer products; household products; industry standards; international recommendations; national standards; product standards; recommended practices; specifications; test methods.

This tabulation is a revised and enlarged version of NBS Technical Note 705, "Tabulation of Voluntary National Standards, Industry Standards, International Recommendations and Certification Programs for Consumer Products," issued December 1971.

Technical Note 705 was a revision of the Draft Tabulation compiled by the American National Standards Institute and issued in April 1970. The categories and products covered in the tabulation were originally based on those listed in the Consumer Product Safety Index (CPSI) of the National Commission on Product Safety, published in July 1970. The products and categories in the current revision are based on those developed for the National Electronic Injury Surveillance System (NEISS) of the Food and Drug Administration. The NEISS listings are an expansion and revision of the CPSI. NEISS product areas were slightly altered to conform to the scope of this tabulation.

The tabulation lists over 700 product areas and over 1000 standards' titles covering products found in and around the home. (The major consumer product areas not included are foods, beverages, and drugs.) The tabulation also indicates the applicable voluntary national, industrial, and international standards which deal primarily with either safety or performance or both aspects of the products listed. For some of the product areas, there are no applicable standards. Available information on certification programs and standards under development, and the Standard Industrial Classification (SIC) numbers for the products are also provided. Supersedes NBS Technical Note 705.

TN763. **A set of debugging and monitoring facilities to improve the diagnostic capabilities of a compiler,** E. N. Fong, Nat. Bur. Stand. (U.S.), Tech. Note 763, 25 pages (Mar. 1973) 50 cents, SD Catalog No. C13.46:763.

Key words: Compiler; debugging; error diagnostic; high-level programming languages; monitoring; procedural-oriented languages.

Increasing concern with the quality of computer software today makes it important to evaluate critically the debugging facilities available in high-level languages. This paper presents a collection of program debugging and monitoring facilities to improve the diagnostic capabilities of a compiler. A distinction is made between debugging and monitoring facilities performed at compile time, at link/load time and at execution time. These facilities are described in terms of this breakdown with a conscious attempt to move the detection of errors from execution time to compile or link/load time, and to collect information when the information is available during the compilation process.

TN764. **An investigation of the stability of and insulation leakage in some high temperature resistance thermometers: an interim report,** S. D. Wood, Nat. Bur. Stand. (U.S.), Tech. Note 764, 31 pages (May 1973) 50 cents, SD Catalog No. C13.46:764.

Key words: Freezing point of zinc; high temperature resistance thermometer; insulation resistance; platinum resistance thermometer; resistance thermometer; stability; tungsten thermometer; zinc.

Data are presented concerning the stability of high temperature resistance thermometers. Two types of platinum and one type of tungsten thermometer were tested at 1065 °C and 960 °C. Some of the platinum thermometers were also tested at 900 °C and at the freezing point of zinc. Results of tests are also given on the insulation resistance of sensor supports and lead assemblies for the two types of platinum thermometers. A new design for a zinc-point cell is discussed briefly. Suggestions for future work are indicated.

TN765. **Low temperature thermometry: interim report,** G. Cataland and H. H. Plumb, Nat. Bur. Stand. (U.S.), Tech. Note 765, 23 pages (May 1973) 40 cents, SD Catalog No. C13.46:765.

Key words: Acoustical thermometer; calibrator; germanium thermometers; heat conduction; NBS P2-20 (1965) scale; "speed of sound" isotherms; viscosity.

Earlier acoustical thermometer "speed of sound" isotherms are compared with recent measurements. Where systematic deviations had appeared in "smoothing" through acoustically derived temperatures via germanium thermometers, a possible solution has emerged; more precise temperature control of the acoustical thermometer is desirable and has been realized. A cursory examination of the applicability of the Helmholtz-Kirchhoff equation was made with a modified sonic chamber. Measurements with the modified instrument have shown no changes in the experimental results.

The maintenance of the NBS P2-20 (1965) scale is described. A new calibration apparatus was constructed to accommodate more germanium thermometers thus reducing the calibration cost per thermometer during a calibration run.

TN766. **A gamma ray moments computer code, GAMMON-I,** C. M. Eisenhauer, G. L. Simmons, and L. W. Spencer, Nat. Bur. Stand. (U.S.), Tech. Note 766, 41 pages (Apr. 1973) 75 cents, SD Catalog No. C13.46:766.

Key words: Computer code; gamma rays; gamma ray transport; gauss quadrature; moments; shielding.

In this paper we describe a computer code for generating spatial-angular moments of gamma ray energy fluence in an infinite medium. The equation for moments of the energy fluence is given and the techniques used for the solution are discussed. The structure of the code and of the main subroutines is also given. Details of the input and output data are presented and the printout from a sample problem is included.

TN767. **Microelectronic interconnection bonding with ribbon wire,** H. K. Kessler and A. H. Sher, Nat. Bur. Stand. (U.S.), Tech. Note 767, 31 pages (Apr. 1973) 50 cents, SD Catalog No. C13.46:767.

Key words: Aluminum wire; bonding; fabrication (wire bonds); microelectronics; ribbon wire; round wire; testing (wire bond); ultrasonic bonding; wire bond.

The feasibility of using aluminum ribbon wire for ultrasonic bonding of semiconductor microelectronic interconnections was studied, and several advantages over the use of round wire of equivalent cross-sectional area were found. Ribbon wire bonds exhibited little deformation or heel damage, and a greater percentage of bonds of a certain quality (as judged by pull strength and appearance) could be made over much greater ranges of the bonding machine parameters, time and tool tip displacement, using ribbon wire than was possible with round wire. The ease of positioning ribbon wire was indicated by making multiple ribbon wire bonds side-by-side on a 5-mil square pad, or by stacking up to four bonds one on top of another. However, bonding with harder than normal wire, previously thought to offer certain advantages with respect to higher bond tensile strength, yielded inconsistent results.

TN768. **Nonmetallic coatings for concrete reinforcing bars. Coating materials,** J. R. Clifton, H. F. Beeghly, and R. G. Mathey, Nat. Bur. Stand. (U.S.), Tech. Note 768, 40 pages (Apr. 1973) 65 cents, SD Catalog No. C13.46:768.

Key words: Chlorides; concrete; corrosion; epoxy coatings; organic coating; steel reinforcing bars.

This work was undertaken in order to determine the feasibility of using organic coatings, especially epoxies, to protect steel reinforcing bars embedded in concrete from accelerated corrosion attributed to the depassivation of steel by chloride ions.

Coatings have been evaluated on the basis of their chemical and physical durabilities as well as their protective qualities. In this study, attention has also been directed to the following: application methods; surface preparation of the steel reinforcing bar; and site of application.

TN770. **Hazard elimination procedures for leaded paints in housing,** D. Waksman, L. F. Skoda, and E. J. Clark, Nat. Bur. Stand. (U.S.), Tech Note 770, 99 pages (May 1973) $1.25, SD Catalog No. C13.46:770.

Key words: Building material; housing; leaded paint; lead hazard elimination methods; lead paint poisoning; performance attributes.

Methods currently used to control the hazard caused by leaded paints in housing vary in effectiveness from complete elimination of the hazard to a minimal effort that runs a high risk for recurrence of the hazard. A series of guidelines has been drawn up to acquaint municipal planners and other decision makers with the factors that should be considered in implementing a hazard elimination program. Formats are presented to describe attributes of the various methods that should be considered.

TN771. **Some experiments on the stirring of viscous liquids,** A. Napolitano, Nat. Bur. Stand. (U.S.), Tech. Note 771, 60 pages (May 1973) 85 cents, SD Catalog No. C13.46:771.

Key words: Agitators; borosilicate glass; glass melt; glass tank; liquids; stirrer; viscosity.

The stirring actions of several designs of small stirrers were observed and photographed in transparent viscous model liquids. The fluidity of the liquids was comparable to that of a molten borosilicate glass at fining temperatures. The most efficient features of one or more of these stirrers were incorporated into larger model stirrers and observed under actual stirring conditions. As a result of these performance tests, a final design of stirrer was selected and fabricated of platinum-rhodium metal and used in an experimental glass tank. The design of one of the pots in the experimental glass tank was modified to obtain the maximum stirring action with the selected stirrer.

TN775. **Coordinated evaluation system (CES) project, model documentation for building regulation,** R. D. Dikkers, Nat. Bur. Stand. (U.S.), Tech. Note 775, 16 pages (May 1973) 35 cents, SD Catalog No. C13.46:775.

Key words: Building regulation; evaluation; inspection; manufactured building; mobile homes; model documents; state-of-art study.

Background information, objectives and the current status (February, 1973) of various tasks and reports pertaining to the Coordinated Evaluation System (CES) project are described. The goal of the CES Project is to develop model informational documentation that will assist state building regulatory agencies in establishing a coordinated and uniform evaluation, approval and inspection system. The model documentation will be related to the following building regulatory functions: (1) data submittal, (2) evaluation, (3) approval, (4) compliance assurance (inspection), (5) installation, and (6) owner information.

This column lists all outside publications by the NBS staff, as soon after issuance as practical. For completeness, earlier references not previously reported may be included from time to time.

Armstrong, G. T., **Some current topics in thermochemistry and calorimetry at the National Bureau of Standards,** *Proc. Colloq. Int. de Thermochimie, Marseille, France, June 30-July 2, 1971,* No. 201, 77-96 (Centre National de la Recherche Scientifique, Colloques Internationaux, Paris, France, 1972).

Key words: Calorimetry, flow; calorimetry, solution; chlorine monofluoride; fluorine dissociation; hydrofluoric acid solution calorimetry; microcalorimetry; quartz, standard reference materials; standard reference material for calorimetry.

The current program of the Thermochemistry Section at the National Bureau of Standards includes approximately equal proportions of experimental research and data compilation and evaluation activities. Experimental studies of calorimetric accuracy, reference materials for calorimetry, and the properties of selected key substances are in progress. The enthalpy of solution in aqueous hydrofluoric acid (24.4 percent and other concentrations) at 80 °C and as a function of temperature has been determined for α-quartz to permit its issuance as a reference material for mineralogical calorimetry. A Calvet microcalorimeter has been placed in operation with digital data-logging accessories with a sensitivity of about 0.1 μW. It has been shown to operate effectively in a temperature-scanning mode. Flow calorimetry using the reaction:

$$\left[ClF_n(g) + \left(\frac{n+1}{2}\right)H_2(g) + mH_2O(l) = [HCl + nHF + mH_2O](l)\right] \quad (1)$$

has led to enthalpies of formation of ClF, ClF_3 and ClF_5. The binding energy per atom in the gaseous molecules varies only from 128.0 to 122.3 kJ mol^{-1} in the series. The enthalpy of formation of ClF provides some (inconclusive) evidence that the zero point dissociation energy of fluorine is less than 153.8 kJ mol^{-1}. Other experimental programs are also active but are not covered here.

Barnett, J. D., Block, S., Piermarini, G. J., **An optical fluorescence system for quantitative pressure measurement in the diamond-anvil cell,** *Rev. Sci. Instrum.* **44,** No. 1, 1-9 (Jan. 1973).

Key words: Diamond-anvil cell; fluorescence; pressure measurement; ruby.

An optical system for rapid routine pressure measurement is described which utilizes a pressure shift in the sharp *R*-line fluorescence spectrum of ruby or similar materials. The system, which consists of a standard polarizing microscope and a 1/4 m monochromator with associated photodetection system, is used with

the diamond-anvil pressure cell, but can be employed with suitable modification in any pressure system which has optical access. The precision of the pressure measurement in a hydrostatic environment up to 100 kilobar is 0.5 kilobar using ruby as the pressure sensor. This precision is better than the accuracy of the present pressure scale above 40 kilobar. The merits of fluorescent materials other than ruby as pressure sensors are also discussed. A description of a Waspaloy diamond cell with some modifications in design is given. This improved cell and associated techniques extends the pressure range in gasketed systems up to 200 kilobar at room temperature and to moderate pressures at 700 °C.

Barrett, R. F., Biedenharn, L. C., Danos, M., Delsanto, P. P., Greiner, W., Wahsweiler, H. G., **The eigenchannel method and related theories for nuclear reactions,** *Rev. Mod. Phys.* **45,** No. 1, 44-108 (Jan. 1973).

Key words: Continuum shell model; nuclear reactions; nuclear structure; photonuclear reactions; *s*-matrix.

The theory of the treatment of particle hole states in the continuum is reviewed with emphasis on the eigenchannel method. The results of actual calculations are compared with experimental data. Some aspects of the experiments are rather well reproduced by the calculations. However, in certain other aspects a qualitative disagreement exists between theory and experiment, pointing to an essential inadequacy of the underlying nuclear model.

Barton, J. A., Jr., Eick, J. D., Dickson, G., **Comparison of Brinell and Vickers hardness tests on dental casting gold alloys,** *J. Dent. Res.* **52,** No. 1, 163-169 (Jan.-Feb. 1973).

Key words: Brinell hardness number; dental casting; gold alloy; indentation; Rockwell superficial hardness tester; Vickers hardness number; Vickers hardness tester.

A large group of dental casting gold alloys representing all four types listed in American Dental Association Specification No. 5 were indented, using the Brinell and Vickers methods. The relationship between Vickers and Brinell hardness numbers was found to be linear with the addition of 19 to the Brinell number approximating the Vickers number fairly well. The coefficient of variation for the Brinell test was found to be about 1 percent less than that of the Vickers test. Surface preparation, grain size, and the position of the indentation with respect to grain structure did not affect the precision of the Vickers method. The effects of reading error and sample inhomogeneity on the precision of the Vickers values were also evaluated. The reading error was a large portion of the total error for types I, II, and III, but only about 35 percent of the total error for type IV alloys.

Beers, Y., Klein, G. P., Kirchhoff, W. H., Johnson, D. R., **Millimeter wave spectrum of thioformaldehyde,** *J. Mol. Spectrosc.* **44,** No. 3, 553-557 (Dec. 1972).

Key words: Centrifugal distortion; interstellar molecule; millimeter wave spectra; rotational transition thioformaldehyde.

The rotational spectrum of $H_2{}^{12}C^{32}S$ has been investigated in the millimeter region from 100 to 250 GHz. Twenty-five new *R*-branch transitions have been measured and combined with earlier data in a centrifugal distortion analysis of the spectrum. A set of rotational parameters are presented representing the best fit of all available data on the molecule. These rotational parameters allow reliable predictions for all transitions of $H_2{}^{12}C^{32}S$ up to $J = 30$ and $\nu < 300$ GHz.

Bennett, J. J., Holman, M. A., Tumarkin, J. E., **The economic impact of noise,** *Environmental Protection Agency Report No.* **NTID 300.14,** 104 pages (available as PB206726 from the National Technical Information Service, Springfield, Va. 22151, Dec. 31, 1971).

Key words: Economic impact of noise; noise abatement.

A study has been undertaken to survey the economic impact of noise. Data available on the entire subject of noise and its abatement are so rudimentary that they do not lend themselves to even the most primitive economic analysis. It is demonstrated that the number of sources of noise in homes, in industry, on the highways, and in the air is growing at a dramatic rate. These noise sources are heterogeneous and transient, and therefore, a universal solution for abatement of noise at the source is not available. From the economic viewpoint, it has been demonstrated that substantial costs are associated with noise and its abatement. Costs such as those associated with equipment redesign, right-of-way, and receiver insulation are discussed in detail. The most glaring data gaps highlight the need for research into the relationship between noise, its abatement, and its impact on: wages, prices, productivity, production costs, employment, balance of payments, real property values, and health. Research using the principles of economics must identify and analyze the most cost-effective alternative solutions to noise. A discussion of spending for noise research is included in the study.

Bowen, R. L., Argentar, H., **A stabilizing comonomer: II. Stabilization and polymerization characteristics,** *J. Dent. Res.* **51,** No. 6, 1614-1618 (Nov.-Dec. 1972).

Key words: Antioxidants; biomaterials; comonomers; inhibitors; polymerization; stabilizers; toxicity.

BHM (3,5-di-*t*-butyl-4-hydroxybenzyl methacrylate) was evaluated with regard to its effectiveness as a stabilizer (polymerization inhibitor). This sterically-hindered phenol containing a methacrylate moiety was an effective stabilizer but it had lower efficiency than BHT (2,6-di-*t*-butyl-4-methylphenol). This is attributed to the greater steric hindrance at the *para* position and lower electron-donating nature of the *para*-substituent of the phenol, BHM. The homopolymer of BHM was prepared by polymerization of the methacrylate group, under anaerobic conditions, even though, under aerobic conditions it is an effective stabilizer.

Caswell, R. S., Coyne, J. J., **Secondary particle spectra produced by neutron interactions with tissue,** *Proc. 1st Symp. on Neutron Dosimetry in Biology and Medicine, Neuherberg/Munchen, Germany, May 15-19, 1972,* **1,** EUR 4896 d-f-e, 25-41 (Commission of European Communities, Luxenbourgh, Germany, Sept. 1972).

Key words: Energy deposition; neutron dosimetry; secondary particle spectra; tissue.

Some basic aspects of neutron interactions with tissue are discussed: energy transfer to matter according to element present in the tissue and by type of charged particle produced; calculations of secondary particle spectra produced when neutrons interact with tissue for 1 and 14 MeV neutron energy. Both the primary spectra of secondary particles as produced in the nuclear reactions, and the softer "slowing-down" or "equilibrium" spectra after particle slowing down are determined. The relative importance of the various secondaries (p, d, α, Be, B, C, N, O) are discussed. These spectra provide physical input information for calculations of neutron energy deposition (examples given) and for models of neutron radiation effects on biological materials.

Cezairliyan, A., Beckett, C. W., **Pulse calorimetry of solids at high temperatures,** Chapter 6 in *Thermochemistry and Thermodynamics,* H. A. Skinner, Ed., **10,** 159-175 (Butterworths, London, 1972).

Key words: Measurements at high temperatures; millisecond resolution; pulse calorimetry; solid electrical conductors.

Pulse techniques for the measurement of specific heat of solid electrical conductors at high temperatures are described. Design and operational characteristics of pulse calorimetric systems reported in the literature are summarized. Details of an accurate millisecond resolution pulse calorimeter are given.

Chang, S. S., **A calorimetric method for studying glass transition in highly crystalline polyethylene,** (Papers Presented at

American Chemical Society Meeting, Boston, Mass., Oct. 1971), *Polym. Prepr. Amer. Chem. Soc. Div. Polym. Chem.*, J. E. McGrath, Ed., **13**, No. 1, 322-326 (Apr. 1972).

Key words: Calorimetry; glass transition temperature; partially crystalline polymer; polyethylene; linear and branched; temperature drift method.

A sensitive calorimetric method is employed for the detection of the glass transition phenomena in highly crystalline polymers. This method is based upon the observation of the spontaneous temperature drifts in the glass transition range. The occurrence of the glass transition in a polyethylene sample of 96 percent degree of crystallinity can be demonstrated by this method. Three linear and one branched polyethylene samples were studied. The glass transition in polyethylene is found to occur at 235-240 K.

Chen, C. L., Phelps, A. V., **Absorption coefficients for the wings of the first two resonance doublets of cesium broadened by argon,** *Phys. Rev. A* **7,** No. 2, 470-479 (Feb. 1973).

Key words: Absorption coefficient; argon; broadening; cesium; resonance lines.

Measurements are reported of the absolute absorption coefficients in the wings of the 8944-, 8521-, 4593-, and 4555-Å resonance lines of cesium in the presence of argon at densities between about 6×10^{18} and 2×10^{19} atom cm^{-3}. The data extend from about 0.7 Å to as much as 600 Å from the line center and were obtained using cesium densities between 7×10^{11} and 2×10^{15} atom cm^{-3} and temperatures between 390 and 470 K. The measured absorption coefficients are proportional to the product of the cesium and argon densities as expected from line broadening produced by binary collisions between cesium and argon atoms. Using the quasistatic theory as a guide for interpretation, the line profiles for wings of the first resonance doublet show a transition from a wavelength dependence determined by long-range van der Waals forces to a dependence determined by the short-range internuclear potentials discussed by Hedges, Drummond, and Gallagher (HDG). The far-wing absorption profiles obtained in the present experiments are in good agreement with those calculated from the fluorescence data of HDG.

Christ, B. W., Smith, L. C., **A chemical polish for quick removal of grinding and lapping scratches from iron and low-carbon steel,** *J. Iron Steel Inst. Tech. Note*, p. 155 (Feb. 1973).

Key words: Chemical polish; iron; low-carbon steel; single phase alloys; swabbing.

The composition and use of a chemical polish for iron and low-carbon steel is described. Swabbing metallographic samples with this polish completely removes scratches left by 600 grit silicon carbide in about 5 seconds. Furthermore, the polished surfaces are flat enough for grain size analysis via optical microscope observation.

Costrell, L., **CAMAC: A review and status report,** (Proc. Symp. on Nuclear Science, Miami, Fla., Dec. 8, 1972), *IEEE Trans. Nucl. Sci.* **NS-20,** No. 1, 557-561 (Feb. 1973).

Danos, M., Greiner, W., Rafelski, J., **Fields nonlocal in Clifford space. I. Classical gauge-invariant nonlinear field theory,** *Phys. Rev. D* **6,** No. 12, 3476-3491 (Dec. 15, 1972).

Key words: Fermion-boson interactions; field theory; gauge invariance; hypercomplex coordinates; interacting fields; nonlinear field theory; nonlocal field theory.

A fully gauge-invariant, Lorentz-covariant, nonlocal, and nonlinear theory, for coupled spin-1/2 fields, ψ, and vector fields, A, i.e., "electrons" and "photons," is constructed. The field theory is linear in the ψ fields. The nonlinearity in the A fields arises unambiguously from the requirement of gauge invariance. The coordinates are generalized to admit hypercomplex values, i.e., they are taken to be Clifford numbers. The nonlocality is limited to the hypercomplex component of the coordinates. As the size of the nonlocality is reduced toward zero, the theory goes over into the inhomogeneous Dirac theory. The nonlocality parameter corresponds to an inverse mass and induces self-regulatory properties of the propagators. It is argued that in a gauge-invariant theory a graph-by-graph convergence is impossible in principle, but it is possible that convergence may hold for the complete solution, or for sums over classes of graphs.

Das, E. S. P., Marcinkowski, M. J., Armstrong, R. W., de Wit, R., **The movement of Volterra disclinations and the associated mechanical forces,** *Phil. Mag.* **27,** No. 2, 369-391 (Feb. 1973).

Key words: Disclination; dislocation; glide; plasticity; twist; Volterra; wedge.

An analysis is made of conservative and non-conservative movement of Volterra disclinations and the associated mechanical forces. It is shown that both disclination lines and their axes can experience a force under the action of an applied stress. A general equation is derived for the force on a disclination loop and its axis. The condition for conservative movement is derived. Examples illustrating these principles are given. Glide surfaces for disclination loops are defined. The motion is conservative on a surface generated by rotating the disclination line around its axis, and on a plane normal to the axis. It is shown how a twist loop can be converted to a wedge loop and, *vice versa*, conservatively.

Davis, D. D., Braun, W., Bass, A. M., **Reactions of $Cl^2P_{3/2}$: Absolute rate constants for reaction with H_2, CH_4, C_2H_6, CH_2Cl_2, C_2Cl_4, and c-C_6H_{12},** *Int. J. Chem. Kinet.* **II,** 101-114 (1970).

Key words: Absolute rate constants; atom-molecule reactions; chlorine atoms; resonance fluorescence.

The absolute rate constants have been measured for several gas-phase chlorine atom-molecule reactions at 25 °C by resonance fluorescence. These reactions and their corresponding rate constants in units of cm^3 mole^{-1} sec^{-1} are:

$$Cl^2P_{3/2}+H_2 \xrightarrow{k_1} HCl+H \qquad k_1=1.4\pm0.1\times10^{-14}$$

$$Cl^2P_{3/2}+CH_4 \xrightarrow{k_2} HCl+CH_3 \qquad k_2=1.5\pm0.1\times10^{-13}$$

$$Cl^2P_{3/2}+CH_2Cl_2 \xrightarrow{k_5} HCl+CHCl_2 \qquad k_5=5.5\pm0.5\times10^{-13}$$

$$Cl^2P_{3/2}+C_2Cl_4 \xrightarrow{k_6} C_2Cl_5 \qquad k_6=5.3\pm0.5\times10^{-12}$$

$$Cl^2P_{3/2}+C_2H_6 \xrightarrow{k_7} HCl+C_2H_5 \qquad k_7=6.7\pm0.7\times10^{-11}$$

$$Cl^2P_{3/2}+c\text{-}C_6H_{12} \xrightarrow{k_8} HCl+c\text{-}C_6H_{11} \qquad k_8=2.0\pm0.2\times10^{-10}$$

The effects of varying the substrate pressure, total pressure, light intensity and chlorine-atom source on the value of the bimolecular rate constants have been investigated for all these reactions. Conditions under which no competing side reaction occurs were established and the reported rate constants were measured under these conditions. For reactions (2), (5), (6), (7), and (8), there is a discrepancy of a factor of two between the rate constants measured in this work and values in the literature; it is suggested that this is due to an error in the previously measured value of k_{CH_4}/k_{H_2} upon which the relative measurements in the literature ultimately depend.

Davis, D. D., Herron, J. T., Huie, R. E., **Absolute rate constants for the reaction $O(^3P)+NO_2\rightarrow NO+O_2$ over the temperature range 230-339 K,** *J. Chem. Phys.* **58,** No. 2, 530-535 (Jan. 15, 1973).

Key words: Kinetics; nitrogen dioxide; oxygen atoms; rate constants; stratosphere.

Using the technique of flash photolysis-resonance fluorescence, absolute rate constants have been measured for the reaction $O(^3P)+$

$NO_2 \rightarrow NO + O_2$. Over the temperature range 230-339 K, the rate constant was found to have the value $k = 9.12 \pm 0.44 \times 10^{-12}$ cm^3 molecule^{-1} sec^{-1}, independent of temperature. At stratospheric temperatures, this rate constant is about a factor of two faster than indicated from previous measurements.

Dibeler, V. H., Walker, J. A., **Photoionization of acetylene near threshold,** *Int. J. Mass Spectrom. Ion Phys.* **11,** 49-56 (1973).

Key words: Franck-Condon factors; mass spectrometry; photoionization; Rydberg series; vacuum ultraviolet.

Photoion yield curves for C_2H_2 and C_2D_2 cooled to 118 K are remeasured at 0.2 Å intervals from ionization threshold to about 0.6 eV above threshold. Clearly defined autoionization features are observed superimposed on vibrational step structure. The latter observation suggests molecular predissociation occurring in competition with the autoionization process. A simple means of estimating Franck-Condon factors for the direct ionization in the presence of autoionization gives values in agreement with photoelectron spectroscopy data. Comparisons of observed and calculated Rydberg levels converging to vibrationally excited states of the molecular ion are discussed briefly.

Dillon, T. A., Stephenson, J. C., **Calculation of vibrational and rotational energy transfer between HF, DF, HCl, and CO_2,** *J. Chem. Phys.* **58,** No. 5, 2056-2064 (Mar. 1, 1973).

Key words: Energy transfer; HF, DF, CO_2; linewidth; unitary.

A theory of vibrational energy transfer which retains the exponential form of the scattering operator is applied to energy transfer between vibrationally excited HF, DF, HCl, and CO_2. The calculations contain several new features, including use of curved classical trajectories and vibrational wavefunctions obtained numerically from an RKR potential. Cross sections for multiquantum pure rotational changes caused by the dipole-quadrupole interaction are calculated. These multiquantum rotational transitions play an important role in vibrational energy exchange by allowing large vibrational energy defects to be absorbed by the rotational degrees of freedom. Agreement between theory and experiment is excellent. Cross sections calculated for simultaneous transfer of two vibrational quanta from HF or HCl to CO_2 are very small. However, for DF-CO_2 the calculated two-quantum-transfer cross section is only a factor of 2-6 smaller than that for single-quantum transfer.

Garvin, D., **Critical data for the physical sciences,** (Papers Presented to the Council of Biology Editors, Carleton University, Ottawa, Canada, May 11, 1970), *CBE Newsletter,* pp. 6-11 (Sept. 1970).

Geist, J., Zalewski, E., **Chinese restaurant nomenclature for radiometry,** *Appl. Opt.* **12,** No. 2, 435-436 (Feb. 1973).

Greer, S. C., **The CH_4=Kr solid phase diagram,** *Phys. Lett.* **43A,** No. 1, 73-74 (Feb. 12, 1973).

Key words: Crystal structure; krypton; methane; mixture, binary solid.

X-ray diffraction studies on solid mixtures of CH_4 and Kr show complete miscibility on a face-centered cubic lattice from 21K to the melting curve.

Hadley, S. G., Keller, R. A., **Direct determination of the singlet → triplet intersystem crossing quantum yield in naphthalene, phenanthrene, and triphenylene,** *J. Phys. Chem.* **73,** No. 12, 4356-4359 (1969).

Key words: Aromatics; electronic spectroscopy; intersystem crossing; quantum yields; triplet states.

Radiationless singlet → triplet intersystem crossing quantum yields have been directly determined. The technique used depends upon using previously determined extinction coefficients to relate the optical density of the triplet ← triplet absorption and the absolute intensity of the light used to generate triplet state molecules to the intersystem crossing quantum yield. The quantum yields at 77 K in a rigid matrix and their estimated uncertainties were found to be naphthalene-h_8, 0.25 ± 0.05; naphthalene-d_8, 0.25 ± 0.05; phenanthrene-h_{10}, 0.35 ± 0.07; phenanthrene-d_{10}, 0.45 ± 0.09; triphenylene-h_{12}, 0.54 ± 0.11; and triphenylene-d_{12}, 0.88 ± 0.18. No significant deuterium isotope effects were noted on the intersystem crossing quantum yields.

Hagan, L., **Reports of observatories for 1971/72, National Bureau of Standards, Washington, D.C.,** *Bull. Amer. Astron. Soc.* **5,** No. 1, Part II, 201-204 (Jan. 1973).

Hall, J. L., **The lineshape problem in laser-saturated molecular absorption,** Paper in *Lectures in Theoretical Physics,* K. T. Mahanthappa and W. E. Brittin, Eds., **XII,** 161-210 (Gordon and Breach, Sci. Publ. Inc., New York, N.Y., Mar. 1973).

Key words: Absorption; laser; molecular; saturation.

The use of lasers makes it possible to observe non-linear optical absorption in molecules. Experiments involving two running waves represent a particularly interesting case, as they allow observation of a very sharp "emission" feature when the radiation frequency matches the natural molecular absorption frequency. This resonance feature has a width characteristic of *natural* rather than Doppler broadening. This paper presents a physical discussion of the main features of the saturated absorption process, with particular emphasis on realistically representing inherent experimental conditions as they affect the mathematical formulation. In a certain approximation, one finds a power-broadened Lorentzian lineshape, in agreement with a fairly broad class of experimental results. A pair of coupled differential equations is derived which should represent the lineshape under more general conditions. The saturation process provides a selection mechanism *against* particles which experience a collision during their coherent interaction with the radiation. The implications of this effect for laser collision physics experiments are examined in some details.

Herron, J. T., **An evaluation of rate data for the reactions of atomic oxygen (O^3P) with methane and ethane,** *Int. J. Chem. Kinet.* **1,** 527-539 (1969).

Key words: Atomic oxygen; ethane; evaluation; methane; rate data.

This review presents in tabular and graphical form rate data on the reactions of atomic oxygen (O^3P) with methane and ethane. The reliability of these data is discussed and suggested values of the rate constants are given over specified temperature intervals. Specific values are given for 298 and 1000 K.

Herron, J. T., Huie, R. E., **Rate constants for the reactions of O_2 $^1\Delta_g$ with 2,3-dimethyl-2-butene and 2,5-dimethylfuran,** *J. Chem. Phys.* **51,** No. 9, 4164-4165 (Nov. 1, 1969).

Key words: Chemical kinetics; mass spectrometry; olefins; rate constant; singlet oxygen; O_2 $^1\Delta_g$.

Rate constants for the gas phase reactions of O_2 $^1\Delta_g$ have been measured using a mass spectrometric technique at 300 K. Results are k(2,5-dimethylfuran) $= 1.6 \pm 0.4 \times 10^{10}$ cm^3 mol^{-1} s^{-1} and k(2,3-dimethyl-2-butene) $= 1.0 \pm 0.3 \times 10^9$ cm^3 mol^{-1} s^{-1} (estimated uncertainties). Additional rate constants relative to the rate constant for 2,3-dimethyl-2-butene have been measured as follows: 2,3 dimethyl-2-pentene, 0.7; 1-methylcyclopentene, 0.015; 1,2-dimethylcyclopentene, 0.4; 1,2-dimethylcyclohexene, 0.4; and 1,3-cyclohexadiene, 0.09.

Horn, W. A., **Determining optimal container inventory and routing,** *Transp. Sci.* **5,** No. 3, 225-231 (1971).

Horn, W. A., **Some fixed point theorems for compact maps and flows in Banach spaces,** *Trans. Amer. Math. Soc.* **149,** 391-404 (June 1970).

Hougen, J. T., **Reinterpretation of molecular beam hyperfine data for $^{14}NH_3$ and $^{15}NH_3$,** *J. Chem. Phys.* **57,** No. 10, 4207-4217 (Nov. 15, 1972).

Key words: Centrifugal distortion; hyperfine structure; inversion doublet; molecular beam; NH_3; quadrupole splitting.

Reassignments are presented for the hyperfine patterns of six $^{15}NH_3$ inversion doublets. The new assignments alter the sign of the nitrogen-hydrogen spin-spin interaction constant. Previous disagreement between theory and experiment for the hyperfine pattern of the $J=3$, $K=2$ $^{14}NH_3$ inversion doublet is removed by including the effect of centrifugal distortion on the quadrupole splitting. An explanation is presented for a discrepancy remaining in the fit of the $J=K=6$ hyperfine pattern of $^{15}NH_3$.

Kaldor, A., Maki, A. G., Dorney, A. J., Mills, I. M., **The assignment of ν_2 and ν_4 of SO_3,** *J. Mol. Spectrosc.* **45,** No. 2, 247-252 (Feb. 1973).

Key words: Air pollution; infrared spectra; molecular structure; Raman spectra; spectra; sulfur trioxide.

Three experiments have been performed to resolve an uncertainty in the assignment of ν_2 and ν_4 for SO_3: (i) the gas phase Raman spectrum has been measured; (ii) the infrared active combination band $\nu_3+\nu_4$ has been measured; (iii) a band contour calculation has been performed taking account of the l-type resonance in ν_4 and a strong Coriolis resonance between ν_2 and ν_4. These experiments establish beyond any doubt that ν_2 lies at about 497.5 cm^{-1} and ν_4 lies at about 530.2 cm^{-1}. The contour calculation also shows that the Coriolis resonance gives rise to a positive intensity perturbation.

Keller, R. A., **Effect of quenching of metastable triplet states in organic dye lasers,** *IEEE J. Quantum Electron.* **QE-6,** No. 7, 411-416 (July 1970).

Key words: Dye lasers; lasers; quenching agents; triplet states.

The effect of quenching of metastable triplet states upon the efficiency of organic dye lasers is considered in detail by solving the coupled differential equations describing the laser process. It is shown that specific quenching agents for excited triplet states can 1) cause a dramatic increase in the laser efficiency, 2) negate the previous requirements of very fast pumping sources, and 3) permit the use of dyes with relatively small fluorescence quantum yields. The addition of quenching agents that quench both singlet and triplet states (such as molecular oxygen) generally improves the efficiency although not as dramatically. Steady-state solutions were developed that lead to analytical expressions for the laser efficiency and the concentrations of the excited states as a function of time.

Kessler, E. G., Jr., **Determination of the Rydberg constant from the He II n=3-4 (469-nm) line complex,** *Phys. Rev. A* **7,** No. 2, 408-415 (Feb. 1973).

Key words: Fine structure; helium; Rydberg constant.

The Rydberg constant has been determined from absolute wavelength measurements on two fine-structure components of the He II n=3-4 transition. The He II transition was excited in a liquid-nitrogen-cooled hollow cathode. A pressure-scanned Fabry-Perot spectrometer was used to compare the He II wavelengths with a ^{198}Hg standard source. The measured value of the Rydberg is $R_\infty=109\,737.3208\pm0.0085$ cm^{-1}, where the uncertainty is one standard deviation.

Krauss, M., **Energy surfaces for energy transfer and chemical reaction,** *Proc. IBM Scientific Computing Symp. on Computers in Chemistry, Poughkeepsie, N.Y., Oct. 6-17, 1968,* pp. 65-76 (1969).

Key words: *Ab initio* calculations; HF approximation; schematic mechanism; simple prototypes.

The calculations described are an indication of the possibilities of *ab initio* calculations. They provide the necessary data for an accurate scattering calculation or a test of a schematic mechanism deduced from experiment. For carefully chosen systems, the HF approximation is sufficient and the present results point to obviously analogous systems, for which these results would be useful. The extent to which this is done depends almost entirely on the cost. Table I gives the time on an IBM 7094-I for a representative point on the surface depicted herein. The systems are simple prototypes, and the extension to larger, more practicable ones would considerably increase the times. This is especially true for the correlated calculations which must be seriously considered for the general problem. But the present results and those from many other sources would strongly indicate that it is very worthwhile to spend the effort required to adapt these problems to the new generation of computers.

Kulin, G., **Discussion of the paper "Free overfall as a flow measuring device" by S. W. Bauer and W. H. Graf,** *Proc. Amer. Soc. Civil Eng., Irrigation Drainage Div.* **98,** IR1, Paper 8750, 159-165 (Mar. 1972).

Kurylo, M. J., Huie, R. E., **Flash photolysis resonance fluorescence study of the addition of $O(^3P)$ atoms to C_2H_4 and C_2D_4 at 298 K,** *J. Chem. Phys. Letters to Editor* **58,** No. 3, 1258-1259 (Feb. 1, 1973).

Key words: Ethylene; flash photolysis; kinetics; oxygen atoms; resonance fluorescence.

The flash photolysis resonance-fluorescence technique has been used to measure the rates of the reactions $O+C_2H_4$ and $O+C_2D_4$ at atom concentrations near 10^{11} cm^{-3}. A computer simulation of the reaction system indicates that at values of $[C_2H_4]/[O]>1000$ secondary reactions of the O atoms are nonexistent. Under these conditions we confirm our earlier number for $O+C_2H_4$ with $k_1(C_2H_4)=7.96\times10^{-13}$ cm^3 $molec^{-1}$ s^{-1} and find $k_1(C_2D_4)=8.18\times10^{-13}$ cm^3 $molec^{-1}$ s^{-1}. The estimated precision is ±10 percent.

Kurylo, M. J., Peterson, N. C., Braun, W., **Absolute rates of the reactions $H+C_2H_4$ and $H+C_2H_5$,** *J. Chem. Phys.* **53,** No. 7, 2776-2783 (Oct. 1, 1970).

Key words: Ethyl radicals; ethylene; hydrogen atoms; kinetics; resonance fluorescence.

The hydrogen atom–ethylene system was studied at 298 K employing the methods of resonance fluorescence and absorption by hydrogen atoms of Lyman α radiation at 1216 Å. The contribution of hydrogen atom–radical reactions was evaluated under varying experimental conditions, and the rate of disappearance of H atoms in ethylene was measured under conditions where stoichiometric corrections became significant. Measurements in the literature of reaction rates for $H+C_2H_4$ at low total pressure are now in good agreement; however the limiting high-pressure absolute rate constants thus far reported differ depending on the assignment of stoichiometric factors. Our results indicate that stoichiometric factors obtained under low-pressure conditions may not be applicable to high pressure. Furthermore, extrapolations based on plots of inverse rate constant vs inverse pressure may be in error due to significant curvature in such plots. Our high-pressure limiting rate constant for $H+C_2H_4$, extrapolated from data at pressures higher than those used by other workers, is free to stoichiometric corrections and is in agreement with our earlier measurements. Absolute rate constants obtained in this work are

$$H+C_2H_4\rightarrow k_1=13.6\pm1.9\times10^{-13}\ (cm^3\ molecule^{-1}\cdot sec^{-1})$$
(extrapolated to infinite He pressure),

$$H+C_2H_5\rightarrow k_4=6.0\pm2.0\times10^{-11}\ (cm^3\ molecule^{-1}\cdot sec^{-1})$$(50 torr He).

The latter rate has been estimated from the variation of the rate of disappearance of H atoms as a function of initial H atom concentration at 50 torr total pressure.

Ledbetter, H. M., **Poisson's ratio for polycrystals,** *J. Phys. Chem. Solids* **34,** No. 4, 721-723 (Apr. 1973).

Key words: Cauchy relations; elastic constants of solids; elasticity; Poisson ratio; polycrystals.

Accepted views concerning Poisson's ratio for central-force polycrystals are amended. For polycrystals the ratio can vary from 1/4, which is actually a lower limit. An upper limit of Poisson's ratio exists also. Both limits can be calculated from single-crystal elastic data. The limits correspond to Voigt's and Reuss's states of uniform local strain and of uniform local stress, respectively.

Lester, W. A., Jr., Krauss, M., **Interaction potential between Li and HF,** *J. Chem. Phys.* **52,** No. 9, 4775-4781 (May 1, 1970).

Key words: Hartree-Fock approximation; induction energy; interaction potential; radial coefficients; scattering calculations.

The interaction potential between Li and HF has been determined in the Hartree-Fock approximation. An expression for the interaction potential has been determined in the case of fixed internuclear distance of HF in a form suitable for scattering calculations. The results are tabulated as radial coefficients for the intermolecular potential expressed as $V(r,\theta)=\Sigma_l v_l(r)P_l(\cos\theta)$. At long range, the Hartree-Fock calculation determines the induction energy of a spherical atom Li interacting with a dipolar molecule HF. For the approach of the Li atom toward the F atom, there is a minimum in the energy for a Li to HF center-of-mass distance of 4 a.u. Most of the hemisphere on the F side of the surface ultimately leads to reaction. On the other hand, the spherically symmetric component of the intermolecular potential, $(v_0(r)$, has a minimum at about 9 a.u. which is related to the potential well deduced from glory scatter data.

Levin, I. W., Abramowitz, S., **Isotopic splitting in matrix isolated BF_3,** *Chem. Phys. Lett.* **9,** No. 3, 247-248 (May 1, 1971).

Key words: BF_3; Coriolis; isotope effects; vibrational force field.

Small isotopic frequency shift information, if precisely determined, provides an effective constraint on intramolecular force fields. The most precise data for these frequency shift parameters $\Delta\theta$ are derived from high resolution, gas-phase infrared spectral analyses. In the present study, we compare for BF_3 the isotopic frequency shift $\Delta\theta_4$ from a recently published gas-phase study with the value for $\Delta\theta_4$ that we obtain from the spectrum of matrix isolated BF_3. The excellent agreement between the two methods suggests further applications of the matrix technique for obtaining precise frequency shift data.

Linzer, M., Stokesberry, D. P., **A frequency-lock method for the measurement of Q factors of reflection and transmission resonators,** *IEEE Trans. Instrum. Meas.* **IM-22,** No. 1, 61-77 (Mar. 1973).

Key words: Automatic Q measurement; frequency-lock method; Q measurement; reflection resonators; transmission resonators.

A new method for the measurement of Q factors of reflection (single-ended) and transmission (double-ended) resonators has been developed. The basis of the technique is the locking of an oscillator to some point away from the center of the resonator response curve. This is accomplished by the introduction of a phase offset into a conventional oscillator-resonator stabilization circuit so as to make the stabilizer sensitive to both the real and imaginary portions of the voltage transfer coefficient of the resonator. From a determination of the phase and frequency shifts, the Q factor may be evaluated.

The frequency-lock method shows promise of having significant advantages in speed, convenience, and accuracy over previous techniques. The basic features of this approach were successfully demonstrated in a measurement of the Q factor of an X-band reflection cavity. A circuit for fully automatic Q determinations is proposed. In this mode of operation, the device should be insensitive to changes in the eigen-frequency of the resonator and should be capable of measuring very small changes in Q.

Loebenstein, W. V., **Heats of adsorption of ammonia and carbon dioxide on tooth components,** *J. Dent. Res.* **51,** No. 6, 1529-1536 (Nov.-Dec. 1972).

Key words: Adsorption; ammonia adsorption; carbon dioxide adsorption; dentin; dental adhesive; heats of adsorption; surface area.

The study demonstrates how heats of adsorption and area of coverage can be used as criteria for comparing the ultimate strength of chemically reactive groups for incorporation in potential dental adhesives. Carbon dioxide and ammonia were chosen as the reactants because they typified acidic and basic groups, respectively, and were both gases. Measurements were confined to the region of reversible adsorption in order to assure reproducibility of the adsorbent surface. The presence of collagen exerted a profound influence on the BET area depending upon the gas used when compared with nitrogen. Ammonia exhibited a higher surface area as well as a higher heat of adsorption on dentin than did carbon dioxide. It would therefore qualify as a better adhesive under the conditions of comparison. The surface area of dentin available to ammonia, however, was no greater than the surface area of anorganic dentin. The average heat of adsorption of ammonia on anorganic dentin based on anorganic whole teeth is estimated to be at least as large as it is for whole dentin. Thus, it would appear that the presence of collagen did not contribute to the adhesive strength of ammonia.

Maienthal, E. J., **Determination of trace elements in silicate matrices by differential cathode ray polarography,** *Anal. Chem.* **45,** No. 4, 644-648 (Apr. 1973).

Key words: Alloys; analyses; cast irons; differential cathode ray polarography; high-purity materials; metals; steels; trace elements.

Methods are described for the analysis of some new Trace Elements in Glass Standard Reference Materials by differential cathode ray polarography. Iron and titanium were determined in the 500-, 50-, 1-, 0.02-ppm and base glasses after cupferron and ammonium hydroxide separations. Nickel was determined in the 500- and 1-ppm samples after extraction with dimethylglyoxime.

Marshall, H. E., **Cost sharing and multiobjectives in water resource development,** *Water Resour. Res.* **9,** No. 1, 1-10 (Feb. 1973).

Meijer, P. H. E., Colwell, J. H., Shah, B. P., **A note on the morphology of heat capacity curves,** *Amer. J. Phys.* **41,** No. 3, 332-339 (Mar. 1973).

Key words: Brillouin function; density of states; Einstein function; energy levels; harmonic oscillator; heat capacity; molecular field; molecular rotation; Schottky anomaly.

In this article we try to relate the general features of several types of heat capacity curves to the underlying energy level spectrum. We are interested in heat capacity "anomalies" (i.e., heat capacities which occur in addition to the usual lattice vibration and conduction electron contributions) and restrict ourselves to systems which can be described on an independent particle basis. We begin by considering Schottky anomalies and show the effects on the heat capacity of varying the spacings and degeneracies of the energy levels. The relation between the Schottky anomaly arising from the equally spaced nondegenerate levels of the Brillouin function and the heat capacity of the Einstein function is discussed. The effects on the heat capacity of a marked local change in the density of states of an otherwise uniform energy-level spectrum is considered. The heat capacities of the free rotor and the molecular field model are used to exemplify particular points of the discussion.

Meijer, P. H. E., Niemeijer, Th., **Search for the ground state of cerous magnesium nitrate by an extended Luttinger-Tisza method,** *Phys. Rev. B* **7,** No. 5, 1984-1988 (Mar. 1, 1973).

Key words: Antiferromagnetism; cerium magnesium nitrate; digital representation; dipole-dipole interaction; ground state; Luttinger-Tisza method; neodimium magnesium nitrate; superlattice.

The ground state of cerous magnesium nitrate is determined using the assumptions that the spins are coupled by purely dipolar forces, the magnetic structure is periodic after eight or less lattice periods, and the spins can be considered as classical vectors. The ground state has a layered antiferromagnetic structure as described in the text. A study is made to see whether this result is dependent on the assumption that the g factor parallel to the crystallographic c axis is zero or almost zero for this specific salt. The conclusion is that this is to a large extent not the case. The ground state lies at an energy -1.867 mdeg K, using the lattice constants as given by Schiferl.

Melmed, A. J., Carroll, J. J., **Field-ion microscopy of osmium,** *J. Less-Common Metals* **30,** 199-204 (1973).

Key words: Field-ion microscopy; osmium.

Osmium has been successfully imaged in the field-ion microscope using helium ions at temperatures of about 87 K and lower. Specimen preparation procedures and details of image characteristics are described.

Meshkov, S., **Review of hadron spectroscopy,** (Proc. Int. Conf. on Duality and Symmetry in Hadron Physics, Tel Aviv, Israel, Apr. 5-7, 1971), Chapter 8 in *International Conference on Duality and Symmetry in Hadron Physics,* E. Gotsman, Ed., pp. 252-316 (The Weizmann Science Press of Israel and The Jerusalem Academic Press, Jerusalem, Israel, 1971).

Mies, F. H., **Molecular theory of atomic collisions: Calculated cross sections for $H^+ + F(^2P)$,** *Phys. Rev. A* **7,** No. 3, 957-967 (1973).

Key words: Atomic collisions; fine-structure transitions; HF^+ molecule; molecular states; quantum chemistry.

The results of a close-coupling calculation of the fine-structure transitions $(j,m_j \rightarrow j',m_j')$ are presented for collisions between photons and $F(^2P_{j,mj})$. The theory is formulated in the perturbed-stationary-state approximation using accurate molecular wave functions for the ground $^2\Pi$ and $^2\Sigma$ states of HF^+. Comparison is made to the predictions of the Born approximation. The magnetic selection rule $(j,m_j \rightarrow j,-m_j)$ is strongly violated in the $j=3/2$ state and less strongly violated in the $j=1/2$ state. It is concluded that the important region of interaction for the $j=1/2 \rightarrow j=3/2$ transition is at short-to-intermediate distances where accurate molecular potentials are required and close-coupling effects are dominant.

Mies, F. H., **Molecular theory of atomic collisions: Fine-structure transitions,** *Phys. Rev. A* **7,** No. 3, 942-957 (Mar. 1973).

Key words: Atomic collisions; fine-structure transitions; HF^+ molecule; molecular states; quantum chemistry.

The theory of fine-structure transitions in atom-atom collisions is formulated in terms of the molecular states of the diatomic collision complex. The Born-Oppenheimer (BO) electronic wave functions are implicit functions of the interatomic coordinate R, and the molecular theory is analogous to the "perturbed-stationary-state" method. Expansion in *molecular* channel states incorporates the effects of polarization, exchange, and valence forces on the electronic portion of the scattering wave function and embodies the "adiabatic" contribution of the entire set of closed-channel excited states that are generated in the more usual asymptotic-atomic-state expansion. The channel states are expressed explicitly in terms of the body-fixed molecular wave functions, and the resultant interaction matrix elements in the close-coupling scattering formalism are related to the molecular potentials. The theory is developed specifically for proton collisions with the fluorine atom in its ground $^2P_{j,mj}$ state, with explicit account being taken of the spin-orbit splitting between the $j=3/2$ and $j=1/2$ multiplet states. Use is made of the accurate $HF^+(^2\Pi)$ and $HF^+(^2\Sigma)$ wave functions calculated by Wahl, Julienne, and Krauss. These molecular states asymptotically approach $H^+ + F(^2P)$, and accurate quadrupole and induced-dipole interaction parameters which describe the asymptotic interaction potentials are obtained from the calculations. Estimates are made of the BO coupling terms and they are found to be negligible compared to the spin-orbit couplings. In the following paper close-coupling calculations are made of the cross sections for the fine-structure transitions $(j,m_j \rightarrow j',m_j)$.

Paffenbarger, G. C., Rupp, N. W., **Research techniques used in evaluating dental materials,** *J. Amer. Dent. Ass.* **86,** 643-651 (Mar. 1973).

Key words: Biological; chemical; physical; reliable; specification; use; valid.

Evaluation of dental materials is an exact science that is dependent on several disciplines to be effective. Physical, mechanical, chemical, biological and clinical or user tests must be coordinated with maximum and/or minimum values for each evaluation. In the acceptance of a material for use in dentistry each of these areas must be accurately defined. Then for specifications prescribing the quality of a material for use in dentistry each of these areas must be accurately defined. Then for specifications prescribing the quality of a material the pertinent or relevant properties are determined and tests established to measure these characteristics. The design of suitable specification tests that are both reliable and valid is no mean research task. By reliable it is meant that a test can be repeated satisfactorily by different laboratories. By valid is meant that the tests will predict the behavior of the materials in service. These tests will predict the behavior of the materials in service. These tests of necessity must provide answers quickly within days as compared to years in service, thus are often abusive in nature. Silicate cements and acrylic resins are two materials used to illustrate various tests and their development.

Paffenbarger, G. C., **The role of dental materials in the prevention of dental diseases,** *Int. Dent. J.* **22,** No. 3, 343-349 (Sept. 1972).

Key words: Caries; dental materials; plastics; prevention; sealants; tooth loss.

The permanent tooth loss per hundred of 13 year olds averaged 6 for Norwegians and 100 for Americans because of early treatment of caries of the Norwegians with dental restorative materials.

Recurrent caries occurs less frequently around restorations of silicate cement than around any other restorative material. The same holds for caries of surfaces of adjacent teeth in contact with silicate cement restorations. The anticariogenic effect is probably caused by the transfer of fluoride ions to the dental enamel, thereby rendering it less soluble. Newly developed plastic formulations appear to seal developmental defects in teeth so as to greatly retard dental caries which so frequently occurs at such sites.

Recurrent caries around restorations should be reduced if a chemical bond of the tooth-filling interface could be achieved. Promising developments are available.

Radebaugh, R., Frederick, N. V., Siegwarth, J. D., **Flexible laminates for thermally grounded terminal strips and shielded electrical leads at low temperatures,** *Cryogenics* **13,** No. 1, 41-43 (Jan. 1973).

Key words: Cryostat; laminate; photoetching; thermal grounding; transmission line.

It is shown how to make compact, thermally grounded terminal strips for electrical leads in cryostats from flexible electrical laminates composed of copper foil bonded to a polyimide film. Laminates of lead foil and polyimide film are used to make a superconducting strip line, a type of transmission line in which it is easy to thermally ground both conductor and shield. The thermal resistance across a laminate was measured between 0.02 and 4 K from which the thermal conductivity of polyimide film is deduced between 0.1 and 4 K.

Rasberry, S. D., **Investigation of portable x-ray fluorescence analyzers for determining lead on painted surfaces,** *Appl. Spectrosc.* **27,** No. 2, 102-108 (Mar.-Apr. 1973).

Key words: *In situ* lead detection; lead detection; leaded paint detection; portable lead detectors; portable x-ray fluorescence analyzers.

Four portable x-ray fluorescence analyzers have been examined to ascertain the detection limits and precision with which they can be used for determining lead on painted surfaces. The tests consisted of using the analyzers to determine the weight of lead present (mg/cm²) on each of several substrates which had been coated with weighed quantities of paints of known composition. All of the instruments tested had detection limits lower than 1.0 mg/cm². In some measurements, where lead was present between 1.0 and 6.6 mg/cm², errors as large as 30 to 50 percent occurred; thus, it was concluded that the portable analyzers tested would be useful mainly for screening painted walls for high lead levels.

Rodriguez-Pasqués, R. H., Steinberg, H. L., Harding, J. E., Mullen, P. A., Hutchinson, J. M. R., Mann, W. B., **Low-level radioactivity measurements on aluminum, steel and copper,** *Int. J. Appl. Radiat. Isotop.* **23,** No. 10, 445-464 (1972).

Roth, R. S., Parker, H. S., Brower, W. S., **Comments on the system Ag_2S-In_2S_3,** *Mater. Res. Bull.* **8,** 333-338 (1973).

Key words: Chalcopyrite-type; silver indium sulfide; spinel-type; wurtzite-type.

The high temperature polymorph of $AgInS_2$ has been found to be orthorhombic with $a=7.001$, $b=8.278$, $c=6.698$Å, space group probably $Pna2_1$ with a distorted wurtzite structure. The phase transition temperature was found to be 620 ± 10 °C and the melting point 880 ± 10 °C. A new cubic spinel type phase was found at the composition $AgIn_5S_8$ with $a=10.827$Å.

Roth, R. S., Parker, H. S., Brower, W. S., **Crystal chemistry of lithium in octahedrally coordinated structures. III. A new structure-type in the system K_2O:Li_2O:TiO_2 ($K_xLi_xTi_{4-x/2}O_8$),** *Mater. Res. Bull.* **8,** 327-332 (1973).

Key words: Coordination of Li^+ ion; crystal structure; non-stoichiometric phase; system K_2O:Li_2O:TiO_2.

A new compound in the system K_2O:Li_2O:TiO_2 corresponding to the formula $K_xLi_xTi_{4-x/2}O_8$ was found to be orthorhombic with a= 3.821, b= 15.921, c= 2.973A space group Cmcm. The similarity between this unit cell and those of $Rb_xMn_xTi_{2-x}O_4$ and FeO(OH) has been used to predict the structure of this new phase. From the composition of this phase and that of the hollandite and ramsdellite phases in this system, it can be deduced that some of the Li^+ ions occur in the tunnels as well as in octahedral coordination substituting for titanium.

Rowe, J. M., Hinks, D. G., Price, D. L., Susman, S., Rush, J. J., **Single crystal neutron diffraction study of sodium cyanide,** *J. Chem. Phys.* **58,** No. 5, 2039-2042 (Mar. 1, 1973).

Key words: Angular distribution; crystal structure; cyanide ion; Debye-Waller factor; neutron diffraction; orientational disorder; potassium cyanide; sodium cyanide.

The neutron diffraction pattern of a single crystal of cubic NaCN has been measured at 295 K. These data and earlier results for KCN at 180 and 295 K have been analyzed in terms of a model which expands the angular distribution of CN^- orientations in symmetry-adapted spherical harmonics. From this analysis, the distributions of CN^- in these crystals have been derived, and these indicate a monotonic trend in the series KCN (295 K) thru KCN (180 K) to NaCN (295 K) involving a shift in preferential orientation from the [111] toward the [100] directions in the crystal. Unusually large translational Debye-Waller factors have also been derived for NaCN and KCN from the fitting procedure, in agreement with earlier results and analysis on KCN. In addition, an average C ≡ N bond distance of 1.18 Å is obtained.

Seltzer, S. M., Berger, M. J., **Photoneutron production in thick targets,** *Phys. Rev. C* **7,** No. 2, 858-861 (Feb. 1972).

Stromberg, R. R., McCrackin, F. L., **Ellipsometry as a tool for the characterization of surfaces,** (Proc. Symp. on Clean Surfaces: Their Preparation and Characterization for Interfacial Studies, North Carolina State University, Raleigh, N.C., Apr. 1968), Chapter in *Clean Surfaces: Their Preparation and Characterization for Interfacial Studies,* G. Goldfinger, Ed., pp. 65-76 (Marcel Dekker, Inc., New York, N.Y., 1970).

Key words: Characterization surface; ellipsometry; interfacial studies; optical constants; polarization of light; reflectivity.

The application of ellipsometry to the characterization of surfaces is discussed. The technique is very sensitive and is applicable to the detection of very thin contaminating films. It is often possible to characterize a surface under the same conditions required for further interfacial studies of the surface. The sensitivity of the method and the dependence of this sensitivity on factors such as refractive index differences, angle of incidence, and number of reflections are discussed relative to the problem of surface characterization and detection of contaminating films. The technique is not limited to highly reflecting surfaces and its applications to studies of surfaces of transparent materials are also described.

Waclawski, B. J., Plummer, E. W., **Field emission and photoemission surface studies (Extended Abstract),** *J. Vac. Sci. Technol.* **10,** No. 1, 292 (Jan./Feb. 1973).

Key words: Adsorption; carbon monoxide; field emission; hydrogen; metal surfaces; oxygen photoemission; tungsten.

Since the earliest days of vacuum science, one of the major goals sought by numerous investigators has been the understanding of the nature of the surface bond. Fundamental to this understanding is a determination of the electronic energy levels of a given adsorbate-adsorbent system. Recent advances in experimental techniques show promise of developing a "surface spectroscopy" analogous to the fruitful optical spectroscopy of atoms and molecules. The application of field emission and photoemission to surface spectroscopy has been investigated at NBS for a number of years. Field emission and photoemission electron energy distributions have been measured for tungsten under ultrahigh vacuum conditions and with exposures to gaseous contaminants. The following discussion will illustrate the capabilities, limitations, and complementary features of the techniques.

Wasik, S. P., Roscher, N. M., **Diffusion coefficients of paraffin-chain salts and the formation energetics of micelles,** *J. Phys. Chem.* **74,** No. 14, 2784-2787 (1970).

Key words: Decyltrimethyl ammonium bromide; diffusion coefficient; dodecyltrimethyl ammonium bromide; standard free energy; tetradecyltrimethyl ammonium bromide.

The diffusion coefficients of the colloidal electrolytes decyl, dodecyl, and t tradecyltrimethylammonium bromide have been measured as a function of concentration in aqueous solutions at 25°. These values compared favorably with values obtained from the theoretical expression derived by Hartley. A method is presented for determining the standard Gibbs free energy change of micelle formation from diffusion coefficient *vs.* concentration plots.

Wasik, S. P., Tsang, W., **Gas chromatographic determination of partition coefficients of some unsaturated hydrocarbons and their deuterated isomers in aqueous silver nitrate solutions,** *J. Phys. Chem.* **74,** No. 15, 2970-2976 (1970).

Key words: Aromatics; gas analysis; gas chromatography; isotope effect; isotopic separation; olefins; silver nitrate.

Experiments using aqueous solutions of silver nitrate as a gas chromatographic liquid phase have been carried out. Stability constants for the reaction, $(Ag^+)_{aq} + (Hydrocarbon)_{aq} \rightleftarrows (Ag^+.Hydrocarbon)_{aq}$, where $(Hydrocarbon)_{aq}$ are various light olefins, aromatics, or some of their deuterated isomers have been determined. For the olefins these values are in quantitative agreement with those obtained from conventional static techniques. In the case of ethylene $\Delta H = -23$ kJ/mol and $\Delta S = -38$ J/mol deg. The isotope effect for the solubility of benzene-d_6 (compared to the lightest isomer) in water is 1.05. Aqueous silver nitrate columns should also have interesting analytical applications, particularly in the field of isotopic separations. They appear to be more efficient than the conventional ethylene glycol-silver nitrate columns.

Waterstrat, R. M., **The vanadium-platinum constitution diagram,** *Met. Trans.* **4,** 455-466 (Feb. 1973).

Key words: Alloys; constitution diagram; equilibrium diagram; phase diagram; platinum; vanadium.

The system V-Pt was investigated over the entire composition range by metallography, x-ray diffraction and electron microprobe studies. There are at least four equilibrium intermediate phases in this system and they are stable to progressively high temperatures with increasing vanadium concentration. The phases which have been observed are: γ', cubic, Cu_3Au type; θ, tetragonal, $TiAl_3$ type; δ, orthorhombic, $MoPt_2$ type; ζ, orthorhombic, AuCd type; and β, cubic, Cr_3Si type (A15). The γ' phase is possibly metastable. A very stable ribbon-like growth of ζ phase in the fcc platinum terminal solid solution has been observed in alloys containing about 43 at. pct V. The platinum terminal solid solution forms a congruent melting maximum at about 1805 °C. A eutectic reaction occurs at 1720 ± 10 °C and a peritectic reaction is indicated at 1800 ± 10 °C. Vanadium is soluble in the fcc platinum terminal solid solution up to about 57 at. pct at 1720 °C. Platinum dissolves only to the extent of about 12 at. pct at 1800 °C in bcc α-V.

Yahalom, J., Ives, L. K., Kruger, J., **On the nature of films over corrosion pits in stainless steel,** *J. Electrochem. Soc.* **120,** No. 3, 384-386 (Mar. 1973).

Key words: Corrosion pits; electron microscopy; Fe-Cr alloys; passive films; stainless steel.

Thin films over corrosion pits in two commercial austenitic stainless steels, AISI 304 and 316, and three ferritic Fe-Cr alloys containing 5, 12 and 19 wt.% Cr were studied by means of transmission elec tron microscopy and scanning electron microscopy. It is shown that these films originally existed as the passive film on the metal surface. Electron diffraction and energy-dispersive x-ray analysis results are presented.

Young, R. H., Brewer, D., Keller, R. A., **The determination of rate constants of reaction and lifetimes of singlet oxygen in solution by a flash photolysis technique,** *J. Amer. Chem. Soc.* **95,** No. 2, 375-379 (Jan. 24, 1973).

Key words: Lasers; photochemistry; photooxidation; $^1\Delta O_2$.

A flash photolysis technique, employing a dye-laser as the flash excitation source, was developed to determine, directly, the rate constant of decay (k_d) of singlet oxygen ($O_2{}^1\Delta_g$) and rate constant of reaction (k_{rx}) between singlet oxygen and 1,3-diphenylisobenzofuran, DPBF, in a variety of solvents. Some results are the following: methanol, $k_d = (9.0 \pm 0.6) \times 10^4$ sec^{-1}, $k_{rx} = (1.3 \pm 0.1) \times 10^9$ sec^{-1} M^{-1}, $k_d/k_{rx} = 7.2 \times 10^{-5}$ M; *n*-butyl alcohol, $k_d = (5.2 \pm 0.8) \times 10^4$ sec^{-1}, $k_{rx} = (0.80 \pm 0.2) \times 10^9$ sec^{-1} M^{-1}, $k_d/k_{rx} = 6.5 \times 10^{-6}$ M; *tert*-butyl alcohol, $k_d = (3.0 \pm 0.4) \times 10^4$ sec^{-1}, $k_{rx} = (0.57 \pm 0.08) \times 10^9$ sec^{-1} M^{-1}, $k_d/k_{rx} = 5.3 \times 10^{-5}$ M. Values in benzene:methanol(4:1), bromobenzene:methanol(4:1), pyridine, dioxane, methanol:water(1:1), methanol:glycol(1:1), and glycol were also obtained. The resulting β values (k_d/k_{rx}) are in good agreement with β values determined in other ways. The technique was also shown useful for determination of absolute rate constants of reaction with or quenching of singlet oxygen by compounds such as 2,5-diphenylfuran and *N,N*-dimethylaniline.

Zimmerman, J. E., **A review of the properties and applications of superconducting point contacts,** *Proc. Conf. Applied Superconductivity, Annapolis, Md., May 1-3, 1972,* pp. 544-561 (IEEE, Inc., New York, N.Y., 1972).

Key words: Josephson effect; point contacts; superconductivity.

Superconducting small-area ("point") contacts are easily made in a number of forms, and are used in a wide variety of devices, some of which are quite highly evolved. For many practical purposes no special contact surface preparation is required. Electrical properties are often said to be "tunnel-junction like" or "metal-bridge like," but the meaning of these terms is not clear. New evidence shows that perfectly-clean metallic contacts often exhibit all the features expected of low-capacitance tunnel junctions. Permanently-stable point-contact devices have been made by one or a combination of several techniques, but their vulnerability to electrical and other transients has led to the development of simple and effective adjusting mechanisms. Certain point contacts, with minimum possible shunt capacitance and shunt normal conductance, approach the ideal of pure Josephson current elements ($i = i_c \sin \theta$) more closely than any other type of Josephson junction, and, for this reason, appear to be the best type of junction for millimeter-wave and far-infrared applications. Paradoxically, the dc-IV characteristics of such pure Josephson elements can be very complex if they are closely coupled to external circuit elements such as microwave cavities and resonances of impurity molecules.

**Publications with prices and SD Catalog numbers may be purchased directly from the Superintendent of Documents, U.S. Government Printing Office, Washington, D.C. 20402 (foreign: one-fourth additional). Microfiche copies are available from the National Technical Information Service (NTIS), Springfield, Va. 22151. Reprints from outside journals and the NBS Journal of Research may often be obtained directly from the authors.*

U. S. GOVERNMENT PRINTING OFFICE : 1973 O - 508-076

SJRA UNIVE300UA R 1
UNIVERSITY MICROFILMS INC
ATTN SERIALS SECTION
300 NORTH ZEEB RD
ANN ARBOR MI 48106

UNITED S
GOVERNMENT PRI
PUBLIC DOCUMENTS DEPARTMENT
WASHINGTON, D.C. 20402

OFFICIAL BUSINESS
PENALTY FOR PRIVATE USE, $300

S. DEPARTMENT OF COMMERCE
POSTAGE AND FEES PAID
375

JOURNAL OF RESEARCH of the National Bureau of Standards
A. Physics and Chemistry

Vol. 77A, No. 5 Sept.–Oct. 1973

Contents

Page

Enthalpies of precipitation of silver halides; entropy of the aqueous silver ion. Donald D. Wagman and Marthada V. Kilday. 569

Enthalpies of reaction of tris(hydroxymethyl)aminomethane in HCl(aq) and in NaOH(aq). Edward J. Prosen and Marthada V. Kilday. 581

The enthalpy of reaction of tris(hydroxymethyl)aminomethane with hydrochloric acid. Anthony P. Brunetti, Edward J. Prosen, and Robert N. Goldberg. 599

Theory of disclinations: IV. Straight disclinations. Roland deWit. 607

Optical properties of U centers in alkali halides and alkaline earth fluorides. Herbert S. Bennett. 659

Air flow rate as a test for gage block wringing. L. A. Guildner, R. L. Anderson, and R. E. Edsinger. 667

Low frost-point humidity generator. Lewis Greenspan. 671

Publications of the National Bureau of Standards. 679

Library of Congress Catalog Card Number: 62–37059

For sale by the Superintendent of Documents, U.S. Government Printing Office, Washington, D.C. 20402. (Order by SD Catalog No. C 13.22/sec.A:77/5). Single copy price varies. This issue $3. Subscription price $17.00 a year; $4.25 additional for foreign mailing.

UNITED STATES GOVERNMENT PRINTING OFFICE, WASHINGTON : 1973